frontiers | Research Topics

Extreme environmental microbial products: Structures, functions, biosynthesis

Edited by
Junfeng Wang, Xian-Wen Yang, Li Liao and Martina Cappelletti

Published in
Frontiers in Microbiology

ISSN 1664-8714
ISBN 978-2-83251-701-7
DOI 10.3389/978-2-83251-701-7

About Frontiers

Frontiers is more than just an open access publisher of scholarly articles: it is a pioneering approach to the world of academia, radically improving the way scholarly research is managed. The grand vision of Frontiers is a world where all people have an equal opportunity to seek, share and generate knowledge. Frontiers provides immediate and permanent online open access to all its publications, but this alone is not enough to realize our grand goals.

Frontiers journal series

The Frontiers journal series is a multi-tier and interdisciplinary set of open-access, online journals, promising a paradigm shift from the current review, selection and dissemination processes in academic publishing. All Frontiers journals are driven by researchers for researchers; therefore, they constitute a service to the scholarly community. At the same time, the *Frontiers journal series* operates on a revolutionary invention, the tiered publishing system, initially addressing specific communities of scholars, and gradually climbing up to broader public understanding, thus serving the interests of the lay society, too.

Dedication to quality

Each Frontiers article is a landmark of the highest quality, thanks to genuinely collaborative interactions between authors and review editors, who include some of the world's best academicians. Research must be certified by peers before entering a stream of knowledge that may eventually reach the public - and shape society; therefore, Frontiers only applies the most rigorous and unbiased reviews. Frontiers revolutionizes research publishing by freely delivering the most outstanding research, evaluated with no bias from both the academic and social point of view. By applying the most advanced information technologies, Frontiers is catapulting scholarly publishing into a new generation.

What are Frontiers Research Topics?

Frontiers Research Topics are very popular trademarks of the *Frontiers journals series*: they are collections of at least ten articles, all centered on a particular subject. With their unique mix of varied contributions from Original Research to Review Articles, Frontiers Research Topics unify the most influential researchers, the latest key findings and historical advances in a hot research area.

Find out more on how to host your own Frontiers Research Topic or contribute to one as an author by contacting the Frontiers editorial office: frontiersin.org/about/contact

Extreme environmental microbial products: Structures, functions, biosynthesis

Topic editors

Junfeng Wang — South China Sea Institute of Oceanology, Chinese Academy of Sciences (CAS), China

Xian-Wen Yang — Third Institute of Oceanography, State Oceanic Administration, China

Li Liao — Polar Research Institute of China, China

Martina Cappelletti — University of Bologna, Italy

Citation

Wang, J., Yang, X.-W., Liao, L., Cappelletti, M., eds. (2023). *Extreme environmental microbial products: Structures, functions, biosynthesis*. Lausanne: Frontiers Media SA. doi: 10.3389/978-2-83251-701-7

Table of contents

frontiers | Frontiers in Microbiology

TYPE Editorial
PUBLISHED 02 February 2023
DOI 10.3389/fmicb.2023.1122106

OPEN ACCESS

EDITED AND REVIEWED BY
Andreas Teske,
University of North Carolina at Chapel Hill, United States

*CORRESPONDENCE
Junfeng Wang
✉ wangjunfeng@scsio.ac.cn
Xianwen Yang
✉ yangxianwen@tio.org.cn
Li Liao
✉ liaoli@pric.org.cn

SPECIALTY SECTION
This article was submitted to Extreme Microbiology, a section of the journal Frontiers in Microbiology

RECEIVED 12 December 2022
ACCEPTED 17 January 2023
PUBLISHED 02 February 2023

CITATION
Wang J, Yang X, Liao L, Cappelletti M and Basen M (2023) Editorial: Extreme environmental microbial products: Structures, functions, biosynthesis.
Front. Microbiol. 14:1122106.
doi: 10.3389/fmicb.2023.1122106

Editorial: Extreme environmental microbial products: Structures, functions, biosynthesis

Junfeng Wang[1]*, Xianwen Yang[2]*, Li Liao[3]*, Martina Cappelletti[4] and Mirko Basen[5]

[1]CAS Key Laboratory of Tropical Marine Bio-Resources and Ecology/Guangdong Key Laboratory of Marine Materia Medica, South China Sea Institute of Oceanology, Chinese Academy of Sciences, Guangzhou, China, [2]State Key Laboratory Breeding Base of Marine Genetic Resources, Third Institute of Oceanography, State Oceanic Administration, Xiamen, China, [3]Key Laboratory for Polar Science, Ministry of Natural Resources, Polar Research Institute of China, Shanghai, China, [4]Department of Pharmacy and Biotechnology, University of Bologna, Bologna, Italy, [5]Institute of Biosciences, Faculty of Mathematics and Natural Sciences, University of Rostock, Rostock, Germany

KEYWORDS

extremophiles, antitumor, anti-inflammatory, pro-angiogenic, functional substances

Editorial on the Research Topic
Extreme environmental microbial products: Structures, functions, biosynthesis

Microbial products such as penicillin and cyclosporine and others have made phenomenal contributions to the health and wellbeing of people throughout the world. There is growing evidence that microbes can provide bioactive natural products for drug discovery and development, which account for half of all pharmaceuticals on the market. Nevertheless, as research progressed, untapped environmental microorganism resources became increasingly scarce. Chemical, ecological, and pharmacological investigations on microorganisms from extreme environments have increased significantly in recent years. Extreme habitats are characterized by extreme temperatures, ultraviolet (UV) radiation, pH, salt content, or other factors. Faced with multiple extreme environmental stresses, extremophiles have evolved specialized genetic capabilities to produce novel bioactive products. Microbial products from extreme environments have important roles in adaptation to environments, in species communication, and in biotechnological as well as pharmaceutical applications.

Extremophiles continue to attract the attention of chemists, ecologists and pharmacologists, resulting in the stimulation of numerous initiatives to study the structure, synthesis and pharmaceutical applications of products from extreme environments. Under the Research Topic "Extreme environmental microbial products: Structures, functions, biosynthesis," a total of 11 articles were published, covering a variety of topics involving marine microorganisms including microbial isolation from different habitats and the discovery of novel, bioactive functional substances such as chaetofanixins A–E, adametizine C, streptocarbazoles F–H, and QsGH13 (a alpha-glycosidase). Also, new microbial enzymes were reported, focusing on structure, function, and thermo-halo-alcohol adaptation of enzymes in extreme environments.

Halotolerant and acidotolerant fungi isolated from mangroves have been extensively studied (Cai et al.; Ren et al.; Wang W. et al.; and Wang G. et al.). Cai et al. investigated the antitumor and anti-inflammatory components isolated from the mangrove soil-derived fungi *Penicillium ludwigii* SCSIO 41408. Adametizine C displayed significant inhibitory activities against LPS-induced NF-κB with IC_{50} value of 8.2 μM. Ren et al. evaluated the potential anti-inflammatory candidate, 5-chloro-6-hydroxymellein, which further alleviated

the pathological lung injury of lipopolysaccharide (LPS)-administrated mice and protected RAW264.7 macrophages against LPS-induced inflammation through the phosphatidylinositol 3-kinase/protein kinase B (PI3K/AKT) pathway *in vivo*. Also, eschscholin B and daldilene A showed significant cell-based anti-inflammatory activities reported by Wang G. et al.. Further more, eschcholin B suppressed the release of LPS-induced iNOS and COX-2 inflammatory cytokines and the MAPK and NF-κB signaling pathways participated in the regulation of LPS-induced inflammatory processes. Wang W. et al. discovered seven pairs of azaphilones *E*/*Z* isomers from the mangrove-derived fungus *Penicillium sclerotiorum* HY5. Among them, some azaphilone derivatives exhibited potent phytotoxicity against the growth of radicle and plumule on *Amaranthus retroflflexus* L.

In the past 50 years, about 20,000 natural products have been reported from marine microorganisms. However, the number of natural products reported from deep-sea microorganisms is very low, and microorganisms from hadal trench environments (>6,000 m) are seldom investigated. Fan et al. isolated a fungal strain YP-106, identified as *Chaetomium globosum* from the hadal seawater collected at a depth of 6,215 m from Yap Trench in the western Pacific Ocean. Chaetofanixins A-E produced by this fungus were identified as azaphilone derivatives characterized by a pyranoquinone oxabicyclic skeleton. Using the zebrafish screening model, new chaetofanixins A–E showed excellent pro-angiogenic activities in a dose-dependent manner, possessing the potential to be developed as natural cardiovascular disease agents.

Xia et al. identified a fungus *Pestalotiopsis* sp. XWS03F09 isolated from the sponge *Phakellia fusca* collected in Xisha Islands; secondary metabolites from this strain included the ergosterol compound LH-1. Melanoma cells were more sensitive to LH-1 than other cancer cell lines. The IC50 value of LH-1 on B16-F10 melanoma cells was 16.57 μM at 72 h, compared to IC50 values >60 μM at 72 h for other cell lines. Further investigations of biological activities against melanoma *in vitro* and *in vivo* showed that LH-1 could inhibit proliferation and migration of cancer cells, induce apoptosis *via* the mitochondria apoptotic pathway, and upregulate *OBSCN* gene expression in melanoma cells.

Pelagic microorganisms can produce highly active secondary metabolites. Xia et al. identified a fungus *Pestalotiopsis* sp. XWS03F09 isolated from the sponge *P. fusca* collected in Xisha Islands; secondary metabolites from this strain included the ergosterol compound LH-1. Melanoma cells were more sensitive to LH-1 than other cancer cell lines. The IC_{50} value of LH-1 on B16-F10 melanoma cells was 16.57 μM at 72 h, compared to IC_{50} values >60 μM at 72 h for other cell lines. Further investigations of biological activities against melanoma *in vitro* and *in vivo* showed that LH-1 could inhibit proliferation and migration of cancer cells, induce apoptosis *via* the mitochondria apoptotic pathway, and upregulate *OBSCN* gene expression in melanoma cells.

The Yellow mushroom (*Floccularia luteovirens*) grows widely on the Qinghai-Tibet Plateau, a high-altitude habitat characterized by extreme ultraviolet irradiation. Guo et al. investigated the adaptation of *F. luteovirens* to strong UV irradiation, for example the production of the vitamin riboflavin.

Bacteria are important producers of antibiotics and other allopathic active substances. Under the guidance of global natural product social (GNPS) molecular networking, Cui et al. identified a staurosporine-producing strain, *Streptomyces* sp. OUCMDZ-5380, and characterized three new indolocarbazoles as streptocarbazoles F–H. These three new compounds showed a selective antiproliferation on the acute myeloid leukemia cell line MV4–11 with the IC_{50} values of 0.81, 0.55, and 1.88 μM, respectively. Wen et al. isolated the *Bacillus amyloliquefaciens* strain W0101 with remarkable antifungal activity from a sediment sample of the Arctic Ocean. An antifungal peptide (W1) with potential applicability in the biocontrol of plant diseases was purified and shown to be derived from the fragment of preprotein translocase subunit YajC.

Some biological enzymes, derived from special habitats, have some unique physical and chemical functions. Zhai et al. detected a novel GH13 family α-glucosidase, QsGH13, from the deep-sea bacterium *Qipengyuania seohaensis* sp. SW-135. QsGH13 is highly substrate specific and only hydrolyzes sugars containing alpha-1,4 glucoside bonds. Cen et al. reported two loops of exo-inulinase InuAMN8, which was isolated from a cold-adapted bacterium *Arthrobacter* sp. MN8. Inulin is an abundant water-soluble storage polysaccharide after starch in nature. Elucidation of the structure of exo-inulinases is helpful for its application in the hydrolysis of inulin.

Author contributions

All authors listed have made a substantial, direct, and intellectual contribution to the work and approved it for publication.

Funding

This work was financially supported by the Finance Science and Technology Project of Hainan Province (ZDKJ202018), National Natural Science Foundation of China (Nos. 41976224 and 41776169), and Guangdong MEPP Funds (No. GDNRC [2021]48).

Conflict of interest

The authors declare that the research was conducted in the absence of any commercial or financial relationships that could be construed as a potential conflict of interest.

Publisher's note

frontiers in Microbiology

ORIGINAL RESEARCH
published: 03 March 2022
doi: 10.3389/fmicb.2022.849585

Structure and Function Insight of the α-Glucosidase QsGH13 From *Qipengyuania seohaensis* sp. SW-135

Xingyu Zhai[1,2], Kaijuan Wu[1], Rui Ji[3], Yiming Zhao[2], Jianhong Lu[2], Zheng Yu[2], Xuewei Xu[4] and Jing Huang[1]**

[1] Department of Parasitology, School of Basic Medical Science, Central South University, Changsha, China, [2] Department of Microbiology, Xiangya School of Medicine, Central South University, Changsha, China, [3] State Key Laboratory of Genetic Engineering, School of Life Sciences, Fudan University, Shanghai, China, [4] Key Laboratory of Marine Ecosystem Dynamics, Second Institute of Oceanography, Ministry of Natural Resources, Hangzhou, China

The α-glucosidases play indispensable roles in the metabolic mechanism of organism, prevention, and treatment of the disease, and sugar hydrolysis, and are widely used in chemical synthesis, clinical diagnosis, and other fields. However, improving their catalytic efficiency and production to meet commercial demand remains a huge challenge. Here we detected a novel GH13 family α-glucosidase, QsGH13, from the deep-sea bacterium *Qipengyuania seohaensis* sp. SW-135. QsGH13 is highly substrate specific and only hydrolyzes sugars containing alpha-1,4 glucoside bonds. For example, its enzymatic activity for *p*-nitrophenyl-α-D-glucopyranoside was 25.41 U/mg, and the K_m value was 0.2952 ± 0.0322 mM. The biochemical results showed that the optimum temperature of QsGH13 is 45°C, the optimum pH is 10.0, and it has excellent biological characteristics such as alkali resistance and salt resistance. The crystal structure of QsGH13 was resolved with a resolution of 2.2 Å, where QsGH13 is composed of a typical TIM barrel catalytic domain A, a loop-rich domain B, and a conserved domain C. QsGH13 crystal belonged to the monoclinic space group $P2_12_12_1$, with unit-cell parameters a = 58.816 Å, b = 129.920 Å, c = 161.307 Å, α = γ = β = 90°, which contains two monomers per asymmetric unit. The β → α loop 4 of QsGH13 was located above catalytic pocket. Typical catalytic triad residues Glu202, Asp266, and Glu329 were found in QsGH13. The biochemical properties and structural analysis of QsGH13 have greatly improved our understanding of the catalytic mechanism of GH13 family. This study provides new ideas to broaden the application of α-glucosidase in alcohol fermentation, glycolysis, and other industries.

Keywords: QsGH13, α-glucosidase, characterization, β → α loop, crystal structure

OPEN ACCESS

Edited by:
Martina Cappelletti, University of Bologna, Italy

Reviewed by:
Martin González-Andrade, National Autonomous University of Mexico, Mexico
Muhammad Aleem Ashraf, Khwaja Fareed University of Engineering and Information Technology (KFUEIT), Pakistan

***Correspondence:**
Jing Huang
jing_huang@csu.edu.cn
Xuewei Xu
xuxw@sio.org.cn

Specialty section:
This article was submitted to Extreme Microbiology, a section of the journal Frontiers in Microbiology

Received: *06 January 2022*
Accepted: *21 January 2022*
Published: *03 March 2022*

Citation:
Zhai X, Wu K, Ji R, Zhao Y, Lu J, Yu Z, Xu X and Huang J (2022) Structure and Function Insight of the α-Glucosidase QsGH13 From Qipengyuania seohaensis sp. SW-135. Front. Microbiol. 13:849585. doi: 10.3389/fmicb.2022.849585

INTRODUCTION

The CAZy database[1] classifies proteins into glycoside hydrolases (GHs), glycosyl transferases, polysaccharide lyases, carbohydrate esterases, auxiliary activities, and carbohydrate-binding modules based on amino acid sequence similarity and spatial structure of their catalytic structural domains (Henrissat, 1991; Cantarel et al., 2009). The GH13 family belongs to the GHs members and

[1] http://www.cazy.org/

is mainly composed of $(\beta/\alpha)_8$-barrel fold catalytic domain A, a loop-rich domain B, and a conserved domain C (Banner et al., 1975). The enzymes of the GH13 family catalyze reactions mainly through a double-displacement mechanism, in which catalytic nucleophilic (Asp) and acid/base catalyst (Glu) play an essential role (McCarter and Withers, 1994).

The α-glucosidases (EC:3.2.1.20) are members of GHs and are widely distributed in all organisms that are specific mainly for the exohydrolysis of α-1,4-glycosidic linkages at the non-reducing end of polysaccharides, such as maltooligosaccharides, and release α-D-glucose. Alternatively, it combines free glucose residues with the α-1,4-glycosidic linkages in oligosaccharides to form α-1,6-glycosidic linkages, and obtain non-fermentative oligosaccharides (McCarter and Withers, 1994; Hondoh et al., 2008). The α-glucosidases play key roles in clinical detection, prevention, and treatment of the disease, metabolic mechanism of the organism, and alcohol fermentation, sugar hydrolysis, widely used in chemical fields such as chemical synthesis. Most commercially used α-glucosidases are produced by fungi, but they all have certain limitations, such as moderate thermostability, high acidic pH requirements, many byproducts, and slow catalytic activity, which greatly increase production cost. Therefore, it is urgent to find novel α-glucosidase to improve glucose production and catalytic efficiency.

In this study, the gene *qsgh13* encoding α-glucosidase (QsGH13) was identified from the marine bacteria *Qipengyuania seohaensis* sp. SW-135 (*Qs*. SW-135) and heterologously expressed in soluble form in *Escherichia coli* BL21(DE3) plus. Biochemical results showed that QsGH13 has strong substrate specificity and excellent biological properties such as alkali and salt resistance. Structural analysis showed that QsGH13 has a typical TIM barrel catalytic domain A, the loop-rich domain B, and the conserved domain C. The β → α loop 4 of QsGH13, located above the catalytic pocket was significantly different from other enzymes in GH13, suggesting that it is related to substrate specificity (Noguchi et al., 2003). Investigation into the biochemical characteristics and structure of QsGH13 might greatly improve our understanding of the molecular mechanism of the GH13 family and further indicate their physiological and biochemical basis for adapting to extreme conditions, thus, improving the industrial application value of α-glucosidase.

MATERIALS AND METHODS

Bioinformatic Analysis

The amino acid sequences with the first 100 similarities to QsGH13 sequences were obtained using NCBI BLASTp.[2] Clustal was used for amino acid multiple sequence alignment of QsGH13 and its homologs[3] (Larkin et al., 2007). Secondary structure alignment results were obtained using ESpript based on multiple sequence alignment results and QsGH13 spatial coordinates[4] (Robert and Gouet, 2014). The maximum likelihood estimation (MLE) in MEGA X was used to construct the phylogenetic tree (Kumar et al., 2018).

Cloning, Expression, and Purification of Recombinant Proteins

Qs. SW-135 (basionym: *Erythrobacter seohaensis* sp. SW-135) (Taxonomy ID: 266951, GenBank Accession: GCA_002795865.1) (Kwon et al., 2007; Xu et al., 2020; **Supplementary Figure 1**), belonging to the family Erythrobacteraceae, was isolated from deep-sea sediment samples that were collected from the East Pacific Seamount region. The QsGH13-encoding gene (*qsgh13*) was identified and cloned from the genome of *Qs.* SW-135. To be specific, the *qsgh13* gene was amplified by PCR (forward: 5′-GGCGGATCCATGAGCGGCAAGCTGCCTTG-3′, *Bam*HI, reverse: 5′-GCGGAGCTCTCATGTGTCGGTCTCCAGGATGA-3′, *Sac*I) and inserted into the expression vector pSMT3 (Li et al., 2012) using the *Bam*HI and *Sac*I restriction sites.

The recombinant *E. coli* BL21(DE3) plus/pSMT3-*qsgh13* was cultured in LB medium containing 50 μg/ml of kanamycin and 34 μg/ml of chloramphenicol at 37°C. When the OD_{600} reached 0.8, the recombinant protein expression was induced by 0.5 mM isopropyl-β-D-thiogalactopyranoside (IPTG) for 20 h at 16°C (Shen et al., 2019). Cells were harvested by centrifugation at 5,000 rpm for 15 min at 4°C. The cell precipitation was resuspended in a lysis buffer [50 mM Tris, pH 8.0; 500 mM NaCl; 1% (v/v) glycerol; 10 mM imidazole; 1 mM β-Me; 0.2 mM PMSF] and was disrupted on ice with an ultrasonic crusher (SCIENIZ, Ningbo, China). The separated supernatant was purified by Ni-NTA affinity chromatography. After the recombinant protein with 6xHis-Sumo tag was digested with Ulp1 enzyme, the target protein was obtained in the flow-through fractions and was concentrated with a 50-kDa concentrator. Then QsGH13 protein was purified in a buffer (20 mM Tris, pH 7.4; 100 mM NaCl; 2 mM DTT) by gel-filtration chromatography (Superdex 200 16/600, GE, United States). The protein was determined by SDS-PAGE, and the concentration was measured by the method of Bradford with bovine serum albumin (BSA) as a standard (Huang et al., 2016).

Functional Characterization

The enzymatic activity and substrate specificity of wild-type QsGH13 were determined by p-nitrophenol method (Irma et al., 1992). The 100-μl standard reaction buffer consisted of 1 mM *p*NPαGlu, 20 mM Gly-NaOH buffer (pH 10.0), and an appropriate amount of purified enzyme. The enzymatic activity was determined by continuously measuring the amount of released *p*-nitrophenol at the absorbance of 405 nm using Multiskan FC (ThermoFisher, MA, United States), at 45°C, and the inactivated enzyme solution was used as the blank control. All results were carried out in three independent experiments. The absorbance of 405 nm was measured every 2 min, and the total reaction time was 30 min.

The substrate specificity of the enzyme was determined using *p*-nitrophenyI-β-D-glucopyranoside (*p*NPβGlu), *p*-nitrophenyl-α-D-glucopyranoside (*p*NPαGlu), *p*NP-α-L-arabinopyranoside (*p*NPαArap), *p*-nitrophenyl

[2]https://blast.ncbi.nlm.nih.gov/Blast.cgi

[3]http://www.clustal.org/

[4]https://espript.ibcp.fr/ESPript/ESPript/esp_tutorial.php

-β-D-lactopyranoside (*p*NPβLac), *p*-nitrophenyI-α-D-galacto pyranoside (*p*NPαGal), *p*-nitrophenyI-β-D-galactopyranoside (*p*NPβGal), *p*-nitrophenyI-β-D-mannopyranoside (*p*NPβ Man), *p*-nitrophenyI-β-D-xylopyranoside (*p*NPβXyl), and *p*-nitrophenyI-β-D-cellobioside (*p*NPβCel) as substrates, respectively. All the substrates were purchased from Shanghai Yuanye Bio-Technology Co., Ltd.

The kinetic parameters were examined using *p*NPαGlu as a substrate at different concentrations varying from 0.025 to 2.0 mM. The Michaelis–Menten constant (K_m) and maximum velocity (V_{max}) were analyzed by the Michaelis–Menten equation using GraphPad Software (GraphPad prism5, United States) (Huang et al., 2019).

The optimum temperature of the enzyme was determined with different temperatures varying from 4 to 70°C. Buffers with different pH were used to determine the optimal pH of the enzyme, including 20 mM citrate buffer (pH 3.0–pH 6.5), 20 mM phosphate buffer (pH 6.5–pH 7.5), 20 mM Tris–HCl buffer (pH 7.5–pH 9.0), and 20 mM Gly-NaOH buffer (pH 9.0–pH 13.0).

The influence of metal ions on the enzyme activity was determined by adding 10 mM of cations (Ba^{2+}, Ca^{2+}, Co^{2+}, Cu^{2+}, K^{+}, Fe^{2+}, Fe^{3+}, Mg^{2+}, Mn^{2+}, Na^{+}, Ni^{2+}, Sr^{2+}, Zn^{2+}) and ethylene diamine tetraacetic acid (EDTA) to the standard reaction buffer. The effect of organic solvents on enzyme activity was investigated in the presence of 10% (v/v) acetonitrile, acetone, dimethyl sulfoxide, ethanol, formic acid, isopropanol, methanol, respectively. The influences of the detergents on enzyme activity were examined by using 10% (v/v) Triton X-100, Triton X-114, Tween 20, Tween 80, and SDS. The enzyme activity assay was carried out under optimal standard reaction buffer with 20 mM Gly-NaOH buffer (pH 10.0) at 45°C, and the enzyme activity in the blank group was defined as 100% without additives.

The salt tolerance of enzyme was measured in the presence of 1.0, 2.0, 3.0, 4.0, or 5.0 M NaCl, and the enzyme activity in the blank group without NaCl was defined as 100%. The tolerance of enzyme on products were tested by adding 0.5, 1.0, 1.5, 2.0, 2.5, and 3.0 M glucose to 20 mM Gly-NaOH buffer (pH 10.0). In the absence of the substrate, the thermostability of the enzyme was determined by measuring the residual activity at the optimum conditions after incubating the enzyme for different periods of time at 4°C, respectively. Similarly, in the absence of the substrate, the alkali resistance of enzyme was measured by testing the residual activity at the optimum conditions after incubating the enzyme for 2, 24 h in buffers of different pH at 4°C.

High-Performance Liquid Chromatography

The enzymatic activities of QsGH13 toward maltose, sucrose, isomaltose, panose, and isommaltose were determined by HPLC. First, glucose, maltose, isomaltose, panose, and isommaltose trisaccharide were dissolved in mobile phase to establish the standard curve. Second, the reaction buffer contained 15% substrate (w/v), 1 mg/ml of QsGH13, and 20 mM Gly-NaOH buffer (pH 10.0), which were used to catalyze the reaction at 45°C. Meanwhile, QsGH13 in the reaction buffer was replaced by the deactivation of QsGH13, which served as a negative control. The reaction of the samples were terminated by high-temperature denaturation, and the supernatant was collected by centrifugation at 12,000 rpm for 10 min. The samples were detected by Thermo Scientific™ Hypersil™ APS-2 HPLC with 72% acetonitrile and 28% water as mobile phase. Glucose concentration was calculated according to the standard curve.

Data Collection for Crystallographic Structure Determination

The purified QsGH13 was concentrated to 10 mg ml^{-1} using Amicon Ultra 50K ultrafiltration devices (Merck Millipore, Darmstadt, Germany). The crystallization of QsGH13 was prepared by handing drop vapor diffusion methods by mixing 1 μl of QsGH13 (10 mg ml^{-1}) with an equal volume of reservoir solution at 4°C. It was grown in a condition of 0.1 M Tris–HCl (pH 8.5), 0.2 M NaCl, and 20% PEG 3,350. The crystals were briefly soaked with the cryoprotectant solution, and then flash cooled directly in liquid nitrogen at −173°C. The x-ray diffraction data were collected at the BL17U beamline of SSRF (Shanghai Synchrotron Radiation Facility, Shanghai, China). The data were processed and scaled using *XDS* (Kabsch, 2010). The collected data and processing details are shown in **Table 1**.

TABLE 1 | Data collection and refinement statistics of QsGH13.

Items	QsGH13
Data collection	
Wavelength	0.9793
Resolution range (Å)	50.00–2.20 (2.80–2.20)
Space group	$P2_12_12_1$
a, b, c (Å)	*a* = 58.816, *b* = 129.920, *c* = 161.307
α, γ, β (°)	α = γ = β = 90.00
Total reflections	841,069
Unique reflections	121,073
Completeness (%)	99.40 (97.70)
R_{merge}	11.5 (24.6)
I/σ (I)	14.36 (6.55)
$CC_{1/2}$	99.3 (93.2)
Refinement statistics	
Resolutions (Å)	34.28–2.20 (2.33–2.20)
Completeness (%)	99.54
Reflection used in refinement	63,429 (6,188)
Final R_{work}	0.2112 (0.2252)
Final R_{free}	0.2678 (0.2785)
No. of atoms	
Water	771
Protein residues	1,036
Total	9,014
RMSD	
Bond lengths (Å)	0.013
Angles (°)	1.620
Average B-factor ($Å^2$)	23.95
Ramachandran plot	
Ramachandran favored (%)	95.41
Ramachandran allowed (%)	4.10
Ramachandran outliers (%)	0.49
Rotamer outliers (%)	1.30
PDB code	7VOH

The structure of QsGH13 was determined by molecular replacement method with Phaser (McCoy et al., 2007), using the crystal structure of α-glucosyltransferase XgtA from *Xanthomonas campestris* WU-9701 (PDB entry: 6AAV, 51% identity to QsGH13) (Watanabe et al., 2020) as a search model. The refinement data of QsGH13 was performed using REFMAC and Phenix (Liebschner et al., 2019). Coot was used to further modify and adjust the structure (Emsley and Cowtan, 2004). The refinement statistics data of QsGH13 are shown in **Table 1**.

Structure Visualization

The disordered area of QsGH13 sequence was predicted using IUPred2A.[5] The catalytic pocket of QsGH13 was predicted using POCASA.[6] The visualization of the tunnel in the QsGH13 structure used CAVER 3.0 PyMol plugin. The docking model between QsGH13 and its substrate was predicted with AutoDock 4 (Morris et al., 2009). All of the 3D structures were analyzed and drawn using PyMOL program (Version 2.0 Schrödinger, LLC).

[5]https://iupred2a.elte.hu/plot_new

[6]http://g6altair.sci.hokudai.ac.jp/g6/service/pocasa/

RESULTS

Cloning, Expression, and Purification of QsGH13

Nucleotide sequence analysis showed that the open reading frame of 1,587 bp *qsgh13* gene sequence from deep-sea sediment metagenomic screening encodes a protein of 528 amino acids with a theoretical molecular weight of 59.3 kD. Phylogenetic tree sequence analysis based on NCBI, PDB, and CAZy databases showed that the protein QsGH13 belongs to the GH13 family (**Supplementary Figure 1**), and predicted that the protein QsGH13 had α-glucosidase characteristics. To explore the physicochemical characterizations of protein QsGH13, we constructed the gene *qsgh13* into the recombinant plasmid with an N-terminal His_6-SUMO label in *E. coli*

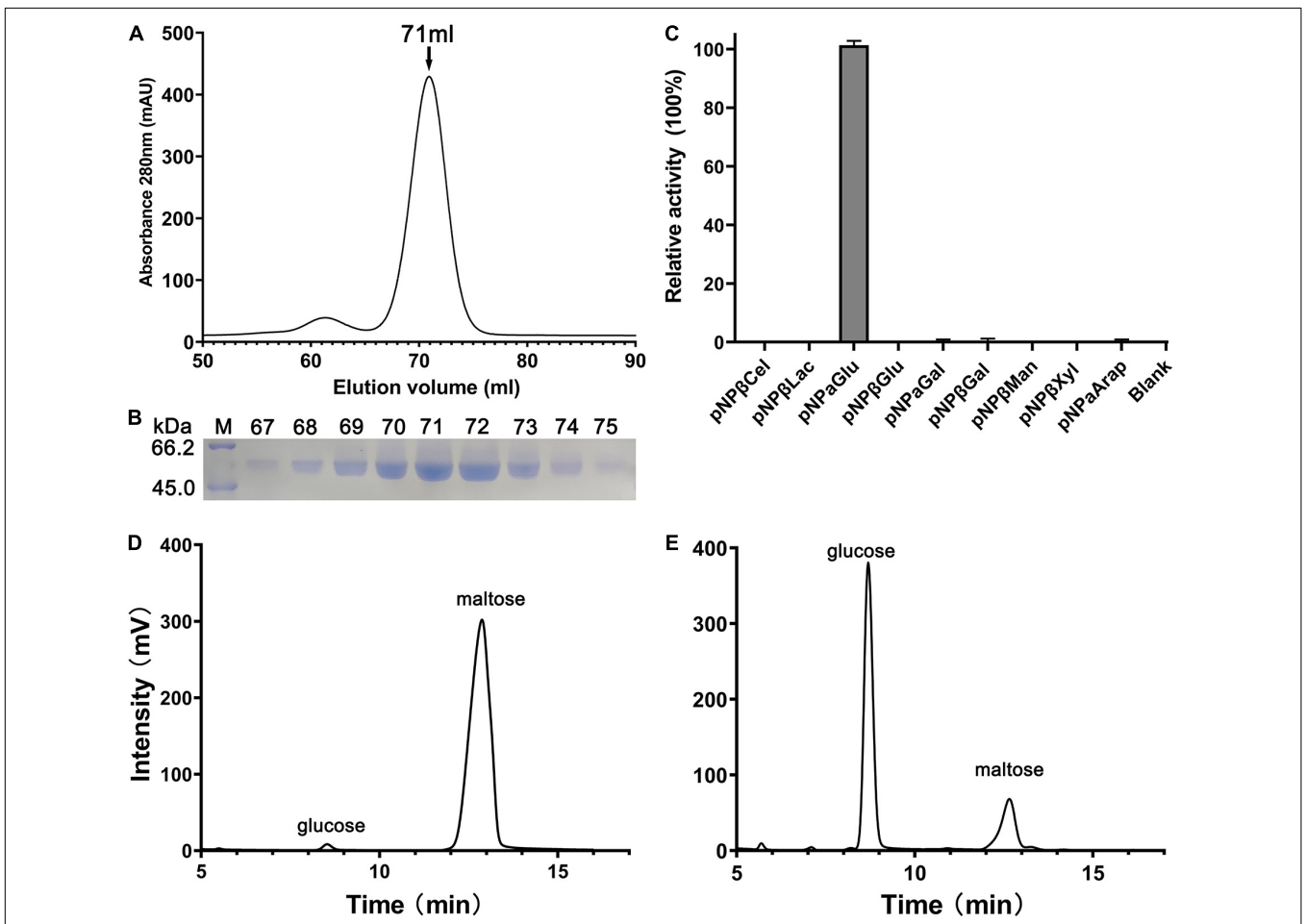

FIGURE 1 | Purification and substrate specificity of QsGH13. **(A)** The QsGH13 protein was purified by gel-filtration chromatography, and it was eluted at the peak of 71 ml. **(B)** The QsGH13 protein was determined by SDS-PAGE. **(C)** The substrate specificity of the enzyme was determined using different substrates. **(D,E)** The enzymatic activities of QsGH13 toward maltose was determined by HPLC. Maltose (substrate) and glucose (product) came out at the peak positions of 12.723 and 8.831 min, respectively. Panel **(D)** is before the reaction, and Panel **(E)** is after the reaction.

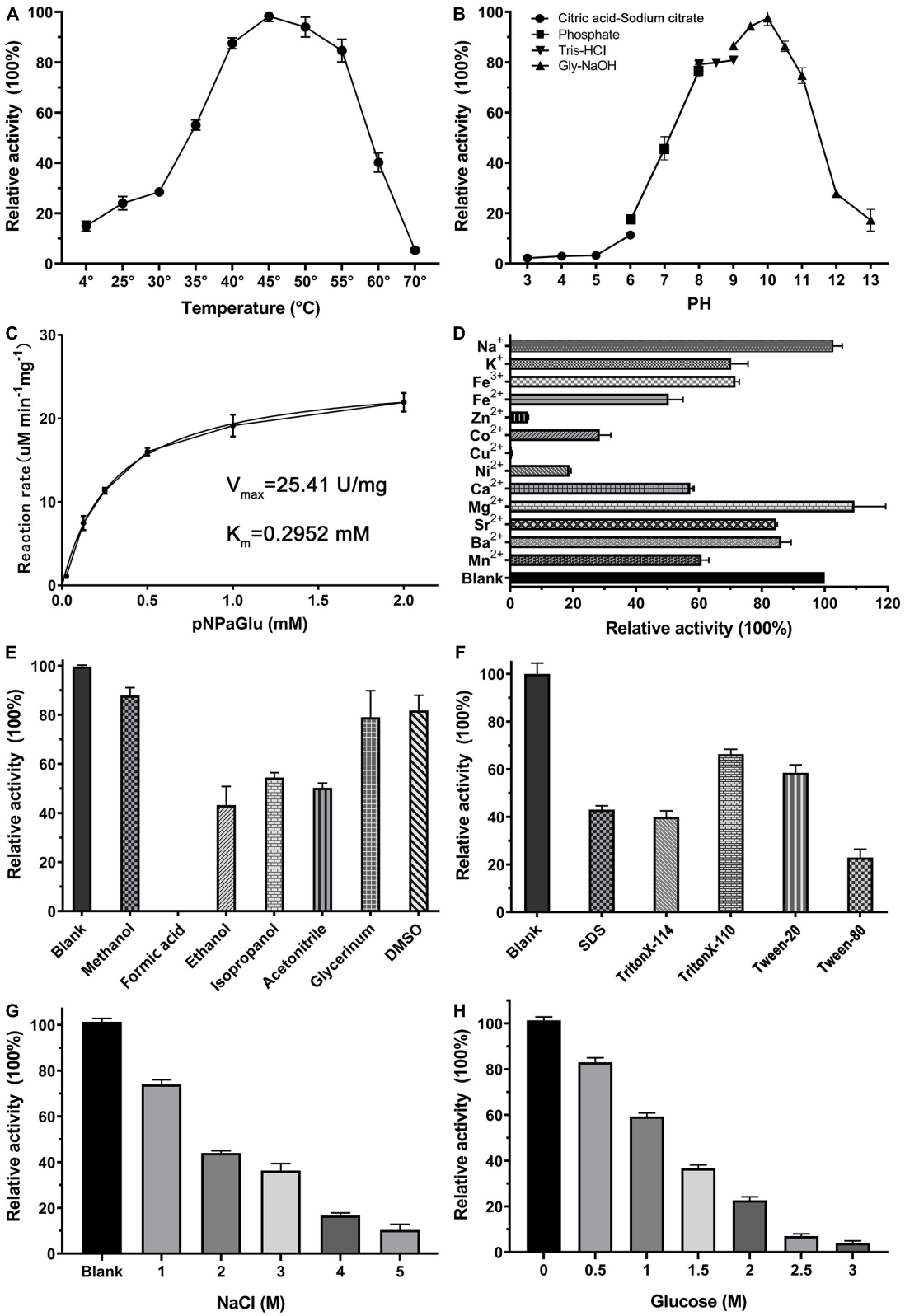

FIGURE 2 | Biochemical characterization of QsGH13. **(A,B)** The effect of temperature and pH on enzyme activity of QsGH13. The value obtained at 45°C and pH 10.0 was taken as 100%, respectively. **(C)** The specific activity of QsGH13. **(D–H)** Effects of different metal ions (10 mM), detergents [10% (v/v)], organic solvents [10% (v/v)], NaCl concentration, and glucose concentration on the enzymatic activity. The values of blank control were taken as 100%.

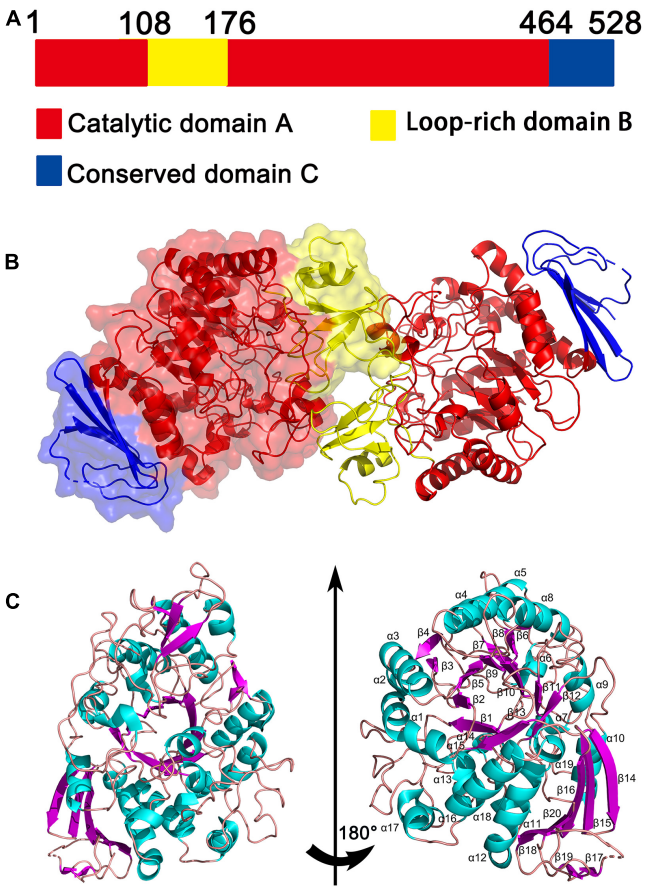

FIGURE 3 | The overall structure of QsGH13. **(A)** QsGH13 is composed of the catalytic domain A (red), loop-rich domain B (yellow), and conserved domain C (blue). **(B)** Schematic of the overall structure of the CmGH1 protein. **(C)** Cartoon representation of QsGH13 with the labeled secondary structure elements. α-Helices were shown in magenta; β-strands were denoted as lake blue arrows.

DH5α and expressed the protein QsGH13 in *E. coli* BL21 (DE3) plus. Cells were cultured and enriched, and protein His_6-SUMO-QsGH13 was extracted. After the His_6-SUMO tag was removed by Ulp1 enzyme, the protein QsGH13 was purified by gel-filtration chromatography to 95% homogeneity. Pure QsGH13 (12.6 ± 2.9 mg) was obtained from 1-L cultures. SDS-PAGE was used to show the molecular weight of QsGH13 (**Figures 1A,B**). QsGH13 was found to specifically hydrolyze *p*-nitrophenyl-α-D-glucopyranoside (*p*NPαGlu), but no other substrates (**Figure 1C**). The enzymatic activities of QsGH13 toward maltose was determined by HPLC. Maltose (substrate) and glucose (product) came out at the peak positions of 12.68 and 8.69 min, respectively (**Figures 1D,E** and **Supplementary Figure 2**). Therefore, QsGH13 was identified as α-glucosidase.

Biochemical Characterization of QsGH13

We have studied the optimum reaction conditions of QsGH13 toward *p*NPαGlu. QsGH13 was able to maintain 80% catalytic activity toward *p*NPαGlu at a temperature range of 40–55°C and a pH range of 8.0–11.0; QsGH13 showed the highest catalytic activity at 45°C and pH 10.0 (**Figures 2A,B**). The catalytic activity of QsGH13 was almost unchanged when stored at 4°C for 24 h (**Supplementary Figure 3A**). The catalytic activity of QsGH13 was decreased with the increase in incubation time in different pH buffers (**Supplementary Figure 3B**). The enzymatic activity of QsGH13 was 25.41 U/mg, and the K_m value was 0.2952 ± 0.0322 mM (**Figure 2C**).

Furthermore, we investigated the tolerance ability of QsGH13 to the addition of different cations, detergents, organic solvents, and different concentrations of NaCl and glucose added into the reaction buffer under optimum temperature and pH conditions (**Figures 2D–H**). The α-glucoside activity of QsGH13 was completely eliminated with the addition of Cu^{2+}, and only about 10–30% was retained with Zn^{2+}, Ni^{2+}, Co^{2+}, and 50–80% activity remained with K^{+}, Fe^{2+}, Fe^{3+}, and the activity of QsGH13 reached more than 100% with Mg^{2+}, Na^{+}. Moreover, the α-glucosidase activity of QsGH13 was comparative with the blank under the addition of 10% (v/v) organic solvents (methanol, formic acid, ethanol, isopropanol, acetonitrile, glycerol, and DMSO) or 10% (v/v) detergent (SDS Triton X-T114, Triton X-100, Tween20, and Tween80); it was attenuated. Especially, it is completely inactivated after the addition of formic acid (**Figures 2E,F**). In addition, the

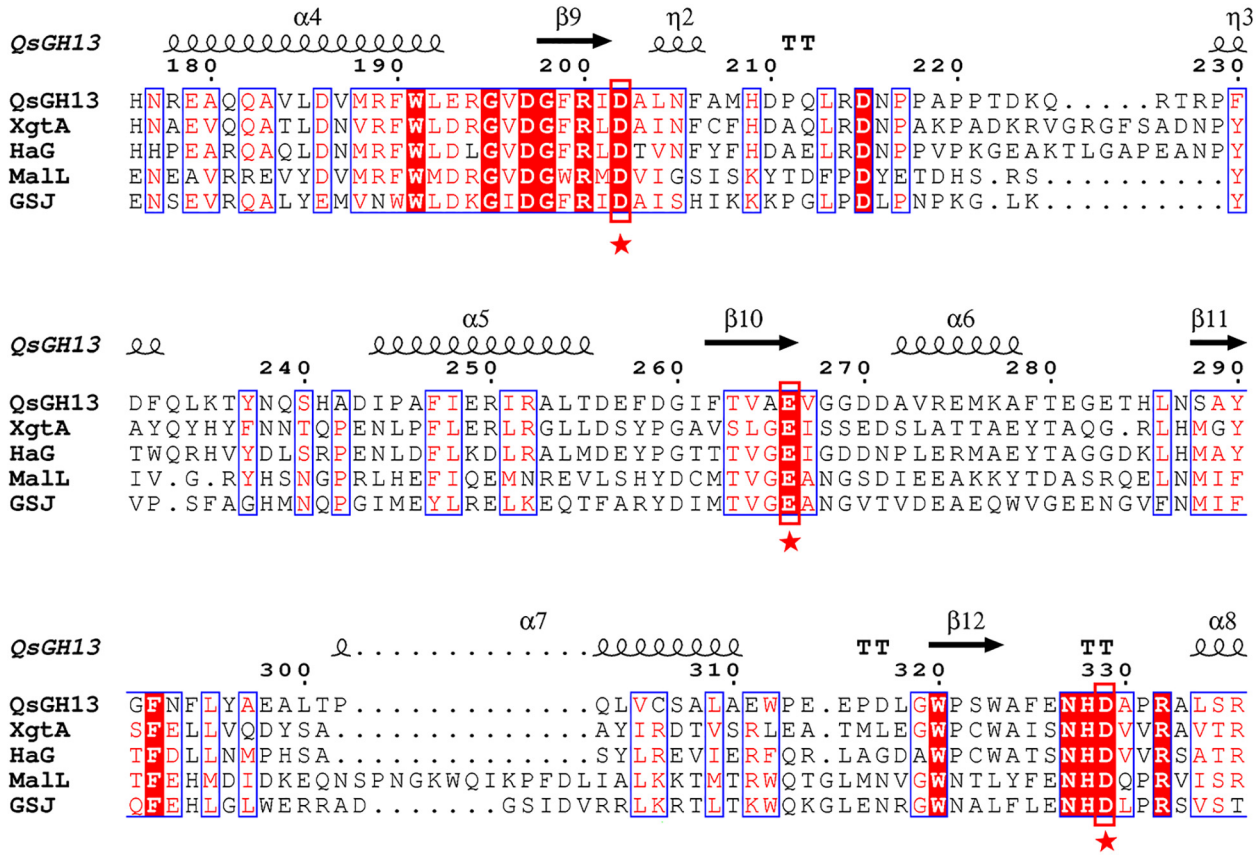

FIGURE 4 | Multiple sequence alignment of QsGH13 and other members of the GH13 family. The sequences include alpha-glucosyl transfer enzyme XgtA from *Xanthomonas campestris* (PDB ID:6AAV), alpha-glucosidase HaG from *Halomonas* sp. H11 (PDB ID:3WY1), oligo-1,6-glucosidase MalL from *Bacillus subtilis* subsp. subtilis (PDB ID:4M56), and alpha-glucosidase GSJ from *Geobacillus* sp. HTA-462 (PDB ID: 2ZE0). The conserved catalytic residues in the GH13 family were marked with a red box. The asterisk represents the catalytic residue.

α-glucosidase activity of QsGH13 was decreased with the increase in NaCl concentration. The α-glucosidase activity of QsGH13 was less than 40% of the blank group under the addition of 4 M NaCl (**Figure 2G**). QsGH13 still retained 30% activity compared with the blank group under the condition of 2 M glucose, but with an increase in glucose concentration, its activity was gradually abolished (**Figure 2H**).

The Overall Structure of QsGH13

The crystal structures of QsGH13 molecules were fully built to 2.2-Å resolution with the satisfied R_{work} and R_{free} values of 21.83 and 27.38%, respectively. According to the diffraction dataset, the QsGH13 crystal belongs to the monoclinic space group $P2_12_12_1$, with unit-cell parameters a = 58.815 Å, b = 129.920 Å, c = 161.304 Å, α = γ = β = 90°, which contains two monomers per asymmetric unit (**Table 1**). Phylogenetic tree analysis showed that QsGH13 belonged to α-glucosidase (EC 3.2.1.20), GH13 family, subfamily 23 (**Supplementary Figure 1**). QsGH13 has typical and conserved characteristics of the GH13 family (**Figure 3A**), where the catalytic domain A (residues 1–107, 176–463) is composed of a typical TIM barrel, sandwiched between the loop-rich domain B and the conserved domain C, and it is mainly composed of (β/α) eight-barrel structures, including eight α-helical and eight β-fold. The loop-rich domain B (residues 108–175) is derived from the domain A, including an α-helix and three β-fold, which are involved in the formation of QsGH13 dimers and forms catalytic pockets with domain A. Domain C (residues 464–525) is composed of multiple highly conserved β-folds that stabilizes the entire protein structure (Shen et al., 2015; **Figures 3B,C**). In order to achieve catalytic activity, dimers formed by two monomers are essential in the GH13 family of enzymes (Watanabe et al., 2020; Wangpaiboon et al., 2021). The QsGH13 monomers formed dimers mainly through five hydrogen bonds and 105 non-bonded contacts (**Supplementary Figure 4**). After the superposition of two monomers, the root-mean-square deviation (r.m.s.d.) value was 0.250 Å using the DALI server[7] (Holm, 2020). It shows that the two chains are very similar in structure and has no obvious biological significance, so we only study one monomer.

Multiple sequence alignments showed that QsGH13 had high homology with other members of the GH13 family, such as XgtA (PDB entry: 6AAV), an α-glucosyl transfer enzyme derived from *Xanthomonas* campestris WU-9701 (Watanabe et al., 2020);

[7]http://ekhidna2.biocenter.helsinki.fi/dali/

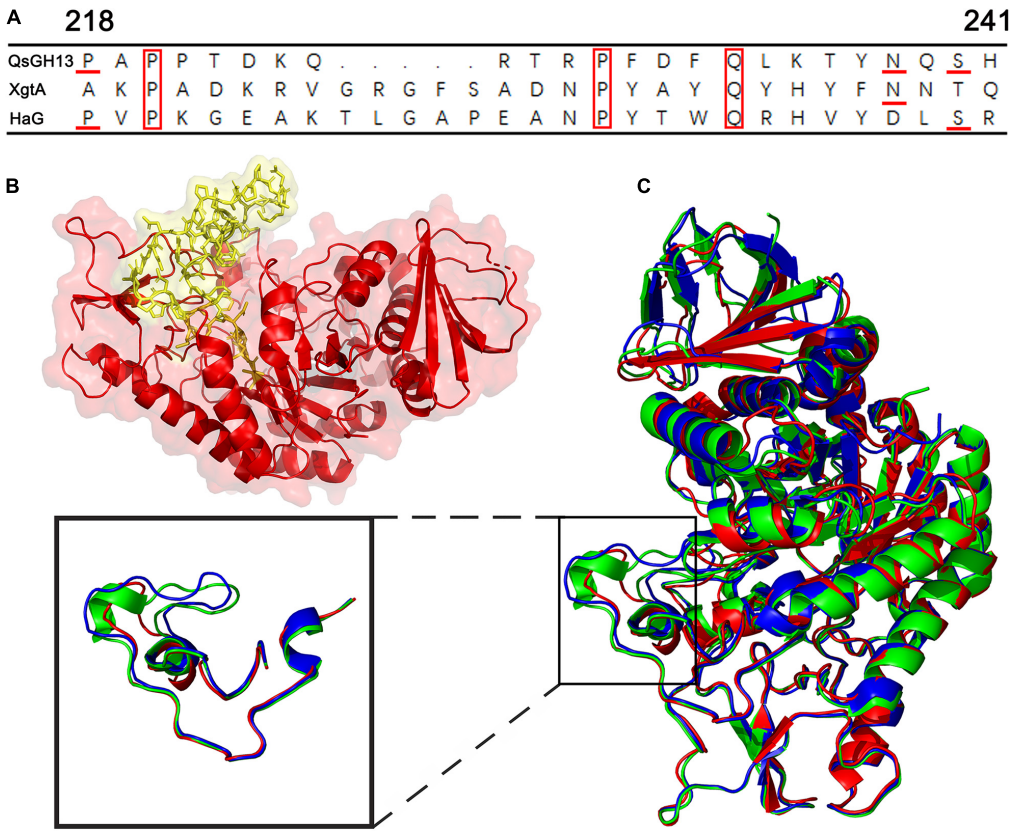

FIGURE 5 | The β → α loop 4 of QsGH13 in comparison with other proteins. **(A)** Superposition of amino acid residues of QsGH13 with amino acid residues of other proteins in the β → α loop 4; the red box represents the conserved amino acid residue. **(B)** Sticks represent the β → α loop 4 of QsGH13. **(C)** The monomer structure comparison of QsGH13 (red), XgtA (green), and HaG (blue). The blue box represents the β → α loop 4 domain of the protein. The β → α loop 4 domain of the protein; the black box represents the different structures of the three proteins.

HaG (PDB entry: 3WY1), an α-glucosidase produced from *Halomonas* sp. H11 (Shen et al., 2014); GSJ (PDB entry: 2ZE0), an α-glucosidase from *Geobacillus* sp. strain HTA-42 (Shirai et al., 2008); and MalL (PDB entry: 4m8u), an oligo-1,6-glucosidase from *bacillus subtilus* (Hobbs et al., 2013; **Supplementary Table 1**). The similarity of amino acid sequence from high to low is 51.3, 47.8, 39.6, and 37.5% (**Figure 4**).

The β → α Loop 4 of QsGH13

The overall structures of these GH13 families were similar through superimposing the overall structures of QsGH13 on XgtA, HAG, and GSJ, as indicated by r.m.s.d. values between Cαs in these three structures and the QsGH13 (0.680, 0.722, and 1.426 Å, respectively). However, as shown in **Figure 5A**, their β-α loop 4 regions were significantly different. The β → α loop 4 of QsGH13 is located above the catalytic pocket (**Figure 5B**), and it is associated with substrate specificity. It controls substrate entry by maintaining structural integrity around the catalytic pocket, and its amino acid sequence is poorly conserved. The β → α loop 4 of QsGH13 has some differences in composition and structure compared with the other three proteins. Amino acid sequence analysis showed that QsGH13 has the highest similarity with XgtA (51.3%); however, the amino acid sequence at 203–242 of QsGH13 just shows a homology of 17.4% (4/23 amino acids are identical) with that of XgtA and a homology of 21.7% with that of HaG. The size of β → α loop 4 of QsGH13 is between GSJ and HaG (**Figure 5C**). The β → α loop 4 of QsGH13 is demonstrated to be more dynamic than other regions of QsGH13 and the β → α loop 4 of HaG and XgtA by IUPred2A analysis[8] (Erdõs and Dosztányi, 2020). Furthermore, the more dynamic β → α loop 4 of QsGH13 may be involved in the acquisition and recognition of regulatory substrates (**Supplementary Figure 5**). The structural differences between QsGH13, XgtA, HaG, and GSJ at the β → α loop 4 region may, therefore, result in the differences observed for the formation of byproducts during α-glucosylation reaction.

The Catalytic Pocket of QsGH13

The predicted results of the QSGH13 catalytic pocket are consistent with the structure comparison results, and the channel volume is 672 $Å^3$, and the average VD is 3.70238 (**Figures 6A,B**). As shown in **Figure 6C**, the β → α loop 4 of HaG covers most of the entrance of the catalytic pocket, hinders the entry of long-chain substrates, and almost only hydrolyzes disaccharides (**Figure 6C**). Compared with HaG, the entrance

[8]https://iupred2a.elte.hu/plot_new

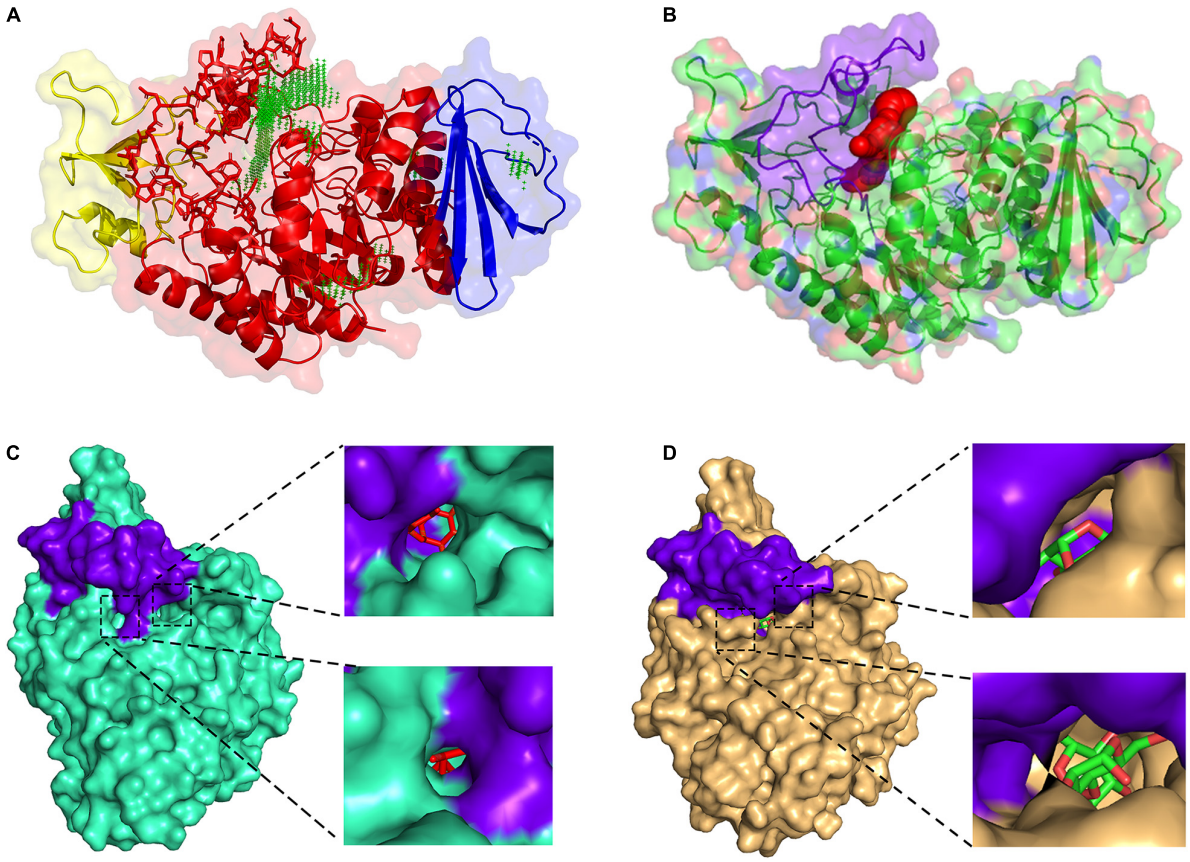

FIGURE 6 | Comparison of the catalytic pocket of QsGH13 and HaG. **(A)** QsGH13 catalytic pocket prediction result; green represents catalytic pocket. **(B)** The shape and size of the QsGH13 catalytic pocket. **(C)** The schematic diagram of the catalytic pocket of HaG. **(D)** The schematic diagram of the catalytic pocket of QsGH13. Purple represents the β → α loop 4 region; on the left is the overall schematic diagram of the protein catalytic pocket, the upper right is the right view of the catalytic pocket, and the lower right is the left view of the catalytic pocket.

region of the catalytic site of QsGH13 is relatively large, and the two tunnels are connected to the active center, but the channel is relatively narrow, and the larger substrate cannot pass through (**Figure 6D**).

QsGH13 forms a deep and narrow catalytic pocket of 14 residues in (β/α) eight-barrel structures (TIM) away from the dimeric interface. Among these residues, there are eight residues, including Tyr65, His105, Arg200, Glu266, Asp202, Phe292, His328, and Asp329, that are conserved in the GH13 family. Six residues, Asp62, Phe147, Phe166, Thr203, Phe206, and Arg396, are conserved between QsGH13 and HaG (**Figure 7A**). The enzymatic hydrolysis of glycosidic bond takes place *via* general acid catalysis that requires two critical residues. In the catalytic pocket of HaG, Asp202, Glu271 (3wy4-Gln271), and Asp333 constitute the catalytic site, of which Asp202 is the nucleophilic residue, Glu271 is the proton acceptor/donor, and Asp333 helps to stabilize Glu271 residue (**Figure 7B**). Similarly, the structure of QsGH13-maltose formed by docking shows not only how maltose is bound prior to hydrolysis but also the roles of Glu266 as a proton donor for interglycosidic oxygen of maltose and Asp202 as a catalytic nucleophile (**Figure 7C**). The distance between the proton acceptor/donor (Glu266) and the catalytic nucleophile (Asp202) is 6 Å, and similar conditions have been observed in other retaining glycosidases (Davies and Henrissat, 1995).

DISCUSSION

The commercial demands for α-glucosidases are so great that even small increments in catalytic efficiency and production might provide enormous commercial value. Traditional genetic engineering techniques have largely solved the production problem, but the main challenge remains to improve its process performance to a practical level. Thus, the key in identifying highly efficient and enhanced α-glucosidases lies in screening for microorganisms and molecules in different environments or engineering existing enzymes. α-Glucosidase, derived from extreme environmental microbes, has some unique physical and chemical functions. For example, marine-derived α-glucosidases usually have excellent properties associated with the marine environment, such as temperature stability, salt tolerance, and alkali tolerance (Sala et al., 2021). Currently, most commercialized α-glucosidases have a hydrolytic amylase activity

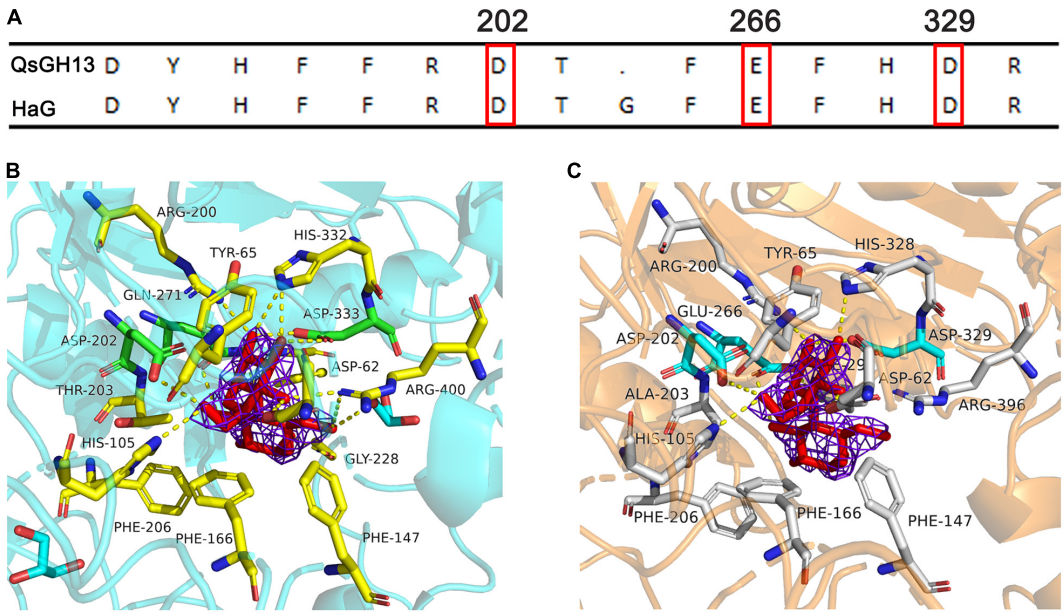

FIGURE 7 | Comparison of QsGH13 and HaG of amino acid residues near the active site. **(A)** Alignment of amino acid residues near the substrate recognition site. The red box indicates the catalytic site. **(B)** Fifteen amino acid residues around the catalytic sites of HaG. **(C)** Fourteen amino acid residues around the catalytic sites of QsGH13. Dashed lines indicate hydrogen bonding with the enzyme and substrate. The purple network represents the electron density cloud.

of 1,000–30,000 U and a transglycosidase activity of 30–5,000 U (**Supplementary Table 2**; Yamamoto et al., 2004; Naested et al., 2006; Wang et al., 2009; Chen et al., 2010), such as *Aspergillus* of the Japanese AMANO and *Aspergillus oryzae* of Novozymes A/S, both produced by fungi and have an acidic optimum pH and a high optimum temperature. However, deep-sea bacteria-derived QsGH13 reached the highest catalytic activity at 45°C and pH 10.0, which showed high tolerance to salt and alkali. This is related to the evolutionary difference of *Qs*. SW-135, which is an adaptive selection for extreme deep-sea environments. The thermal stability of α-glucosidase may be positively correlated with the number of hydrophobic amino acids, such as glycine and alanine, which may be due to hydrophobic forces that lead to tighter enzyme structures (Krohn and Lindsay, 1993). Mg^{2+} and Na^{+} ions can increase the relative activity of QsGH13, and it is likely due to Mg^{2+} and Na^{+} ions directly coordinating with the functional group of the transition state, which, in turn, stabilizes the space structure and charge in the transition state to enhance enzyme activity (Gohara and Di Cera, 2016), or they can bind to a site not indirectly contacting with the substrate and improve catalytic activity through conformational transitions (Gan et al., 2002; Wheatley et al., 2015; Gohara and Di Cera, 2016).

Compared with other α-glucosidases, QsGH13 has extremely high substrate specificity, which reduces byproducts and improves catalytic efficiency. This excellent characteristic may be related to the conformation of the β → α loop 4 region and the volume of the catalytic pocket. For example, the β → α loop 4 of HaG covers most of the entrance of the catalytic pocket, hinders the entry of long-chain substrates, and almost only hydrolyzes disaccharides (Shen et al., 2014). The β → α loop 4 of XgtA is similar in length to that of HaG, and the channel is relatively narrow and occupied by water molecules that are strongly held by surface amino acids, thus, blocking the entry of hydrophobic substances, such as L-menthol (Watanabe et al., 2020), while α-glucosidase GSJ from *Geobacillus* sp., which has bigger catalytic pocket, can utilize a variety of substrates, even quite large molecules, such as curcumin (Shirai et al., 2008). The size of the β → α loop 4 of QsGH13 is between GSJ and HaG. The entrance region of the catalytic site of QsGH13 is large, with two tunnels connected to the active center, but due to the relatively narrow channel, the larger substrate cannot pass through, so only *p*NPαGlu and maltose can be hydrolyzed by QsGH13. Unlike GSJ, which is able to produce oligosaccharides as a byproduct, QsGH13, XgtA, and HAG hardly ever produce oligosaccharides because they have a long β → α loop 4, which hinders the acceptor-maltose from entering the center of the catalytic pocket, leading to an impossible α-glycosylation reaction (Shirai et al., 2008; Shen et al., 2014; Watanabe et al., 2020). Moreover, compared with other conserved domains, the β → α loop 4 has a larger structural flexibility and reduces the energy potential of the conformation change (**Supplementary Figure 5**), so it is easier to realize the change in various conformations; thus, it participates in the acquisition and recognition of regulatory substrates. Unlike HaG, which can hydrolyze maltose and sucrose, QsGH13 just hydrolyzes maltose, not sucrose. Although there is enough space for sucrose to successfully enter the substrate catalytic pocket and bind to the recognition sites, sucrose cannot be hydrolyzed because its fructosyl group fails to be recognized due to the substitution of amino acid residues (Shen et al., 2014). These structural differences may lead to differences in product formation.

Compared with other α-glucosidases, QsGH13 has higher catalytic activity (25.41 U/mg), which may be related to its unique catalytic mechanism. Most enzymes of the family GH13 perform catalytic reactions through a two-step double-displacement mechanism, including the formation and decomposition of a covalent glycosyl-enzyme intermediate. Both steps are performed through an oxocarbenium ion transition state (McIntosh et al., 1996; Ravaud et al., 2007; Shen et al., 2015). The structure of QsGH13-maltose formed by docking shows not only how maltose is bound prior to hydrolysis but also the roles of Glu266 as a proton donor for interglycosidic oxygen of maltose and Asp202 as a catalytic nucleophile. First, QsGH13 recognizes substrates specifically by β → α loop 4, allowing maltose to enter the catalytic pocket and binding to residue Asp202 specifically, assisted by residue Asp329. Since the near-linear interaction between maltose O-1 and Glu266 would minimize the proton transfer energy barrier in the catalytic process, subsequently, the catalytic nucleophile Asp202 attacks the C1 of maltose to displace the aglycon, and form an oxocarbenium ion transition state and a molecule of glucose. Meanwhile, the proton receptor/donor Glu266 protonates the glycosidic oxygen as the bond cleaves. Finally, QsGH13 is hydrolyzed by water, with the residue Glu266 deprotonating the water molecule as water attacks. The QsGH13 catalytic pocket is relatively large, with a volume of about 672 $Å^3$. When the substrate occupies the pocket, the activity center of QsGH13 provides water continuously and efficiently while releasing the product (**Supplementary Figure 6**). This process greatly improves catalytic efficiency (Robert et al., 2003). Research has shown that the substrate specificity and the modes of action of these enzymes are controlled by exquisite details of their 3D structures rather than by their overall structures (Davies and Henrissat, 1995). Although it is not clear how many amino acids are involved in the catalytic process of QsGH13, we found that eight residues in the catalytic pocket, including Tyr65, His105, Arg200, Glu266, Asp202, Phe292, His328, and Asp329, are conserved in the family of GH13. Six residues Asp62, Phe147, Phe166, Thr203, Phe206, and Arg396 are conserved in the homologs.

In this study, α-glucosidase (QsGH13) was screened from the marine bacterium *Qs.* SW-135, which has strong substrate specificity and excellent biological properties such as alkali resistance and salt tolerance. Meanwhile, structural analysis showed that QsGH13 has a typical α/β-fold structure of the GH13 family and a special β → α loop 4 region. These studies might greatly improve our understanding of the molecular mechanism of the GH13 family, and further indicate their physiological and biochemical basis for adapting to extreme conditions, which would help to use these foundations to improve the industrial application value of α-glucosidases. Meanwhile, it has expanded the application of α-glucosidase in alcohol fermentation, glycolysis, and other industries.

DATA AVAILABILITY STATEMENT

The datasets presented in this study can be found in online repositories. The names of the repository/repositories and accession number(s) can be found below: doi: 10.2210/pdb7VOH/pdb.

AUTHOR CONTRIBUTIONS

JH and XZ conceived the study. XZ, KW, RJ, YZ, JL, and ZY performed the experiments and analyzed the data. XZ, XX, and JH wrote and edited its final manuscript. All authors contributed to the article and approved the submitted version.

FUNDING

This work was supported by the Natural Science Foundation of Hunan Province (2020JJ5700 to JH and 2020JJ5702 to ZY), and the start-up funding for young talents of Central South University (202045004 to JH).

ACKNOWLEDGMENTS

We thank Jixi Li from the Fudan University for the vector construction and study design. We thank the staff from the BL17U1 beamlines at Shanghai Synchrotron Radiation Facility for the assistance during the data collection. We also thank Weidong Liu from the Tianjin Institute of Industrial Biotechnology, Chinese Academy of Sciences, for the structure determination.

SUPPLEMENTARY MATERIAL

The Supplementary Material for this article can be found online at: https://www.frontiersin.org/articles/10.3389/fmicb.2022.849585/full#supplementary-material

REFERENCES

Banner, D. W., Bloomer, A. C., Petsko, G. A., Phillips, D. C., and Pogson, C. I. (1975). Structure of chicken muscle triose phosphate isomerase determined crystallographically at 2.5 angstrom resolution using amino acid sequence data. *Nature* 255, 609–614. doi: 10.1038/255609a0

Cantarel, B. L., Coutinho, P. M., Rancurel, C., Bernard, T., and Lombard, V. (2009). The carbohydrate-active enzymes database (CAZy): an expert resource for glycogenomics. *Nucleic Acids Res.* 37, D233–D238. doi: 10.1093/nar/gkn663

Chen, D. L., Tong, X., Chen, S. W., Chen, S., Wu, D., Fang, S. G., et al. (2010). Heterologous expression and biochemical characterization of alpha-glucosidase from aspergillus niger by pichia pastroris. *J. Agr. Food. Chem.* 58, 4819–4824. doi: 10.1021/jf1000502

Davies, G., and Henrissat, B. (1995).). Structures and mechanisms of glycosyl hydrolases. *Structure* 3, 853–859. doi: 10.1016/S0969-2126(01)00220-9

Emsley, P., and Cowtan, K. (2004). Coot: model-building tools for molecular graphics. *Acta Cryst. D Biol. Cryst.* 60, 2126–2132. doi: 10.1107/S0907444904019158

Erdõs, G., and Dosztányi, Z. (2020). Analyzing protein disorder with IUPred2A. *Curr. Prot. Bioinform.* 70:99. doi: 10.1002/cpbi.99

Gan, L., Petsko, G. A., and Hedstrom, L. (2002). Crystal structure of a ternary complex of tritrichomonas foetus inosine 5′-monophosphate dehydrogenase:

NAD+ orients the active site loop for catalysis. *Biochemistry* 41, 13309–13317. doi: 10.1021/bi0203785

Gohara, D. W., and Di Cera, E. (2016). Molecular mechanisms of enzyme activation by monovalent cations. *J. Biol. Chem.* 291, 20840–20848. doi: 10.1074/jbc.R116.737833

Henrissat, B. (1991). A classification of glycosyl hydrolases based on amino acid sequence similarities. *Biochem. J.* 280(Pt. 2), 309–316. doi: 10.1042/bj2800309

Hobbs, J. K., Jiao, W., Easter, A. D., Parker, E. J., Schipper, L. A., and Arcus, V. L. (2013). Change in heat capacity for enzyme catalysis determines temperature dependence of enzyme catalyzed rates. *ACS Chem. Biol.* 8, 2388–2393. doi: 10.1021/cb4005029

Holm, L. (2020). *Using Dali for Protein Structure Comparison*. New York, NY: Springer, 29–42. doi: 10.1007/978-1-0716-0270-6_3

Hondoh, H., Saburi, W., Mori, H., Okuyama, M., Nakada, T., et al. (2008). Substrate recognition mechanism of alpha-1,6-glucosidic linkage hydrolyzing enzyme, dextran glucosidase from *Streptococcus mutans*. *J. Mol. Biol.* 378, 913–922. doi: 10.1016/j.jmb.2008.03.016

Huang, J., Huo, Y., Ji, R., Kuang, S., and Ji, C. (2016). Structural insights of a hormone sensitive lipase homologue Est22. *Sci. Rep.* 6:550. doi: 10.1038/srep28550

Huang, J., Yu, Z., Groom, J., Cheng, J., Tarver, A., et al. (2019). Rare earth element alcohol dehydrogenases widely occur among globally distributed, numerically abundant and environmentally important microbes. *ISME J.* 13, 2005–2017. doi: 10.1038/s41396-019-0414-z

Irma, F. H., Ana, M. M. R., Caren, M. Z., Peter, J. P., and Cees, A. M. J. J. (1992). Cloning and expression of a member of the *Aspergillus niger* gene family encoding α-galactosidase. *MGG Mol. General Genet.* 233, 404–410. doi: 10.1007/BF00265437

Kabsch, W. (2010). Xds. *Acta Cryst. D Biol. Cryst.* 66, 125–132. doi: 10.1107/S0907444909047337

Krohn, B. M., and Lindsay, J. A. (1993). Cloning of the cyclomaltodextrinase gene from *Bacillus subtilis* high-temperature growth transformant H-17. *Curr. Microbiol.* 26, 217–222. doi: 10.1007/BF01577379

Kumar, S., Stecher, G., Li, M., Knyaz, C., and Tamura, K. (2018). MEGA X: molecular evolutionary genetics analysis across computing platforms. *Mol. Biol. Evolu.* 35, 1547–1549. doi: 10.1093/molbev/msy096

Kwon, K. K., Woo, J., Yang, S., Kang, J., and Kang, S. G. (2007). Altererythrobacter epoxidivorans gen. nov., sp. nov., an epoxide hydrolase-active, mesophilic marine bacterium isolated from cold-seep sediment, and reclassification of erythrobacter luteolus yoon et al. 2005 as altererythrobacter luteolus comb. *Nov. Int. J. Syst. Evol. Micr.* 57, 2207–2211. doi: 10.1099/ijs.0.64863-0

Larkin, M. A., Blackshields, G., Brown, N. P., Chenna, R., and McGettigan, P. A. (2007). Clustal W and clustal X version 2.0. *Bioinformatics* 23, 2947–2948. doi: 10.1093/bioinformatics/btm404

Li, J., McQuade, T., Siemer, A. B., Napetschnig, J., and Moriwaki, K. (2012). The RIP1/RIP3 necrosome forms a functional amyloid signaling complex required for programmed necrosis. *Cell* 150, 339–350. doi: 10.1016/j.cell.2012.06.019

Liebschner, D., Afonine, P. V., Baker, M. L., Bunkóczi, G., and Chen, V. B. (2019). Macromolecular structure determination using X-rays, neutrons and electrons: recent developments inPhenix. *Acta Cryst. Section D Struct. Biol.* 75, 861–877. doi: 10.1107/S2059798319011471

McCarter, J. D., and Withers, S. G. (1994). Mechanisms of enzymatic glycoside hydrolysis. *Curr. Opin. Struct. Biol.* 4:885. doi: 10.1016/0959-440x(94)90271-2

McCoy, A. J., Grosse-Kunstleve, R. W., Adams, P. D., Winn, M. D., and Storoni, L. C. (2007). Phaser crystallographic software. *J. Appl. Cryst.* 40, 658–674. doi: 10.1107/S0021889807021206

McIntosh, L. P., Hand, G., Johnson, P. E., Joshi, M. D., Körner, M., Plesniak, L. A., et al. (1996). The pKa of the general acid/base carboxyl group of a glycosidase cycles during catalysis: a 13C-NMR study of bacillus circulans xylanase. *Biochemistry* 35, 9958–9966. doi: 10.1021/bi9613234

Morris, G. M., Huey, R., Lindstrom, W., Sanner, M. F., and Belew, R. K. (2009). AutoDock4 and autodocktools4: automated docking with selective receptor flexibility. *J. Comput. Chem.* 30, 2785–2791. doi: 10.1002/jcc.21256

Naested, H., Kramhøft, B., Lok, F., Bojsen, K., Yu, S., and Svensson, B. (2006). Production of enzymatically active recombinant full-length barley high pI alpha-glucosidase of glycoside family 31 by high cell-density fermentation of Pichia pastoris and affinity purification. *Protein Exp. Purif.* 46, 56–63. doi: 10.1016/j.pep.2005.10.008

Noguchi, A., Nakayama, T., Hemmi, H., and Nishino, T. (2003). Altering the substrate chain-length specificity of an alpha-glucosidase. *Biochem. Biophys. Res. Commun.* 304, 684–690. doi: 10.1016/s0006-291x(03)00647-8

Ravaud, S., Robert, X., Watzlawick, H., Haser, R., and Mattes, R. (2007). Trehalulose synthase native and carbohydrate complexed structures provide insights into sucrose isomerization. *J. Biol. Chem.* 282, 28126–28136. doi: 10.1074/jbc.M704515200

Robert, X., and Gouet, P. (2014). Deciphering key features in protein structures with the new ENDscript server. *Nucleic Acids Res.* 42, W320–W324. doi: 10.1093/nar/gku316

Robert, X., Haser, R., Gottschalk, T. E., Ratajczak, F., and Driguez, H. (2003). The structure of barley α-amylase isozyme 1 reveals a novel role of domain c in substrate recognition and binding. *Structure* 11, 973–984. doi: 10.1016/S0969-2126(03)00151-5

Sala, E., Mayorga, J., Bradley, D., Cabral, R. B., and Atwood, T. B. (2021). Protecting the global ocean for biodiversity, food and climate. *Nature* 592, 397–402. doi: 10.1038/s41586-021-03371-z

Shen, X., Saburi, W., Gai, Z. Q., Komoda, K., and Yu, J. (2014). Crystallization and preliminary X-ray crystallographic analysis of alpha-glucosidase HaG from halomonas sp. strain H11. *Acta Cryst. F Struct. Biol. Commun.* 70, 464–466. doi: 10.1107/S2053230X14001940

Shen, X., Saburi, W., Gai, Z., Kato, K., and Ojima-Kato, T. (2015). Structural analysis of the α-glucosidase HaG provides new insights into substrate specificity and catalytic mechanism. *Acta Cryst. D Biol. Cryst.* 71, 1382–1391. doi: 10.1107/S139900471500721X

Shen, Y., Li, Z., Huo, Y., Bao, L., and Gao, B. (2019). Structural and functional insights into CmGH1, a novel GH39 family β-glucosidase from deep-sea bacterium. *Front. Microbiol.* 10:e02922. doi: 10.3389/fmicb.2019.02922

Shirai, T., Hung, V. S., Morinaka, K., Kobayashi, T., and Ito, S. (2008). Crystal structure of GH13 alpha-glucosidase GSJ from one of the deepest sea bacteria. *Proteins* 73, 126–133. doi: 10.1002/prot.22044

Wang, Y. H., Jiang, Y., and Duan, Z. Y. (2009). Expression and characterization of an α-glucosidase from thermoanaerobacter ethanolicus JW200 with potential for industrial application. *Biologia* 64, 1053–1057. doi: 10.2478/s11756-009-0197-1

Wangpaiboon, K., Laohawuttichai, P., Kim, S. Y., Mori, T., and Nakapong, S. (2021). A GH13 alpha-glucosidase from weissella cibaria uncommonly acts on short-chain maltooligosaccharides. *Acta Cryst. D Struct. Biol.* 77, 1064–1076. doi: 10.1107/S205979832100677X

Watanabe, R., Arimura, Y., Ishii, Y., and Kirimura, K. (2020). Crystal structure of α-glucosyl transfer enzyme XgtA from *Xanthomonas campestris* WU-9701. *Biochem. Bioph. Res.* 526, 580–585. doi: 10.1016/j.bbrc.2020.03.109

Wheatley, R. W., Juers, D. H., Lev, B. B., Huber, R. E., and Noskov, S. Y. (2015). Elucidating factors important for monovalent cation selectivity in enzymes: E. coli β-galactosidase as a model. *Phys. Chem. Chem. Phys.* 17, 10899–10909. doi: 10.1039/c4cp04952g

Xu, L., Sun, C., Fang, C., Oren, A., and Xu, X. (2020). Genomic-based taxonomic classification of the family erythrobacteraceae. *Int. J. Syst. Evol. Micr.* 70, 4470–4495. doi: 10.1099/ijsem.0.004293

Yamamoto, K., Nakayama, A., Yamamoto, Y., and Tabata, S. (2004). Val216 decides the substrate specificity of alpha-glucosidase in saccharomyces cerevisiae. *Eur. J. Biochem.* 271, 3414–3420. doi: 10.1111/j.1432-1033.2004.04276.x

Conflict of Interest: The authors declare that the research was conducted in the absence of any commercial or financial relationships that could be construed as a potential conflict of interest.

Publisher's Note: All claims expressed in this article are solely those of the authors and do not necessarily represent those of their affiliated organizations, or those of the publisher, the editors and the reviewers. Any product that may be evaluated in this article, or claim that may be made by its manufacturer, is not guaranteed or endorsed by the publisher.

frontiers in Microbiology

ORIGINAL RESEARCH
published: 28 March 2022
doi: 10.3389/fmicb.2022.857041

Thiodiketopiperazines and Alkane Derivatives Produced by the Mangrove Sediment–Derived Fungus *Penicillium ludwigii* SCSIO 41408

Jian Cai[1,2], Xueni Wang[1], Zaizhun Yang[3], Yanhui Tan[4], Bo Peng[5,6]*, Yonghong Liu[1,7] and Xuefeng Zhou[1,2]**

[1] CAS Key Laboratory of Tropical Marine Bio-Resources and Ecology, Guangdong Key Laboratory of Marine Materia Medica, South China Sea Institute of Oceanology, Chinese Academy of Sciences, Guangzhou, China, [2] College of Earth and Planetary Sciences, University of Chinese Academy of Sciences, Beijing, China, [3] Guangxi Zhuang Yao Medicine Center of Engineering and Technology, Guangxi University of Chinese Medicine, Nanning, China, [4] State Key Laboratory for Chemistry and Molecular Engineering of Medicinal Resources, School of Chemistry and Pharmaceutical Sciences, Guangxi Normal University, Guilin, China, [5] Guangdong Eco-Engineering Polytechnic, Guangzhou, China, [6] Guangdong Ocean Association, Guangzhou, China, [7] Wuya College of Innovation, Shenyang Pharmaceutical University, Shenyang, China

OPEN ACCESS

Edited by:
Xian-Wen Yang,
Third Institute of Oceanography, Ministry of Natural Resources, China

Reviewed by:
Chang-Lun Shao,
Ocean University of China, China
Kandasamy Saravanakumar,
Kangwon National University, South Korea

***Correspondence:**
Yanhui Tan
tyh533@126.com
Bo Peng
pengbo@gig.ac.cn
Xuefeng Zhou
xfzhou@scsio.ac.cn

Specialty section:
This article was submitted to Extreme Microbiology, a section of the journal Frontiers in Microbiology

Received: 18 January 2022
Accepted: 16 February 2022
Published: 28 March 2022

Citation:
Cai J, Wang X, Yang Z, Tan Y, Peng B, Liu Y and Zhou X (2022) Thiodiketopiperazines and Alkane Derivatives Produced by the Mangrove Sediment–Derived Fungus Penicillium ludwigii SCSIO 41408. Front. Microbiol. 13:857041. doi: 10.3389/fmicb.2022.857041

A new trithiodiketopiperazine derivative, adametizine C (**1**), and five new alkane derivatives (**7–11**), were isolated from the mangrove sediment–derived fungus *Penicillium ludwigii* SCSIO 41408, together with five known dithiodiketopiperazine derivatives (**2–6**). Their structures were elucidated on the basis of spectroscopic analysis, and the absolute configuration of **1** was determined by X-ray crystallographic analysis. In a variety of bioactivity screening, **1**–**5** exhibited some selective antifungal or antibacterial activities. Compounds **1**–**3** showed cytotoxicity against prostate cancer cell line 22Rv1 with half maximal inhibitory concentration (IC_{50}) values of 13.0–13.9 μM; moreover, **3** showed obvious activity against another prostate cancer PC-3 cells with an IC_{50} value of 5.1 μM. Further experiments revealed that **3** could significantly reduce PC-3 cells colony formation and induce apoptosis in a dose-dependent manner. Several compounds also exhibited obvious inhibitory activities of lipopolysaccharide–induced nuclear factor-κB with IC_{50} values range from 8.2 to 21.5 μM, and **1**, **5**, and **9** were further evaluated for their effects on receptor activator of NF-κB ligand (RANKL)-induced osteoclastogenesis. Adametizine C (**1**), with the strongest inhibitory activity against RANKL-induced osteoclast differentiation in bone marrow macrophage cells with 10 μM, was suggested to be the promising lead compound for the treatment of osteoclast-related diseases.

Keywords: mangrove-sediment-derived fungus, *penicillium ludwigii*, thiodiketopiperazines, PC-3, NF-κB, osteoclast differentiation

INTRODUCTION

Mangroves, a special ecosystem characterized by high salinity, muddy or sandy soil, and low pH, as well as partly anoxic and periodically soaked by the tides, play an important role in tropical and subtropical coastal ecosystems. Mangroves nourish various microorganisms due to their complex ecosystem. The variety and complexity of the mangrove soil environment leads

to the diversity of soil microorganisms (He et al., 2019). Mangrove soil or sediment-derived microbes play an essential role in maintaining the biosphere balance and are also a prolific source of structurally unique and novel bioactive secondary metabolites (Li et al., 2022). Mainly derived from marine fungi, thiodiketopiperazines have been recently reported to have a broad range of significant biological activities, such as brine shrimp lethality (Liu et al., 2015a), antibacterial (Liu et al., 2015a), antifungal (Liu et al., 2015b), cytotoxic (Yurchenko et al., 2016), and C-terminal inhibitor (Dai et al., 2019) activities. During our ongoing search for novel bioactive secondary metabolites from mangrove fungi (Luo et al., 2018; Luo et al., 2019; Chen et al., 2021a,b; Cai et al., 2021), a new trithiodiketopiperazine, five new alkane derivatives (**7–11**), and five dithiodiketopiperazine derivatives (**2–6**) (**Figure 1**) were isolated from the mangrove sediment–derived fungus *Penicillium ludwigii* SCSIO 41408. We performed screening for antibacterial and antifungal activities, cytotoxicity against anti-prostate cancer cells, and inhibitory activities of lipopolysaccharide (LPS)–induced nuclear factor-κB (NF-κB) activation. NF-κB exhibited an important role in receptor activator of NF-κB ligand (RANKL)-induced osteoclast differentiation (Hong et al., 2020; Tan et al., 2020; Zhou et al., 2020). Our further research found that Adametizine C (**1**) was suggested to be the promising lead compound for the treatment of osteoclast-related diseases.

MATERIALS AND METHODS

General Experimental Procedures

Optical rotations were measured on a PerkinElmer MPC 500 (Waltham) polarimeter. The UV, IR, and CD spectra were recorded on a Shimadzu UV-2600 PC spectrometer (Shimadzu), an IR Affinity-1 spectrometer (Shimadzu), and a Chirascan circular dichroism spectrometer (Applied Photophysics), respectively. NMR spectra were recorded on a Bruker Avance spectrometer (Bruker) operating at 500 and 700 MHz for ^{1}H NMR and 125 and 175 MHz for ^{13}C NMR that used tetramethylsilane as an internal standard. High resolution electrospray ionization mass spectroscopy (HRESIMS) spectra were acquired on a Bruker miXis TOF-QII mass spectrometer (Bruker). Column chromatography was performed over silica gel (200–300 mesh) (Qingdao Marine Chemical Factory). Spots were detected on TLC (Qingdao Marine Chemical Factory) under 254-nm UV light. All solvents employed were analytical grade (Tianjin Fuyu Chemical and Industry Factory). Semipreparative HPLC was performed using an octadecylsilyl (ODS) column (YMC-pack ODS-A, YMC Co., Ltd., 10 mm × 250 mm, 5 μm). Artificial sea salt was a commercial product (Guangzhou Haili Aquarium Technology Company).

Fungal Material

The fungal strain *Penicillium ludwigii* SCSIO 41408 was isolated from a mangrove sediment sample, collected in the Hongsha River estuary to South China Sea, in Sanya city, Hainan Island. The fungus was identified according to the internally transcribed spacer (ITS) region sequence data of the rDNA, and the sequence was deposited in GenBank with the accession number OL823084. The strain was stored on Muller Hinton broth agar (malt extract, 15 g; sea salt, 10 g; agar, 15 g; H_2O, 1 L; pH 7.4–7.8) at 4°C and deposited in the CAS Key Laboratory of Tropical Marine Bioresources and Ecology, South China Sea Institute of Oceanology, Chinese Academy of Sciences, Guangzhou, China.

Fermentation, Extraction, and Isolation

The strain *Penicillium ludwigii* SCSIO 41408 was cultured in the seed medium (malt extract, 15 g; sea salt, 10 g; H_2O, 1 L; pH 7.4–7.8) for 4 days at 28°C on a rotating shaker (180 rpm). A large scale of fermentation was incubated statically at 26°C for 60 days in 1 L × 65 conical flasks with a rice medium (each flack contains 180 g of rice, 3 g of sea salt, 200 ml of H_2O). The fermented cultures were overlaid and extracted with EtOAc three times to afford a brown extract (346.6 g).

The EtOAc crude extract was chromatographed over a silica gel column eluted with PE/CH_2Cl_2 (0–100%, v/v) and CH_2Cl_2/MeOH (0–100%, v/v) in a gradient to yield fourteen fractions (Frs. 1–14). Fr. 2 (0.9 g) was separated by semipreparative HPLC (65% MeCN/H_2O, 2 ml/min) to afford **9** (3.4 mg, t_R = 17.0 min) and Fr. 2-1. Fr. 2-1 was separated again by semipreparative HPLC (40% MeCN/H_2O, 2.7 ml/min) to afford **7** (6.7 mg, t_R = 16.1 min) and **8** (7.5 mg, 14.5 min). Fr. 4 (6.4 g) was separated by semipreparative HPLC (48% MeCN/H_2O, 3 ml/min) to afford **6** (2.1 mg, t_R = 17.3 min). Fr. 8 (8.5 g) was purified by semipreparative HPLC (65% MeOH/H_2O, 2 ml/min) to afford **2** (5.2 mg, t_R = 10.1 min). Fr.10 was divided into four subfractions by ODS silica gel chromatography eluting with MeOH/H_2O (10–100%). Fr. 10 was divided into four subfractions by Sephadex LH-20. Fr.10-1 was purified by semipreparative HPLC (35% MeCN/H_2O, 2 ml/min) to afford **11** (10.2 mg, t_R = 8.1 min) and **1** (6.0 mg, t_R = 27.1 min). Fr. 10-4 was purified by semipreparative HPLC (55% MeOH/H_2O, 3 ml/min) to afford **3** (6.0 mg, t_R = 7.5 min). Fr. 13 was divided into four subfractions by ODS silica gel chromatography eluting with MeOH/H_2O (10–100%). Fr. 13-1 was further purified by semipreparative HPLC (45% MeOH/H_2O, 2.7 ml/min) to afford **4** (26.0 mg, t_R = 12.4 min), **5** (5.7 mg, t_R = 14.1 min), and **10** (16.4 mg, t_R = 21.9 min).

*Adametizine C (**1**)*: colorless needles; [α]25 D, −128.5 (c 0.1, MeOH); UV (MeOH) λ_{max} (log ε), 205 (3.52) nm; ECD (0.36 mM, MeOH) λ_{max} (Δε), 203 (−10.98), 242 (−9.06), and 293(+1.33); IRν_{max}, 3,352, 2,945, 2,835, 1,670, 1,506, 1,431, 1,250, 1,204, 1,096, 1,018, 831, 795, 677, 601, and 557 cm^{-1}; ^{1}H and ^{13}C NMR, data see **Table 1**; HRESIMS at *m/z* 563.0381 $[M + H]^+$ (calculated for $C_{21}H_{24}ClN_2O_8S_3$, 563.0378).

*2-methyl-3-(5-oxohexyl) maleic acid (**7**)*: colorless oil; UV (MeOH) λ_{max} (log ε), 250 (3.95) and 207 (3.69) nm; IRν_{max}, 2,938, 2,866, 1,759, 1,712, 1,362, 1,273, 916, and 735 cm^{-1}; ^{1}H and ^{13}C NMR data, see **Tables 2**, **3**; HRESIMS at *m/z* 227.0927 $[M-H]^-$ (calculated for $C_{11}H_{15}O_5$, 227.0925).

*2-(4-hydroxyhexyl)-3-methylmaleic acid (**8**)*: colorless oil; [α]25 D, −0.7 (c 0.1, MeOH); ECD (2.46 mM, MeOH) λ_{max} (Δε), 203 (−2.49) and 213 (+2.27); UV (MeOH) λ_{max} (log ε), 250 (3.25), 206 (3.65) nm; IRν_{max}, 3,390, 2,943, 1,763, 1,682, 1,435, 1,283, 1,202, 1,136, 1,026, 800, and 721 cm^{-1}; ^{1}H and ^{13}C

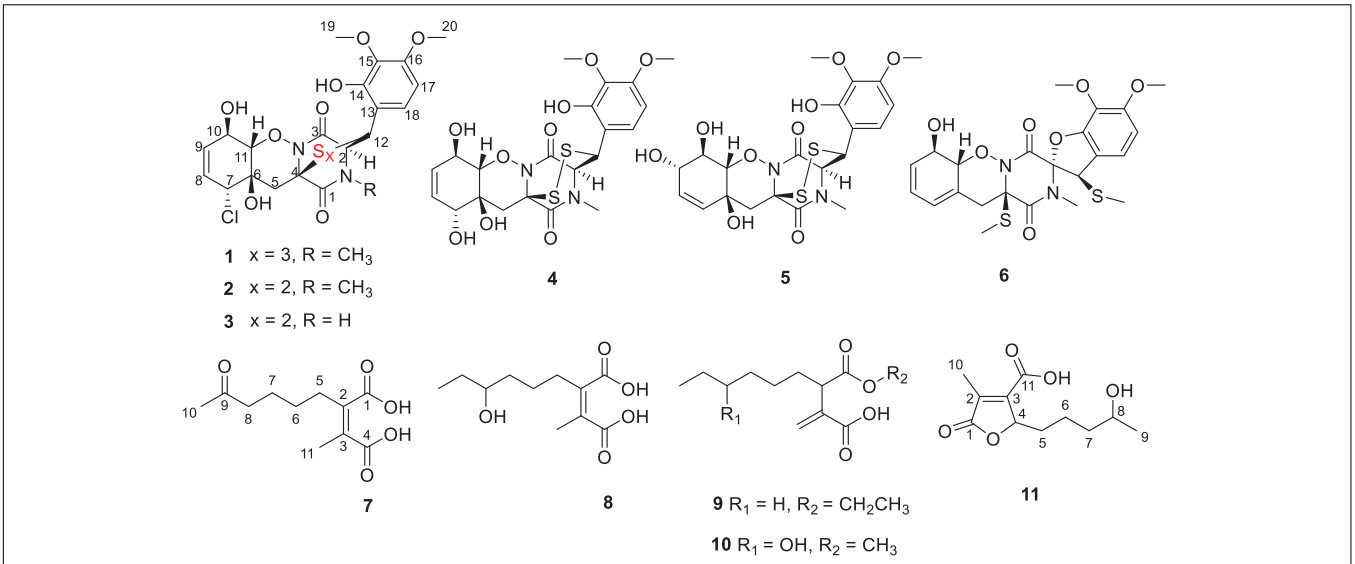

FIGURE 1 | Chemical structures of compounds **1**-**11**.

NMR data, see **Tables 2**, **3**; HRESIMS at *m*/*z* 229.1082 $[M\text{-}H]^-$ (calculated for $C_{11}H_{17}O_5$, 229.1081).

*3-(ethoxycarbonyl)-2-methylenenonanoic acid (**9**)*: brown oil; [α]25 D, +5.9 (c 0.1, MeOH); ECD (3.83 mM, MeOH) λ_{max} (Δε) 200 (−10.62), 214 (+0.68), and 227 (−2.64); UV (MeOH) λ_{max} (log ε), 204 (3.86) nm; IRν_{max}, 2,955, 2,928, 2,857, 1,732, 1,715, 1,202, 1,153, 1,113, 1,036, 953, and 835 cm^{-1}; ^1H and ^{13}C NMR data, see **Tables 2**, **3**; HRESIMS at *m*/*z* 243.1594 $[M + H]^+$ (calculated for $C_{13}H_{23}O_4$, 243.1591).

*7-hydroxy-3-(methoxycarbonyl)-2-methylenenonanoic acid (**10**)*: colorless oil; $[\alpha]_D^{25}$, +1.9 (c 0.1, MeOH); ECD (2.05 mM, MeOH) λ_{max} (Δε), 200 (−3.34), 201 (+4.57), 205 (+2.35), and 211 (−0.98); UV (MeOH) λ_{max} (log ε), 205 (2.93) nm; IRν_{max}, 3,447, 2,936, 2,866, 1,717, 1,628, 1,456, 1,435, 1,204, 1,155, 1,024, 9,54.8, and 824 cm^{-1}; ^1H and ^{13}C NMR data, see **Tables 2**, **3**; HRESIMS at *m*/*z* 245.1388 $[M + H]^+$ (calculated for $C_{12}H_{21}O_5$, 245.1384).

*2-(4-hydroxypentyl)-4-methyl-5-oxo-2,5-dihydrofuran-3-carboxylic acid (**11**)*: brown oil; $[\alpha]_D^{25}$, +2.6 (c 0.1, MeOH); ECD

TABLE 1 | ^1H (700 MHz) and ^{13}C (175 MHz) NMR data for compound 1 in DMSO-d_6.

Position	δ_C, type	δ_H (*J* in Hz)	HMBC	COSY
1	162.7, C			
2	66.9, CH	4.63, d (1.1)	3, 12, 13, 21	
3	161.9, C			
4	76.4, C			
5	37.5, CH_2	α 2.54, dd (14.8, 2.0) β 2.09, d (14.8)	4, 6, 11 1, 4	5b 5a, 6-OH
6	71.4, C			
7	66.8, CH	4.88, m	5, 6, 8, 9	
8	131.5, CH	5.63, dt (10.3, 2.5)	7, 11	
9	127.0, CH	5.58, dt (10.3, 2.0)	6, 10	
10	65.0, CH	4.43, m	9, 8, 11	10-OH, 11
11	87.0, CH	4.10, dd (7.3, 1.9)	5, 6, 10	11
12	56.2, CH	5.39(s)	2, 3, 13, 14, 18	
13	117.8, C			
14	147.5, C			
15	136.1, C			
16	153.4, C			
17	103.4, CH	6.53, d (8.8)	13, 15, 16	18
18	125.5, CH	7.08, d (8.8)	14, 16	17
19	60.8, CH_3	3.69, s	15	
20	56.1, CH_3	3.78, s	16, 17	
21 N-CH_3	32.9, CH_3	3.12, s	1, 2	
6-OH		6.11, d (2.3)	5, 6, 11	
10-OH		5.17, d (6.6)	8, 10, 11	
14-OH		9.64, s	13, 14, 15	

TABLE 2 | ^{13}C NMR data for compounds 7–11 (δ in ppm) in DMSO-d_6.

Position	7[a]	8[a]	9[b]	10[a]	11[b]
1	166.7, C	166.8, C	173.1, C	173.7, C	173.6, C
2	143.7, C	141.4, C	46.5, CH	46.8, CH	133.9, C
3	141.5, C	144.1, C	141.7, C	139.5, C	151.5, C
4	166.9, C	167.0, C	168.1, C	167.7, C	81.7, CH
5	24.0, CH_2	24.2, CH_2	31.1, CH_2	31.0, CH_2	32.5, CH_2
6	26.9, CH_2	23.9, CH_2	27.0, CH_2	23.8, CH_2	21.1, CH_2
7	23.3, CH_2	36.5, CH_2	28.5, CH_2	36.8, CH_2	39.0, CH_2
8	42.7, CH_2	71.1, CH	22.0, CH_2	71.3, CH	66.0, CH
9	208.8, C	30.4, CH_2	30.8, CH_2	30.4, CH_2	24.2, CH_3
10	30.2, CH_3	10.5, CH_3	13.9, CH_3	10.5, CH_3	10.7, CH_3
11	9.8, CH_3	9.8, CH_3	123.3, CH_2	126.8, CH_2	164.2, C
12			59.8, CH_2	52.1, CH_3	
13			14.1, CH_3		

[a]*Data were recorded at 500 MHz.*
[b]*Data were recorded at 700 MHz.*

TABLE 3 | ^{1}H NMR data for compounds 7–11 (δ in ppm) in DMSO-d_6.

Position	7[a]	8[a]	9[b]	10[a]	11[b]
2			3.41, t (3.7)	3.43, t (7.3)	
4					5.13, m
5	2.40, t (6.8)	2.40, m	a 1.71, m b 1.56, m	a 1.78, m b 1.60, m	a 1.97, m b 1.54, m
6	1.48, m	a 1.62, m b 1.50, m	1.23, m	1.23, m	1.36, m
7	1.46, m	1.33, m	1.23, m	1.30, m	1.29, m
8	2.44, t (6.6)	3.30, m	1.23, m	3.28, m	3.55, m
9		1.30, m	1.23, m	1.35, m	1.01, dd (6.1, 1.8)
10	2.07, s	0.83, t (7.4)	0.85, t (7.1)	0.84, t (7.4)	2.02, s
11	2.00, s	1.99, s	a 6.07, s, b 5.50, s,	a 6.23, s b 5.73, s	
12			4.02, q (7.0)	3.59, s	
13			1.13, t (7.1)		
8-OH		4.32, d (5.4)			

[a]*Data were recorded at 500 MHz.*
[b]*Data were recorded at 700 MHz.*

(4.39 mM, MeOH) λ_{max} ($\Delta\varepsilon$), 200 (−10.62), 214 (+0.68), and 227 (−2.64); UV (MeOH) λ_{max} (log ε), 225 (3.85) nm; IRν_{max}, 3,414, 2,932, 1,744, 1,715, 1,337, 1,231, 1,117, 1,024, 947, 764, and 721 cm^{-1}; HRESIMS at m/z 229.1076 $[M + H]^+$ (calculated for $C_{11}H_{17}O_5$, 229.1072).

X-Ray Crystal Structure Analysis

The crystallographic data of compound **1** obtained in MeOH were collected with a Rigaku XtaLAB PRO single-crystal diffractometer using Cu Kα radiation (λ = 1.54184). Briefly, their X-ray crystal structure was solved using SHELXS97, expanded by difference Fourier techniques, and refined by full-matrix least-squares calculation finally. The non-hydrogen atoms were refined anisotropically, and hydrogen atoms were fixed at calculated positions. The crystallographic data of compound **1** have been deposited in the Cambridge Crystallographic Data Centre.

*Crystal Data for adametizine C (**1**)*: $C_{21}H_{31}ClN_2O_{12}S_3$, M_r = 635.11, crystal size 0.1 mm × 0.08 mm × 0.06 mm, orthorhombic, a = 9.16490 (10) Å, b = 11.25800 (10) Å, c = 27.3339 (2) Å, α = β = γ = 90°, V = 2407.9 (4) $Å^3$, Z = 4, T = 100.00 (10) K, Space group $P2_12_12_1$, μ = 3.837 mm^{-1}, ρ_{calc} = 1.496 g/cm^3, 14,343 reflections measured (6.468° ≤ 2Θ ≤ 148.482°), 5,546 unique (R_{int} = 0.0275, R_{sigma} = 0.0325). The final R_1 values were 0.0287 [$I > 2\sigma(I)$]. The final wR (F^2) values were 0.0758 [$I > 2\sigma(I)$]. The final R_1 values were 0.0299 (all data). The final wR (F^2) values were 0.0764 (all data). The goodness of fit on F^2 was 1.049. The Flack parameter is 0.002 (6) (CDCC 2130918).

Antibacterial Activity Assay

The antimicrobial activities against five bacteria (*Erysipelothrix rhusiopathiae* WH13013, *Streptococcus suis* SC19, *Escherichia coli* ATCC 25922, *Pseudomonas aeruginosa* ATCC 27853, and *Staphylococcus aureus* ATCC 25923) and four fungi (*Botrytis cinerea*, *Septoria nodorum* Berk., *Fusarium graminearum* Schw., and *Rhizoctonia solani* Kühn) were evaluated using the methods described previously (Wan et al., 2014). Cephalosporin and cycloheximide were used as positive controls against bacteria and fungi, respectively.

NF-κB Bioassay

The inhibitory activities of LPS-induced NF-κB activation in RAW264.7 cells were evaluated as detected by luciferase reporter gene assay as described previously (Tan et al., 2020). In brief, the RAW264.7 cells stably transfected with a luciferase reporter gene were plated in 96-well plates and then pretreated with tested compounds (20 μM) and BAY11-7082 (NF-κB inhibitor as positive control, 5 μM, Sigma-Aldrich) for 30 min, followed by LPS stimulation (5 μg/ml) for 8 h. Cells were harvested, and luciferase activities of the triplicate tests were measured by the luciferase assay system (Promega, Madison, WI, United States). For further study of compounds **1**, **5**, and **9** on osteoclastogenesis, bone marrow macrophage cells (BMMCs) were added with macrophage-stimulating factor (50 ng/ml) and RANKL (100 ng/ml) stimulation at 5 μM concentrations for 3 days. Then, the cells were fixed and stained for TRAP activity, and the images were photographed by using an inverted microscope (Nikon, Japan). Data are expressed as the mean ± SD and analyzed using GraphPad Prism 7.0 software (San Diego, CA, United States). Statistical differences among groups were performed using one-way analysis of variance with Bonferroni *post hoc* test. A p-value of < 0.05 was considered statistically significant.

Cytotoxicity Bioassay

Cell viability was analyzed by 3-(4,5)-dimethylthiahiazo (-z-y1)-3,5-di-phenytetrazoliumromide (MTT) assay as previous described (Wang et al., 2021). In brief, cells were seeded in 96-well plate at a density of 5×10^3 per well overnight and treated with compounds for demand time. OD_{570} values were detected using a Hybrid Multi-Mode Reader (Synergy H1, BioTek). The experiment was repeated three times independently.

Plate Clone Formation Assay

PC-3 cells were seeded in six-well plate at a density of 1,000 cell per well overnight, and then, cells were treated with dimethyl sulfoxide (DMSO) (0.1%, v/v), docetaxel (1 μM), and compound **3** (1.25, 2.5, 5, and 10 μM), respectively, for demand time. The cell clone colonies were formed after treating for 2 weeks, and cells were fixed with 4% formaldehyde for 30 min, washed with phosphate buffer saline (PBS) buffer, and then stained with crystal violet stain solution for 30 min. The dye solution was removed, and the cells were washed with PBS buffer again. Cell colonies were recorded and analyzed by the colony count analysis system (GelCount, Oxford Optronix). The experiment was repeated three times independently.

Apoptosis Assay

PC-3 cells were seeded in six-well plate at a density of 2.0×10^5 cell per well overnight and treated with DMSO (0.1%, v/v), docetaxel (1 μM), and compound **3** (1.25, 2.5, 5, and 10 μM),

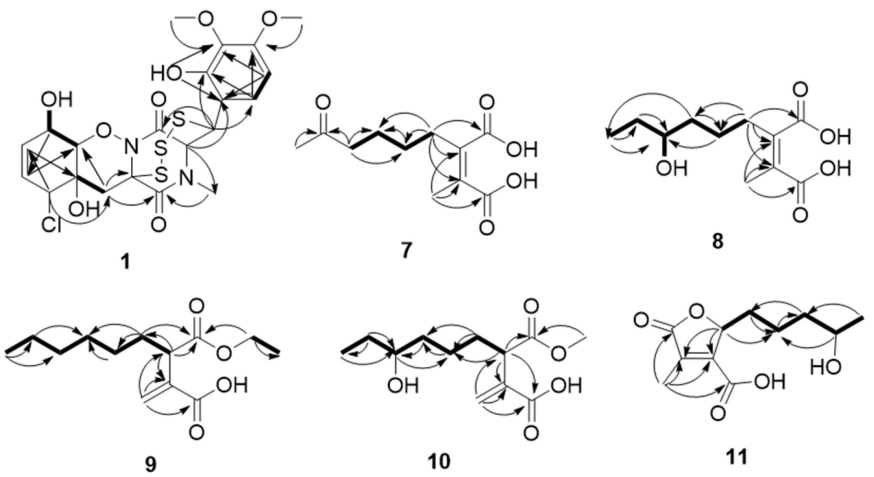

FIGURE 2 | Key HMBC (arrows) and COSY (bold lines) correlations of compounds **1** and **7**-**11**.

respectively, for 48 h. Then, cells were collected and stained with annexin V–fluoresceine isothiocyanate (FITC) and propidium iodide (PI) solution following the manufacturer's manual (BMS500FI-300, Thermo Fisher Scientific). The apoptotic rate of PC-3 cells was examined and analyzed by flow cytometer (NovoCyte, Agilent). Each experiment was repeated three times independently.

RESULTS AND DISCUSSION

Structural Elucidation

Compound **1** was obtained as colorless needles and had the molecular formula $C_{21}H_{23}ClN_2O_8S_3$ with 11 degrees of unsaturation as established by HRESIMS. The ^{1}H-NMR (**Table 1**) and HSQC experiment of **1** showed the typical pattern of an thiodiketopiperazines skeleton with three exchangeable protons, assigned to 14-OH (δ_H 9.64, s), 10-OH (δ_H 5.17, d, J = 6.6 Hz), and 6-OH (δ_H 6.11, d, J = 2.3 Hz), two aromatic methine protons [H-17 (δ_H 6.53, d, J = 8.8 Hz) and H-18 (δ_H 7.08, d, J = 8.8 Hz)], two olefinic protons [H-8 (δ_H 5.63, dt, J = 10.3, 2.5 Hz) and H-9 (δ_H 5.58, dt, J = 10.3, 2.0 Hz)], five methines [H-2 (δ_H 4.63, d, J = 1.1 Hz), H-7 (δ_H 4.88, m), H-10 (δ_H 4.43, m), H-11 (δ_H 4.10, dd, J = 7.3, 1.9 Hz), and H-12 (δ_H 5.39, s)], one methylene [H_2-5α (δ_H 2.54, dd, J = 14.8, 2.0 Hz) and H_2-5β (δ_H 2.09, d, J = 14.8 Hz)], one *N*-methyl [H_3-21 (δ_H 3.12, s)], and two *O*-methyl [H_3-19 (δ_H 3.69, s) and H_3-20 (δ_H 3.78, s)]. Besides the above 13 corresponding hydrogen-bearing carbons, eight non-protonated (with six sp^2 and two sp^3) carbon atoms remained in the ^{13}C NMR spectrum. Detailed analysis of the above NMR data and 2D NMR correlations (**Figure 2** and **Table 1**) resulted in the elucidation of the planar structure of **1**. Upon slow evaporation of the solvent MeOH, which was achieved by storing the sample in a refrigerator for 4 weeks, single crystals of adequate quality of **1** were obtained, making an X-ray diffraction study possible that could unequivocally confirm the chemical structure of **1**. The absolute configuration was determined on the basis of measuring the anomalous dispersion effects by collecting Friedel pair reflections in the X-ray diffraction experiment (**Figure 3**).

Compound **7** was isolated as colorless oil, and its molecular formula was determined as $C_{11}H_{16}O_5$ with four degrees of unsaturation, as a deprotonated ion peak at m/z 227.0927 $[M-H]^-$ in the HRESIMS spectrum. The NMR data of **7** (**Tables 2**, **3**) indicated the presence of a ketone group (δ_C 208.8), two carboxylic groups (δ_C 166.7, 166.9), one double bond (δ_C 143.7, 141.5), two methyl group (δ_C 30.2, 9.8), and four aliphatic methylene groups. Through inspection of the ^{1}H-^{1}H COSY spectrum, we easily established a long spin system that started from H_2-5 (δ_H 2.40, t) and terminated at H_2-8 (δ_H 2.44, t) (**Figure 2**). In the HMBC spectrum, the H_2-5 showed correlations to the double bond (C-2/C-3), as well as to carboxylic group (C-1,

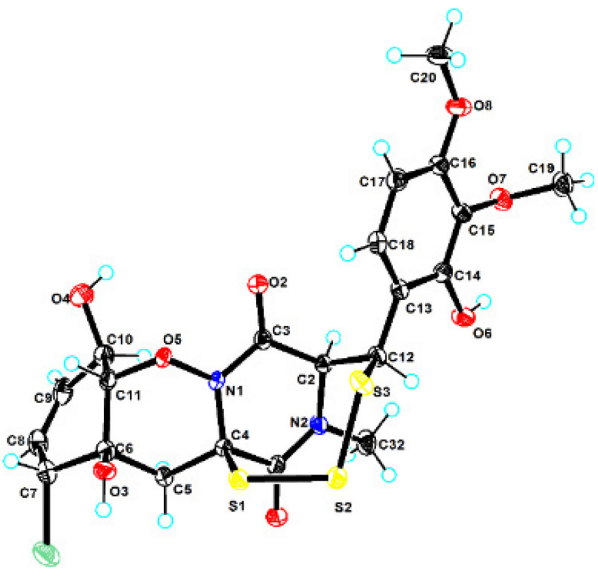

FIGURE 3 | X-ray single-crystal structure of compound **1**.

TABLE 4 | Antibacterial, antifungal, cytotoxic, and anti-inflammatory activities of the obtained compounds.

Comp.	Antibacterial(MIC, μg/mL)		Antifungal(MIC, μg/mL)		Cytotoxic(IC_{50}, μM)		Antiinflammatory(IC_{50}, μM)
	E. rhusiopathiae	*S. suis*	*B. cinerea*	*S. nodorum*	22Rv1	PC-3	NF-κB
1	50	100	>100	>100	13.9	44.0	8.2
2	100	>100	25	25	13.0	>50	15.1
3	50	50	>100	>100	13.6	5.1	>50
4	100	100	>100	>100	>50	>50	>50
5	50	100	>100	>100	>50	>50	12.6
6	>100	>100	>100	>100	>50	>50	>50
7	>100	>100	>100	>100	>50	>50	>50
8	>100	>100	>100	>100	>50	>50	>50
9	>100	>100	>100	>100	>50	>50	10.7
10	>100	>100	>100	>100	>50	>50	>50
11	>100	>100	>100	>100	>50	>50	21.5
Pos.	0.78	0.78	6.25	6.25	/	/	/

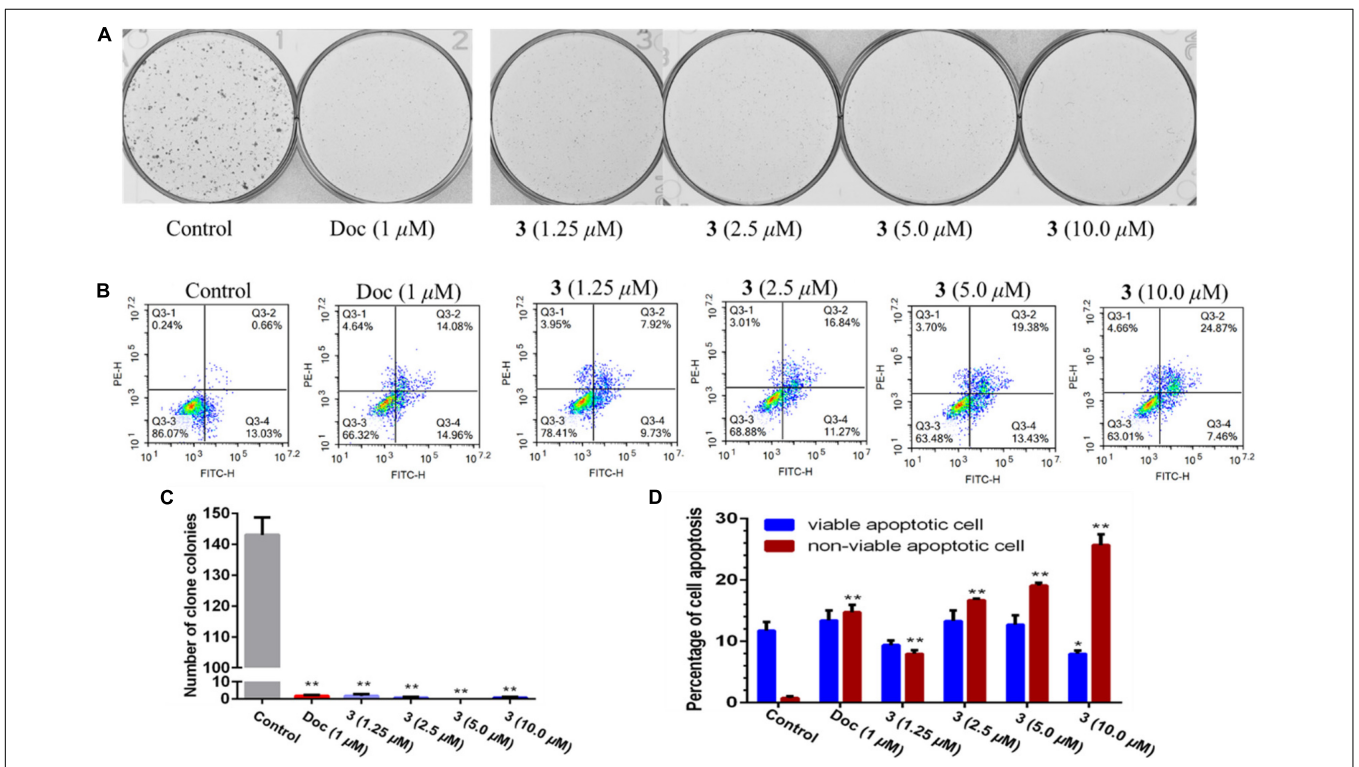

FIGURE 4 | Compound **3** reduced PC-3 cells colony formation **(A,C)** and induced apoptosis **(B,D)**. All results were presented as mean ± SD. Statistical significance was determined with one-way ANOVA. $^{*}P < 0.05$ and $^{**}P < 0.01$ were considered statistically significant.

δ_C 166.7), indicating that C-5 and C-1 were attached to the allylic carbon (C-2). The HMBC correlations from H_3-11 to double bond (C-3/C-2), as well as to C-4, indicating that C-11 and C-4 were attached to the allylic carbon (C-2). C-9 connected to C-10 and C-8 was substantiated by the HMBC correlations from H_2-8 to C-9 and from H_3-10 to C-9 and C-8. Therefore, **7** was established as 2-methyl-3-(5-oxohexyl) maleic acid.

Compound **8** exhibited UV maximum absorption at 206 and 250 nm similar to that of **7**, indicating that they shared a similar chromophore. The HRESIMS data of **8** determined the molecular formula $C_{11}H_{18}O_5$, with two hydrogen atoms more than **7**. Compared to the NMR data, **8** contained one less carbonyl group at C-9, but one more hydroxyl group at C-8 than **7**. Thus, **8** was determined as 2-(4-hydroxyhexyl)-3-methylmaleic acid.

Compound **9** showed a prominent peak at *m/z* 243.1594 $[M + H]^+$ in the HRESIMS spectrum, corresponding to the molecular formula $C_{13}H_{23}O_4$. Analysis of the NMR data (**Tables 2**, **3**) of **9** revealed that it was also structurally related to **7**. Compound **9** established a long chain from C-5 to C-10 through COSY spectrum (**Figure 2**). The position of the double bond

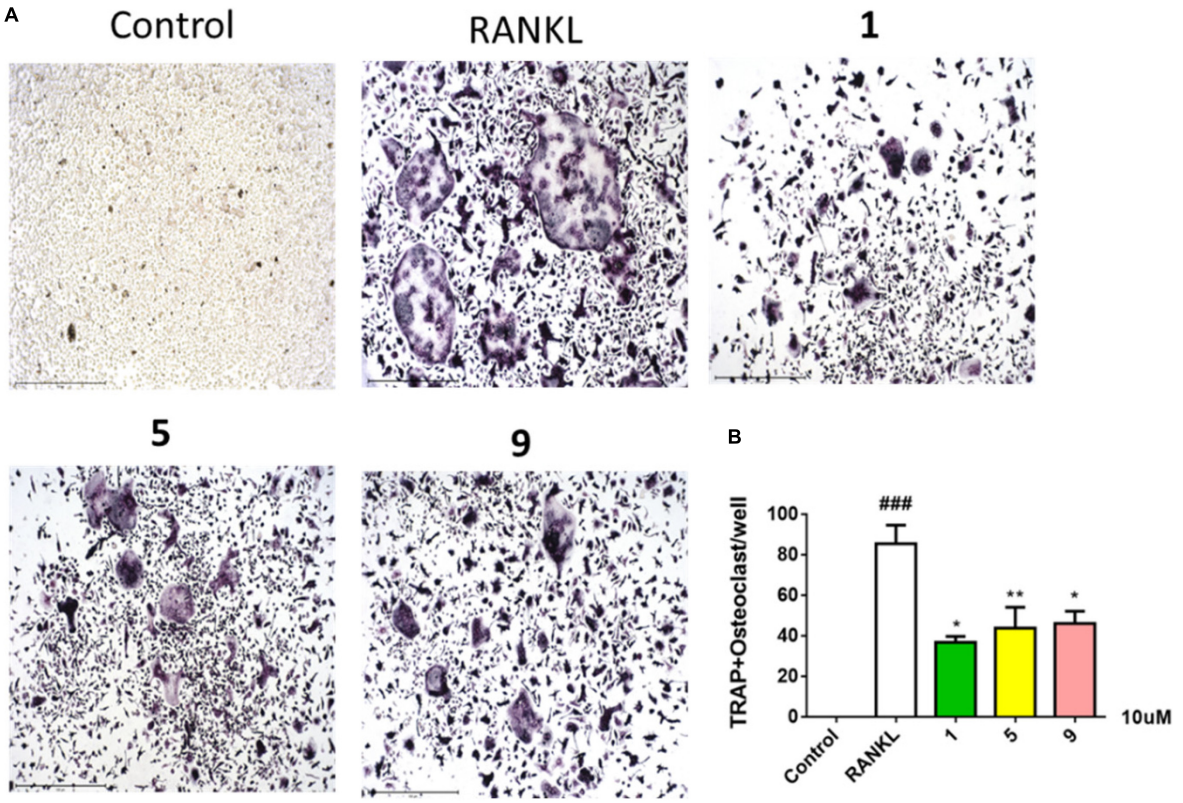

FIGURE 5 | Compounds **1**, **5**, and **9** suppressed RANKL-induced osteoclast differentiation. Representative images of osteoclasts from BMMCs treated with **1**, **5**, and **9** (10 μM) for 3 days, tartrate-resistant acidic phosphatase (TRAP)–positive multinucleated cells were regarded as osteoclasts **(A)** and quantified **(B)**. All experiments were performed at least three times. The data are presented as the mean ± SD of representative experiments. $^{###}p < 0.001$ vs. control group; $^{*}p < 0.05$ and $^{**}p < 0.01$ vs. RANKL group.

is at C-3/C-11 and an ethyl group attached to the ester group (C1). Thus, compound **9** was determined as 3-(ethoxycarbonyl)-2-methylenenonanoic acid.

Compound **10**, a colorless oil, was found to have the molecular formula $C_{12}H_{21}O_5$ on the basis of HRESIMS data. In addition, **10** exhibited a similar UV maximum absorption as **9** at 206 nm, indicating that they have similar chromophores. The NMR spectrum of **10** (**Tables 2**, **3**) is similar to that of **9**, with one more oxygen atom and one methylene group. The ^{1}H-^{1}H COSY correlations (**Figure 2**) of H_2-7/H-8 and H-8/H_2-9, as well as HMBC correlations from H-8 to C-6 and from C-8 to H_3-10, H_2-9, and H_2-7 indicated that the position of the oxymethine (δ_H 3.28; δ_C 71.3). Thus, **10** was elucidated as 7-hydroxy-3-(methoxycarbonyl)-2-methylenenonanoic acid.

Compound **11** was obtained as brown oil. HREIMS ion peak at *m*/*z* 229.1076 $[M + H]^+$ gave the molecular formula $C_{11}H_{17}O_5$, suggesting four degrees of unsaturation. The ^{13}C NMR spectrum (**Table 2**) revealed two carbonyl carbons (δ_C 173.6 and 164.2), together with a fully substituted double bond (δ_C 133.9 and 151.5). The ^{1}H–^{1}H COSY spectrum (**Figure 2**) revealed a spin system consistent with an *n*-pentyl chain (from C-5 to C-9). An oxymethine of C-8 (δ_H 3.55; δ_C 66.0) had HMBC correlations extending to C-6 (δ_C 21.1). The HMBC correlations from δ_H 5.13 (1H, m, H-4) to C-2 (δ_C 133.9) and C-3 (δ_C 151.5) constructed an α, β-unsaturated five-member lactone ring. In addition, a methyl group substituted at C-2 was supported by the HMBC correlations of C-10 (δ_H 2.02, δ_C 10.7) to C-1, C-2, and C-3, and a carboxyl substituted at C-3 was supported by the correlations of H-10 to C-11. Finally, compound **11** was identified and named 2-(4-hydroxypentyl)-4-methyl-5-oxo-2,5-dihydrofuran-3-carboxylic acid.

The optical rotations of compounds **8**–**11** were close to zero, and these compounds showed little cotton effect in CD spectroscopy, suggesting them to be racemic mixtures (**Supplementary Material**). The α-hydro-carbon and C-8 with hydroxyl groups led to chiral centers. It had been reported in the literature that the alkane derivatives were found as enantiomers (Akone et al., 2014).

In addition, the known thiodiketopiperazine derivatives were elucidated as adametizine A (**2**) (Liu et al., 2015a), DC1149B (**3**) (Yamazaki et al., 2015), outovirin B (**4**) (Kajula et al., 2016), pretrichodermamide E (**5**) (Yurchenko et al., 2016), and peniciadametizine A (**6**) (Liu et al., 2015b), respectively, by comparing their physicochemical properties and spectroscopic data with the reported literature values.

Bioassays of Compounds

All obtained compounds were evaluated for their antibacterial and antifungal activities. Compounds **1**–**5** exhibited weak antibacterial activities against *Erysipelothrix rhusiopathiae*

WH13013 and *Streptococcus suis* SC19, with the minimal inhibitory concentration (MIC) values of 50–100 μg/ml. Compound **2** also exhibited activity against fungi *Botrytis cinerea* and *Septoria nodorum* Berk., with the MIC values of 25 μg/ml. However, all isolated compounds showed no activities against the other three bacteria (*Escherichia coli* ATCC 25922, *Pseudomonas aeruginosa* ATCC 27853, and *Staphylococcus aureus* ATCC 25923) and two fungi (*Fusarium graminearum* Schw. and *Rhizoctonia solani* Kühn). Cephalosporin and cycloheximide were used as the positive controls in the antibacterial (MIC values of 0.78 μg/ml) and antifungal (MIC values of 6.25 μg/ml) tests, respectively (**Table 4**).

Two human prostate cancer cell lines, PC-3 (androgen receptor negative) and 22Rv1 (androgen receptor positive), were used in the cytotoxicity tests. Compounds **1–3** exhibited cytotoxicity against 22Rv1 cells with half maximal inhibitory concentration (IC_{50}) values of 13.9, 13.0, and 13.6 μM, respectively, whereas **1** and **3** showed activities against PC-3 cells with IC_{50} values of 44.0 and 5.1 μM, respectively. Compound **3** was further evaluated for its anti-tumor effect by plate clone formation assay and flow cytometry on PC-3 cells. The results showed that **3** reduced PC-3 cells colony formation (**Figures 4A,C**) and induced cell apoptosis in a dose-dependent manner (**Figures 4B,D**).

Compounds **1–11** were screened for their inhibitory activities of LPS-induced NF-κB activation in RAW264.7 cells. Compounds **1**, **2**, **5**, **9**, and **11** exhibited obvious inhibitory activities against LPS-induced NF-κB with IC_{50} values of 8.2, 15.1, 12.6, 10.7, and 21.5 μM, respectively. Moreover, in the further study for evaluation with their effects on RANKL-induced osteoclastogenesis, **1**, **5**, and **9** could suppress the RANKL-induced osteoclast differentiation in BMMCs obviously, with the concentration of 10 μM. The new trithiodiketopiperazine derivative adametizine C (**1**) showed the strongest activity, relatively (**Figure 5**). Consequently, it is revealed that these compounds could be the promising osteoclast differentiation inhibitors for the treatment of osteoclast-related diseases.

In addition, we also found that the thiodiketopiperazine derivatives exhibited various activities reported in the literatures. For example, pretrichodermide A was active against *Mycobacterium tuberculosis* (Seephonkai et al., 2006); Adametizine A (**2**) was found to be active against a variety of bacteria (Liu et al., 2015a); Outovirin C was active against fungus *Botrytis cinerea* (Kajula et al., 2016). Gliovirin showed inhibitory effects on the expression of cytokines [tumor necrosis factor (TNF)-α and interleukin-2 (IL-2)] and pro-inflammatory enzymes [cyclooxygenase-2 (COX-2) and inducible nitric oxide synthase (INOS)] in T cells and monocytes/macrophages (Rether et al., 2007).

CONCLUSION

In summary, chemical investigation of the mangrove sediment–derived fungus *Penicillium ludwigii* SCSIO41408 led to the isolation of a new trithiodiketopiperazine, five new alkane derivatives (**7–11**), and five dithiodiketopiperazine derivatives (**2–6**). In a variety of bioactivity screening, **1–5** exhibited some selective antifungal or antibacterial activities; **1–3** showed cytotoxicity against prostate cancer cell line 22Rv1or PC-3 cells; moreover, **3** could significantly reduce PC-3 cells' colony formation and induce apoptosis in a dose-dependent manner. Several compounds also exhibited obvious inhibitory activities of LPS-induced NF-κB, and **1**, **5**, and **9** were suppressed RANKL-induced osteoclast differentiation in BMMCs at 10 μM. Adametizine C (**1**), with the strongest inhibitory activity against RANKL-induced osteoclast differentiation, was suggested to be the promising lead compound for the treatment of osteoclast-related diseases.

DATA AVAILABILITY STATEMENT

The datasets presented in this study can be found in online repositories. The names of the repository/repositories and accession number(s) can be found in the article/**Supplementary Material**.

AUTHOR CONTRIBUTIONS

JC, BP, YL, and XZ contributed to the conception and design of the study. JC performed the experiments, analyzed data, and wrote the manuscript. XZ reviewed and revised the manuscript. XW and ZY performed the cytotoxicity against 22Rv1 and PC-3 cells. YT did the inhibitory activities of LPS-induced NF-κB activation. All authors contributed to manuscript revision and reviewed and approved the submitted version.

FUNDING

This work was supported by grants from the Guangdong Local Innovation Team Program (2019BT02Y262), the Marine Economy Development Project of Guangdong Province [GDNRC (2021)52], National Natural Science Foundation of China (U20A20101, 81973235), K. C. Wong Education Foundation (GJTD-2020-12), and Liao Ning Revitalization Talents Program (XLYC1802037).

ACKNOWLEDGMENTS

We are grateful to the analytical facilities (Xiao, Zheng, Sun, Zhang, and Ma) in SCSIO.

SUPPLEMENTARY MATERIAL

The Supplementary Material for this article can be found online at: https://www.frontiersin.org/articles/10.3389/fmicb.2022.857041/full#supplementary-material

REFERENCES

Akone, S. H., Rahn, S., Henrich, B., Daletos, G., Vardamides, J. C., Nkengfack, A. E., et al. (2014). 2-Pentenedioic acid derivatives from a soil-derived fungus *Gongronella butleri*. *Phytochem. Lett.* 10, 184–188. doi: 10.1016/j.phytol.2014.09.001

Cai, J., Chen, C. M., Tan, Y. H., Chen, W. H., Luo, X. W., Luo, L. X., et al. (2021). Bioactive polyketide and diketopiperazine derivatives from the mangrove-sediment-derived fungus. *Aspergill. Mol.* 26:4851. doi: 10.3390/molecules26164851

Chen, C. M., Chen, W. H., Pang, X. Y., Liao, S. R., Wang, J. F., Lin, X. P., et al. (2021a). Pyrrolyl 4-quinolone alkaloids from the mangrove endophytic fungus *Penicillium steckii* SCSIO 41025: Chiral resolution, configurational assignment, and enzyme inhibitory activities. *Phytochemistry* 186:112730. doi: 10.1016/j.phytochem.2021.112730

Chen, C. M., Chen, W. H., Tao, H. M., Yang, B., Zhou, X. F., Luo, X. W., et al. (2021b). Diversified polyketides and nitrogenous compounds from the mangrove endophytic fungus *Penicillium steckii* SCSIO 41025. *Chin. J. Chem.* 39, 2132–2140. doi: 10.1002/cjoc.202100226

Dai, J. J., Chen, A., Zhu, M. L., Qi, X., Tang, W., Liu, M., et al. (2019). Penicisulfuranol A, a novel C-terminal inhibitor disrupting molecular chaperone function of Hsp90 independent of ATP binding domain. *Biochem. Pharmacol.* 163, 404–415. doi: 10.1016/j.bcp.2019.03.012

He, F., Li, X. B., Yu, J. H., Zhang, X. Y., Nong, X. H., Chen, G. Y., et al. (2019). Secondary metabolites from the mangrove sediment-derived fungus *Penicillium pinophilum* SCAU037. *Fitoterapia* 136:104177. doi: 10.1016/j.fitote.2019.104177

Hong, G. J., Zhou, L., Han, X. R., Sun, P., Chen, Z. Q., He, W., et al. (2020). Asiatic acid inhibits OVX-induced osteoporosis and osteoclastogenesis via regulating RANKL-mediated NF-κB and NFATC1 signaling pathways. *Front. Pharmacol.* 11:331. doi: 10.3389/fphar.2020.00331

Kajula, M., Ward, J. M., Turpeinen, A., Tejesvi, M. V., Hokkanen, J., Tolonen, A., et al. (2016). Bridged epipolythiodiketopiperazines from *Penicillium raciborskii*, an endophytic fungus of *Rhododendron tomentosum* harmaja. *J. Nat. Prod.* 79, 685–690. doi: 10.1021/np500822k

Li, K. L., Chen, S. Q., Pang, X. Y., Cai, J., Zhang, X. Y., Liu, Y. H., et al. (2022). Natural products from mangrove sediments-derived microbes: Structural diversity, bioactivities, biosynthesis, and total synthesis. *Eur. J. Med. Chem.* 2022:117. doi: 10.1016/j.ejmech.2022.114117

Liu, Y., Li, X. M., Meng, L. H., Jiang, W. L., Xu, G. M., Huang, C. G., et al. (2015a). Bisthiodiketopiperazines and acorane sesquiterpenes produced by the marine-derived fungus *Penicillium adametzioides* AS-53 on different culture media. *J. Nat. Prod.* 78, 1294–1299. doi: 10.1021/acs.jnatprod.5b00102

Liu, Y., Mándi, A., Li, X. M., Meng, L. H., Kurtán, T., and Wang, B. G. (2015b). Peniciadametizine A, a dithiodiketopiperazine with a unique spiro [furan-2,7'-pyrazino [1,2-b][1,2]oxazine] skeleton, and a related analogue, peniciadametizine B, from the marine sponge-derived fungus *Penicillium adametzioides*. *Mar. Drugs* 13, 3640–3652. doi: 10.3390/md13063640

Luo, X. W., Chen, C. M., Tao, H. M., Lin, X. P., Yang, B., Zhou, X. F., et al. (2019). Structurally diverse diketopiperazine alkaloids from the marine-derived fungus *Aspergillus Versicolor* SCSIO 41016. *Org. Chem. Front.* 6, 736–740. doi: 10.1039/C8QO01147H

Luo, X. W., Lin, X. P., Tao, H. M., Wang, J. F., Li, J., Yang, B., et al. (2018). Isochromophilones A–F, cytotoxic chloroazaphilones from the marine mangrove endophytic fungus *Diaporthe* sp. SCSIO 41011. *J. Nat. Prod.* 81, 934–941. doi: 10.1021/acs.jnatprod.7b01053

Rether, J., Serwe, A., Anke, T., and Erkel, J. (2007). Inhibition of inducible tumor necrosis factor-α expression by the fungal epipolythiodiketopiperazine gliovirin. *Biol. Chem.* 388, 627–637. doi: 10.1515/BC.2007.066

Seephonkai, P., Kongsaeree, S., Prabpai, S., Isaka, M., and Thebtaranonth, Y. (2006). Transformation of an irregularly bridged epidithiodiketopiperazine to trichodermamide A. *Org. Lett.* 8, 3073–3075. doi: 10.1021/ol061046l

Tan, Y. H., Dang, W. D., Yang, Y. Y., Ke, M. H., Zou, B. H., Luo, X. W., et al. (2020). A marine fungus-derived nitrobenzoyl sesquiterpenoid suppresses receptor activator of NF-κB ligand-induced osteoclastogenesis and inflammatory bone destruction. *Brit. J. Pharmacol.* 177, 4242–4260. doi: 10.1111/bph.15179

Wan, Z. Y., Fang, W., Shi, L. Q., Wang, K. M., Zhang, Y. N., and Zhang, Z. G. (2014). Novonestmycins A and B, two new 32-membered bioactive macrolides from *Streptomyces phytohabitans* HBERC-20821. *J. Antibiot.* 68, 185–190. doi: 10.1038/ja.2014.123

Wang, X., Zhu, J., Yan, H., Shi, M., Zheng, Q., Wang, Y., et al. (2021). Kaempferol inhibits benign prostatic hyperplasia by resisting the action of androgen. *Eur. J. Pharmacol.* 907:174251. doi: 10.1016/j.ejphar.2021.174251

Yamazaki, H., Takahashi, O., Murakami, K., and Namikoshi, M. (2015). Induced production of a new unprecedented epitrithiodiketopiperazine, chlorotrithiobrevamide, by a culture of the marine-derived *trichoderma* cf. *brevicompactum* with dimethyl sulfoxide. *Tetrahed. Lett.* 56, 6262–6265. doi: 10.1016/j.tetlet.2015.09.113

Yurchenko, A. N., Smetanina, O. F., Ivanets, E. V., Kalinovsky, A. I., and Dyshlovoy, S. A. (2016). Pretrichodermamides D–F from a marine algicolous fungus *Penicillium* sp. KMM 4672. *Mar. Drugs* 14, 122. doi: 10.3390/md14070122

Zhou, Y., Wang, C. W., Si, J. Y., Wang, B. X., Zhang, D. H., Ding, D., et al. (2020). Melatonin up-regulates bone marrow mesenchymal stem cells osteogenic action but suppresses their mediated osteoclastogenesis via MT2 -inactivated NF-κB pathway. *Brit. J. Pharmacol.* 177, 2106–2122. doi: 10.1111/bph.14972

Conflict of Interest: The authors declare that the research was conducted in the absence of any commercial or financial relationships that could be construed as a potential conflict of interest.

frontiers | Frontiers in Microbiology

ORIGINAL RESEARCH
published: 19 April 2022
doi: 10.3389/fmicb.2022.880874

Phytotoxic Azaphilones From the Mangrove-Derived Fungus *Penicillium sclerotiorum* HY5

Wei Wang[1], Mei Wang[2], Xian-Bo Wang[3], Yi-Qiang Li[2], Ji-Lin Ding[3], Ming-Xian Lan[1], Xi Gao[1], Dong-Lin Zhao[2], Cheng-Sheng Zhang[2]* and Guo-Xing Wu[1]**

[1] College of Plant Protection, Yunnan Agricultural University, Kunming, China, [2] Tobacco Research Institute of Chinese Academy of Agricultural Sciences, Qingdao, China, [3] Guizhou Tobacco Company, Zunyi Branch, Zunyi, China

Mangrove is a unique marine ecosystem growing in the intertidal zone of tropical and subtropical coast, with the characteristics of hypoxia tolerance, high salinity, and high humidity. In order to discover novel leading compounds with potent phytotoxicity, seven pairs of azaphilones *E/Z* isomers, isochromophilone H (**1a**/**1b**), sclerotiorins A and B (**2a**/**2b** and **3a/3b**), ochlephilone (**4a**/**4b**), isochromophilone IV (**5a**/**5b**), isochromophilone J (**6a**/**6b**), and isochromophilone I (**7a**/**7b**), were isolated from the culture broth of the mangrove-derived fungus, the *Penicillium sclerotiorum* HY5, by various chromatographic methods. Among them, **1a**, **1b**, **2a**, **3a**, **4a**, **5a, 6a**, and **6b** were new compounds. Their chemical structures and absolute configurations were elucidated based on high resolution electrospray ionization mass spectroscopy (HRESIMS), 1D/2D nuclear magnetic resonance (NMR) spectroscopic analysis, and comparisons of electronic circular dichroism (ECD) data. Compounds **3**, **4**, and **7** exhibited potent phytotoxicity against the growth of radicle and plumule on *Amaranthus retroflexus* L., with EC_{50} values ranging from 234.87 to 320.84 μM, compared to the positive control glufosinate-ammonium, with EC_{50} values of 555.11 μM for radicle, and 656.04 μM for plumule. Compounds **4** and **7** also showed inhibitory effects on the growth of velvetleaf (*Abutilon theophrasti* Medikus), with EC_{50} values ranging from 768.97 to 1,201.52 μM. This study provides new leading compounds for the research and development of marine-derived bioherbicides.

Keywords: azaphilones, phytotoxicity, bioherbicide, weeds, *Penicillium sclerotiorum*

OPEN ACCESS

Edited by:
Junfeng Wang,
South China Sea Institute of Oceanology (CAS), China

Reviewed by:
Fandong Kong,
Chinese Academy of Tropical Agricultural Sciences, China
Min Chen,
Yangzhou University, China

***Correspondence:**
Dong-Lin Zhao
zhaodonglin@caas.cn
Cheng-Sheng Zhang
zhchengsheng@126.com
Guo-Xing Wu
wugx1@163.com

Specialty section:
This article was submitted to Extreme Microbiology, a section of the journal Frontiers in Microbiology

Received: *22 February 2022*
Accepted: *14 March 2022*
Published: *19 April 2022*

Citation:
Wang W, Wang M, Wang X-B, Li Y-Q, Ding J-L, Lan M-X, Gao X, Zhao D-L, Zhang C-S and Wu G-X (2022) Phytotoxic Azaphilones From the Mangrove-Derived Fungus Penicillium sclerotiorum HY5. Front. Microbiol. 13:880874. doi: 10.3389/fmicb.2022.880874

INTRODUCTION

Weeds are common, pernicious, and troublesome plant species, which can cause serious yield reduction and inferior quality in crop production. It is estimated that the production loss caused by weeds is approximately 34% of the crop yield worldwide (Harding and Raizada, 2015; Shi et al., 2020). In the present situation, control weeds in farmland on a global scale are mainly dependent on chemical treatments (Travaini et al., 2016; Vurro et al., 2018); however, there are many long-term problems with the intensive application of agrochemical herbicides, such as environmental pollution, pesticide residue accumulation, and the emergence of weed resistance, which increase the difficulty of weeds control management (Kim et al., 2020; Shi et al., 2020). With the continuous discoveries of a great number of biocontrol microbial resources, exploration of microbes with excellent biological activity from extreme conditions such as marine-derived microorganisms, in recent years, have attracted much attention of scientists (Shen et al., 2020). Marine surroundings

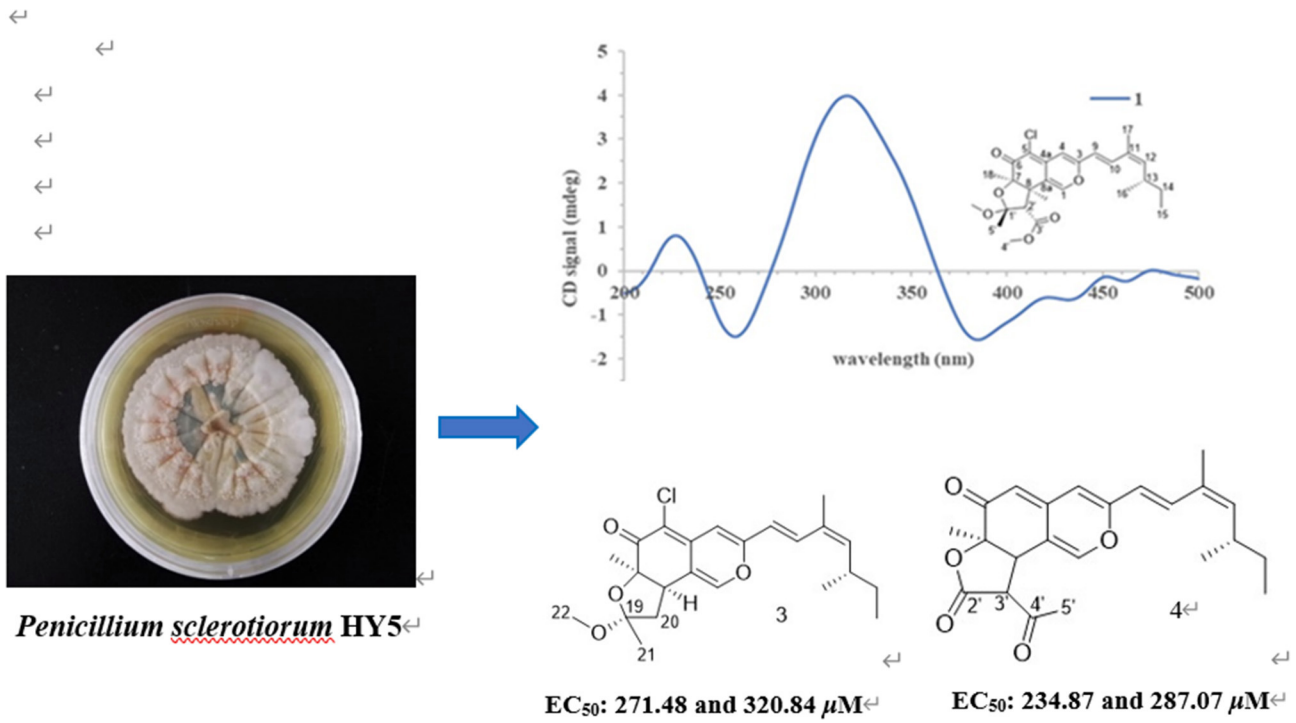

Graphical Abstract | Representative phytotoxic azaphilones from *Penicillium sclerotiorum* HY5.

provide abundant microbial resources because of their geographic and climatic characteristics. These features make it become an important field for discovering bioactive natural products with agricultural applications (Yang et al., 2015; Carroll et al., 2020).

Azaphilones are a class of fungi-derived polyketide secondary metabolites with novel structures having an oxabicyclic skeleton and can be divided into 18 different categories, which have numerous chiral centers and flexible side chains (Gao et al., 2013; Makrerougras et al., 2017). Previous reports have shown that they exhibited broad-spectrum activities in many biological tests, including antimicrobial, antiviral, anti-inflammatory, antioxidant, cytotoxic, hypoglycemic, and nematocidal activities (Luo et al., 2018; Wang et al., 2020). More than 430 azaphilones, isolated from both marine and terrestrial fungi, have been reported until 2019, representing an important class of natural products (Qian et al., 2019). However, most of the azaphilones were utilized for drug development, and their agricultural bioactivities need to be explored.

During our ongoing search for phytotoxic compounds with agricultural applications (Huang et al., 2018; Zhao et al., 2019, 2020), the mangrove-derived strain *Penicillium sclerotiorum* HY5 attracted our attention because its culture extracts demonstrated potent phytotoxicity toward *Amaranthus retroflexus* L., and the high-performance liquid chromatography (HPLC) profile highlighted a rich array of ultraviolet absorption peaks similar to that of azaphilones. Further chemical investigation on the fungal extracts resulted in the isolation of seven pairs of azaphilones *E/Z* isomers, isochromophilone H (**1a** and **1b**), sclerotiorin A (**2a** and **2b**), sclerotiorin B (**3a** and **3b**), ochlephilone (**4a** and **4b**), isochromophilone IV (**5a** and **5b**), isochromophilone J (**6a** and **6b**), and isochromophilone I (**7a** and **7b**; **Figure 1**). Here, we report the isolation, structural elucidation, and phytotoxic evaluation of isolated azaphilones.

MATERIALS AND METHODS

General Experimental Procedures

Optical rotations were measured at 25°C using a JASCO P-1020 digital polarimeter (JASCO Ltd., Tokyo, Japan). The UV spectra were determined on a Techcomp UV2310II spectrophotometer (Techcomp, Ltd., Shanghai, China). Electronic circular dichroism (ECD) spectra were acquired with a JASCO J-815 CD spectrometer (JASCO Ltd., Tokyo, Japan) at 25°C. The NMR spectra were recorded on a DD2 NMR spectrometer (Agilent Technologies, Santa Clara, CA, USA; 500 MHz for ^{1}H and 125 MHz for ^{13}C) and a JNM-ECP NMR spectrometer (JEOL, Japan; 600 MHz for ^{1}H and 150 MHz for ^{13}C) using tetramethylsilane (TMS) as an internal standard, and $CDCl_3$ as solvent. The Electrospray ionization mass spectrometry (ESIMS) was taken on a Micromass Q-TOF spectrometer (Waters, Ltd., Milford, Massachusetts, USA), and high-resolution ESIMS spectra were collected on a Thermo Scientific LTQ Orbitrap XL spectrometer (Thermo Fisher Scientific, Waltham, MA, USA). Semipreparative HPLC was conducted on a Waters e2695 separation system (Milford,

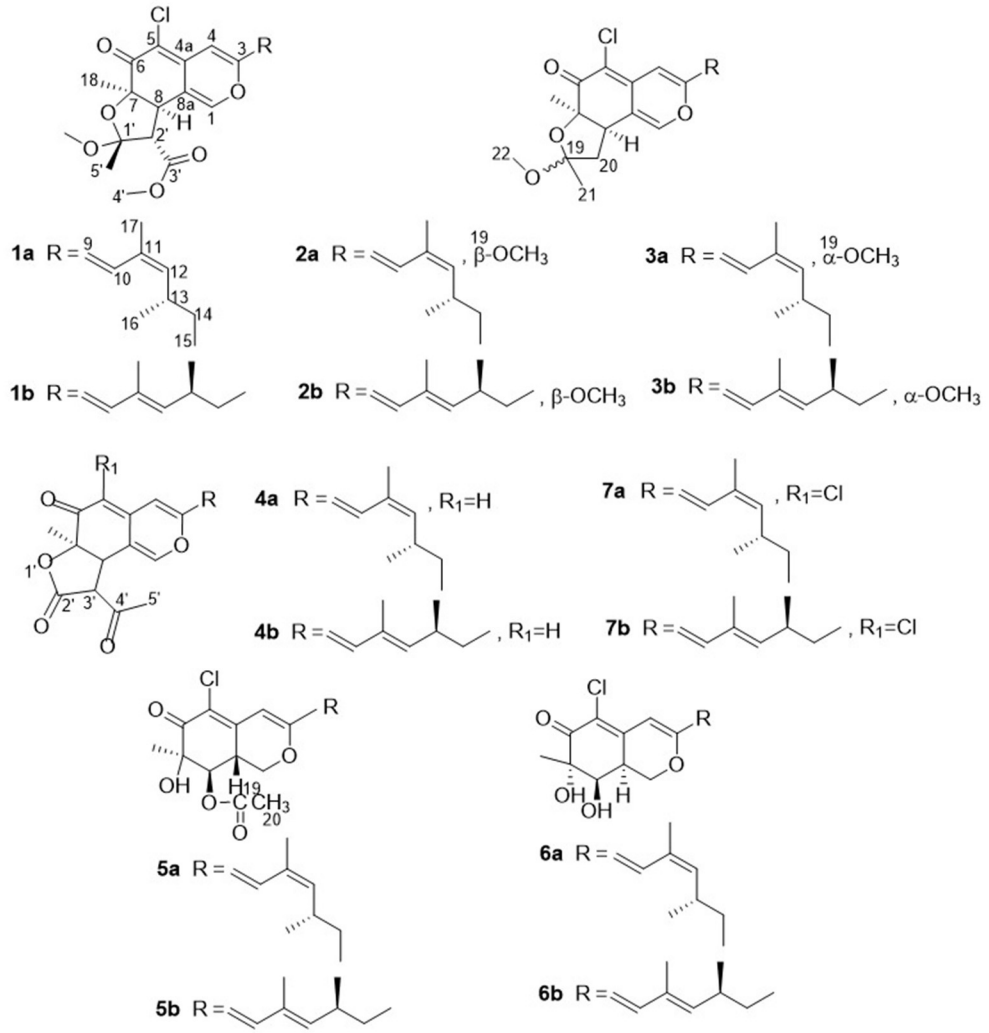

FIGURE 1 | Chemical structures of compounds **1–7.**

MA, USA), equipped with a Waters 2998 photodiode array detector and a Waters X-Bridge C_{18} (5 μm, 10 × 250 mm) preparative column, and the flow rate was 2 mL/min. Column chromatography (CC) was performed using Silica gel (100–200, 200–300 mesh; Qingdao Marine Chemical Inc., Qingdao, China), Sephadex LH-20 (GE Healthcare, Pittsburgh, PA, USA), and octadecylsilyl silica gel (ODS) (40–63 μm, merck, MA, USA). Precoated silica gel plates (Yantai Zi fu Chemical Group Co., Yan Tai, China; GF254) were used for thin layer chromatography (TLC) analysis. Spots were detected by UV light (254 nm) and colored by spraying heated silica gel plates with 12% H_2SO_4 in H_2O containing saturated vanillin.

Fungal Material

The studied strain was isolated from an unidentified mangrove sample collected from coastal marine habitats of the South China Sea, Haikou, China, in May 2017. This strain was identified as *P. sclerotiorum* HY5 by amplifying and analyzing its internal transcribed spacer (ITS) sequence, as well as morphological features. The ITS sequence of this fungus was deposited at the GenBank database (accession number MG827186), and the isolated strain was preserved in the Marine Agriculture Research Center, Tobacco Research Institute of Chinese Academy of Agricultural Sciences, Qingdao, China.

Fermentation, Extraction, and Isolation

The purified fungus was grown on PDA plates for 5 days at 28°C. The mycelial disc were inoculated into 500 mL Erlenmeyer flasks containing 200 mL of potato dextrose water (PDW) medium with 3% salinity and shaken on a rotary shaker (175 rpm) at 28°C for 3 days to obtain seed culture. Aliquots (5 mL) of the seed culture were transferred into 1,000 mL Erlenmeyer flasks containing 400 mL of production media, consisting of PDW medium with 3% salinity for 30 days at 28°C, and the fermentation scale was 80 L in total. After fermentation, the culture broth was filtered to separate the culture media and mycelia. The culture

broth was extracted three times with equal volumes of EtOAc. The mycelia were mechanically broken, and then, extracted ultrasonically twice with a mixture (1:1, v/v) of dichloromethane (CH_2Cl_2) and methanol (MeOH), and concentrated in vacuo to obtain an aqueous solution, which was further extracted thrice with equivalent EtOAc. The culture broth and mycelia extracts were combined and evaporated under reduced pressure to yield EtOAc extract (74.61 g), which was then subjected to vacuum liquid chromatography (VLC) on silica gel using a step gradient elution of EtOAc–petroleum ether from 0 to 100% and 10 to 50% MeOH–EtOAc to afford six fractions (Fr.1–Fr.6) based on their TLC profiles. The Fr.2 was chromatographed repeatedly on silica gel CC eluting with mixtures of EtOAc–petroleum ether (10–50%, v/v) to give three subfractions (Fr.21–Fr.23). The Fr.23 was first fractionated *via* reverse silica *gel* CC eluting with a gradient MeOH–H_2O (from 50:50 to 100:0, v/v), and then, separated by Sephadex LH-20 CC eluting with CH_2Cl_2-MeOH (1:1, v/v) to obtain two subfractions (Fr.231–Fr.232). The Fr.231 was then chromatographed repeatedly with a gradient elution of EtOAc–petroleum ether (from 0 to 100%, v/v) and MeOH–EtOAc (from 10 to 50%, v/v) to give four subfractions (Fr.2311–Fr.2314). The Fr.2311 was applied to semipreparative HPLC separation using an isocratic elution of MeOH–H_2O with 0.1% trifluoroacetic acid (TFA) (75% MeOH in H_2O, v/v) to afford compound **7** (119.8 mg). The Fr.2313 was subjected to semipreparative HPLC using an isocratic elution of 70% MeCN in H_2O to yield compound **1** (26.8 mg). Following the same procedures, Fr.3 was also subjected to silica gel CC using a step gradient elution of EtOAc–petroleum ether (0 to 100%, v/v) and MeOH–EtOAc (10 to 50%, v/v) to give two subfractions (Fr.31–Fr.32). The Fr.31 was separated by octadecylsilyl (ODS) CC (MeOH–H_2O; from 50:50 to 100:0, v/v), and then, subjected to Sephadex LH-20 CC eluting with CH_2Cl_2-MeOH (1:1, v/v) to obtain two subfractions (Fr.311–Fr.312). The Fr.311 was further purified by using semipreparative HPLC with isocratic MeOH–H_2O (75:25, v/v) as mobile phase to yield compound **5** (166.3 mg). The Fr.312 was subjected to semipreparative HPLC using MeOH in H_2O (25%) to obtain compounds **2** (28.4 mg) and **3** (28.1 mg). The Fr.32 was eluted using a MeOH–H_2O gradient system (from 50:50 to 100:0, v/v) and sequentially subjected to Sephadex LH-20 CC (CH_2Cl_2-MeOH, 1:1, v/v) to give three subfractions (Fr.321–Fr.323). The Fr.322 was applied to semi-preparative HPLC (60% MeCN in H_2O) to afford compound **4** (164 mg). The Fr.323 was purified by semipreparative HPLC (75% MeOH in H_2O) to generate compound **6** (63 mg). In order to achieve the requirements of the NMR test, the purities of all the isolated compounds were >95% based on the peak area normalization methods.

Isochromophilone H ***(1):*** yellow amorphous powder; $[\alpha]_D^{25.0}$ −15.9 (*c*, 0.46, MeOH); UV(MeOH) λ_{max} (log ε) 202 (3.38), 248 (3.23), and 387 (3.35) nm; ECD (*c* 1.08 mM, MeOH) λ_{max} ($\Delta\varepsilon$) 223 (+0.34), 257 (−0.51), 312 (+1.18), 385 (−0.51) nm; ^{1}H, and ^{13}C NMR data (**Tables 1**, **2**); HRESIMS *m/z* 463.1892 [M+H]$^+$(calculated for $C_{25}H_{31}O_6Cl$, 463.1882).

Sclerotiorin A ***(2):*** yellow amorphous powder; $[\alpha]_D^{25.0}$ +3.1 (*c*, 0.37, MeOH); UV(MeOH) λ_{max} (log ε) 200 (3.46), 249 (3.34), and 390 (3.47) nm; ECD (*c* 1.23 mM, MeOH) λ_{max} ($\Delta\varepsilon$) 238 (+0.84), 258 (−0.94), 312 (+3.82), and 387 (−1.13) nm; ^{1}H and ^{13}C NMR data (**Tables 1**, **2**); HRESIMS *m/z* 405.1832 [M+H]$^+$(calculated for $C_{23}H_{29}O_4Cl$, 405.1827).

Sclerotiorin B ***(3):*** yellow amorphous powder; $[\alpha]_D^{25.0}$ +28.8 (*c*, 0.34, MeOH); UV(MeOH) λ_{max} (log ε) 201 (3.72), 250 (3.67), and 392 (3.82) nm; ECD (*c*, 0.62 mM, MeOH) λ_{max} ($\Delta\varepsilon$) 235 (+1.84), 259 (−1.97), 313 (+8.85), and 381 (−2.37) nm; ^{1}H and ^{13}C NMR data (**Tables 1**, **2**); HRESIMS *m/z* 405.1835 [M+H]$^+$(calculated for $C_{23}H_{29}O_4Cl$, 405.1827).

Ochlephilone ***(4):*** orange amorphous powder; $[\alpha]_D^{25.0}$ +195.3 (*c*, 0.54, MeOH); UV (MeOH) λ_{max} (log ε) 204 (3.89), 250 (4.04), 395 (4.25) nm; ECD (*c* 1.30 mM, MeOH) λ_{max} ($\Delta\varepsilon$) 239 (+2.84), 267 (−0.56), 310 (+6.11), and 340 (+7.14) nm; ^{1}H and ^{13}C NMR data (**Tables 1**, **2**); HRESIMS *m/z* 383.1856 [M+H]$^+$(calculated for $C_{23}H_{26}O_5$, 383.1853).

Isochromophilone IV ***(5):*** yellow amorphous powder; $[\alpha]_D^{25.0}$ −69.1 (*c* 0.44, MeOH); UV(MeOH) λ_{max} (log ε) 200 (3.33), 265 (2.98), 388 (3.83) nm; ECD (*c* 0.63 mM, MeOH) λ_{max} ($\Delta\varepsilon$) 257 (−5.03), 285 (+1.04), 325 (+0.32), 383 (−7.82) nm; ^{1}H and ^{13}C NMR data (**Tables 1**, **2**); HRESIMS *m/z* 395.1627 [M+H]$^+$(calculated for $C_{21}H_{27}O_5Cl$, 395.1620).

Isochromophilone J ***(6):*** yellow amorphous powder; $[\alpha]_D^{25.0}$ +113.3 (*c*, 0.15, MeOH); UV(MeOH) λ_{max} (log ε) 208 (3.38), 265 (3.15), and 390 (3.94) nm; ECD (*c* 1.42 mM, MeOH) λ_{max} ($\Delta\varepsilon$) 214 (−1.87), 255 (+3.47), 321(−0.34), and 388 (+1.88) nm; ^{1}H and ^{13}C NMR data (**Tables 1**, **2**); HRESIMS *m/z* 353.1524 [M+H]$^+$(calculated for $C_{19}H_{25}O_4Cl$, 353.1514).

Phytotoxicity Bioassays

Phytotoxicity was evaluated by seed germination methods. The bioassay experiments were performed on representative weeds in farmlands, including two types of grass [wild oat (*Avena fatua* L.), ryegrass (*Lolium perenne* L.)] and two broadleaf species [redroot amaranth (*A. retroflexus* L.), and velvetleaf (*Abutilon theophrasti* Medikus)], based on previously reported assay methods with some modifications (Travaini et al., 2016; Adetunji et al., 2018).

The tested seeds were pre-incubated in 9-cm diameter Petri dishes with 5 mL of distilled water for about 5 h at 25°C. After that period, the seeds of the target weeds were disinfected with 5% sodium hypochlorite for 10 min and rinsed with distilled water. One layer of sterile filter paper was placed at the base of each Petri dish (for *A. retroflexus* L., 12-well plates were used). Then, 3 mL (for *A. retroflexus* L., 330 μL) of the methanolic solution containing compounds were dropped on the filter paper. The final concentrations of tested compounds were 500, 250, 125, 62.5, and 31.25 μg/mL, respectively. The equivalent sterilized water was added to each well and Petri dish after the escape of methanol. Twenty-five (for *A. retroflexus* L., 10) viable seeds of weeds were placed on a filtrate paper. The herbicide glufosinate-ammonium was used as a positive control, and the methanol solution was then used as solvent control. Lids were sealed with Parafilm and incubated at 28°C, with 12 h supplemental light provided by 400 W Philips lamps and 26°C with 12 h darkness per day. The radicle and plumule lengths were measured and inhibition rates were calculated after 4 days. All treatments were carried out in triplicate. The experimental results are expressed

TABLE 1 | ^{1}H nuclear magnetic resonance (NMR) data of compounds **1–6** (chloroform-*d*, δ in ppm, *J* in Hz).

No.	1a	1b	2a	3a	4a	5a	6a	6b
1α	7.56, s	7.53, s	7.12, s	7.21, s	7.43, s	3.87, dd (10.8,13.2)	4.30, dd (11.4,12.6)	4.27, dd (11.5, 13.0)
1β						4.43, dd (4.8,10.8)	4.55, dd (4.8, 11.4)	4.52, dd (5.0, 11.5)
4	6.53, s	6.51, s	6.52, s	6.53, s	6.11, s	6.14, s	6.12, s	6.10, s
5					5.42, d (1.0)			
8	3.80, d (12.6)	3.79, d (12.6)	3.06, dd (10.0,10.0)	3.43, dd (7.5,13.0)	3.85, d (12.0)	5.03, d (10.2)	4.14, d (3.0)	4.12, d (3.0)
8a						3.49, ddd (4.8,10.2,13.2)	3.09 ddd (3.0, 4.8, 12.6)	3.07 ddd (3.0, 5.0, 13.0)
9	6.14, d (15.6)	6.05, d (15.6)	6.15, d (16.0)	6.15, d (15.5)	6.04, d (15.5)	6.09, d (15.0)	6.09, d (15.6)	6.00, d (15.5)
10	7.41, d (15.6)	7.02, d (15.6)	7.36, d (15.5)	7.39, d (15.5)	7.36, d (15.5)	7.36, d (15.0)	7.38, d (15.6)	7.01, d (16.0)
12	5.49, d (10.2)	5.63, d (10.2)	5.47, d (10.0)	5.48, d (10.0)	5.48, d (10.0)	5.46, d (10.2)	5.47, d (9.6)	5.63, d (10.0)
13	2.64, m	2.48, m	2.64, m	2.65, m	2.59, m	2.60, m	2.66, m	2.49, m
14	1.33,1.44, m	1.33,1.44, m	1.31, 1.43, m	1.33, 1.40, m	1.31, 1.44, m	1.30, 1.40, m	1.31, 1.43, m	1.31, 1.43, m
15	0.85, t (7.2)	0.85, t (7.2)	0.85, t (7.5)	0.84, t (7.5)	0.84, t (7.5)	0.85, t (7.2)	0.86, t (7.8)	0.84, t (7.0)
16	1.01, d (6.6)	1.00, d (6.6)	1.00, d (7.0)	1.00, d (6.5)	1.00, d (7.0)	0.99, d (7.2)	0.99, d (6.6)	0.99, d (7.0)
17	1.89, s	1.82, s	1.89, d (1.0)	1.89, d (1.0)	1.87, d (1.0)	1.88, s	1.88, s	1.80, s
18	1.45, s	1.45, s	1.37, s	1.42, s	1.59, s	1.43, s	1.38, s	1.37, s
20			2.14, dd (10.0,13.0)	2.07, dd (7.5,12.5)		2.22, s		
			2.39, dd (10.0,13.0)	2.15, dd (7.5,12.5)				
21			1.46, s	1.44, s				
22			3.21, s	3.33, s				
2′	3.04, d (12.6)	3.04, d (12.6)						
3′					3.79, d (12.0)			
4′	3.74, s	3.73, s						
5′	1.58, s	1.57, s			2.47, s			
1′-OCH_3	3.32, s	3.31, s						
7-OH						2.16, s	4.08, s	
8-OH							2.78, s	

*Recorded at 600 MHz (**1a**, **1b**, **5a**, **6a,** and **6b**). Recorded at 500 MHz (**2a**, **3a,** and **4a**).*

TABLE 2 | ^{13}C NMR data of compounds **1–6** (chloroform-*d*, δ in ppm).

Position	1a	1b	2a	3a	4a	5a	6a	6b
1	146.0, CH	146.0, CH	142.8, CH	143.6, CH	147.4, CH	67.8, CH_2	68.2, CH_2	68.2, CH_2
3	157.7, C	157.9, C	157.0, C	157.5, C	156.8, C	163.1, C	162.7, C	162.9, C
4	105.8, CH	105.1, CH	106.0, CH	105.6, CH	108.2, CH	102.2, CH	102.8, CH	102.1, CH
4a	114.2, C	114.2, C	138.8, C	139.4, C	144.5, C	145.5, C	145.4, C	145.6, C
5	109.3, C	109.3, C	110.9, C	110.0, C	106.3, CH	118.9, C	115.6, C	115.4, C
6	188.4, C	188.4, C	188.6, C	189.4, C	191.1, C	187.0, C	192.8, C	192.7, C
7	83.6, C	83.6, C	83.9, C	84.8, C	82.8, C	74.9, C	77.3, C	77.3, C
8	44.6, CH	44.6, CH	44.6, CH	43.5, CH	42.8, CH	73.1, CH	73.6, CH	73.6, CH
8a	140.3, C	140.3, C	117.1, C	116.3, C	113.9, C	35.6, CH	36.9, CH	36.9, CH
9	118.8, CH	116.4, CH	119.2, CH	119.0, CH	118.4, CH	121.2, CH	121.3, CH	118.9, CH
10	133.4, CH	141.8, CH	132.6, CH	133.0, CH	133.1, CH	133.5, CH	133.4, CH	141.9, CH
11	129.8, C	131.9, C	129.9, C	129.9, C	129.7, C	130.2, C	130.2, C	132.2, C
12	145.1, CH	147.6, CH	144.5, CH	144.8, CH	145.0, CH	144.8, CH	144.7, CH	147.1, CH
13	34.0, CH	35.0, CH	34.0, CH	34.0, CH	34.0, CH	34.0, CH	33.9, CH	34.9, CH
14	30.2, CH_2	30.1, CH_2	30.3, CH_2	30.2, CH_2	30.2, CH_2	30.3, CH_2	30.3, CH_2	30.1, CH_2
15	12.0, CH_3	11.9, CH_3	12.0, CH_3	12.0, CH_3	12.0, CH_3	12.0, CH_3	12.0, CH_3	11.9, CH_3
16	20.9, CH_3	20.2, CH_3	20.9, CH_3	20.9, CH_3	20.9, CH_3	20.9, CH_3	21.0, CH_3	20.3, CH_3
17	20.1, CH_3	12.4, CH_3	20.1, CH_3	20.1, CH_3	20.1, CH_3	20.1, CH_3	20.2, CH_3	12.4, CH_3
18	24.6, CH_3	24.6, CH_3	24.1, CH_3	24.7, CH_3	23.2, CH_3	20.7, CH_3	23.4, CH_3	23.4, CH_3
19			106.4, C	105.6, C		170.3, C		
20			47.1, CH_2	45.5, CH_2		20.6, CH_3		
21			22.6, CH_3	21.7, CH_3				
22			49.0, CH_3	48.9, CH_3				
1′	105.6, C	105.5, C						
2′	58.2, CH	58.3, CH			168.5, C			
3′	169.3, C	169.2, C			57.3, CH			
4′	52.2, CH_3	52.2, CH_3			200.0, C			
5′	21.5, CH_3	21.5, CH_3			30.2, CH_3			
1′-OCH_3	49.2, CH_3	49.2, CH_3						

*Recorded at 150 MHz (**1a**, **1b**, **5a**, **6a,** and **6b**). Recorded at 125 MHz (**2a**, **3a,** and **4a**).*

as the mean ± SD, and the EC_{50} values were calculated from the regression equations.

The inhibition rate (expressed as a percentage) was calculated as follows:

$$\frac{\text{radicle (plumule) length in the control} - \text{radicle (plumule) length in the treatment}}{\text{radicle (plumule) length in the control}}$$

RESULTS AND DISCUSSION

Structure Elucidation of the Isolated Compounds

Compound **1** was isolated as a yellow, amorphous powder, and its molecular formula was deduced as $C_{25}H_{31}O_6Cl$ by HRESIMS (**Supplementary Figure S7**), corresponding to 10 degrees of unsaturation. The chlorine atom was confirmed by an isotopic peak for $[M+H]^+$:$[M+H+2]^+$ with an intensive ratio of 3:1 in the molecule. It existed as inseparable mixtures of two isomers according to HPLC analysis on either ODS or chiral column, due to spontaneous isomerization. The ^1H and ^{13}C NMR spectra (**Tables 1**, **2**) of **1** showed two sets of resonances with a ratio of 1:4 for the **1a** and **1b** isomers. The ^1H NMR spectroscopic data and heteronuclear singular quantum correlation (HSQC) correlations (**Supplementary Figure S3**) of **1a** revealed seven methyl groups, including five singlets (δ_H/δ_C 1.45/24.6, 1.58/21.5, 1.89/20.1, 3.32/49.2, and 3.74/52.2), one doublet (δ_H/δ_C 1.01/20.9), one triplet (δ_H/δ_C 0.85/12), one methylene (δ_H/δ_C 1.33/30.2, 1.44/30.2), three aliphatic methines (δ_H/δ_C 2.64/34, 3.04/58.2, and 3.80/44.6), and five olefinic protons (δ_H/δ_C 5.49/145.1, 6.14/118.8, 6.53/105.8, 7.41/133.4, and 7.56/146). Additionally, the ^{13}C NMR spectra of **1a** revealed the presence of 25 carbons, including one conjugated ketone carbonyl at δ_C 188.4, one ester carbonyl at δ_C 169.3, one oxygenated quaternary olefinic carbon at δ_C 157.7, two sp^3 oxygenated quaternary carbons signal at δ_C 83.6/105.6, and four quaternary olefinic carbons signal at δ_C 109.3/114.2/129.8/140.3. These NMR spectroscopic data indicated that **1a** belonged to the family of azaphilones and the planar structure was the same as that of isochromophilone C (Luo et al., 2018). Further examination found that

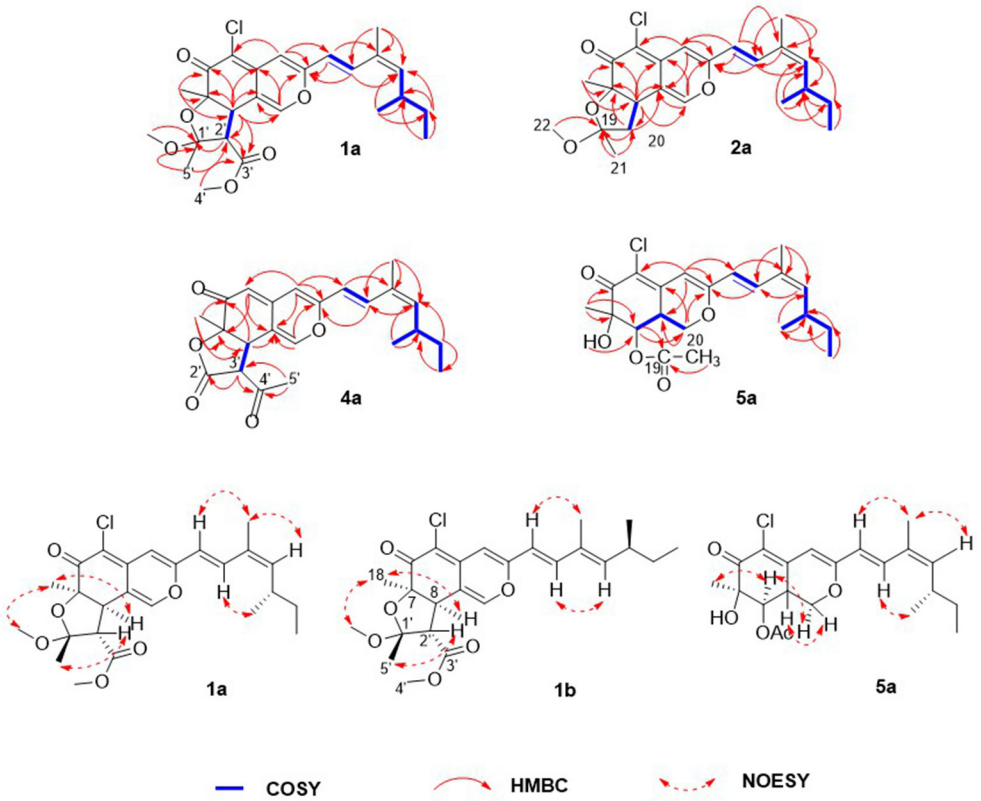

FIGURE 2 | Selected key nuclear overhauser effect spectroscopy (NOESY), correlation spectroscopy (COSY), and heteronuclear multiple bond correlation (HMBC) correlations of **1a, 1b, 2a, 4a, and 5a.**

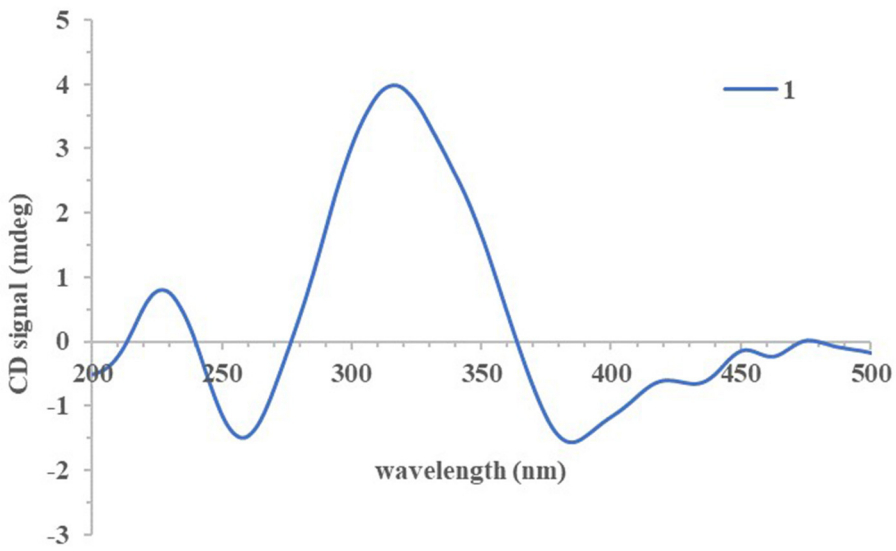

FIGURE 3 | Experimental electronic circular dichroism (ECD) spectrum of compound **1.**

the key nuclear overhauser effect spectroscopy (NOESY) correlations (**Figure 2**, **Supplementary Figure S6**) had obvious differences between **1a** and isochromophilone C, indicating they were diastereoisomers.

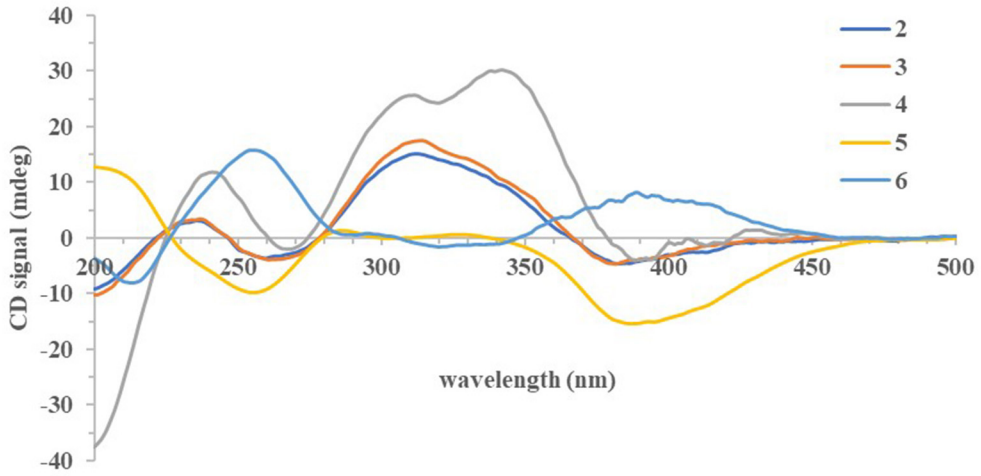

FIGURE 4 | Experimental ECD spectra of compounds **2–6.**

The relative configuration of **1a** was established by NOESY correlations (**Figure 2**, **Supplementary Figure S6**) and corresponding proton coupling constants (Luo et al., 2018; Qian et al., 2019). The large coupling constant (J = 12.6 Hz) between H-2' and H-8 suggested these two protons were on the opposite orientation. The NOESY correlations observed for H_3-18, H-8, and 1'-OCH_3 indicated that these protons were located on the same face. Thus, the stereochemistry of the azaphilone skeleton of **1a** was determined. Furthermore, the coupling constant between H-9 and H-10 (J = 15.6 Hz) in addition to the NOESY correlations between H-9/H-12 and 17-CH_3, and between H-10 and 16-CH_3 illustrated that the double bond at C-9 and C-10 was *E* configuration, and C-11/C-12 was *Z* configuration. Therefore, the relative configuration of **1a**, differing from that of isochromophilone C, was assigned as *rel*-(7*R*,8*R*,9*E*,11*Z*,1′*R*,2′*S*), and given the name as isochromophilone H.

The ^{1}H and ^{13}C NMR data of **1b** were similar to those of **1a.** The differences between them were the NMR data of C-9 to C-13, and C-17, indicating **1a**/**1b** were a pair of *E*/*Z* isomers, which was confirmed by the NOESY correlations of H-9/17-CH_3, and H-10/H-12. Hence, **1b** was defined as *rel*-(7*R*,8*R*,9*E*,11*E*,1′*R*,2′*S*)-isochromophilone H.

Compounds **2–7** were also isolated as six pairs of C-11 *E*/*Z* isomers. Among them, **2a**, **3a**, **4a**, **5a**, and **6a** were new compounds with 11-(*Z*) configuration, which were confirmed by NOESY correlations of H-9/H-12 and 17-CH_3, and H-10/16-CH_3. The relative configuration of **5b** was also determined for the first time by the NOESY correlations (**Supplementary Figure S34**), combined with the proton coupling constants. The coupling constants calculated for H-8 (J = 10.2 Hz) and H-8a (J = 4.8, 10.2, and 13.2 Hz), indicated the ax/ax relationship of these two protons. The NOESY correlations observed for H-1α/H_3-18 and H-8 suggested that these protons were cofacial. Accordingly, the relative configuration of **5b** was established as *rel*-(7*R*,8*R*,8a*R*).

The absolute configurations of all the isolated compounds were determined by comparison of experimental ECD spectra, and biosynthetic considerations. Among these compounds, the stereogenic carbon at C-13 in the side chain moiety was established to be *S* due to the aliphatic branch of this kind of azaphilones having a shared biosynthetic pathway (Gao et al., 2013). The absolute configuration of C-7 in compounds **1**–**5** was assigned to be *R* based on positive Cotton effects at 312 (Δε + 1.18, **1**), 312 (Δε + 3.82, **2**), 313 (Δε + 8.85, **3**), 310 (Δε + 6.11, **4**), and 325 nm (Δε + 0.32, **5**), respectively (**Figures 3**, **4**; Qian et al., 2019). In addition, combined with the NOESY correlations, the absolute configurations of **1a** and **1b** were assigned as 7*R*,8*R*,13*S*,1′*R*,2′*S* (Luo et al., 2018). The absolute configurations of **2**, **3**, **4**, and **5** were suggested to be (7*R*,8*R*,19*S*), (7*R*,8*R*,19*R*), (7*R*,8*R*,3′*R*), and (7*R*,8*R*,8a*R*) by comparisons of experimental ECD data to those reported in the literature (**Figure 4**; Arai et al., 1995; Matsuzaki et al., 1995; Qian et al., 2019). Contrary to ECD data of **5** and *epi*-isochromophilone III, the ECD spectrum (**Figure 4**) in MeOH of **6** exhibited Cotton effects at 388 (Δε +1.88), 321 (Δε −0.34), 255 (Δε +3.47), and 214 nm (Δε −1.87), indicating the absolute configuration at C-7 of **6** was *S*. Thus, **6** was identified as a new compound, and the absolute configurations of **6a** and **6b** were confirmed as 7*S*,8*R*,8a*S*,13*S* (Hemtasin et al., 2016). Compounds **2b**–**5b** were identified as the isomers of **2a**–**5a** with 11-(*E*) configuration reported in the literature (Arai et al., 1995; Matsuzaki et al., 1995; Pairet et al., 1995; Qian et al., 2019). Compounds **7a** and **7b** were identified as isochromophilone Ib and Ia by comparing their NMR data with those in the literature (Omura et al., 1993; Matsuzaki et al., 1995).

Phytotoxicity Bioassays

Numerous studies have reported that azaphilones have broad-spectrum biological activities. However, there were relatively few reports about their phytotoxic activity of them. Chaetomugilin A, D, S, and O, four chlorine-containing azaphilone derivatives,

TABLE 3 | EC_{50} values of compounds **3**, **4,** and **7** in Redroot Amaranth.

Compound	EC_{50} (μM)	
	Plumule	Radicle
3	320.84	271.48
4	287.07	234.87
7	288.36	240.30
Glufosinate ammonium[a]	656.04	555.11

[a]*Positive control.*

TABLE 4 | EC_{50} Values of Compounds **4** and **7** in Velvetleaf.

Compound	EC_{50} (μM)	
	Plumule	Radicle
4	939.49	1122.17
7	768.97	1201.52
Glufosinate ammonium[a]	555.11	807.43

[a]*Positive control.*

isolated from the endophytic *Chaetomium globosum* TY1, showed a higher response index and lower IC_{50} values to eight species of herbaceous plant seeds than positive control glyphosate (Wang et al., 2017). Chaetomugilin D and J, isolated from the EtOAc extract of the fermentation medium of *C. globosum*, exhibited phytotoxicity to lettuce seeds, with IC_{50} values for root inhibition of 24.2 and 22.6 ppm, respectively, while those for shoot inhibition were 27.8 and 21.9 ppm, respectively (Piyasena et al., 2015). Acetosellin, isolated from large-scale cultures of the fungus *Cercosporella acetosella*, inhibited the growth of the root of *Lepidium sativum* and *Zea mais* at 640 μM (Gianluca et al., 2002). In the present work, all the isolated compounds were evaluated for their phytotoxicity against four weeds species (*A. fatua* L., *L. perenne* L., *A. retroflexus* L., *A. theophrasti* Medikus) in farmland. The experimental results indicated that sclerotiorin B (**3**), ochlephilone (**4**), and isochromophilone I (**7**) exhibited potent phytotoxicity against the growth of radicle and plumule of *A. retroflexus* L., with EC_{50} values ranging from 234.87 to 320.84 μM, compared to positive control glufosinate-ammonium (**Table 3**). Compounds **4** and **7** also showed inhibitory activities against the growth of velvetleaf (*A. theophrasti* Medikus; **Table 4**). These tested compounds had no significant inhibitory effects on the growth and germination of wild oat (*A. fatua* L.) and ryegrass (*L. perenne* L.).

CONCLUSIONS

In conclusion, we described seven pairs of azaphilones 11-(*E/Z*) isomers, including eight new compounds. Their structures and absolute configurations were elucidated based on comprehensive spectroscopic analysis and the comparisons of ECD data. Sclerotiorin B (**3**), ochlephilone (**4**), and isochromophilone I (**7**) exhibited potent phytotoxicity toward the growth of radicle and plumule of *A. retroflexus* L., compared to glufosinate-ammonium. This will provide new leading compounds for the research and development of marine-derived bioherbicides.

DATA AVAILABILITY STATEMENT

The original contributions presented in the study are included in the article/**Supplementary Material**, further inquiries can be directed to the corresponding author/s.

AUTHOR CONTRIBUTIONS

G-XW and C-SZ conceived and designed the experiments. WW and MW performed the experiments. WW, D-LZ, X-BW, J-LD, Y-QL, M-XL, and XG analyzed the experimental data. WW wrote the manuscript. D-LZ revised the article. All authors contributed to the article, reviewed the manuscript, and approved the submitted version.

FUNDING

This work was financially supported by Reserve Talents for Yunnan Young and Middle-aged Academic and Technical Leaders (No.202105AC160037), the National Natural Science Foundation of China (41806194), the Agricultural Science and Technology Project of Guizhou Province (2021XM10 and 201803), and the Fundamental Research Funds for Central Non-profit Scientific Institution (1610232021007).

SUPPLEMENTARY MATERIAL

The Supplementary Material for this article can be found online at: https://www.frontiersin.org/articles/10.3389/fmicb.2022.880874/full#supplementary-material

REFERENCES

Adetunji, C. O., Oloke, J. K., Prasad, G., Bello, O. M., Osemwegie, O. O., Pradeep,·R. S. et al. (2018). Isolation, identification, characterization, and screening of rhizospheric bacteria for herbicidal activity. *Org. Agric.* 8, 195–205. doi: 10.1007/s13165-017-0184-8

Arai, N., Shiomi, K., Tomoda, H., Tabata, N., Yang, D. J., Masuma, R., et al. (1995). Isochromophilones III∼VI, inhibitors of Acyl-CoA: cholesterol acyltransferase produced by *Penicillium multicolor* FO-3216. *J. Antibiot.* 48, 696–702. doi: 10.1002/chin.199601275

Carroll, A. R., Copp, B. R., Davis, R. A., Keyzers, R. A., and Prinsep, M. R. (2020). Marine natural products. *Nat. Prod. Rep.* 37, 175–223. doi: 10.1039/c9np00069k

Gao, J. M., Yang, S. X., and Qin, J. C. (2013). Azaphilones: chemistry and biology. *Chem. Rev.* 113, 4755–4811. doi: 10.1021/cr300402y

Gianluca, N., Alberto, A., Gemma, A., Gabriele, C., and Orso, V. P. (2002). Structure and absolute configuration of acetosellin, a new polyketide from a phytotoxic strain of *Cercosporella acetosella*. *Tetrahedron Lett.* 43, 1665–1668. doi: 10.1016/S0040-4039(02)00091-6

Harding, D. P., and Raizada, M. N. (2015). Controlling weeds with fungi, bacteria and viruses: a review. *Front. Plant Sci.* 6:659. doi: 10.3389/fpls.2015.00659

Hemtasin, C., Kanokmedhakul, S., Moosophon, P., Soytong, K., and Kanokmedhakul, K. (2016). Bioactive azaphilones from the fungus penicillium multicolor CM01. *Phytochem. Lett*. 16, 56–60. doi: 10.1016/j.phytol.2016.03.004

Huang, R. H., Gou, J. Y., Zhao, D. L., Wang, D., Liu, J., Ma, G. Y., et al. (2018). Phytotoxicity and anti-phytopathogenic activities of marine-derived fungi and their secondary metabolites. *RSC Adv*. 8, 37573–37580. doi: 10.1039/c8ra08047j

Kim, H. J., Bo, A. B., Kim, J. D., Kim, Y. S., Khaitov, B., Ko, Y. K., et al. (2020). Herbicidal characteristics and structural identification of the potential active compounds from *Streptomyces* sp. KRA17-580. *J. Agric. Food Chem*. 68, 15373–15380. doi: 10.1021/acs.jafc.0c01974

Luo, X. W., Lin, X. P., Tao, H. M., Wang, J. F., Li, J. Y., Yang, B., et al. (2018). Isochromophilones A–F, cytotoxic chloroazaphilones from the marine mangrove endophytic fungus *Diaporthe* sp. SCSIO 41011. *J. Nat. Prod*. 81,934–941. doi: 10.1021/acs.jnatprod.7b01053

Makrerougras, M., Coffinier, R., Oger, S., Chevalier, A., Sabot, C., and Franck, X. (2017). Total synthesis and structural revision of chaetoviridins A. *Org. Lett*. 19, 4146–4149. doi: 10.1021/acs.orglett.7b02053

Matsuzaki, K., Tanaka, H., and Omura, S. (1995). Isochromophilones I and II, Novel inhibitors against gp120-CD4 binding produced by *Penicillium multicolor* FO-2338. *J. Antibiot*. 48, 708–713. doi: 10.7164/antibiotics.48.708

Omura, S., Tanaka, H., Matsuzaki, K., and Ikeda, H., Masuma, R. (1993). Isochromophilones I and II, novel inhibitors against gp120-CD4 binding from *Penicillium* sp. *J. Antibiot*. 46, 1908–1911. doi: 10.7164/antibiotics.46.1908

Pairet, L., Wrigley, S. K., Chetland, I., Reynolds, E. E., Hayes, M. A., Holloway, J., et al. (1995). Azaphilones with endothelin receptor binding activity produced by *Penicillium sclerotiorum*: taxonomy, fermentation, isolation, structure elucidation and biological activity. *J. Antibiot*. 48, 913–923. doi: 10.7164/antibiotics.48.913

Piyasena, K. G. N. P., Wickramarachchi, W. A. R. T., Kumar, N. S., Jayasinghe, L., and Fujimoto, Y. (2015). Two phytotoxic azaphilone derivatives from *Chaetomium globosum*, a fungal endophyte isolated from *Amaranthus viridis* leaves. *Mycology* 6,158–160. doi: 10.1080/21501203.2015.1089332

Qian, J., Du, Y. Q., Wang, C., Wang, Y., Zhu, T., H., et al. (2019). Azaphilones from the marine sponge-derived fungus *Penicillium sclerotiorum* OUCMDZ-3839. *Mar. Drugs* 17:260. doi: 10.3390/md17050260

Shen, N. X., Liang, Z. Y., Liu, Q., Tu, C. D., Dong, K. M., Wang, C. Y., et al. (2020). Antifungal secondary metabolites isolated from mangrove rhizosphere soil-derived *Penicillium* fungi. *J. Ocean Univ. China*. 19, 717–721. doi: 10.1007/s11802-020-4360-1

Shi, L. Q., Wu, Z. Y., Zhang, Y. N., Zhang, Z. G., Fang, W., Wang, Y. Y., et al. (2020). Herbicidal secondary metabolites from actinomycetes: structure diversity, modes of action, and their roles in the development of herbicides. *J. Agric. Food Chem*. 68, 17–32. doi: 10.1021/acs.jafc.9b06126

Travaini, M. L., Sosa, G. M., Ceccarelli, E. A., Walter, H., Cantrell, C. L., Carrillo, N. J., et al. (2016). Khellin and visnagin, furanochromones from *Ammi visnaga* (L.) Lam., as potential bioherbicides. *J. Agric. Food Chem*. 64, 9475–9487. doi: 10.1021/acs.jafc.6b02462

Vurro, M., Boari, A., Casella, F., and Zonno, M. C. (2018). Fungal phytotoxins in sustainable weed management. *Curr. Med. Chem*. 25, 268–286. doi: 10.2174/0929867324666170426152331

Wang, D. C., Zhang, Y. M., Li, X., Pan, H. Y., Chang, M. Y., Zheng, T. Y., et al. (2017). Potential allelopathic azaphilones produced by the endophytic *Chaetomium globosum* TY1 inhabited in *Ginkgo biloba* using the one strain-many compounds method. *Nat. Prod. Res*. 31, 724–728. doi: 10.1080/14786419.2016.1217208

Wang, W. Y., Yang, J., Liao, Y. Y., Cheng, G., Chen, J., Cheng, X. D., et al. (2020). Cytotoxic nitrogenated azaphilones from the deep-sea-derived fungus *Chaetomium globosum* MP4-S01-7. *J. Nat. Prod*. 83, 1157–1166. doi: 10.1021/acs.jnatprod.9b01165

Yang, J., Wang, W., Yang, P., Tao, B., Yang, Z., Dong, J. G., et al. (2015). Isolation and identification of *Serratia marcescens* Ha1 and herbicidal activity of Ha1 'pesta' granular formulation. *J. Integr. Agr*. 14, 1348–1355. doi: 10.1016/S2095-3119(14)60967-9

Zhao, D. L., Han, X. B., Wang, D., Liu, M. H., Gou, J. Y., Peng, Y. L., et al. (2019). Bioactive 3-decalinoyltetramic acids derivatives from a marine-derived strain of the fungus *Fusarium equiseti* D39. *Front. Microbiol*. 10:1285. doi: 10.3389/fmicb.2019.01285

Zhao, D. L., Han, X. B., Wang, M., Zeng, Y. T., Li, Y. Q., Zhang, P., et al. (2020). Herbicidal and antifungal xanthone derivatives from the alga-derived fungus *Aspergillus versicolor* D5. *J. Agric. Food Chem*. 68, 11207–11214. doi: 10.1021/acs.jafc.0c04265

Conflict of Interest: X-BW and J-LD are employed by Guizhou Tobacco Company.

The remaining authors declare that the research was conducted in the absence of any commercial or financial relationships that could be construed as a potential conflict of interest.

Publisher's Note: All claims expressed in this article are solely those of the authors and do not necessarily represent those of their affiliated organizations, or those of the publisher, the editors and the reviewers. Any product that may be evaluated in this article, or claim that may be made by its manufacturer, is not guaranteed or endorsed by the publisher.

frontiers | Frontiers in Microbiology

ORIGINAL RESEARCH
published: 10 May 2022
doi: 10.3389/fmicb.2022.900227

Diversified Polyketides With Anti-inflammatory Activities From Mangrove Endophytic Fungus *Daldinia eschscholtzii* KBJYZ-1

Guisheng Wang[1], *Zhenhua Yin*[1], *Senye Wang*[1], *Yilin Yuan*[1], *Yan Chen*[1,2]* *and Wenyi Kang*[1,2,3]*

[1] National R&D Center for Edible Fungus Processing Technology, Henan University, Kaifeng, China, [2] Joint International Research Laboratory of Food and Medicine Resource Function, Kaifeng, China, [3] Kaifeng Key Laboratory of Functional Components in Health Food, Kaifeng, China

In total, five new polyketide derivatives: eschscholin B (**2**), dalditone A and B (**3** and **4**), (1*R*, 4*R*)-5-methoxy-1,2,3,4-tetrahydronaphthalene-1,4-dio (**5**), and daldilene A (**6**), together with 10 known as analogs (**1**, **7**–**15**) were isolated from the mangrove endophytic fungus *Daldinia eschscholtzii* KBJYZ-1. Their structures and absolute configurations were established by extensive analysis of NMR and HRESIMS spectra data combined with ECD calculations and the reported literature. Compounds **2** and **6** showed significant cell-based anti-inflammatory activities with IC_{50} values of 19.3 and 12.9 μM, respectively. In addition, western blot results suggested that compound **2** effectively inhibits the expression of iNOS and COX-2 in LPS-induced RAW264.7 cells. Further molecular biology work revealed the potential mechanism of **2** exerts anti-inflammatory function by inactivating the MAPK and NF–κB signaling pathways.

Keywords: mangrove endophytic fungus, *Daldinia eschscholtzii*, anti-inflammatory activity, NF-κB, MAPK

OPEN ACCESS

Edited by:
Xian-Wen Yang,
Ministry of Natural Resources, China

Reviewed by:
Cong Wang,
Guangxi University for Nationalities, China
Qingying Zhang,
Peking University Health Science Centre, China

***Correspondence:**
Yan Chen
cychemistry@163.com
Wenyi Kang
kangwenyi@henu.edu.cn

Specialty section:
This article was submitted to Extreme Microbiology, a section of the journal Frontiers in Microbiology

Received: *20 March 2022*
Accepted: *04 April 2022*
Published: *10 May 2022*

Citation:
Wang G, Yin Z, Wang S, Yuan Y, Chen Y and Kang W (2022) Diversified Polyketides With Anti-inflammatory Activities From Mangrove Endophytic Fungus Daldinia eschscholtzii KBJYZ-1. Front. Microbiol. 13:900227. doi: 10.3389/fmicb.2022.900227

INTRODUCTION

Mangrove endophytic fungi have proven to be a promising source of novel chemical backbones and bioactive metabolites owing to extreme environments (tidal flooding, high salinity, anaerobic soil, and high temperature) of mangroves (Chen S. et al., 2022; Chen Y. et al., 2022). *Daldinia eschscholtzii* is an endophytic fungus isolated commonly from mangrove plants (Yang et al., 2017). The diverse bioactivity metabolites, including tetralones (Liao et al., 2019a), lactones (Kongyen et al., 2015), naphthoquinones (Wutthiwong et al., 2021), chromones (Barnes et al., 2016), and polyphenols (Zhang et al., 2016), have attracted much attention. For instance, naphthoquinones 5-hydroxy-2-methoxy-6,7-dimethyl-1,4-naphthoquinone form *D. eschscholtzii* HJ004 showed antibacterial activity (Liao et al., 2019b), and chromones 5-hydroxy-8-methoxy-2-methyl-4H-chromen-4-one from *D. eschscholtzii* GsE13 showed phytotoxicity (Flores-Reséndiz et al., 2021).

It is well known that excessive inflammation could lead to tissue damage, loss of function, and many more related diseases, such as arthritis, systemic lupus erythematosus, ulcerative colitis, and cancer (Zhang Y. et al., 2021). The most often used therapeutic medicines, such as non-steroidal anti-inflammatory drugs (NSAIDs), have been shown to significantly reduce prostaglandin production by reducing the activity of cyclooxygenase (COX) enzymes (Bindu et al., 2020). Whereas,

various side effects might be caused by NSAIDs, including gastrointestinal mucosal injury, liver, and kidney toxicity (Wang et al., 2020). As a result, the discovery of new anti-inflammatory medications has become an unavoidable trend. The metabolites from mangrove endophytic fungus were the key sources of the anti-inflammatory lead compounds due to their novel structure, low toxicity, and significant inhibitory effect (Chen et al., 2021). As part of our continuing investigation into searching for novel anti-inflammatory natural compounds derived from mangrove endophytic fungi, a fungus *D. eschscholtzii* KBJYZ-1, which was isolated from *Pluchea indica* Less., aroused our interest because the ethyl acetate extract of the fungal culture displayed excellent anti-inflammatory activity. As a result, five new compounds (**2**–**6**) and ten known compounds (**1**, **7**–**15**) were isolated (**Figure 1**). The anti-inflammatory activity of all isolated compounds was evaluated by the lipopolysaccharides (LPSs) induced NO production in RAW264.7 macrophages. Moreover, the potential anti-inflammatory mechanism of **2** has been investigated.

MATERIALS AND METHODS

General Experimental Procedures

Specific optical rotation was measured on a PerkinElmer 341 instrument at 25°C. Cary 5000 spectrophotometer was used to record UV spectra in MeOH. ECD data were obtained by Model 420SF CD spectrometer (Aviv Biomedical Inc). In KBr discs, IR spectra were obtained using Fourier infrared IS50 spectrometer. All NMR experiments were performed at room temperature on a Bruker AVANCE 500 spectrometer using the signals of residual solvent protons ($CDCl_3$: δ_H 7.26; CD_3OD: δ_H 3.31) and carbons ($CDCl_3$: δ_C 77.1; CD_3OD: δ_C 49.2). HRESIMS spectra were tested by Waters TQ-XS mass spectrometer. Column chromatography (CC) was conducted by silica gel (200–300 mesh, Yantai Huiyou Silica gel company) and Sephadex LH-20 ($CHCl_2$/MeOH, *v/v* 1:1) (Pharmacia Sweden). On silica gel plates, thin layer chromatography (TLC) was conducted (GF 254 Silica gel Thin Layer Plate Yantai Huiyou Silica company). The Typical Culture Preservation Committee Cell Bank, China provided RAW264.7 cells; the fetal bovine serum (FBS) was obtained by Gibco; ProCell provided Dulbecco's modified Eagle's medium (DMEM); Sigma supplied LPS and $_L$-NMMA; Shanghai Beyotime Biotechnology supplied the NO kit. Thermo Fisher Scientific (Shanghai, China) provided the primers for iNOS. Cell Signaling (Beverly, MA, USA) supplied all the antibodies.

Fungal Material

The strain KBJYZ-1 was isolated from the root of *Pluchea indica* Less., which was collected in July 2020 from Zhanjiang Mangrove National Nature Reserve in Guangdong Province, China. Fungal identification was carried out using molecular biological methods to identify fungal species by DNA amplification and ITS sequences (Chen et al., 2018). BLAST analysis showed that this sequence had the highest homology with 100% to the sequence of *Daldinia eschscholtzii* (compared with MW081312.1). Sequence data of the strain is deposited at GenBank with accession no. OM267787. The fungus was preserved at Henan University, China.

Fermentation Extraction and Isolation

The fungus was cultured on solid rice medium (100 numbers of 1,000 ml Erlenmeyer flasks, each containing 120 g rice and 75 ml of 0.3% seawater) at room temperature for one month under static condition. After fermentation, the mediums were extracted with MeOH three times. The organic phase was concentrated under reduced pressure to yield a total residue of 78.6 g. Moreover, a silica gel column was used for chromatography (CC) was used with petroleum ether/ethyl acetate gradient elution from 10:0 to 2:8, to obtain initial ten fractions (Fr.1–Fr.10) were obtained. Fr.2 (200.6 mg) was separated by Sephadex LH-20 to obtain **8** (3.2 mg). The subfraction Fr.2.1 (60.3 mg) was further subject to silica gel CC (CH_2Cl_2:PE *v/v*, 2:1) to obtain **1** (2.6 mg). The subfraction Fr.2.1.4 and Fr.2.3 were pooled and purified by Sephadex LH-20 CC (CH_2Cl_2/MeOH *v/v*, 1:1) to get **5** (2.1 mg) and **6** (3.3 mg), respectively. In total, **7** (4.1 mg) and **9** (2.3 mg) were obtained from subfraction Fr.2.4 (40.9 mg) which was purified by silica gel CC (CH_2Cl_2). Fraction Fr.3 (100.3 mg) was separated by Sephadex LH-20 CC (CH_2Cl_2/MeOH *v/v*, 1:1) to get two subfraction Fr.3.1-3.2. Subfraction Fr.3.2 (80.3 mg) was further purified to obtain six subfractions (3.2.1–3.2.6). **2** (2.2 mg) was obtained by purification Fr.3.2.6 (6.5 mg) using sephadex LH-20 CC (CH_2Cl_2/MeOH *v/v*, 1:1). Fr.4 (450.0 mg) was purified and fractionated into four subfractions (4.1–4.4) by Sephadex LH-20 CC (CH_2Cl_2/MeOH *v/v*, 1:1). Fr.4.1 (125.3 mg) was again fractionated using silica gel CC (CH_2Cl_2/MeOH *v/v*, 125:1∼80:1), and subfractions Fr.4.1.2 (15.3 mg) and Fr.4.1.4(10.3 mg) were purified by Sephadex LH-20 CC (CH_2Cl_2/MeOH *v/v*, 1:1) to obtain **13** (1.8 mg) and **15** (1.3 mg), respectively. Fr.5 (200.3 mg) was purified by Sephadex LH-20 CC (CH_2Cl_2/MeOH *v/v*, 1: 1) to yield **10** (5 mg) and **12** (4.3 mg), and other subfractions (5.1–5.8). Fr.5.3 (20.4 mg) was separated into four subfractions (Fr.5.3.1–Fr.5.3.4) using silica gel CC (CH_2Cl_2/MeOH *v/v*, 100:1, 95:1, 90:1, 80:1), and subfractions Fr.5.3.2 furnished **11**(3.5 mg). Subfractions Fr.5.3.4 purified by Sephadex LH-20 furnished **14**. Fr.6 (585.0 mg) was purified by Sephadex LH-20 furnished to give five fractions (6.1–6.5). Fraction of Fr.6.4 (221.0 mg) purified by silica gel CC resulted four fractions (6.4.1–6.4.4), purification of subfraction Fr.6.4.2 (15.3 mg) and Fr.6.4.3 (10.9 mg) by Sephadex LH-20 furnished **3** (4.2 mg) and **4** (3.5 mg), respectively.

Eschscholin B (**2**): yellow oil; $[\alpha] = -15.1$ (*c* 0.26, MeOH); UV (MeOH) λ_{max} (log ε): 210 (1.68) nm; IR (KBr) ν_{max}: 2,935, 2,856, 2,355, 1,702, 1,464, 1,378, 1,284, 1,053 cm^{-1}; ^1H and ^{13}C NMR ($CDCl_3$) data (**Table 1**); HRESIMS *m/z* 269.2470 $[M + H]^+$ (calcd for $C_{17}H_{33}O$, 269.2468).

Dalditone A (**3**): yellow solid; $[\alpha] = +0.01$ (*c* 0.12, MeOH); UV (MeOH) λ_{max} (log ε): 266 (1.77), 205 (1.89) nm; IR (KBr) ν_{max}: 3,381, 2,928, 2,965, 2,130, 1,760, 1,650, 1,463, 1,064 cm^{-1}; ^1H NMR (MeOH-d_4) data (**Table 1**); ^{13}C NMR (MeOH-d_4) data (**Table 2**); HRESIMS *m/z* 243.0627 $[M + Na]^+$ (calcd for $C_{12}H_{10}O_4Na$, 243.0620).

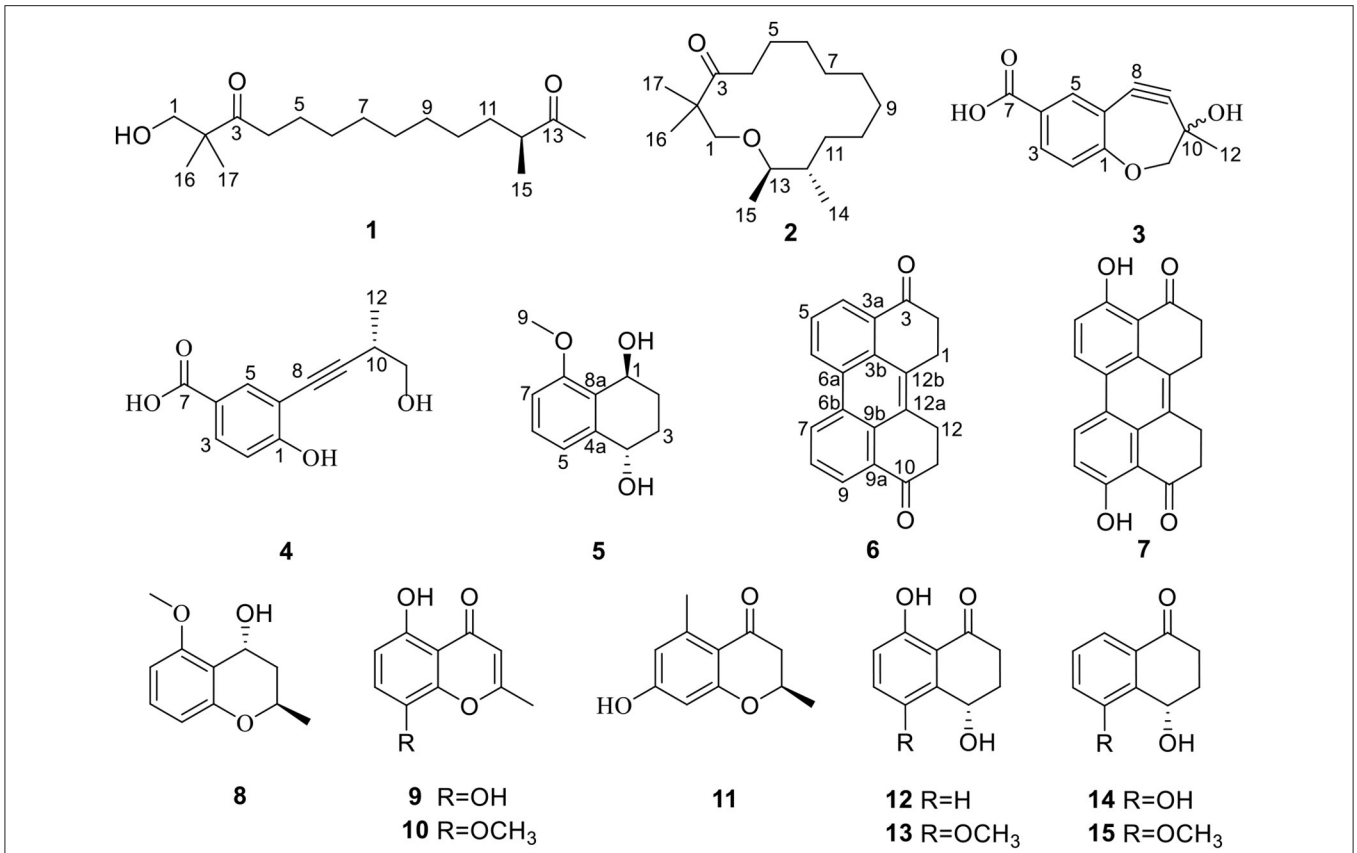

FIGURE 1 | The structures of **1-15**.

TABLE 1 | ^{1}H and ^{13}C NMR data of **2** in $CDCl_3$.

No.	δ_C	δ_H [mult, *J* (Hz)]	No.	δ_C	δ_H [mult, *J* (Hz)]
1	69.3, CH_2	3.43, s	10	27.2, CH_2	1.15, overlap
2	49.0, C		11	29.4, CH_2	1.15, overlap
3	216.9, C		12	39.6, CH	1.29, m
4	37.3, CH_2	2.38, t (7.3)	13	71.1, CH	3.55, td (6.3, 10.7)
5	23.5, CH_2	1.43, dd (7.0, 14.0)	14	14.2, CH_3	0.75, d (6.8)
6	29.8, CH_2	1.30, m	15	20.0, CH_3	1.0, d (6.3)
7	29.4, CH_2	1.15, overlap	16	21.5, CH_3	1.02, s
8	29.1, CH_2	1.15, overlap	17	21.5, CH_3	1.02, s
9	32.4, CH_2	1.15, overlap			

TABLE 2 | ^{1}H and ^{13}C NMR data of **3** and **4** in MeOH-d_4.

No.	3		4	
	δ_C, type	δ_H, mult (*J* in Hz)	δ_C, type	δ_H, mult (*J* in Hz)
1	163.2, C		161.7, C	
2	116.3, CH	6.88, d (8.6)	114.7, CH	6.85, d (8.6)
3	132.7, CH	7.83, dd (2.1, 8.6)	130.7, CH	7.79, dd (2.2, 8.6)
4	123.7, C		123.4, C	
5	136.3, CH	7.98, d (2.1)	134.9, CH	7.92, d (2.2)
6	111.3, C		110.8, C	
7	169.6, C		168.1, C	
8	80.0, C		76.3, C	
9	97.4, C		96.3, C	
10	69.8, C	3.56, dd (6.5, 10.5)	29.8, CH	2.85, dd (6.7, 13.5)
11a	71.1, CH_2	3.61, s	65.8, CH_2	3.65, dd (6.5, 10.5)
11b				3.56, dd (6.5, 10.5)
12	26.2, CH_3	1.53, s	16.2, CH_3	1.27, d (1.9)

Dalditone B (**4**): yellow solid; $[\alpha] = +10.5$ (*c* 0.33, MeOH); UV (MeOH) λ_{max} (log ε): 260 (1.23), 224 (1.84), 201 (1.71) nm; IR (KBr) ν_{max}: 3,288, 2,928, 2,867, 2,200, 1,671, 1,556, 1,460, 1,299, 1,113, 1,039 cm^{-1}; ^{1}H and ^{13}C NMR (MeOH-d_4) data (**Table 2**); HRESIMS *m/z* 219.0649 $[M - H]^-$ (calcd for $C_{12}H_{11}O_4$, 219.0643).

(1*R*, 4*R*)-5-methoxy-1,2,3,4-tetrahydronaphthalene-1,4-dio (**5**): colorless solid; $[\alpha] = +23.2$ (*c* 0.60, MeOH); UV (MeOH) λ_{max} (log ε): 254 (1.80), 210 (1.44) nm; IR (KBr) ν_{max}: 3,389, 3,004, 2,945, 1,728, 1,580, 1,463, 1,269, 1,018, 993, 754 cm^{-1}; ^{1}H and ^{13}C NMR ($CDCl_3$) data (**Table 3**); HRESIMS *m/z* 194.0498 $[M - H]^-$ (calcd for $C_{11}H_{13}O_3$, 194.0490).

Daldilene A (**6**): yellow solid; UV (MeOH) λ_{max} (log ε): 258 (1.5), 206 (2.1) nm; IR (KBr) ν_{max}: 2,917, 2,949, 1,765,

TABLE 3 | ^{1}H and ^{13}C NMR data of **5** and **6** in $CDCl_3$.

No.	5		No.	6	
	δ_C	δ_H [mult, *J* (Hz)]		δ_C	δ_H [mult, *J* (Hz)]
1	63.2, CH	5.06, t (4.7)	1, 12	25.4, CH_2	3.54, t (4.7)
2a	25.7, CH_2	1.88, m	2, 11	37.7, CH_2	3.05, m
2b		2.27, m	3, 10	198.3, C	
3a	27.7, CH_2	1.80, m	4, 9	126.4, CH	8.95, d (8.3)
3b		2.19, m	5, 8	126.5, CH	7.79, t (7.6)
4	67.7, CH	4.79, m	6, 7	128.7, CH	8.38, d (7.4)
4a	139.9, C		3a, 9a	129.2, C	
5	120.9, CH	7.07, d (7.8)	6a, 6b	128.7, C	
6	129.0, CH	7.29, t (8.0)	12a, 12b	131.2, C	
7	109.7, CH	6.85, d (8.2)	3b, 9b	129.0, C	
8	159.5, C				
8a	126.7, C				
9	55.5, CH_3	3.89, s			

1,650, 1,193, 1,068 cm^{-1}; ^{1}H and ^{13}C NMR ($CDCl_3$) data (**Table 3**); HRESIMS *m/z* 287.1054 $[M + H]^+$ (calcd for $C_{20}H_{15}O_2$, 287.1051).

ECD Calculations

The ECD calculations were performed according to the method described previously (Chen et al., 2019). The conformers of compounds **1**, **2**, **4,** and **5** were optimized using DFT calculations at B3LYP/6-31g (d) level in MeOH. Then, ECD calculations were conducted using time-dependent density functional theory (TD-DFT) at B3LYP/DGDZVP, PBEPBE/6-311+G, B3LYP/6-31G, and B3LYP/6-311G levels, respectively.

Anti-inflammatory Assay

Cell Culture

RAW264.7 cells were cultured in Dulbecco's modified Eagle's medium (DMEM) containing 10% fetal bovine serum, 100 U/ml penicillin, and 100 μg/ml streptomycin at 37°C with 5% CO_2.

Cell Viability Assay

The cell viability was evaluated using the MTT assay as described previously (Niu et al., 2021). Briefly, RAW264.7 cells (5×10^4 cells/well) with logarithmic growth were inoculated in 96-well plates for 12 h at 37°C with 5% CO_2. Cells were treated with different concentrations of $_L$-NMMA or the test compounds (10, 20, 30, 40, and 50 μM) and LPS (1 μg/ml) for 24 h. Then, approximately 10 μl of MTT (0.5 mg/ml) was added to each well and incubated for 4 h at 37°C. After completion of the post-incubation, the absorbance was measured at 490 nm.

Measurement of NO Production

RAW264.7 cells were inoculated in 96-well plates and incubated for 14 h at 37°C. Period, different concentrations of L-NMMA or the test compound were added, and stimulated with LPS (1 μg/ml) for 24 h. The levels of NO were measured according to the instructions of the manufacturer. The absorbance was measured at 540 nm.

Western Blot

Briefly, RAW264.7 cells (1×10^6 cells/well) were inoculated into the 6-well plates and incubated with 2 ml DMEM at 37°C. The spent cell culture medium was discarded when the cell fusion reached about 70–80%. Then, cells were stimulated with compounds (25, 12.5, and 6.25 μM), and incubated for 24 h. Western blot was carried out and the assay was done as described previously (Niu et al., 2021). Blots were visualized using enhanced chemiluminescence (ECL) detection kits and analyzed using the Image J software.

Statistical Analysis

All the experiments were repeated at least three times and statistical analyses were evaluated using the GraphPad Prism 7 program. The data were expressed as a means ± SD. $p < 0.05$ indicates statistical significance. A one-way ANOVA analysis was used to determine statistical significance.

RESULTS AND DISCUSSION

Structure Elucidation

Compound **1** was identified as eschscholin A (Liu et al., 2017) by comparing the ^{1}H and ^{13}C NMR data (**Supplementary Table S1**). Here, the absolute configuration of 12*S* was first determined by ECD calculation (**Figure 2**).

Compound **2**, a yellow oil, had a molecular formula of $C_{17}H_{32}O_2$. As established by high-resolution electrospray ionization mass spectrometry (HRESIMS), it showed two degrees of unsaturation. The ^{1}H NMR spectrum (**Table 1**), provided signals for four methyls at δ_H 0.75 (d, J = 6.8 Hz, H_3-14), 0.7 (d, J = 6.8 Hz, H_3-15), 1.02 (s, H_3-16), and 1.02 (s, H_3-17); one oxygenated methylene at δ_H 3.43 (s, H_2-1), 2.38 (t, J = 7.3 Hz, H_2-15); an oxygenated methine group at δ_H 3.55 (td, J = 6.3 Hz, 10.3 Hz, H-13). ^{13}C NMR (**Table 1**) and HSQC spectra data of **2** exhibited 17 carbon signals, including four methyls, ten methylenes, two methines, and one carbonyl carbon. Moreover, the spin system of H_2-4/H_2-5/H_2-6/H_2-7/H_2-8/H_2-9/H_2-10/H_2-11/H-12(/H_3-14)/H-13/H_3-15 from COSY data (**Figure 3**), together with the HMBC correlations (**Figure 3**) from H_3-16 to C-2 and C-1, from H_3-17 to C-2 and C-3, from H_2-4 to C-3, established the preliminary structure. Finally, except for a carbonyl group, the remaining indices of hydrogen deficiency were determined as 14-membered macrocycle. Comparing the NMR data indicated the structure of **2** was a resemblance to eschscholin A (Liu et al., 2017). Thus, the structure of **2** was established as exhibited in **Figure 1**. The relative configuration of **2** was confirmed by the NOESY correlation of H-13/H_3-14, together with the large coupling constant $J_{H-12,H-13}$ = 10.7 Hz (**Figure 4**). Furthermore, the absolute configuration was confirmed by the ECD calculation. The identical experimental and calculated ECD curves (**Figure 2**) assigned the 12*S*, 13*R* configuration of **2**.

Compound **3** was obtained as a yellow solid. The molecular formula was determined as $C_{12}H_{10}O_4$, based on the HRESIMS data. The ^{1}H NMR spectrum (**Table 2**) provided signals for one methyl δ_H 1.53 (s, H_3-12), one oxygenated methylene δ_H 3.61 (s, H_2-11), three methines δ_H 6.88 (d, J = 8.6 Hz, H-2), 7.83 (dd,

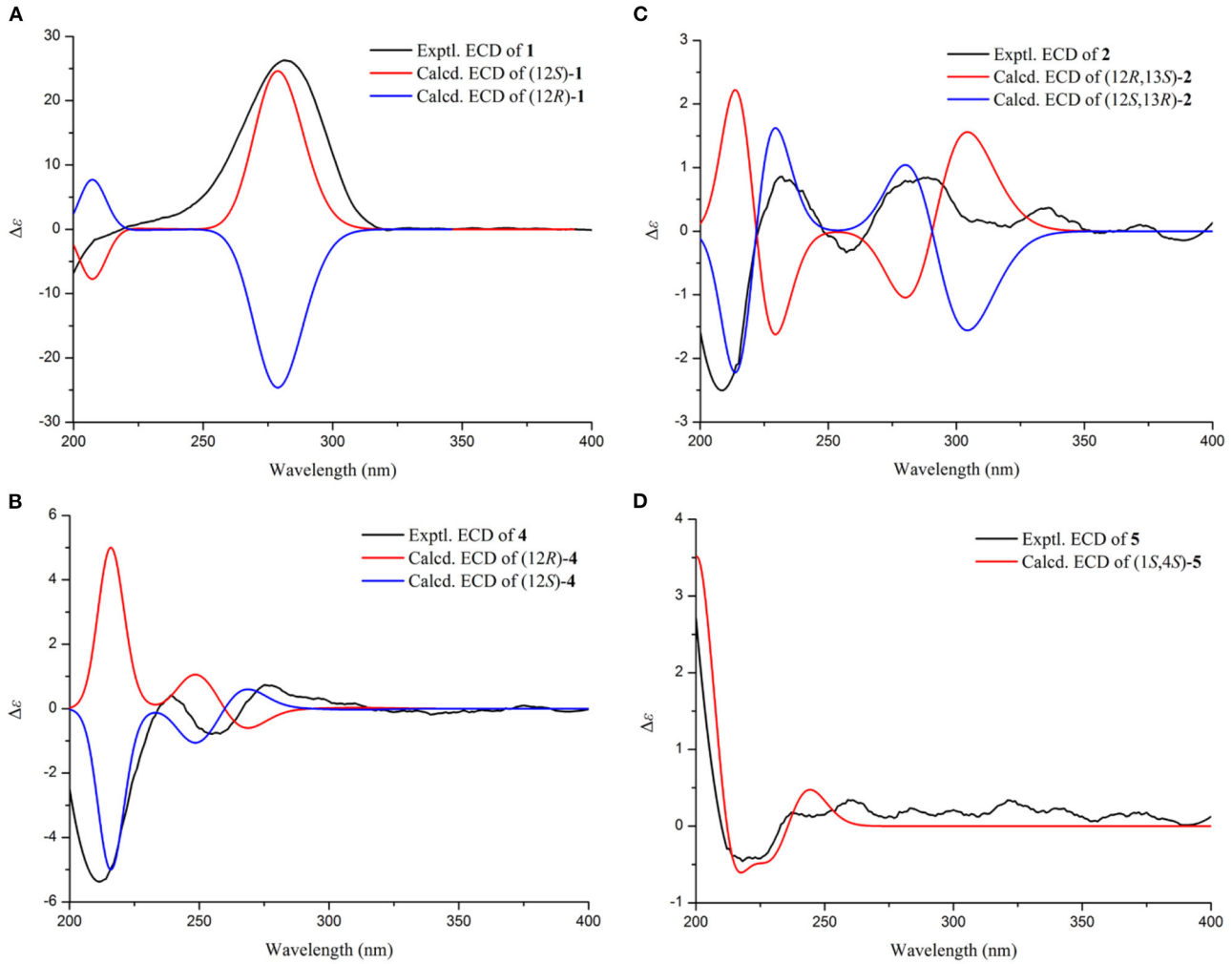

FIGURE 2 | Experimental and calculated ECD curves for **1 (A)**; **2 (B)**; **4 (C)**; **5 (D)**.

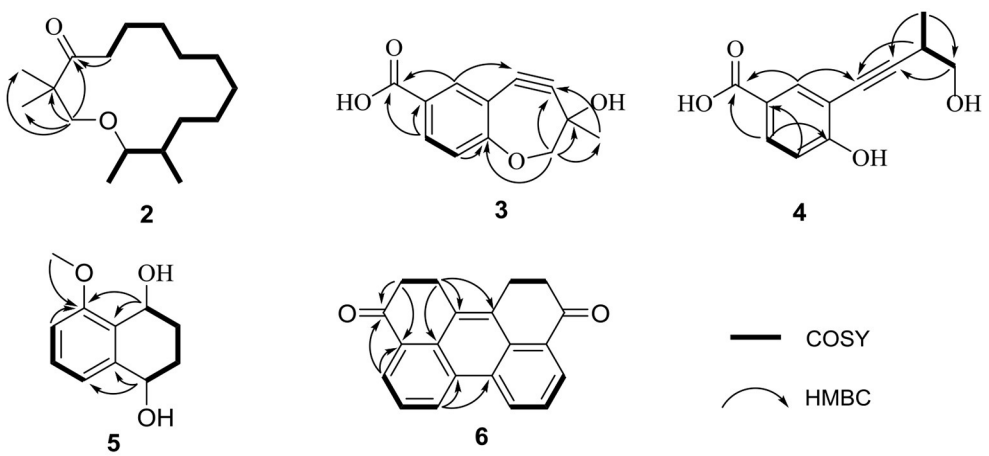

FIGURE 3 | Key HMBC and COSY correlations of **2-6**.

$J = 2.1$ Hz, 8.6 Hz, H-3), 7.98 (d, $J = 2.1$ Hz, H-5). The ^{13}C NMR (**Table 2**) and HSQC spectra displayed 12 carbons, including one methyl, one methylene, six sp^2 carbons, two sp carbons, and one carboxyl carbon. The HMBC correlations (**Figure 3**) from H-5 to C-8, from H_2-11 to C-9, from H_3-12 to C-9, C-10, and C-11, together with the chemical shift at C-8 (δ_C 80.0) and C-9 (δ_C 97.6), supported that the alkynyl group is located at C-6. Furthermore, the weak HMBC correlation from H_2-11 to C-1 confirmed that C-11 and C-1 were connected by an oxygen atom. Compound **3** was determined to be the scalemic mixture as shown by the flat ECD spectra and tiny specific rotation value. The chiral-phase resolution under various circumstances was unsuccessful.

Compound **4**, a yellow solid, its molecular formula determined to be $C_{12}H_{12}O_4$ by the HRESIMS, and indicated seven degrees of unsaturation. Comparing the NMR data (**Table 2**) disclosed a similar structure of **3** and **4**, except for the absence of the hydroxy at C-10 in **4**. The spin system of H_3-12/H-10/H_2-11 was observed from the COSY spectrum (**Figure 3**). The HMBC correlation (**Figure 3**) from H-10 to C-8 further confirmed the deduction. In addition, the HMBC correlation and HRESIMS supported that the ether bond between C-11 and C-1 was fractured. The 12*S* configuration was confirmed by the identical experimental and ECD calculation curves (**Figure 2**).

Compound **5**, a colorless solid, had a molecular formula of $C_{11}H_{14}O_3$ by HRESIMS, and showed five degrees of unsaturation. ^1H NMR (**Table 3**) showed three aromatic signal peaks at δ_H 7.07 (d, $J = 7.8$ Hz, H-5), 7.29 (d, $J = 8.0$ Hz, H-6), 6.85 (d, 8.2 Hz, H-7), two oxygenated methines signal peak δ_H 5.06 (t, $J = 5.1$ Hz, H-1), 4.79 (m, H-4). Comparing the NMR data (**Table 3**) revealed that **5** and **12** (Talapatra et al., 1988) had a similar structure. Except in **5**, where the carbonyl group at C-1 was converted to a hydroxy group. The above conclusion was verified by the H-1/H-2/H-3/H-4 correlation from the COSY spectrum (**Figure 3**), combine with the HMBC correlations (**Figure 3**) from H-1 to C-8 and C-8a. While, according to the HMBC correlation from H_3-9 to C-8, decided that methoxy was located in C-8. The absence of correlation of H-1 and H-4 in the NOESY spectrum showed the 1*S**, 4*S** configuration of **5**. Thereafter, the identical test and calculated ECD curves (**Figure 2**) determined the absolute configuration of compound **5** as 1*S*, 4*S*.

Compound **6**, a yellow solid, its molecular formula was identified as $C_{20}H_{14}O_2$, according to the HRESIMS. The ^1H-NMR (**Table 3**) showed three aromatic protons at δ_H 8.95 (d, $J =$ 8.3 Hz), 7.79 (t, $J = 7.6$ Hz), 8.38 (d, $J = 7.6$ Hz), two methylene peaks δ_H 3.54 (t, $J = 4.7$ Hz) and 3.05 (m). While the ^{13}C NMR (**Table 3**) and HSQC spectra exhibited 20 carbons, including four methyls, six sp carbons, and the rest of the carbons, were quaternary carbon (including two carbonyls). Comparison of the NMR data (**Table 3**) of **6** and **7**, showed a similar structure for **6** and **7**, except for the absence of the hydroxyl group at C-4 and C-9 in **6**. The deduction was supported by the H-4/H-5/H-6 correlation from the COSY spectrum and the HMBC correlations (**Figure 3**) from H-4 to C-3 and C-3a. Thus, the structure of **6** was established.

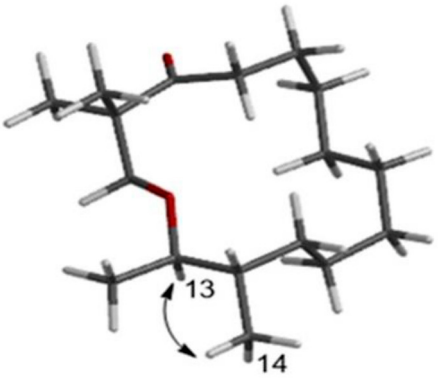

FIGURE 4 | NOESY correlation of **2.**

In total, ten other known compounds were characterized as 4, 9-dihydroxy-1, 2, 11, 12- tetrahydroper-ylene-3,10-quinone (**7**) (Li et al., 2006), (2*R*,4*R*)-3,4-dihydro-5-methoxy-2-methyl-2*H*-1-benzopyran-4-ol (**8**) (Zheng et al., 2016), 4*H*-1-benzopyran-4-ne,5,8-dihydroxy-2-methyl (**9**) (Rao and Venkateswarlu, 1956), 5-hydroxy-8-methoxy-2-methyl-4*H*-1benzopy ran-4-one (**10**) (Sun et al., 2012), (2*R*) 7-hydroxy-2,5-dimethylc-hromone (**11**) (Konigs et al., 2010), (-)-regiolone (**12**) (Talapatra et al., 1988), (4*S*)-4,8-dihydroxy-5-methoxy-*a*-tetralone (**13**) (Machida et al., 2005), (4*S*)-4,5-dihydroxy-α-tetralone (**14**) (Liu et al., 2004), (4*S*)-naphthalenone-3,4-dihydro-4-hydroxy-5-methosy (**15**) (Yamamoto et al., 2003) by comparison of the spectroscopic data with the previous literature.

All compounds were assayed for the anti-inflammatory activities on mouse macrophage RAW264.7 cells. Compounds **2** and **6** showed a considerable inhibitory action, with IC_{50} values of 19.3 μM and 12.9 μM, respectively (positive control $_L$-NMMA: 32.8 μM, **Figure 5**). Compounds **5** and **14,** showed weaker inhibitory activity compared with the positive control (**Figure 5**). Other compounds exhibited no inhibitory action ($IC_{50} > 50$ μM). At the studied concentrations, none of the compounds were cytotoxic to RAW264.7 cells.

Several inducible enzymes in macrophages were significantly up-regulated in the process of inducing inflammation. For example, rate-limiting enzymes responsible for NO production include iNOS. At the same time, inflammatory injury mainly stimulates monocytes, and macrophages induce COX-2 generation, which is a key link in triggering a subsequent inflammatory response. In conclusion, iNOS and COX-2 were considered valuable targets for the treatment of inflammatory diseases (Gao et al., 2021). In the current study, after LPS stimulation, the protein expression levels of iNOS and COX-2 in RAW264.7 cells showed a considerably higher amount than in the control group (**Figure 6**). The expression of iNOS and COX-2 was significantly down-regulated compared with the LPS group, when **2** has been added at different concentrations ($P < 0.001$). The results indicated that **2** could suppress the NO production by

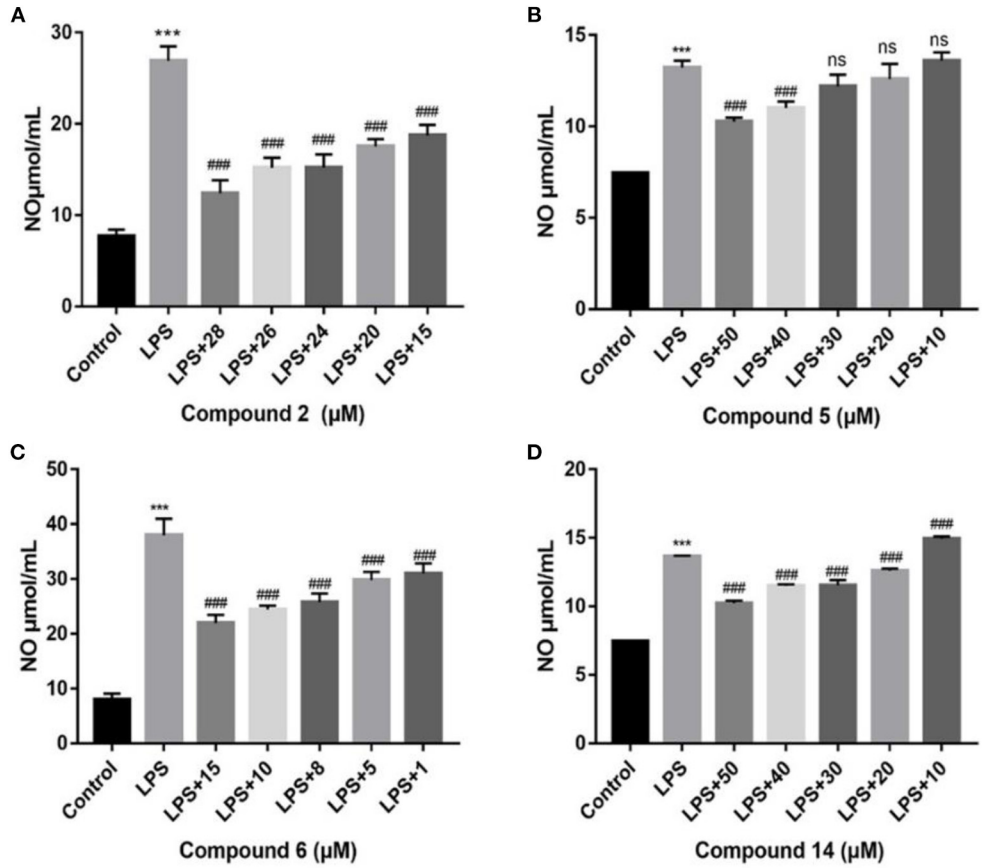

FIGURE 5 | Influences of compounds on NO production for LPS-induced RAW264.7 cells. Compound **2 (A)**; compound **5 (B)**; compound **6 (C)**; compound **14 (D)**. Data rendered are the mean ± SD, $n = 3$. In comparison to the control, $^{***}P < 0.001$. In comparison to LPS, $^{\#\#\#}P < 0.001$.

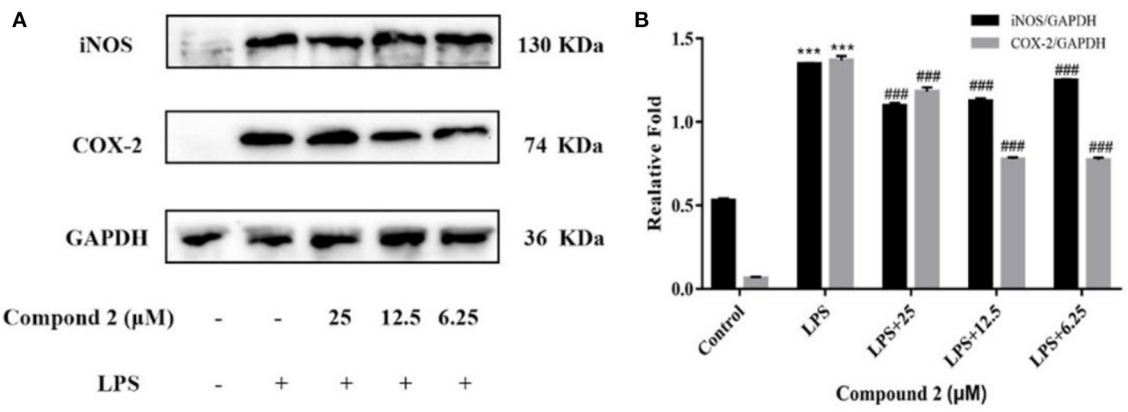

FIGURE 6 | Influences of compound **2** on iNOS, COX-2, and GAPDH protein expression were detected by Western blotting **(A)**. The ratio of the content of iNOS/GAPDH and COX-2/GAPDH **(B)**. Data rendered are the mean ± SD, $n = 3$. In comparison to the control, $^{***}P < 0.001$. In comparison to the LPS group, $^{\#\#\#}P < 0.001$.

inhibiting the protein expression of iNOS, meanwhile inhibiting protein expression of COX-2 in LPS-induced RAW264.7 cells.

In macrophages, NF–κB and MAPK signaling pathways were the main signaling pathways controlling inflammatory responses. In NF–κB signaling, key signaling proteins, including

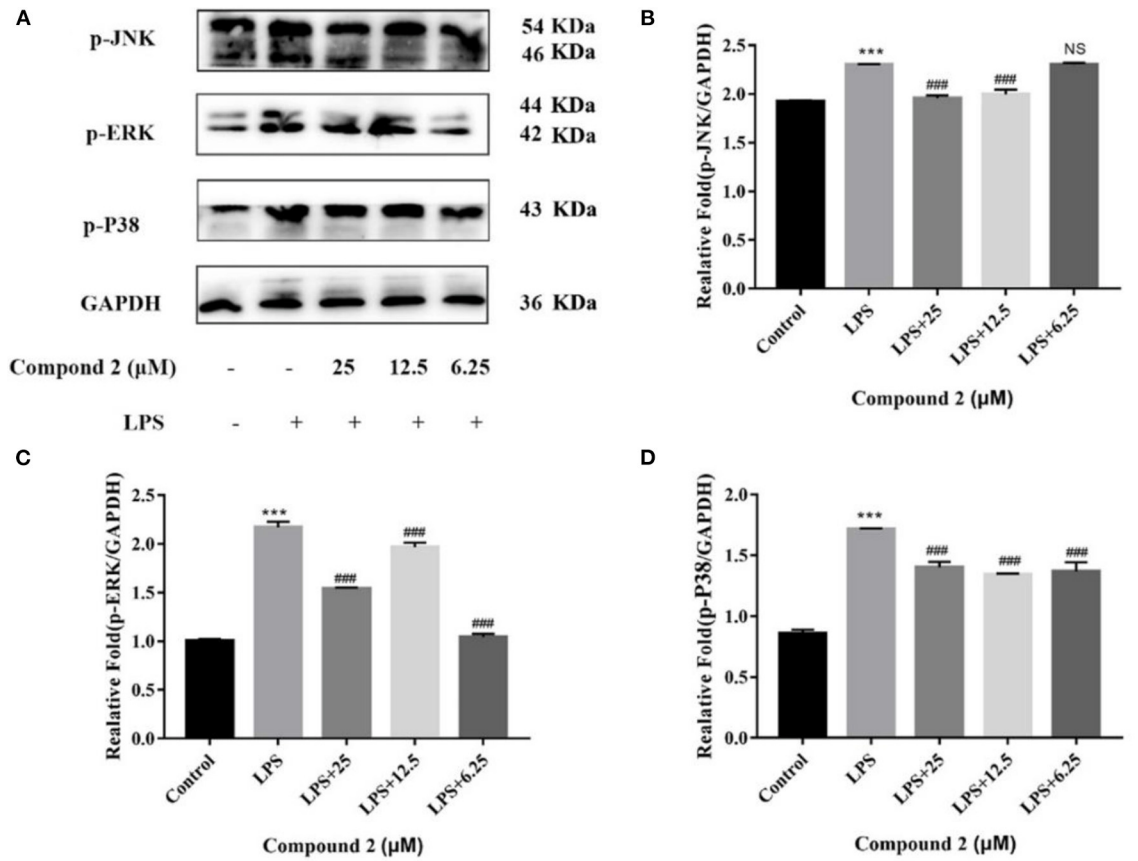

FIGURE 7 | Influences of compound **2** on the MAPK pathway detected by Western blotting. **(A)** The expression levels of p-JNK, p-ERK, p-P38, and GAPDH detected by the western blotting. **(B)** The proportion of p-JNK to GAPDH content. **(C)** The proportion of p-ERK to GAPDH content. **(D)** The proportion of p-P38 to GAPDH content. Data rendered are the mean ± SD, $n = 3$. In comparison to the control, $^{***}P < 0.001$. In comparison to the LPS, $^{\#\#\#}P < 0.001$.

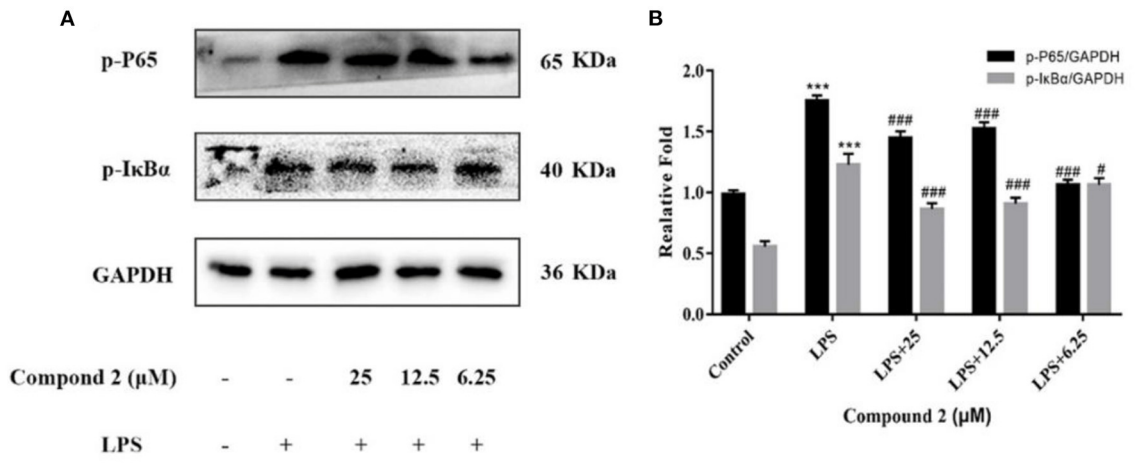

FIGURE 8 | Influences of compound **2** on p-P65, p-IκBα and GAPDH protein expression detected by the western blotting **(A)**. The proportion of p-P65 to GAPDH content and p-IκBα to GAPDH content **(B)**. Data rendered are the mean ± SD, $n = 3$. In comparison to the control, $^{***}P < 0.001$. In comparison to the LPS, $^{\#}P < 0.05$, $^{\#\#\#}p < 0.001$.

IκBα and P65 phosphorylation forms, were chosen as markers of signaling activity; meanwhile, in MAPK signaling pathways, JNK, ERK, and P38 phosphorylation forms were chosen as indicators of signaling activation (Zhang H. et al., 2021). In **Figure 7**, LPS could significantly upregulate JNK, ERK, and P38 protein phosphorylation in RAW264.7 cells in comparison to the control group ($P < 0.001$). Compound **2** to varying degrees inhibited the expression of JNK, ERK, and P38 proteins phosphorylation in LPS stimulated RAW264.7 cells. In conclusion, the anti-inflammatory function of compound **2** might be connected to the suppressed MAPK signaling pathways in RAW264.7 cells. In **Figure 8**, LPS remarkably improves the phosphorylation of IκBα and P65 in RAW264.7 cells in comparison to the control group ($P < 0.001$). Compound **2** inhibited the expression of p-P65 and p-IκBα proteins in LPS-induced RAW264.7 cells. In conclusion, the anti-inflammatory effect of compound **2** may be connected to the suppressed NF–κB signaling pathways in RAW264.7 cells.

CONCLUSION

In total, five new compounds, including eschscholin B (**2**), dalditone A-B (**3**-**4**), (1*R*, 4*R*)-5-methoxy-1,2,3,4-tetrahydronaphthalene-1,4-dio (**5**), and daldilene A (**6**), were isolated from mangrove endophytic fungus *D. eschscholtzii*. Their structures and absolute configurations were determined by spectroscopy data and ECD calculation. The absolute configuration of **1** was first determined by ECD calculation. Compounds **2** and **6** exhibited potent anti-inflammatory activities with IC_{50} values of 19.3 and 12.9 μM, respectively. Compound **2** belongs to the family of macrocyclic ether, which showed various biological activities. For example, eurysoloids B with immunosuppressive and adipogenesis inhibitory activities (Teng et al., 2021), 12*S*, 13*S*-epoxyobtusa-llene IV with cytotoxic activity (Gutiérrez-Cepeda et al., 2016), durumhemiketalolides A and C with anti-inflammatory activity (Cheng et al., 2009) have reported. In addition, further studies showed that compound **2** might play an anti-inflammatory role by inhibiting the activation of MAPK and NF–κB signaling pathways. This study will contribute to the chemical diversity of polyketide and the discovery of potential anti-inflammatory agents from extreme mangrove-derived fungi.

DATA AVAILABILITY STATEMENT

The datasets presented in this study can be found in online repositories. The names of the repository/repositories and accession number(s) can be found in the article/**Supplementary Material**.

AUTHOR CONTRIBUTIONS

GW performed the experiments and wrote the article. ZY, SW, and YY participated in the experiments. YC and WK reviewed the article. WK designed and supervised the experiments. All authors have read and agreed to the published version of the article.

FUNDING

This work was supported by the Key Project in Science and Technology Agency of Henan Province (212102311029 and 222102310236) and the Key Scientific Research Project in Colleges and the Universities of Henan Province (22B350001).

SUPPLEMENTARY MATERIAL

The Supplementary Material for this article can be found online at: https://www.frontiersin.org/articles/10.3389/fmicb.2022.900227/full#supplementary-material

REFERENCES

Barnes, E. C., Jumpathong, J., Lumyong, S., Voigt, K., and Hertweck, C. (2016). Daldionin, an unprecedented binaphthyl derivative, and diverse polyketide congeners from a fungal orchid endophyte. *Eur. J. Med. Chem.* 47, 4551–4555. doi: 10.1002/chin.201631229

Bindu, S., Mazumder, S., and Bandyopadhyay, U. (2020). Non-steroidal anti-inflammatory drugs (NSAIDs) and organ damage: a current perspective. *Biochem. Pharmacol.* 180, 114147. doi: 10.1016/j.bcp.2020.114147

Chen, S., Cai, R., Liu, Z., Cui, H., She, Z. (2022). Secondary metabolites from mangrove-associated fungi: source, chemistry and bioactivities. *Nat. Prod. Rep.* 39, 560–595. doi: 10.1039/D1NP00041A

Chen, Y., Liu, Z. M., Huang, Y., Liu, L., He, J. G., Wang, L., et al. (2019). Ascomylactams A-C, cytotoxic 12- or 13-membered-ring macrocyclic alkaloids isolated from the mangrove endophytic fungus *Didymella* sp. CYSK-4, and structure revisions of phomapyrrolidones A and C. *J. Nat. Prod.* 82, 1752–1758. doi: 10.1021/acs.jnatprod.8b00918

Chen, Y., Liu, Z. M., Liu, H. J., Pan, Y. H., Li, J., Liu, C., and She, Z. G. (2018). Dichloroisocoumarins with potential anti-inflammatory activity from the mangrove endophytic fungus *Ascomycota* sp. CYSK-4. *Mar. Drugs* 16, 54. doi: 10.3390/md16020054

Chen, Y., Wang, G. S., Yuan, Y. L., Zou, G., Yang, W. C., Tan, Q., et al. (2022). Metabolites with cytotoxic activities from the mangrove endophytic fungus *Fusarium* sp. 2ST2. *Front. Chem.* 10, 842405. doi: 10.3389/fchem.2022.842405

Chen, Y., Zou, G., Yang, W. C., Zhao, Y. Y., Tan, Q., Chen, L., et al. (2021). Metabolites with anti-inflammatory activity from the mangrove endophytic fungus Diaporthe sp. QYM12. *Mar. Drugs* 19, 56. doi: 10.3390/md19020056

Cheng, S. Y., Wen, Z. H., Wang, S. K., Chiou, S. F., Hsu, C. H., Dai, C. F., et al. (2009). Unprecedented hemiketal cembranolides with anti-inflammatory activity from the soft coral Lobophytum durum. *J. Nat. Prod.* 72, 152. doi: 10.1021/np800686k

Flores-Reséndiz, M., Lappe-Oliveras, P., and Macías-Rubalcava, M. L. (2021). Mitochondrial damage produced by phytotoxic chromenone and chromanone derivatives from endophytic fungus *Daldinia eschscholtzii* strain GSE13. *Appl. Microbiol. Biotechnol.* 105, 4225–4239. doi: 10.1007/s00253-021-11318-7

Gao, R. C., Shu, W. H., Shen, Y., Sun, Q. C., Jin, W. G., Li, D., et al. (2021). Peptide fraction from sturgeon muscle by pepsin hydrolysis exerts anti-inflammatory effects in LPS-stimulated RAW264.7 macrophages via MAPK and NF-κB pathways. *Food Sci. Hum. Well.* 10, 103–111. doi: 10.1016/j.fshw.2020.04.014

Gutiérrez-Cepeda, A., Fernández, J. J., Norte, M., López-Rodríguez, M., Brito, I., Muller, C. D., et al. (2016). Additional insights into the obtusallene family: components of *Laurencia marilzae*. *J. Nat. Prod.* 79, 1184–1188. doi: 10.1021/acs.jnatprod.5b01080

Kongyen, W., Rukachaisirikul, V., Phongpaichit, S., and Sakayaroj, J. (2015). A new hydronaphthalenone from the mangrove-derived *Daldinia eschscholtzii* PSU-STD57. *Nat. Prod. Res*. 29, 1995–1999. doi: 10.1080/14786419.2015.1022542

Konigs, P., Rinker, B., Maus, L., Niger, M., Rheinheimer, J., and Waldvogel, S. R. (2010). Structural revision and synthesis of altechromone A. *J. Nat. Prod*. 73, 2064–2066. doi: 10.1021/np1005604

Li, P., Xu, N., Meng, D. L., and Sha, Y. (2006). A new perylene quinone from the fruit bodies of Bulgaria inquinans. *J. Asian Nat. Prod. Res*. 8, 743–746. doi: 10.1080/10286020500246626

Liao, H. X., Shao, T. M., Mei, R. Q., Huang, G. L., Zhou, X. M., Zheng, C. J., et al. (2019a). Bioactive secondary metabolites from the culture of the mangrove-derived fungus *Daldinia eschscholtzii* HJ004. *Mar. Drugs* 17, 710. doi: 10.3390/md17120710

Liao, H. X., Zheng, C. J., Huang, G. L., Mei, R. Q., Nong, X. H., Shao, T. M., et al. (2019b). Bioactive polyketide derivatives from the mangrove-derived fungus *Daldinia eschscholtzii* HJ004. *J. Nat. Prod*. 82, 2211–2219. doi: 10.1021/acs.jnatprod.9b00241

Liu, H. X., Tan, H. B., Li, S. N., Chen, Y. C., Li, H. H., and Zhang, W. M. (2017). Two new metabolites from *Daldinia eschscholtzii,* an endophytic fungus derived from *Pogostemon cablin*. *J. Asian Nat. Prod. Res*. 21, 1–7. doi: 10.1080/10286020.2017.1392512

Liu, L. J., Li, W., Koike, K., Zhang, S. J., and Nikaido, T. (2004). New α-tetralonyl glucosides from the fruit of Juglans madshurica. *Chem. Pharm. Bull*. 52, 566–569. doi: 10.1248/cpb.52.566

Machida, K., Matsuoka, E., Kasahara, T., and Kikuchi, M. (2005). Studis on the constituents of Juglans species. I. Structural determination of (4S)- and (4R)-4-hydroxy-α-tetralone derivatives from the fruit of *Juglans mandshurica* MAXIM. var. siboldiana MAKINO. *Chem. Pharm. Bull*. 53, 934–937. doi: 10.1248/cpb.53.934

Niu, Y., Wang, B. G., Zhou, L., Ma, C. Y., Waterhouse, G. I., Liu, Z. H., et al. (2021). Nigella sativa: A dietary supplement as an immune-modulator on the basis of bioactive components. *Front. Nutr*. 8, 521. doi: 10.3389/fnut.2021.722813

Rao, C. R., and Venkateswarlu, V. (1956). Synthesis of 5-and 5,8-dimethoxy-2-methylchromones. *Recl. Trav. Chim. Pays-Bas* 75, 1321–1326. doi: 10.1002/recl.19560751113

Sun, Y. W., Liu, G. M., Huang, H., and Yu, P. Z. (2012). Chromone derivatives from *Halenia elliptica* and their anti-HBV activities. *Phytochemistry* 75, 169–176. doi: 10.1016/j.phytochem.2011.09.015

Talapatra, S. K., Karmacharya, B., De, S. C., and Talapatra, B. (1988). (-)-Regiolone, an α-tetralone from *Juglans regia*: structure, stereochemistry, and conformation. *Phytochemistry* 27, 3929–3932. doi: 10.1016/0031-9422(88)83047-4

Teng, L. L., Mu, R. F., Liu, Y. C., Xiao, C. J., Li, D. S., Guo, K., et al. (2021). Immunosuppressive and adipogenesis inhibitory sesterterpenoids with a macrocyclic ether system from *Eurysolen gracilis*. *Org. Lett*. 23, 2232–2237. doi: 10.1021/acs.orglett.1c00369

Wang, Y., Zhou, Z. Y., Han, M. S., Zhai, J. X., Han, N., Liu, Z. H., et al. (2020). The anti-inflammatory components from the effective fraction of syringae folium (ESF) and its mechanism investigation based on network pharmacology. *Bioorg. Chem*. 99, 103764. doi: 10.1016/j.bioorg.2020.103764

Wutthiwong, N., Suthiphasilp, V., Pintatum, A., Suwannarach, N., Kumla, J., Lumyong, S., et al. (2021). A rare tricyclic polyketide having a chromone unit fused to a δ-lactone and its symmetrical biphenyl dimer, daldiniaeschsone B, from an endophytic fungus *Daldinia eschscholtzii* SDBR-CMUNKC745. *J. Fungi* 7, 358. doi: 10.3390/jof7050358

Yamamoto, K., Hatano, H., Arai, M., Shiomi, K., Tomoda, H., and Omura, S. (2003). Structure elucidation of new monordens produced by Humicola sp. FO-2942. *J. Antibiot*. 56, 533. doi: 10.1002/chin.200343195

Yang, L. J., Liao, H. X., Bai, M., Huang, G. L., Luo, Y. P., Niu, Y. Y., et al. (2017). One new cytochalasin metabolite isolated from a mangrove-derived fungus *Daldinia eschscholtzii* HJ001. *Nat. Prod. Res*. 32, 1–6. doi: 10.1080/14786419.2017.1346641

Zhang, A. H., Liu, W., Jiang, N., Tan, R. X. (2016). Spirodalesol, an NLRP3 inflammasome activation inhibitor. *Org. Lett.* 18, 6496-6499. doi: 10.1021/acs.orgl tt.6b03435

Zhang, H., Guo, Q. F., Liang, Z. H., Wang, M. K., Wang, B. G., Sun-Waterhouse, D. X., et al. (2021). Anti-inflammatory and antioxidant effects of chaetoglobosin V b in LPS-induced RAW264.7 cells: achieved via the MAPK and NF-κB signaling pathways. *Food Chem. Toxicol*. 147, 111915. doi: 10.1016/j.fct.2020.111915

Zhang, Y., Ma, A., Xi, H., Chen, N., Wang, R., Yang, C. H., et al. (2021). Antrodia cinnamomea ameliorates neointimal formation by inhibiting inflammatory cell infiltration through downregulation of adhesion molecule expression in vitro and in vivo. *Food Sci. Hum. Well* 10, 421–430. doi: 10.1016/j.fshw.2021.04.004

Zheng, C. J., Huang, G. L., Xu, Y., Song, X. M., Yao, J., Liu, H., et al. (2016). A new benzopyrans derivatives from a mangrove derived fungus *Penicillium citrinum* from the South China Sea. *Nat. Prod. Res*. 30, 821–825. doi: 10.1080/14786419.2015.1072712

Conflict of Interest: The authors declare that the research was conducted in the absence of any commercial or financial relationships that could be construed as a potential conflict of interest.

Publisher's Note: All claims expressed in this article are solely those of the authors and do not necessarily represent those of their affiliated organizations, or those of the publisher, the editors and the reviewers. Any product that may be evaluated in this article, or claim that may be made by its manufacturer, is not guaranteed or endorsed by the publisher.

frontiers | Frontiers in Microbiology

ORIGINAL RESEARCH
published: 13 June 2022
doi: 10.3389/fmicb.2022.922454

Identification of a New Antifungal Peptide W1 From a Marine *Bacillus amyloliquefaciens* Reveals Its Potential in Controlling Fungal Plant Diseases

Qiao Wen[1], *Ruizhe Liu*[1], *Zhenxiao Ouyang*[1], *Tianliang He*[1]*, *Weini Zhang*[1] and *Xinhua Chen*[1,2]*

[1] Key Laboratory of Marine Biotechnology of Fujian Province, Institute of Oceanology, College of Marine Sciences, Fujian Agriculture and Forestry University, Fuzhou, China, [2] Southern Marine Science and Engineering Guangdong Laboratory, Zhuhai, China

OPEN ACCESS

Edited by:
Xian-Wen Yang,
Third Institute of Oceanography, Ministry of Natural Resources, China

Reviewed by:
Muthukrishnan Sathiyabama, Bharathidasan University, India
Sylvie Françoise Rebuffat, Muséum National d'Histoire Naturelle, France

***Correspondence:**
Tianliang He
htlsf@zju.edu.cn
Xinhua Chen
chenxinhua@tio.org.cn

Specialty section:
This article was submitted to Extreme Microbiology, a section of the journal Frontiers in Microbiology

Received: 18 April 2022
Accepted: 23 May 2022
Published: 13 June 2022

Citation:
Wen Q, Liu R, Ouyang Z, He T, Zhang W and Chen X (2022) Identification of a New Antifungal Peptide W1 From a Marine Bacillus amyloliquefaciens Reveals Its Potential in Controlling Fungal Plant Diseases. Front. Microbiol. 13:922454. doi: 10.3389/fmicb.2022.922454

A bacterium, *Bacillus amyloliquefaciens* W0101, isolated from the Arctic Ocean, showed potent antifungal activity against several plant pathogenic fungi. An antifungal peptide W1, with a molecular weight of approximately 2.4 kDa, was purified from the culture supernatant of the strain W0101 using ion-exchange chromatography and high-performance liquid chromatography. By analysis of Liquid Chromatograph-Mass Spectrometer, the peptide W1 was identified as a new antifungal peptide derived from the fragment of preprotein translocase subunit YajC. Further analysis revealed that W1 could disrupt the hyphae and spores of *Sclerotinia sclerotiorum* and inhibit its growth. W1 suppressed *S. sclerotiorum and Fusarium oxysporum* at a minimum inhibitory concentration of 140 and 58 μg/ml, respectively. The antifungal activity of W1 remained stable at 20–80°C or pH 6–11, with reduced activity at 100–110°C and pH 4–5, and under three protease treatments. Additionally, W1 also had a certain extent of metal ion resistance. These results therefore suggest that the peptide W1 from marine *B. amyloliquefaciens* W0101 may represent a new antifungal peptide with potential application in the biocontrol of plant diseases.

Keywords: plant pathogenic fungi, *Bacillus amyloliquefaciens*, antifungal peptide, antifungal activity, Arctic Ocean

INTRODUCTION

Fungal diseases have always been one of the main restricting factors affecting the good quality and high yield of crops (Montesinos, 2007). According to statistics, about 80% of plant diseases are caused by fungal infection (Someya, 2008). Fungal pathogens, such as *Fusarium oxysporum*, *Alternaria longipes*, and *Magnaporthe grisea*, generally cause necrosis, rot, and wilting in leaves, stems, or fruits of plants, decreasing crop yield and quality (Talbot, 2003; Ajilogba and Babalola, 2013; Shoaib et al., 2014). Moreover, some pathogenic fungi can even produce a variety of mycotoxins and metabolites that are harmful to humans and animals, posing a great threat to

the safety of agricultural products (Hussein and Brasel, 2001). Till present, the utilization of chemical fungicides has been the main approach that controls fungal infections (Kumar and Kumar, 2019). It is estimated that around 3 billion kilograms of agricultural chemicals are applied in the agricultural industry each year. However, the long-term abuse of chemical fungicides in agriculture has resulted in a gradual increase in fungal resistance to chemical fungicides, a detrimental effect on the environment, and a health threat to humans and animals (Sharma et al., 2020). On account of the harmful effects of chemical germicides, ecologically safe and cost-effective measures as an alternative to chemical control are urgently needed to achieve the sustainable development of agriculture (Fisher et al., 2018).

Antifungal peptides (AFPs) are a kind of defensive peptide with antifungal activity that exists widely in plants, animals, and microorganisms (Yan et al., 2015). AFPs generally contain 10–100 amino acid residues with a molecular weight of less than 10 kDa and play an important role in the defense against fungal infection in plants (Montesinos, 2007; Yan et al., 2015). The special cationic and amphiphilic structures make AFPs kill fungal cells by inhibiting the synthesis of fungal cell walls and interacting with components in the membrane and intracellular targets (Li et al., 2021). These special mechanisms, different from chemical fungicides, are considered to be the effective ways to reduce the development of drug resistance (Dhanasekaran et al., 2012). Thus, AFPs may become a new generation of promising antifungal agents in future anti-infectious applications.

During the past few decades, *Bacillus* species have been widely used in the control of crop diseases (Ongena and Jacques, 2008). *B. subtilis* and its metabolites were used to control blue mold on citrus (Waewthongrak et al., 2015). *Bacillus cereus* and *Bacillus safensis* had a significant effect in preventing leaf spot and blight disease (Roy et al., 2018). *Bacillus amyloliquefaciens* was also found to have potential antifungal activity against the pathogens of root rot disease and black rot disease in sweet potatoes (Wang et al., 2020). Several strains of *Bacillus* were also found to produce AFPs against *Aspergillus niger* (*B. amyloliquefaciens* BH072), *Alternaria solani* (*Bacillus marinus* B-9987), *Beauveria bassiana* (*B. amyloliquefaciens* SWB16), *F. oxysporum* (*B. cereus* QQ 308), *Fusarium solani* (*B. cereus* QQ 308), and *Pythium ultimum* (*B. cereus* QQ 308; Chang et al., 2007; Gao et al., 2009; Zhao et al., 2013; Wang et al., 2014). Recently, researchers have isolated several antifungal microbes from the polar regions, such as *Bacillus sp*. ANT_WA51, *B. amyloliquefaciens* PC3 and *Penicillium chrysogenum* A096, which produce active antifungal peptides and show potential application values in agriculture (Chen et al., 2013; Cui et al., 2017; Ding et al., 2018, 2019; Styczynski et al., 2022). Therefore, screening for antifungal bacteria from the polar regions has become a new approach to controlling agricultural diseases (Núñez-Montero and Barrientos, 2018). In this study, we isolated a strain of *B. amyloliquefaciens* W0101 with remarkable antifungal activity from a sediment sample of the Arctic Ocean. An antifungal peptide W1 was purified and identified from the culture supernatant of the strain W0101. We then investigated the mechanisms underlying W1 inhibition of *S. sclerotiorum* and also analyzed the physiochemical properties of W1.

MATERIALS AND METHODS

Tested Strains

The tested fungus *Paecilomyces variotii* (CGMCC 3.776) was provided by the China General Microbiological Culture Collection Center, and *F. oxysporum* (ACCC 31352), *S. sclerotiorum* (ACCC 36081), *Rhizoctonia solani* Kühn (ACCC 36316), *A. longipes* (ACCC 30002), *Colletotrichum gloeosporioides* (ACCC 31200), *Alternaria gaisen* (ACCC 37473), *Botryosphaeria dothidea* (ACCC 38026), and *Phomopsis amygdali* (ACCC 37078) were provided by Agricultural Cultural Collection of China. All fungi were grown on potato dextrose agar (PDA, Haibo Biotechnology Company, China) plates at 30°C.

Isolation of Antifungal Strains

Sediment sample was collected from the Arctic Ocean (168°09′41″W, 69°13′3″7) during the sixth Chinese National Arctic Expedition. The sediment sample was cultured by oscillation with sterile seawater and glass beads at 4°C for 6 h. An aliquot of supernatant liquid homogenized mixture was put into centrifuge tubes containing sterile seawater and a serial 10-fold dilution was done up to 10^{-6}. Approximately 100 μl of the diluted samples were spread on 2216E agar media (Haibo Biotechnology Company, Qingdao, China) in each dilution. Later, all plates were incubated at 28°C for 48 h. The strains were selected based on their morphological features and inoculated into LB medium for further growth to evaluate their antifungal potential.

Antifungal Activity Detection

The disk diffusion method was applied in the determination of antifungal protein produced by strain W0101 (Chen et al., 2013; Ding et al., 2018, 2019) In brief, a hyphal block of tested fungus was inoculated onto the center of PDA plates, and 60 μl of the culture supernatant of strain W0101, purified or synthesized peptide in PBS buffer, was added to symmetrical sites 20 mm away from the pathogen. The plates were cultured for 48 h at 30°C to observe for antifungal activity. The sample treatment was repeated in triplicate.

Identification of Strain W0101

Genomic DNA of strain W0101 was extracted using an E.Z.N.A. Bacterial DNA Kit according to the manufacturer's protocol (Omege Bio-Tek, Guangzhou, China). The 16S rDNA sequence of strain W0101 was amplified using universal primers (27F and 1492R), sequenced by Sangon Biotech (Shanghai, China), and aligned with NCBI rRNA/ITS databases using the blastn algorithm.[1]

For phylogenetic analysis, the 16S rDNA sequences were aligned using the MAFFT program with default parameters (Katoh et al., 2002). A phylogenetic tree was constructed with the maximum likelihood estimate method using the MEGA 7.0 software (Kumar et al., 2016). The tree reliability was assessed by the bootstrap method based on 1,000 replicates.

The genome sequencing of strain W0101 was performed using PacBio and Illumina Miseq sequencing by Majorbio Biotech

[1]https://blast.ncbi.nlm.nih.gov/Blast.cgi

Co., Ltd. (Shanghai, China). The methods of genome assembling for the strain W0101 genome refer to our previous study (Li et al., 2020). An average nucleotide identity (ANI) analysis was performed among the genomes of the strain W0101 and other 8 *Bacillus* strains using Jspecies (version 1.2.1; Richter and Rossello-Mora, 2009).

Isolation and Purification of Antifungal Peptides From W0101

For the isolation and purification of antifungal peptides, refer to our previously published methods (Chen et al., 2013; Wen et al., 2014; Cui et al., 2017; Wu et al., 2018). The stain W0101 was cultured in LB medium at 28°C for 48 h before centrifugation at 8,000 × *g* for 10 min at 4°C. The supernatant was filtered using a 0.45-μm membrane and respectively added ammonium sulfate with six saturation concentrations (0, 20, 40, 60, 80, and 100%) to let stand overnight at 4°C. The crude proteins were collected after centrifugation at 12,000 × *g* for 20 min at 4°C. Then, it was dissolved in a suitable volume of 20 mM Tris–HCl buffer (pH 8.07). After being dialyzed with the same buffer for 48 h at 4°C, the crude protein was concentrated by freeze-dying.

The crude protein sample was separated by ion exchange chromatography with an AKTA Pure 25 system. The sample solution was loaded onto a HiTrap DEAE Sepharose Fast Flow column, which was pre-equilibrated with starting buffer A (20 mM Tris–HCl, pH 8.07) for the primary purification step. The elution procedure was as follows: 0% elution buffer B (20 mM Tris–HCl, 1 M NaCl, pH 8.07), 5 CV (column volume); 25% elution buffer B, 4 CV; 50% elution buffer B, 3 CV; and 100% elution buffer B, 5 CV. Each fraction was collected according to the absorbance of 280 nm. Then, all fractions were concentrated using ultrafiltration and determined their antifungal activity. The antifungal fraction was purified by a HiTrap Q Sepharose Fast Flow column, which was pre-equilibrated with starting buffer C (20 mM piperazine, 400 mM NaCl, pH 9.73). The elution procedure was carried out as follows: 13–34% elution buffer D (20 mM piperazine, 1 M NaCl, pH 9.73), 24 CV; 80% elution buffer D, 5 CV; and 100% elution buffer D, 5 CV. Finally, the purity of antifungal components from the HiTrap Q column was detected by reversed phase-high performance liquid chromatography (RP-HPLC) using Waters Alliance E2695 equipped with an analytic C18 reverse-phase column at a flow rate of 1 ml/min, measured at 280 nm. Solvent A (0.1% (w/v) trifluoroacetic acid (TFA, Sigma-Aldrich, St. Louis, United States) in water and solvent B (0.1% TFA in acetonitrile) were used as the mobile phases in a gradient elution mode (5–90% solvent B, 50 min). All the peaks were collected. The purity of the corresponding compounds was evaluated by sodium dodecyl sulfate-polyacrylamide gel electrophoresis (SDS-PAGE), and their antifungal activity was determined.

Identification of Antifungal Proteins by Liquid Chromatograph-Mass Spectrometer

The purified antifungal peptide was identified at Beijing Bio-Tech Pack Technology Company Ltd. (Beijing, China). The samples were first subjected to trypsin digestion. Liquid Chromatograph-Mass Spectrometer (LC-MS/MS) analysis of the digested samples was performed on an Ultimate 3000 HPLC system (Thermo Fisher Scientific, Waltham, United States) interfaced online to an Orbitrap Fusion^{TM} Lumos^{TM} Tribrid^{TM} Mass Spectrometer (Thermo Fisher Scientific). The mobile phase was composed of 2% acetonitrile with 1% formic acid (solvent A) and 80% acetonitrile with 0.1% formic acid (solvent B). Both mobile phases were degassed for 30 min in a sonicator bath. 5 μl of sample was first loaded onto a trapping column packaged with PepMap RPLC C_{18} (5 mm × 300 μm i.d., 5 μm) at a flow rate of 10 μl/min. After 2 min, the sample was separated on a nanocolumn column packaged with PepMap RPLC C_{18} (150 mm × 150 μm i.d., 1.9 μm) at a flow rate of 200 nl/min using a solvent A and B mixture. The mobile phase gradient was as follows: 4–10% of solvent B in 5 min, 10–22% in 80 min, 22–40% in 25 min, 40–95% in 5 min, and 95% during 5 min.

Subsequently, the sample was infused into the mass spectrometer *via* a dynamic nanospray probe (Thermo Fisher Scientific) and analyzed in positive mode. The parameters of primary mass spectrometry are as follows: resolution, 70,000; AGC target, 3e6; maximum IT, 60 ms; scan range, 300–140 m/z. The parameters of secondary mass spectrometry are as follows: resolution, 17,500; AGC target, 5e4; maximum IT, 15 ms; TopN, 5; scan range, 200–2,000 m/z.

The raw mass data were analyzed using MaxQuant version 1.6.2.10 (Tyanova et al., 2016) to match the protein data of *B. amyloliquefaciens* W0101 (GenBank accession no. NZ_CP090477), whose genome was sequenced in this study. The analysis settings were as follows: fixed modifications, carbamidomethyl (C); variable modifications, oxidation (M) and acetyl (protein N-term); enzyme, trypsin; maximum missed cleavages, 2; peptide mass tolerance, 20 ppm; fragment mass tolerance, 20 ppm; mass values, monoisotopic; significant threshold, 0.01.

Thermostability Assay of W1

To evaluate the thermostability of W1, the purified peptide with a concentration of 160 μg/ml was incubated at 20, 40, 60, 80, 100, 110, and 121°C (autoclaved) for 20 min. After cooling to room temperature, the residual antifungal activity of peptide W1 was tested against *F. oxysporum* using the agar diffusion bioassay, which was described above. The peptide W1 without heat treatment and piperazine buffer (20 mM, pH 9.73) were used as the positive and blank controls, respectively. All assays were repeated three times independently.

pH Stability Test of W1

The purified peptide W1 with a concentration of 160 μg/ml was exposed to a pH range from pH 3.0 to pH 11.0 using 50 mM glycine-HCl (pH 3.0), 50 mM sodium acetate (pH 4.0), 50 mM Na_2HPO_4-citric acid (pH 5.0 and 6.0), 50 mM Na_2HPO_4-NaH_2PO_4 (pH 7.0), 20 mM Tris–HCl (pH 8.0), 50 mM glycine-NaOH (pH 9.0), 20 mM piperazine (pH 10.0), and 50 mM Na_2HPO_4-NaOH (pH 11.0). After incubation for 2 h at room temperature, the antifungal activity against *F. oxysporum* of the

reaction mixture were tested with all buffer solution as the blank controls. All assays were repeated three times independently.

Effect of Metal Ions on the Antifungal Activity of W1

To evaluate the effect of metal ions on the antifungal activity of W1, we selected several common metal ions such as Mg^{2+}, Ca^{2+}, Mn^{2+}, Ba^{2+}, Na^{+}, K^{+}, Fe^{2+}, and Cu^{2+}, which were dissolved in 20 mM piperazine buffer (pH 9.73). The purified peptide W1 with a concentration of 160 μg/ml was treated with different ions solutions at the final concentrations of 20 mM Mg^{2+}, Ca^{2+}, Mn^{2+}, Ba^{2+}, Na^{+}, and K^{+} and 6 mM Fe^{2+} and Cu^{2+}, respectively, at room temperature for 3 h. The antifungal activity against *F. oxysporum* of the reaction mixture was subsequently determined. The peptide W1 without ion solution treatment was used as the positive control, and ion solutions were used as blank controls. All assays were repeated three times independently.

Effect of Proteases on the Antifungal Activity of W1

To detect the sensitivity of W1 to proteases, the purified peptide with a concentration of 160 μg/ml was subjected to treatment with 1 mg/ml proteinase K (Sigma-Aldrich, United States) at 58°C for 2 h, or 1 mg/ml papain (Sigma-Aldrich, United States) at 55°C for 2 h, or 1 mg/ml trypsin (Sigma-Aldrich, United States) at 37°C for 2 h. The purified W1 treated under the same conditions but without proteases was used as control. All assays were repeated three times independently.

MIC Determination of W1

The minimum inhibitory concentration (MIC) of W1 against *F. oxysporum* and *S. sclerotiorum* was determined using the paper disk diffusion method (Wen et al., 2014; Rao et al., 2015). In brief, the purified W1 was diluted into 20 mM piperazine buffer (pH 9.73) with final concentrations of 0.464, 0.232, 0.116, 0.058, and 0.029 μg/μl, respectively. On paper disks placed 2 cm from the hyphal margin of fungus on a PDA plate, 60 μl of serially diluted samples were added. Later, the plate was incubated at 30°C for 24–48 h. The MIC was determined as the lowest concentration of W1 that could inhibit visible mold growth and was calculated as the total peptide concentration added to each paper disk (microgram per disk). The piperazine buffer (20 mM) was used as the blank control. All assays were repeated three times independently.

Scanning Electron Microscope Analysis

To analyze the antifungal mechanism of W1 against pathogenic fungi, 1 ml of PDA medium containing mycelium of *F. oxysporum* or *S. sclerotiorum* was poured on the surface of an aluminum specimen that is used for Scanning Electron Microscope (SEM) and incubated at 30°C for 72 h. After incubation, 20 μl of the purified W1 (160 μg/ml) was added on the surface of the aluminum specimen and continued to incubate at 30°C for 24 h. The PBS solution as control was used to perform the same process. Each specimen was washed in glutaraldehyde solution (1 mM NaH_2PO_4-Na_2HPO_4, 2.5% glutaraldehyde, pH 7.4) and finally fixed in glutaraldehyde solution at 4°C for 12 h. After fixation, the specimens were washed with phosphate solution (1 mM NaH_2PO_4-Na_2HPO_4, pH 7.4) three times for 15 min. The dehydration was performed using a series of acetones (35, 50, 75, 95, and 100%) for 10 min, respectively. Each step of the dehydration was repeated three times. Then, the specimens were critically dried for 90 min and coated with gold in a sputter coater. Images were observed and captured using a JSM-6380LV SEM (JEOL Instruments Inc., Tokyo, Japan) at 15 kV.

Statistical Analysis

Statistical analyses were performed using Origin. Data are shown as the mean ± standard deviation (SD), and the results were from at least three experiments. Analysis of significance (ANOVA) followed by the Duncan multiple ranges test was applied using the SPSS software to determine the significant differences at 99% confidence intervals. Data were considered to be statistically different when $^{*}p < 0.05$, $^{**}p < 0.01$, and $^{***}p < 0.001$.

Bioinformatics Analysis

The molecular weight (MW) and theoretical isoelectric points (pI) of W1 were calculated by the Expert Protein Analysis System (ExPASy; ProParam[2]). The secondary structure was analyzed using online bioinformatics tools at the website of NovoPro.[3] The three-dimensional structure prediction of a peptide was performed using PEP-FOLD3.[4]

RESULTS

Identification of the Strain W0101 With Antifungal Activity

An antifungal strain W0101 was isolated from a sediment sample (168°09′41″W, 69°13′37″N) collected from the Arctic Ocean during the sixth Chinese National Arctic Expedition. The fermentation supernatants of W0101 culture showed obvious inhibitory activity against 9 plant pathogenic fungi, including *A. longipes*, *A. gaisen*, *B. dothidea*, *C. gloeosporioides*, *F. oxysporum*, *P. variotii*, *P. amygdali*, *R. solani* Kühn, and *S. sclerotiorum* (**Figure 1** and **Supplementary Figure 1**). The diameters of the inhibition zone ranged from 17 to 34 mm (**Supplementary Table 1**).

The 16S rDNA sequence of the strain W0101 (NZ_CP090477, locus_tag = LXM91_00040) showed the highest identity of 99.651, 99.65, and 99.65% with that of *Bacillus velezensis* strain CBMB205 (NR_116240.1), *B. amyloliquefaciens* strain NBRC 15535 (NR_041455.1), and *B. amyloliquefaciens* strain MPA 1034 (NR_117946.1), respectively (**Supplementary Table 2**). The phylogenetic tree based on the 16S rDNA sequences also showed that the strain W0101 gathered into one branch with *Bacillus siamensis* strain PD-A10 and *B. velezensis* strain CBMB205 (**Figure 2**). These results indicated that the strain W0101 was classified as *Bacillus*.

[2]http://web.expasy.org/protparam/

[3]https://novopro.cn/tools/secondary-structure-prediction.html

[4]https://mobyle.rpbs.univ-paris-diderot.fr

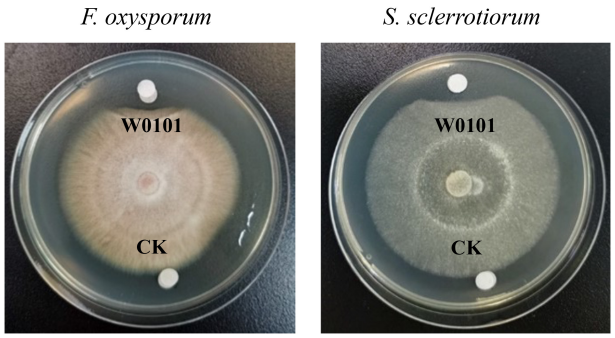

FIGURE 1 | The antifungal activity of the strain W0101 against *Fusarium oxysporum* and *Sclerotinia sclerotiorum*. W0101, culture supernatant of W0101; CK, LB medium as control.

To further confirm the taxonomy of the strain W0101, the complete genome of the strain W0101 was sequenced (Accession no. NZ_CP090477) and used to perform the analysis of average nucleotide identity (ANI). The ANIm value between the strain W0101 and *B. amyloliquefaciens* strain B15 (NZ_CP014783.1) was up to 99.14%, suggesting that the strain W0101 was a *B. amyloliquefaciens* isolate from the Arctic Ocean (**Table 1**).

TABLE 1 | OrthoANI analysis for the strain W0101.

Bacterial strains	Accession no.	ANIm (%)
Bacillus amyloliquefaciens strain B15	NZ_CP014783.1	99.1423
Bacillus velezensis strain BIM B-439D	NZ_CP032144.1	98.7148
Bacillus vallismortis strain NBIF-001	NZ_CP020893.1	98.2246
Bacillus velezensis strain YB-130	NZ_CP054562.1	98.2184
Bacillus amyloliquefaciens strain MBE1283	NZ_CP013727.1	97.8043
Bacillus velezensis strain FJAT-45028	NZ_CP047157.1	97.7934
Bacillus amyloliquefaciens strain DH8030	NZ_CP041770.1	97.7633
Bacillus atrophaeus strain BA59	NZ_CP024051.1	77.6409

Purification of an Antifungal Peptide

The antifungal protein was extracted from the fermentation supernatants of the strain W0101 by salting out at 40% saturation of ammonium sulfate. The crude protein exhibited the strongest antifungal activity against *F. oxysporum* (**Figure 3A**), and was further purified using a two-step ion exchange chromatography. After loading on the DEAE Sepharose Fast Flow column, the crude protein was isolated into three major fractions (D0, D1, and D2; **Figure 3B**), of which fraction D2 was found to possess mighty antimicrobial activity against *F. oxysporum* and *S. sclerotiorum* (**Figures 3C,D**). The result of SDS-PAGE showed that the fraction D2 contained two distinct protein bands with a molecular mass of less than 10 kDa (**Figure 3E**).

Subsequently, three major components (Q0, Q1 and Q2) were separated from the bioactive fraction D2 with the Q Sepharose Fast Flow column (**Figure 4A**), and component Q1 showed antimicrobial activity against *F. oxysporum* and *S. sclerotiorum* by plate inhibition test (**Figures 4B,C**). Component Q1 contained only a single protein band with a molecular weight of less than 3 kDa on the SDS-PAGE, corresponding to one of the two bands of fraction D2 (**Figure 4D**). Finally, the antifungal component Q1 was analyzed on a RP-HPLC, and a unique peak appeared at a retention time of 27.933 min compared with the standard of the buffer solution (**Supplementary Figure 2**).

Mass Spectrometry Analysis and Identification of W1

By LC-MS/MS analysis, W1 was identified as a peptide composed of 21 amino acid residues. This peptide completely matched a partial N-terminal sequence (G5 to Q26) of

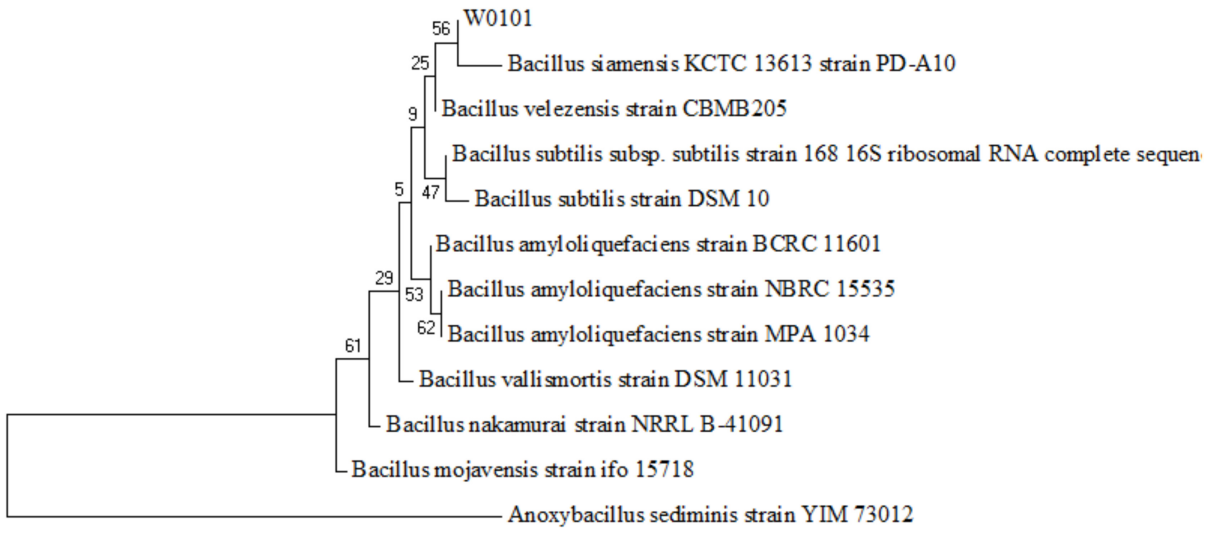

FIGURE 2 | Phylogenetic tree of the strain W0101 based on the 16S rRNA gene sequences. The tree is constructed with the maximum likelihood estimate method by the MEGA 7 software. The numbers on the nodules represent frequency of 1,000 bootstrap replicates.

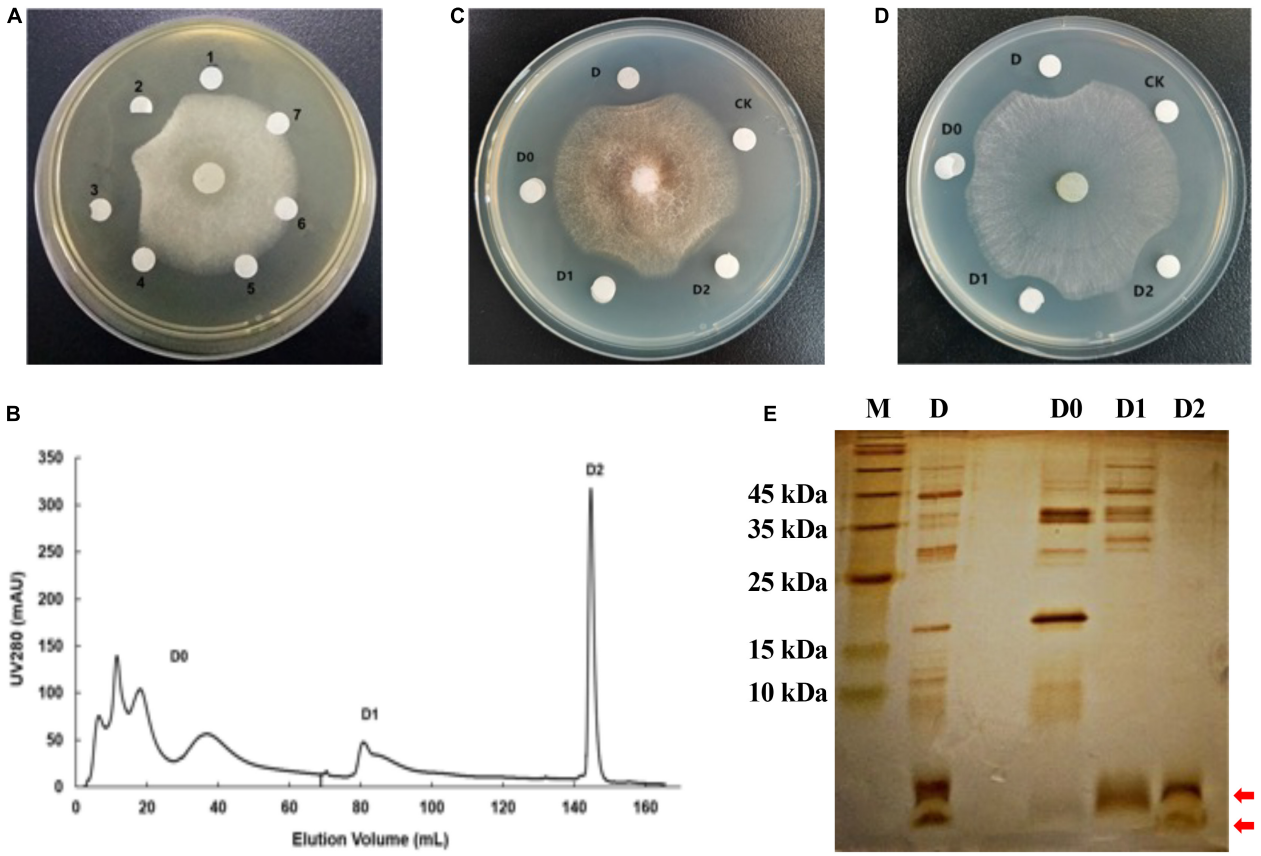

FIGURE 3 | Purification of antifungal protein by DEAE Sepharose Fast Flow column. **(A)** The antifungal activity of crude proteins salted out at six concentrations of ammonium sulfate against *F. oxysporum*. The numbers 1–7 represent the crude proteins salted out at 0, 20, 40, 60, 80, and 100% of ammonium sulfate, respectively. The number 7 represents the fermentation supernatant without protein. **(B)** Chromatographic profile of crude proteins of the strain W0101 extract on HiTrap DEAE Sepharose Fast Flow column using AKTA pure 25 system. **(C)** The antifungal activity of several fractions from crude protein against *F. oxysporum*. **(D)** The antifungal activity of several fractions from crude protein against *S. sclerotiorum*. **(E)** 15% SDS-PAGE profile of several fractions in the separation of crude proteins. The red arrows show the two distinct protein bands of fraction D2.

preprotein translocase subunit YajC of *B. amyloliquefaciens* W0101 (GenBank accession no. UOI89425.1; **Table 2** and **Figure 5A**). The speculated molecular weight of W1 was 2,416.432 Da, consistent with the result of W1 electrophoresis (**Figure 4D**). The secondary structure analysis showed that W1 was a helical peptide and rich in hydrophobic amino acid residues, but contained a cationic, hydrophilic arginine in the C-terminal (**Figure 5A**). The three-dimensional structure of W1 predicted using PEP-FOLD3 also showed a helical structure, which was in agreement with the result of the secondary structure analysis (**Supplementary Figure 3**). These results indicated that W1 might be a peptide fragment cleaved from the YajC protein.

To further identify W1, we artificially synthesized W1 (sW1). As shown in **Figure 5B**, the synthesized peptide showed significant antifungal activity compared with the control group, which was lower than that of purified peptide W1.

Antifungal Mechanism of W1

To investigate the antifungal mechanism of W1 on plant pathogenic fungi, scanning electron microscopy (SEM) was used to examine the effect of W1 on the morphology of the mycelium of *F. oxysporum*. After W1 treatment, the cell surface of hyphae was highly roughened and shriveled, while untreated hyphae cells were intact and smooth (**Figure 6**). Similar morphological changes of hyphae were also observed in *S. sclerotiorum* treated with W1 (**Supplementary Figure 4**). These results suggest that W1 could destroy the cell walls of hyphae of pathogenic fungi.

Physiochemical Properties of Antifungal Protein W1

The antifungal activity of the purified W1 against *F. oxysporum* was decreased by less than 10% when incubating at 40, 60, and 80°C for 20 min, whereas its antifungal activity was approximately retained at 75, 50%, and completely lost after incubating at 100, 110, and 121°C for 20 min, respectively (**Figure 7A**). W1 also had a higher antifungal ability against *F. oxysporum* at pH 6–11, but its antifungal activity was significantly weakened at pH 4.0 and pH 5.0 and rapidly lost at pH 3.0 (**Figure 7B**). The highest antibacterial activity of W1 protein against *F. oxysporum* was found to be at pH 9.0.

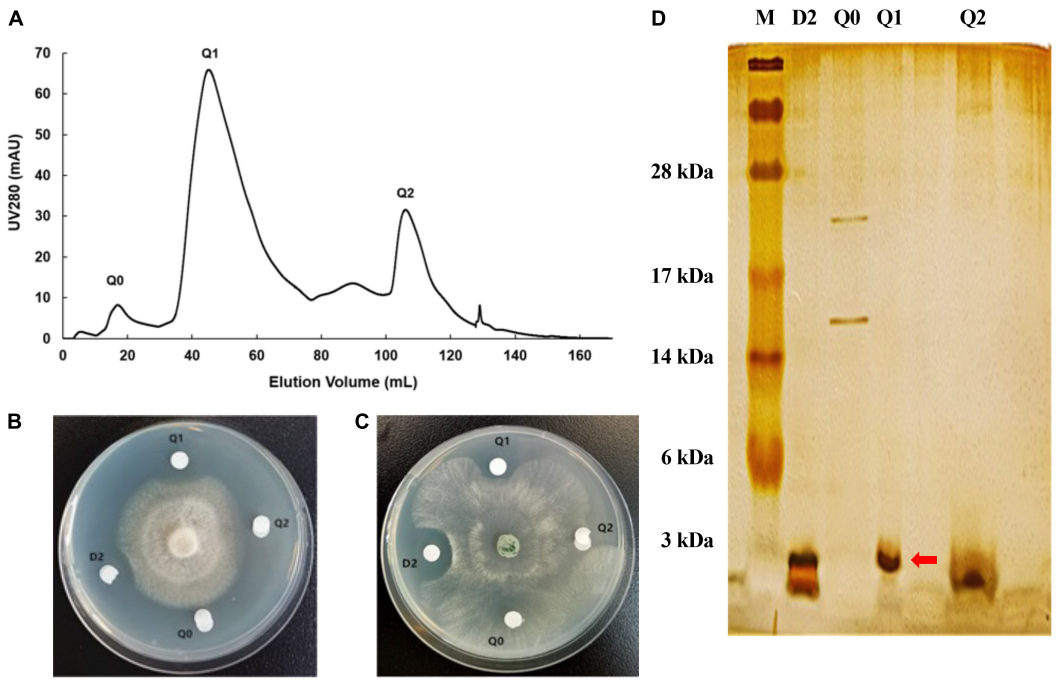

FIGURE 4 | Purification of antifungal protein by Q Sepharose Fast Flow column. **(A)** Chromatographic profile of D2 from DEAE separation on HiTrap Q Sepharose Fast Flow column using AKTA pure 25 system. **(B)** The antifungal activity of several fractions from component D2 against *F. oxysporum*. **(C)** The antifungal activity of several fractions from D2 against *S. sclerotiorum*. **(D)** 15% SDS-PAGE profile of several fractions from Q2. The red arrow shows the distinct protein band of component Q1.

TABLE 2 | Mass spectrum identification of W1.

Peptide sequence	Length	Mass (Da)	Matched protein	Protein ID in database*	Unique sequence coverage (%)	Score
GTIVPIILMFAVLYFLLIRPQ	21	2416.432	YajC	UOI89425.1	24.40%	128.97

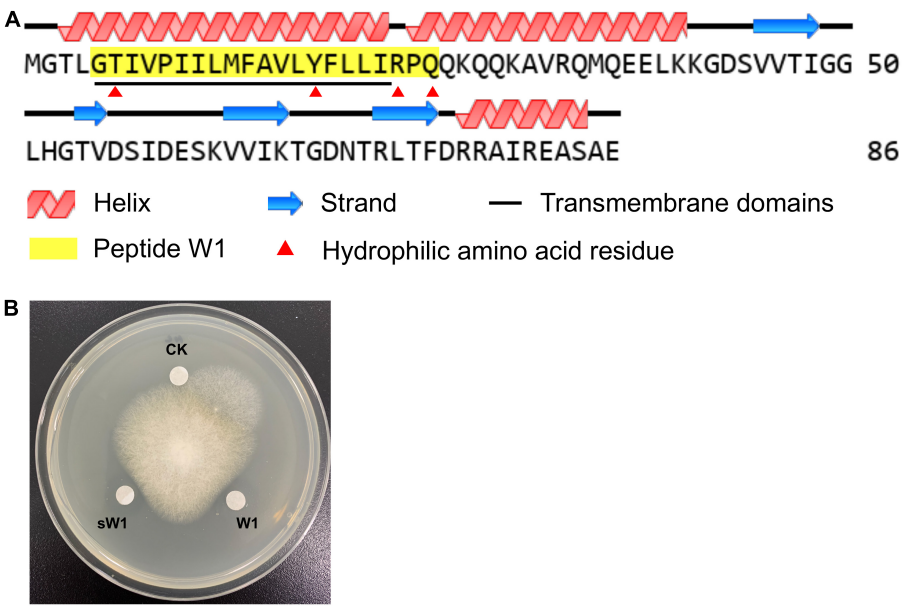

FIGURE 5 | The structure and antifungal activity of W1. **(A)** Protein structure analysis of YajC and W1. The GenBank database reference number of YajC was UOI89425.1. **(B)** The antifungal activity of purified peptide (W1) and synthesized peptide (sW1) against *F. oxysporum*.

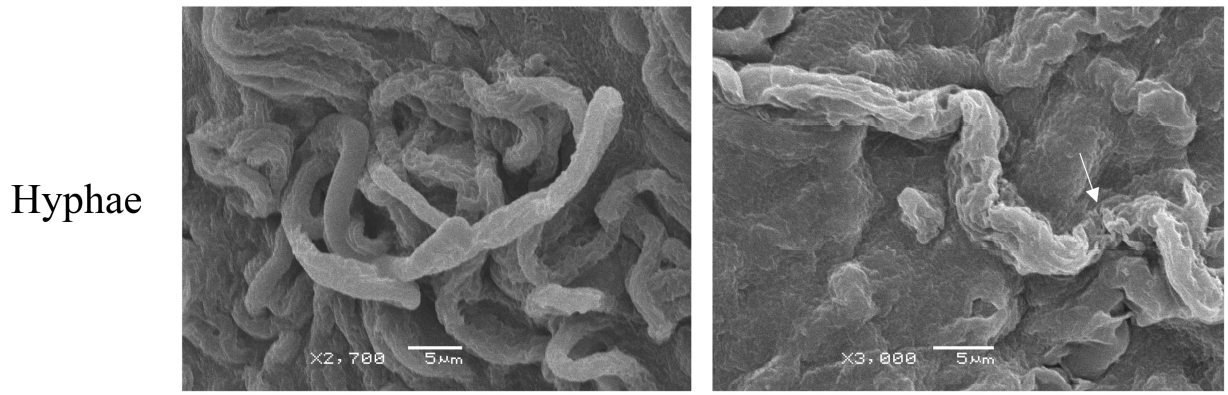

FIGURE 6 | Scanning electron microscopy observation of hyphae of *F. oxysporum* treated with W1. The mycelium of *F. oxysporum* was treated with the purified W1 (160 μg/ml) at 30°C for 24 h, while treated with PBS as control. Images was observed and captured using a JSM-6380LV SEM (JEOL Instruments Inc., Japan) at 15 kV. The white arrows represent the morphological deformation in hyphae when treated with W1.

Moreover, the antifungal activity of the purified W1 was not influenced by 20 mM Na^+ and K^+ and retained at least 70% with 20 mM Mg^{2+}, Ca^{2+}, Mn^{2+}, and Ba^{2+}. However, the antifungal activity was completely inhibited by 6 mM Fe^{2+} and Cu^{2+} (**Figure 7C**). It was also found that 1 mg/ml proteinase K, trypsin, and papain all showed no inhibitory effect on the antifungal activity of W1 (**Figure 7D**). Finally, the MICs of purified W1 against *F. oxysporum* and *S. sclerotiorum* were determined to be 58 and 140 μg/ml, respectively.

DISCUSSION

Fungal diseases have been posing a great threat to the agricultural industry. With the increasingly strict regulation of chemical fungicides, antifungal microorganisms and their metabolites are considered more and more important for controlling plant fungal diseases. In this study, a bacterial strain W0101 isolated from a sediment sample in the Arctic Ocean showed significant antifungal activity. After taxonomic identification, the strain W0101 was classified into *B. amyloliquefaciens*. *B. amyloliquefaciens* is a gram-positive, endospore-forming, and rod-shaped bacterium, which was identified as a new species of *Baccillus* in 1987 (Priest et al., 1987). In the past few decades, many strains of *B. amyloliquefaciens* have been isolated from soil, plants, food, fresh water, and marine water (Chen et al., 2009; Lee et al., 2016; Boottanun et al., 2017; Cui et al., 2017; Yang et al., 2021). Several isolates of *B. amyloliquefaciens* have exhibited their application potential as plant growth promoters, probiotics, and antibiotics. As effective candidates of biocontrol microorganisms in agriculture, *B. amyloliquefaciens* Pc3, S185, PT14, Rdx5, FZB42, and SWB16 suppressed the growth of many fungal or bacterial pathogens, such as *A. longipes*, *C. gloeosporioides*, and *F. oxysporum* (Chen et al., 2009; Wang et al., 2014; Kim et al., 2015; Ding et al., 2019; Dong et al., 2019; Singh et al., 2021). *B. amyloliquefaciens* W0101 isolated here could suppress 9 pathogenic fungi, such as *A. longipes*, *C. gloeosporioides*, *F. oxysporum*, *S. sclerotiorum*, and *P. amygdali*, showing a broad spectrum of antifungal activity. Thus, *B. amyloliquefaciens* W0101 may be a potential source for the development of biocontrolling agents for plant fungal diseases.

Generally, the antifungal substances produced by *B. amyloliquefaciens* include antifungal proteins, peptides, and small molecular compounds (Li et al., 2021). It has been found that *B. amyloliquefaciens* Pc3 produced 11 lipopeptide compounds and a small molecular compound (isotryptophan) with antifungal activity against *R. solani* (Cui et al., 2017; Ding et al., 2019). *B. amyloliquefaciens* SWB16 also produced fengicin and iturin to suppress the growth of *B. bassiana* (Wang et al., 2014). Moreover, Wang et al. (2002) purified and characterized two antifungal chitinases from *B. amyloliquefaciens* V656, which displayed inhibitory activity on fungal growth. In this study, a 2.4 kDa antifungal peptide, tentatively named W1, was isolated from the fermentation supernatants of the strain W0101. However, the amino acid sequence of W1 only matched with a partial sequence of YajC protein of W0101 by mass spectrometry identification. The sequence analysis showed that W1 was located in the transmembrane helix region of YajC protein, which is a small integral membrane protein with a single transmembrane helix (Fang and Wei, 2011). It is a subunit of the bacterial translocase that transports the majority of secretory proteins across and inserts most membrane proteins into the bacterial cytoplasmic membrane (Fang and Wei, 2011). However, there have not been any reports that the YajC protein is associated with antifungal activity. Thus, we speculated that W1 might be a novel antifungal peptide formed by the proteolysis of YajC protein.

In recent years, many studies have reported the biological activities of peptide fragments derived from physiological precursor proteins (Ciociola et al., 2016). It is currently established that many proteins can release the functional units that are endowed with biological activities different or similar to those of the precursor protein (Ciociola et al., 2016).

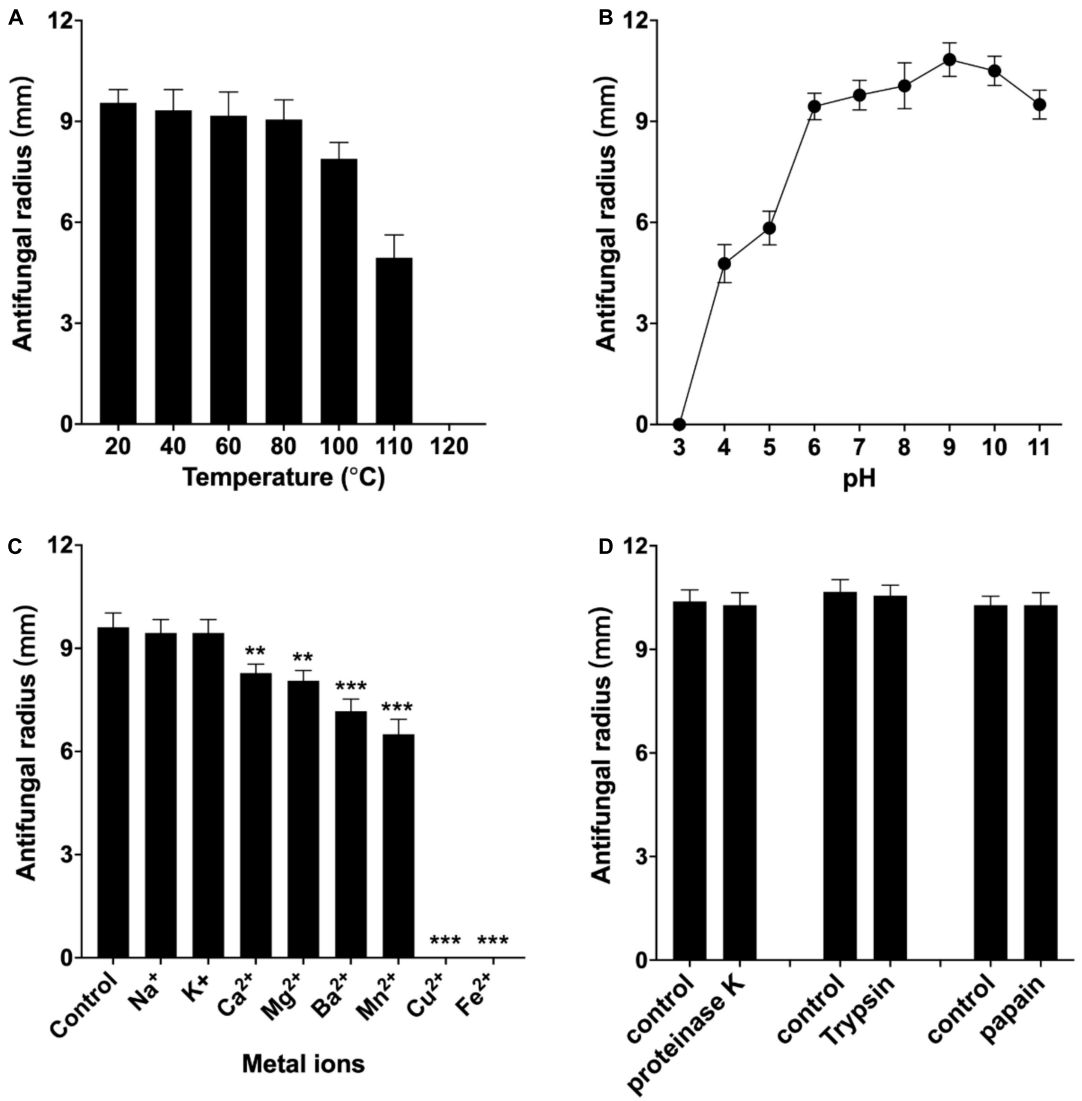

FIGURE 7 | Effect of temperature **(A)**, pH **(B)**, metal ions **(C)**, and proteases **(D)** on antifungal activity of the purified peptide W1 against *F. oxysporum*. The purified W1 with a concentration of 160 μg/ml was used in all assays, which were repeated three times independently. The results are presented as mean ± SD, and representative images are shown. $^{**}p < 0.01$, $^{***}p < 0.001$ vs. normal group.

Many anionic antimicrobial peptides, such as bovine enkelytin and dermcidin, are peptide fragments cleaved from precursor proteins without antimicrobial activity (Harris et al., 2009; Schittek, 2012; Sowa-Jasiłek et al., 2020). A typical example was bovine hemoglobin, which could produce 26 antimicrobial peptides by controlled hydrolysis (Adje et al., 2011). A recent study also reported that a novel peptide CGA-N46 derived from the N-terminus of human Chromogranin A could suppress various *Candida* spp. (Li et al., 2015). In this study, the amino acid sequence of W1 completely matched the part of the N-terminal sequence of YajC protein, indicating that W1 may not be encoded by a bacterial biosynthetic gene of *B. amyloliquefaciens* W0101. We speculated that W1 may be produced by YajC proteolysis, but the details of W1 production need to be further investigated. The three-dimensional structure prediction proposes that W1 is a hydrophobic α-helix peptide with a hydrophilic and cationic arginine residue located at its C-terminal extremity. This amphiphilic structural feature was present in many natural antifungal peptides, such as magainin and cecropins, and made them interact with the lipid bilayer of pathogenic fungal cells (Jin et al., 2005). Thus, these antifungal peptides could inhibit mycelial growth or break the hyphae or spores (Li et al., 2021). It has been found that the α-helix peptide PT14-4a derived from *B. amyloliquefaciens* PT14 causes severe morphological deformation in the conidia and hyphae of *F. solani* and *F. oxysporum* (Kim et al., 2015). The antifungal peptide EP-2, produced by *B. subtilis* E1R-J, can swell and distort the mycelium of the fungi (Wang et al., 2016). Similarly, the SEM observation showed that W1 also ruptured the hyphae of the pathogenic fungi, suppressing the growth of the fungi.

In addition to potent activity, W1 also exhibits remarkable stability of antifungal activity. Its activity remains stable after heating at 100°C–110°C or treatment with solutions of pH 4 and 11. Besides, W1 showed higher tolerance to a variety of proteases against *F. oxysporum*. These characteristics were better than the antifungal peptides produced by *B. amyloliquefaciens* S185, PT14, and *B. velezensis* HNAH 17806 (Kim et al., 2015; Singh et al., 2021; Wang et al., 2021), indicating that W1 has superior application potential in the biocontrol of plant diseases.

DATA AVAILABILITY STATEMENT

The datasets presented in this study can be found in online repositories. The names of the repository/repositories and accession number(s) can be found below: https://www.ncbi.nlm.nih.gov/genbank/, NZ_CP090477.1.

AUTHOR CONTRIBUTIONS

QW performed most of the experiments, analyzed the data, and wrote the manuscript. TH helped with study of antifungal mechanisms and wrote the manuscript. RL help with experimental operations. ZO performed the supplementary SEM observation for manuscript revision. WZ designed the experiments. XC designed the research and revised the manuscript. All authors contributed to the article and approved the submitted version.

FUNDING

This study was supported by the China Ocean Mineral Resources R&D Association program (DY135-B2-16), the China Agriculture Research System of MOF and MARA (CARS-47), the Natural Science Foundation of Fujian Province (2019J05043), and the "Double first-class" scientific and technological innovation capacity and enhancement cultivation plan of Fujian Agriculture and Forestry University (Grant KSYLP001).

SUPPLEMENTARY MATERIAL

The Supplementary Material for this article can be found online at: https://www.frontiersin.org/articles/10.3389/fmicb.2022.922454/full#supplementary-material

REFERENCES

Adje, E. Y., Balti, R., Kouach, M., Dhulster, P., Guillochon, D., and Nedjar-Arroume, N. (2011). Obtaining antimicrobial peptides by controlled peptic hydrolysis of bovine hemoglobin. *Int. J. Biol. Macromol.* 49, 143–153. doi: 10.1016/j.ijbiomac.2011.04.004

Ajilogba, C. F., and Babalola, O. O. (2013). Integrated management strategies for tomato Fusarium wilt. *Biocont. Sci.* 18, 117–127. doi: 10.4265/bio.18.117

Boottanun, P., Potisap, C., Hurdle, J. G., and Sermswan, R. W. (2017). Secondary metabolites from *Bacillus amyloliquefaciens* isolated from soil can kill *Burkholderia pseudomallei*. *AMB Exp.* 7:16. doi: 10.1186/s13568-016-0302-0

Chang, W. T., Chen, Y. C., and Jao, C. L. (2007). Antifungal activity and enhancement of plant growth by *Bacillus cereus* grown on shellfish chitin wastes. *Bioresour. Technol.* 98, 1224–1230. doi: 10.1016/j.biortech.2006.05.005

Chen, X. H., Koumoutsi, A., Scholz, R., Schneider, K., Vater, J., Sussmuth, R., et al. (2009). Genome analysis of *Bacillus amyloliquefaciens* FZB42 reveals its potential for biocontrol of plant pathogens. *J. Biotechnol.* 140, 27–37. doi: 10.1016/j.jbiotec.2008.10.011

Chen, Z., Ao, J., Yang, W., Jiao, L., Zheng, T., and Chen, X. (2013). Purification and characterization of a novel antifungal protein secreted by *Penicillium chrysogenum* from an Arctic sediment. *Appl. Microbiol. Biotechnol.* 97, 10381–10390. doi: 10.1007/s00253-013-4800-6

Ciociola, T., Giovati, L., Conti, S., Magliani, W., Santinoli, C., and Polonelli, L. (2016). Natural and synthetic peptides with antifungal activity. *Future Med. Chem.* 8, 1413–1433. doi: 10.4155/fmc-2016-0035

Cui, P., Guo, W., and Chen, X. (2017). Isotryptophan from Antarctic *Bacillus amyloliquefaciens* Pc3: purification, identification, characterization, and antifungal activity. *Nat. Prod. Res.* 31, 2153–2157. doi: 10.1080/14786419.2016.1274896

Dhanasekaran, D., Thajuddin, N., and Panneerselvam, A. (2012). "Applications of actinobacterial fungicides in agriculture and medicine," in *Fungicides for Plant and Animal Diseases*, ed. D. D. Dhanasekaran (London: IntechOpen), 29–54.

Ding, L., Guo, W., and Chen, X. (2019). Exogenous addition of alkanoic acids enhanced production of antifungal lipopeptides in *Bacillus amyloliquefaciens* Pc3. *Appl. Microbiol. Biotechnol.* 103, 5367–5377. doi: 10.1007/s00253-019-09792-1

Ding, L., Zhang, S., Guo, W., and Chen, X. (2018). Exogenous indole regulates lipopeptide biosynthesis in Antarctic *Bacillus amyloliquefaciens* Pc3. *J. Microbiol. Biotechnol.* 28, 784–795. doi: 10.4014/jmb.1712.12014

Dong, Y., Li, H., Rong, S., Xu, H., Guan, Y., Zhao, L., et al. (2019). Isolation and evaluation of *Bacillus amyloliquefaciens* Rdx5 as a potential biocontrol agent against *Magnaporthe oryzae*. *Biotechnol. Biotechnol. Equip.* 33, 408–418.

Fang, J., and Wei, Y. (2011). Expression, purification and characterization of the *Escherichia coli* integral membrane protein YajC. *Protein Pept. Lett.* 18, 601–608. doi: 10.2174/092986611795222713

Fisher, M. C., Hawkins, N. J., Sanglard, D., and Gurr, S. J. (2018). Worldwide emergence of resistance to antifungal drugs challenges human health and food security. *Science* 360, 739–742. doi: 10.1126/science.aap7999

Gao, W., Tian, L., Zhou, J., Shi, Z., Zheng, L., Cui, Z., et al. (2009). Antifungal mechanism of *Bacillus marinus* B-9987. *Acta Microbiol. Sin.* 49, 1494–1501.

Harris, F., Dennison, S. R., and Phoenix, D. A. (2009). Anionic antimicrobial peptides from eukaryotic organisms. *Curr. Protein Pept. Sci.* 10, 585–606. doi: 10.2174/138920309789630589

Hussein, H. S., and Brasel, J. M. (2001). Toxicity, metabolism, and impact of mycotoxins on humans and animals. *Toxicology* 167, 101–134. doi: 10.1016/s0300-483x(01)00471-1

Jin, Y., Hammer, J., Pate, M., Zhang, Y., Zhu, F., Zmuda, E., et al. (2005). Antimicrobial activities and structures of two linear cationic peptide families with various amphipathic β-sheet and α-helical potentials. *Antimicrob. Agents Chemother* 49, 4957–4964. doi: 10.1128/AAC.49.12.4957-4964.2005

Katoh, K., Misawa, K., Kuma, K., and Miyata, T. (2002). MAFFT: a novel method for rapid multiple sequence alignment based on fast Fourier transform. *Nucleic Acids Res.* 30, 3059–3066. doi: 10.1093/nar/gkf436

Kim, Y. G., Kang, H. K., Kwon, K. D., Seo, C. H., Lee, H. B., and Park, Y. (2015). Antagonistic activities of novel peptides from *Bacillus amyloliquefaciens* PT14 against *Fusarium solani* and *Fusarium oxysporum*. *J. Agric. Food Chem.* 63, 10380–10387. doi: 10.1021/acs.jafc.5b04068

Kumar, S., Stecher, G., and Tamura, K. (2016). MEGA7: molecular evolutionary genetics analysis version 7.0 for gigger datasets. *Mol. Biol. Evol.* 33, 1870–1874. doi: 10.1093/molbev/msw054

Kumar, V., and Kumar, P. (2019). "Pesticides in agriculture and environment: Impacts on human health," in *Contaminants in Agriculture and Environment: Health Risks and Remediation*, eds V. Kumar, R. Kumar, J. Singh, and P. Kumar (Haridwar, India: Publication Cell of AESA), 76–95.

Lee, J. Y., Shim, J. M., Yao, Z., Liu, X., Lee, K. W., Kim, H.-J., et al. (2016). Antimicrobial activity of *Bacillus amyloliquefaciens* EMD17 isolated from Cheonggukjang and potential use as a starter for fermented soy foods. *Food Sci. Biotechnol.* 25, 525–532.

Li, C., Wang, S., Ren, Q., He, T., and Chen, X. (2020). An outbreak of visceral white nodules disease caused by *Pseudomonas plecoglossicida* at a water temperature of 12 degrees C in cultured large yellow croaker (*Larimichthys crocea*) in China. *J. Fish Dis.* 43, 1353–1361. doi: 10.1111/jfd.13206

Li, R. F., Lu, Y. L., Lu, Y. B., Zhang, H. R., Huang, L., Yin, Y., et al. (2015). Antiproliferative effect and characterization of a novel antifungal peptide derived from human Chromogranin A. *Exp. Ther. Med.* 10, 2289–2294. doi: 10.3892/etm.2015.2838

Li, T., Li, L., Du, F., Sun, L., Shi, J., Long, M., et al. (2021). Activity and mechanism of action of antifungal peptides from microorganisms: a review. *Molecules* 26:3438. doi: 10.3390/molecules26113438

Montesinos, E. (2007). Antimicrobial peptides and plant disease control. *FEMS Microbiol. Lett.* 270, 1–11. doi: 10.1111/j.1574-6968.2007.00683.x

Núñez-Montero, K., and Barrientos, L. (2018). Advances in Antarctic research for antimicrobial discovery: a comprehensive narrative review of bacteria from Antarctic environments as potential sources of novel antibiotic compounds against human pathogens and microorganisms of industrial importance. *Antibiotics* 7:90. doi: 10.3390/antibiotics7040090

Ongena, M., and Jacques, P. (2008). *Bacillus* lipopeptides: versatile weapons for plant disease biocontrol. *Trends Microbiol.* 16, 115–125. doi: 10.1016/j.tim.2007.12.009

Priest, F., Goodfellow, M., Shute, L., and Berkeley, R. (1987). *Bacillus amyloliquefaciens* sp. nov., nom. rev. *Int. J. Syst. Evol. Microbiol.* 37, 69–71.

Rao, Q., Guo, W., and Chen, X. (2015). Identification and characterization of an antifungal protein, AfAFPR9, produced by marine-derived *Aspergillus fumigatus* R9. *J. Microbiol. Biotechnol.* 25, 620–628. doi: 10.4014/jmb.1409.09071

Richter, M., and Rossello-Mora, R. (2009). Shifting the genomic gold standard for the prokaryotic species definition. *Proc. Natl. Acad. Sci. U.S.A.* 106, 19126–19131. doi: 10.1073/pnas.0906412106

Roy, T., Bandopadhyay, A., Sonawane, P. J., Majumdar, S., Mahapatra, N. R., Alam, S., et al. (2018). Bio-effective disease control and plant growth promotion in lentil by two pesticide degrading strains of *Bacillus sp. Biol. Control* 127, 55–63. doi: 10.1016/j.biocontrol.2018.08.018

Schittek, B. (2012). The multiple facets of dermcidin in cell survival and host defense. *J. Innate. Immun.* 4, 349–360. doi: 10.1159/000336844

Sharma, A., Shukla, A., Attri, K., Kumar, M., Kumar, P., Suttee, A., et al. (2020). Global trends in pesticides: a looming threat and viable alternatives. *Ecotox. Environ. Saf.* 201:110812. doi: 10.1016/j.ecoenv.2020.110812

Shoaib, A., Akhtar, N., Akhtar, S., and Hafeez, R. (2014). First report of Alternaria longipes causing leaf spot of potato cultivar sante in Pakistan. *Plant Dis.* 98, 1742–1742. doi: 10.1094/PDIS-05-14-0539-PDN

Singh, P., Xie, J., Qi, Y., Qin, Q., Jin, C., Wang, B., et al. (2021). A thermotolerant marine *Bacillus amyloliquefaciens* S185 producing iturin A5 for antifungal activity against *Fusarium oxysporum* f. sp. cubense. *Mar. Drugs* 19:516. doi: 10.3390/md19090516

Someya, N. (2008). Biological control of fungal plant diseases using antagonistic bacteria. *J. Gen. Plant Pathol.* 74, 459–460.

Sowa-Jasiłek, A., Zdybicka-Barabas, A., Stączek, S., Pawlikowska-Pawlęga, B., Grygorczuk-Płaneta, K., Skrzypiec, K., et al. (2020). Antifungal activity of anionic defense peptides: insight into the action of *Galleria mellonella* anionic peptide 2. *Int. J. Mol. Sci.* 21:1912. doi: 10.3390/ijms21061912

Styczynski, M., Biegniewski, G., Decewicz, P., Rewerski, B., Debiec-Andrzejewska, K., and Dziewit, L. (2022). Application of psychrotolerant Antarctic bacteria and their metabolites as efficient plant growth promoting agents. *Front. Bioeng. Biotechnol.* 10:772891. doi: 10.3389/fbioe.2022.772891

Talbot, N. J. (2003). On the trail of a cereal killer: exploring the biology of *Magnaporthe grisea*. *Annu. Rev. Microbiol.* 57, 177–202. doi: 10.1146/annurev.micro.57.030502.090957

Tyanova, S., Temu, T., and Cox, J. (2016). The MaxQuant computational platform for mass spectrometry-based shotgun proteomics. *Nat. Protoc.* 11, 2301–2319. doi: 10.1038/nprot.2016.136

Waewthongrak, W., Pisuchpen, S., and Leelasuphakul, W. (2015). Effect of *Bacillus subtilis* and chitosan applications on green mold (*Penicilium digitatum* Sacc.) decay in citrus fruit. *Postharvest Biol. Technol.* 99, 44–49. doi: 10.1016/j.postharvbio.2014.07.016

Wang, C., Ye, X., Ng, T. B., and Zhang, W. (2021). Study on the biocontrol potential of antifungal peptides produced by *Bacillus velezensis* against *Fusarium solani* that infects the passion fruit *Passiflora edulis*. *J. Agric. Food Chem.* 69, 2051–2061. doi: 10.1021/acs.jafc.0c06106

Wang, C.-J., Wang, Y.-Z., Chu, Z.-H., Wang, P.-S., Liu, B.-Y., Li, B.-Y., et al. (2020). Endophytic *Bacillus amyloliquefaciens* YTB1407 elicits resistance against two fungal pathogens in sweet potato (*Ipomoea batatas* (L.) Lam.). *J. Plant Physiol.* 253:153260. doi: 10.1016/j.jplph.2020.153260

Wang, J., Zhao, D., Liu, Y., Ao, X., Fan, R., Duan, Z., et al. (2014). Antagonism against *Beauveria bassiana* by lipopeptide metabolites produced by entophyte *Bacillus amyloliquefaciens* strain SWB16. *Acta Microbiol. Sin.* 54, 778–785.

Wang, N. N., Yan, X., Gao, X. N., Niu, H. J., Kang, Z. S., and Huang, L. L. (2016). Purification and characterization of a potential antifungal protein from *Bacillus subtilis* E1R-J against Valsa mali. *World J. Microbiol. Biotechnol.* 32:63. doi: 10.1007/s11274-016-2024-5

Wang, S. L., Shih, I. L., Liang, T. W., and Wang, C. H. (2002). Purification and characterization of two antifungal chitinases extracellularly produced by *Bacillus amyloliquefaciens* V656 in a shrimp and crab shell powder medium. *J. Agric. Food Chem.* 50, 2241–2248. doi: 10.1021/jf010885d

Wen, C., Guo, W., and Chen, X. (2014). Purification and identification of a novel antifungal protein secreted by *Penicillium citrinum* from the Southwest Indian Ocean. *J. Microbiol. Biotechnol.* 24, 1337–1345. doi: 10.4014/jmb.1405.05008

Wu, Y., Guo, W., Zhao, J., Ding, L., and Chen, X. (2018). Isolation and identification of a novel LCI like antibacterial protein from *Bacillus sp.* MD-5 reveals its potential application in controlling *Staphylococcus aureus* in food industry. *Food Control* 89, 142–149.

Yan, J., Yuan, S.-S., Jiang, L.-L., Ye, X.-J., Ng, T. B., and Wu, Z.-J. (2015). Plant antifungal proteins and their applications in agriculture. *Appl. Microbiol. Biotechnol.* 99, 4961–4981. doi: 10.1007/s00253-015-6654-6

Yang, Y., Xia, J., Liu, Y., Dong, J., Xu, N., Yang, Q., et al. (2021). Safety evaluation for the use of *Bacillus amyloliquefaciens* in freshwater fish cultures. *Aquac Rep* 21, 100822.

Zhao, X., Zhou, Z. J., Han, Y., Wang, Z. Z., Fan, J., and Xiao, H. Z. (2013). Isolation and identification of antifungal peptides from *Bacillus* BH072, a novel bacterium isolated from honey. *Microbiol Res* 168, 598–606. doi: 10.1016/j.micres.2013.03.001

Conflict of Interest: The authors declare that the research was conducted in the absence of any commercial or financial relationships that could be construed as a potential conflict of interest.

Publisher's Note: All claims expressed in this article are solely those of the authors and do not necessarily represent those of their affiliated organizations, or those of the publisher, the editors and the reviewers. Any product that may be evaluated in this article, or claim that may be made by its manufacturer, is not guaranteed or endorsed by the publisher.

frontiers | Frontiers in Microbiology

ORIGINAL RESEARCH
published: 20 June 2022
doi: 10.3389/fmicb.2022.918491

The Molecular Mechanism of Yellow Mushroom (*Floccularia luteovirens*) Response to Strong Ultraviolet Radiation on the Qinghai-Tibet Plateau

Jing Guo[1,2†], Zhanling Xie[1,2†], Hongchen Jiang[3,4], Hongyan Xu[1,5], Baolong Liu[6], Qing Meng[1,2], Qingqing Peng[1,2], Yongpeng Tang[7] and Yingzhu Duan[8]*

[1] College of Ecological and Environment Engineering, Qinghai University, Xining, China, [2] State Key Laboratory Breeding Base for Innovation and Utilization of Plateau Crop Germplasm, Qinghai University, Xining, China, [3] State Key Laboratory of Biogeology and Environmental Geology, China University of Geosciences, Wuhan, China, [4] Qinghai Provincial Key Laboratory of Geology and Environment of Salt Lakes, Qinghai Institute of Salt Lakes, Chinese Academy of Sciences, Xining, China, [5] Academy of Agriculture and Forestry Sciences, Qinghai University, Xining, China, [6] Key Laboratory of Adaptation and Evolution of Plateau Biota, Northwest Institute of Plateau Biology, Chinese Academy of Sciences, Xining, China, [7] Bureau of Forestry and Grassland, Delingha, China, [8] Test Station for Grassland Improvement, Xining, China

OPEN ACCESS

Edited by:
Xian-Wen Yang, Ministry of Natural Resources, China

Reviewed by:
Li Taotao, South China Botanical Garden (CAS), China
Yuan Sui, Chongqing University of Arts and Sciences, China

***Correspondence:**
Zhanling Xie
xiezhanling2012@126.com

[†] These authors have contributed equally to this work and share first authorship

Specialty section:
This article was submitted to Extreme Microbiology, a section of the journal Frontiers in Microbiology

Received: *12 April 2022*
Accepted: *17 May 2022*
Published: *20 June 2022*

Citation:
Guo J, Xie Z, Jiang H, Xu H, Liu B, Meng Q, Peng Q, Tang Y and Duan Y (2022) The Molecular Mechanism of Yellow Mushroom (Floccularia luteovirens) Response to Strong Ultraviolet Radiation on the Qinghai-Tibet Plateau. Front. Microbiol. 13:918491. doi: 10.3389/fmicb.2022.918491

The Qinghai-Tibet Plateau (QTP) is the highest plateau in the world, and its ultraviolet (UV) radiation is much greater than that of other regions in the world. Yellow mushroom (*Floccularia luteovirens*) is a unique and widely distributed edible fungus on the QTP. However, the molecular mechanism of *F. luteovirens's* response to strong UV radiation remains unclear. Herein, we reported the 205 environmental adaptation and information processing genes from genome of *F. luteovirens*. In addition, we assembled the RNA sequence of UV-affected *F. luteovirens* at different growth stages. The results showed that in response to strong UV radiation, a total of 11,871 significantly different genes were identified, of which 4,444 genes in the vegetative mycelium (VM) stage were significantly different from the young fruiting bodies (YFB) stage, and only 2,431 genes in the YFB stage were significantly different from fruiting bodies (FB) stage. A total of 225 differentially expressed genes (DEGs) were found to be involved in environmental signal transduction, biochemical reaction preparation and stress response pathway, pigment metabolism pathway, and growth cycle regulation, so as to sense UV radiation, promote repair damage, regulate intracellular homeostasis, and reduce oxidative damage of UV radiation. On the basis of these results, a molecular regulation model was proposed for the response of *F. luteovirens* to strong UV radiation. These results revealed the molecular mechanism of adaptation of *F. luteovirens* adapting to strong UV radiation, and provided novel insights into mechanisms of fungi adapting to extreme environmental conditions on the QTP; the production the riboflavin pigment of the endemic fungi (Yellow mushroom) in the QTP was one of the response to extreme environment of the strong UV radiation.

Keywords: *Floccularia luteovirens*, strong UV radiation, molecular regulation model, riboflavin, chlorophyll, Qinghai-Tibet Plateau

INTRODUCTION

Ultravioet (UV) radiation is a component of solar radiation spectrum, which is the most harmful and mutagenic light band (Chen et al., 2021). UV can damage plant growth, development, biomass accumulation, and metabolism (Li et al., 2019a; Ozel et al., 2021). Plants have developed a series of strategies to cope with UV radiation, including activating light defense system, regulating light response pathway, and producing DNA photoproducts to mitigate DNA sequence changes and mutations caused by UV radiation (Azarafshan et al., 2020; Huarte-Bonnet et al., 2020). In addition, UV radiation will also activate the metabolic pathways of anthocyanin, carotenoid and melanin synthesis and anti-DNA oxidative damage system in plants, resulting in the accumulation of pigments such as anthocyanins, carotenoids, melanin, and riboflavin (Mapari et al., 2005; Gmoser et al., 2017; Qi et al., 2021; Zhu et al., 2021). In contrast for fungi, previous studies suggested that UV radiation would reduce the germination rate of conidia of *Magnaporthe oryzae*, and limited the population and diffusion of fungi in nature (Braga et al., 2015; Li et al., 2019a).

The Qinghai-Tibet Plateau (QTP) has the highest intensity of UV radiation in the world (Qiao et al., 2016). There are more than 1,500 kinds of fungi growing in the QTP alpine meadow ecosystem, among which yellow mushroom (*Floccularia luteovirens*) is one of the most flourish and representative macrofungi (Xing et al., 2017; Gan et al., 2020). In the alpine meadow of the QTP, our previous observation found that the wild fruiting bodies of *F. luteovirens* in high-UV environment were more yellowish brighter and showed more sulfur color than those in low-UV, and Liu et al. extracted riboflavin from yellow mushrooms fruiting bodies (Gan et al., 2022). However, the molecular adaptation mechanism of *F. luteovirens* in response to strong UV radiation remains unclear during its evolutionary process to extreme environment on QTP. In this work, we studied the gene expression of *F. luteovirens* at three growth stages [i.e., vegetative mycelium (VM) in lab, young fruiting body (YFB) in natural environment, fruiting body (FB) in natural environment] by using transcriptomics, and we also verified UV stress to cause the accumulation of the riboflavin and chlorophyll pigment in the vegetative mycelium, with the purpose to reveal the molecular adaptation mechanism of *F. luteovirens* to cope with strong UV radiation in the Qinghai-Tibet Plateau.

MATERIALS AND METHODS

Vegetative Mycelium and Fruiting Body Material

In August 2018, three wild fruiting bodies of *F. luteovirens* were collected to transcriptome sequencing from Haiyan County (100°47′13″E, 37°0′37″N), Qinghai Province, China for transcriptome sequencing (**Table 1**). The sampling area is 3,220 m above sea level, with annual sun light of 2517.6–2995.3 h and annual average radiation of 5210.2–6568.3 MJ/m^2 (Zhao Y. T. et al., 2021). According to the pileus diameter, the stage of *F. luteovirens* can be classified into young fruiting bodies (YFB, diameter 2.5–4.5 cm) and fruiting bodies (FB, diameter 4.5–6.6 cm), all of which samples were collected for transcriptome sequencing in three replicates. Vegetative mycelium (VM) was isolated from the fruiting bodies of *F. luteovirens* F18-3 and *F. luteovirens* DTS10, and were then cultivated in Potato Dextrose agar (PDA) medium (glucose 20.0 g/L, potato extract 200.0 g/L, agar 18.0 g/L) for 30 days at 20°C (at the same temperature of outside) in the dark (Xu et al., 2021). Three replicate plates were prepared for transcriptome sequencing and the determination of pigments. In the end of cultivation, the resulting *F. luteovirens* fruiting bodies were immediately frozen in liquid nitrogen and stored at −80°C.

The strain of *F. luteovirens* F18-3 was cultured in PDB medium (glucose 20.0 g/L, potato extract 200.0 g/L) in flask of 500 mL at 200 rpm, at 20°C in liquid for 30 days. Three replicate plates in liquid culture were prepared for the determination of pigments.

Genome Sequencing and Assembly

The genome of *F. luteovirens* fruiting body was sequenced with PacBio Sequel and Illumina Hiseq 2500 Systems (Genewiz Biotechnology Co. Ltd., Suzhou, China). Long reads from PacBio could give a high-quality sequencing length while also generating a 2.5-kb library. The genome size and hybrid rate of *F. luteovirens* was estimated by kmerfreq.[1] Genome assembly was performed by using Canu software and was then assessed by using Benchmarking Universal SingleCopy Orthologs program v3.0 (Gan et al., 2020). The genome sequence of *F. luteovirens* has been deposited at GenBank under accession number of RPFY00000000.1.

RNA Extraction and RNA-Sequencing

Total RNA was extracted from the three samples using TRIzol reagent, according to the manufacturer's instructions (Sangon Biotech, Shanghai, China). The quality and quantity of total RNA were measured by using electrophoresis in 1% agarose gel. cDNA libraries were prepared using TruSeqTM RNA sample prep kit (Illumina). In brief, cDNA was synthesized from mRNA by reverse transcriptase with the use of random primers. Raw sequence reads were obtained by using an Illumina HiSeq sequencing platform. Each read was trimmed individually by setting quality score below 20 to obtain pure reads. Low quality reads were trimmed out and reads of 25 base pairs were filtered out in order to ensure purity. The sequences obtained in this study were deposited in the NCBI Sequence Read Archive (SRA[2]) under accession number SRP279887.

De novo Transcriptome Assembly

Clean data were obtained by removing low-quality reads, adapter sequences, reads with ambiguous bases "N," and reads of <20 bp. In the absence of a reference genome, contigs, and singletons were generated by de novo assembly using the Trinity software package.[3]

[1]https://github.com/fanagislab/kmerfreq

[2]http://www.ncbi.nlm.nih.gov/Traces/sra

[3]https://github.com/trinityrnaseq/trinityrnaseq/wiki

TABLE 1 | Sample information.

Strain number	Sample name	Sample size	Sample source	Environment	
F18-1	YFB	Pileus diameter is 2.5–4.5 cm	Collected from Haiyan County from (100°47′ 13″E, 37°0′37″N, 3220 m), Qinghai Province, China, in August 2018	In nature: the annual sunlight radiation is 2517.6–2995.3 h; the average annual radiation is 5210.2 MJ–6568.3 MJ/m2	
F18-2	FB	Pileus diameter is 4.5–6.6 cm			
F18-3	VM	Isolated from fruiting bodies of *F. luteovirens*		In lab: incubated in PDA medium at 20° for 30 days in the dark	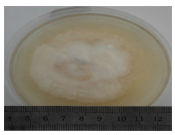

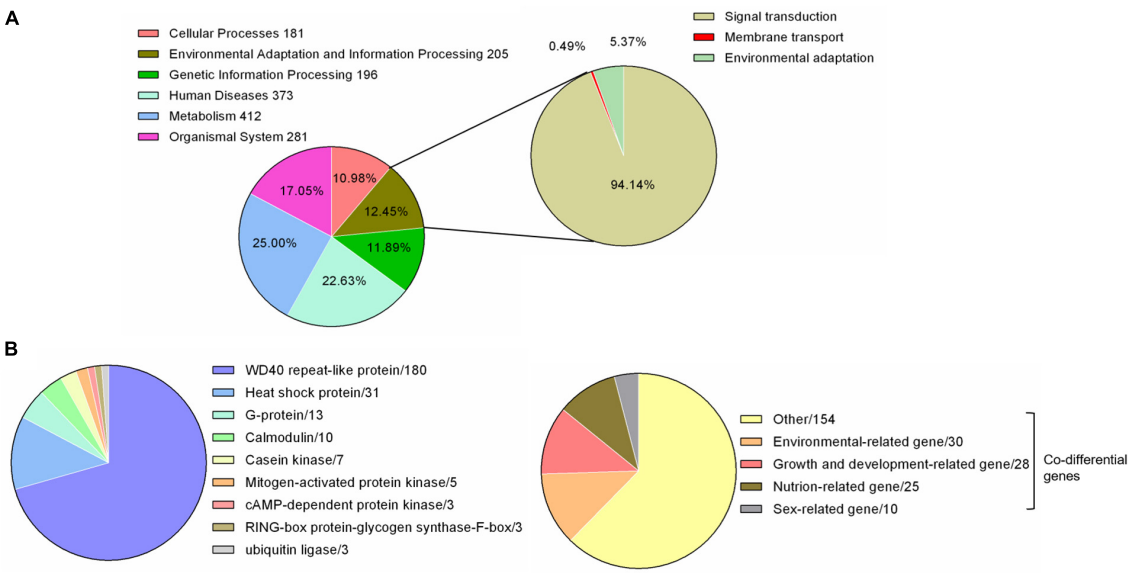

FIGURE 1 | Environmental related genes of *F. luteovirens*. A total of 205–225 genes involved in responding to environment. **(A)** Pie chart of the 205 environmental adaptation and information processing genes from genome. **(B)** Pie chart of the 225 environmental related genes from transcriptome [The 225 genes = DEGs (255) − Co differential genes of environmental-related (30)].

Identification of Differentially Expressed Genes

Differentially expressed genes (DEGs) were identified by comparing gene expression levels using TPM (Transcripts Per Million). TPM is the most commonly used index of gene expression levels, and can reflect the impact of sequencing depth and gene length on read counts (Mortazavi et al., 2008). We used "q Value < 0.05 and $|$ FoldChange$| > 2$" as the threshold to assess the significance of gene expression differences. BLAST analysis was carried out by searching against the NCBI databases and setting the E-value cut off at 10^{-3}. The upregulated and downregulated unigenes were subject to Venn diagram analysis.

Pathway Analysis of Differentially Expressed Genes

For metabolic pathway analysis, DEGs were aligned to the KEGG database through the KOBAS program.[4] In both analyses, q value < 0.05 and $|$ FoldChange$| > 2$ were used as thresholds.

Quantitative Real-Time PCR Validation

Total RNA was extracted from same samples using a Fungal Total RNA Rapid Extraction Kit (Sangon Biotech, Shanghai, China). Then cDNA was synthesized by using an M-MuLV First Strand

[4]http://kobas.cbi.pku.edu.cn/kobas3'

TABLE 2 | Throughput and quality of Illumina sequencing of the *Floccularia luteovirens* transcriptome.

Samples	Raw data			Quality control data		
	VM	YFB	FB	VM	YFB	FB
Total reads	46039192	54524788	47625192	44897648	53152546	46470082
Total length (bp)	6905878800	8178718200	7143778800	6385845795	7648146962	6699352210
Avg. length	150.0	150.0	150.0	142.23	143.89	144.16

cDNA Synthesis kit (Sangon Biotech, Shanghai, China). The 18S ribosomal RNA (rRNA) gene was used as an internal control for normalization (Song et al., 2018). Primers were designed by primer 3.0 online[5] (**Supplementary Table 1**). The qRT-PCR reaction was carried out in a LightCycler 96 system (Bio-Rad Laboratories, Hercules, CA, United States) using a SYBR Green kit (2 × SG Fast qPCR Master Mix, Sangon Biotech, Shanghai, China). Amplification conditions used for qPCR were 95°C for 3 min, followed by 40 cycles of 95°C for 3 s and 60°C for 30 s. For each sample, three biological and two technical replicates were done. Fold changes in gene expression were calculated using the $2^{-\Delta\Delta Ct}$ method (Li et al., 2019b).

Determination of the Pigments on Riboflavin and Chlorophyll in Mycelia From Liquid and Solid Culture

The cultured mycelia of 30 days in liquid of F18-3 and solid culture of DTS10 were stressed by 5400 mW m^{-2} UV radiation for 0, 2, 4, 6, 8, 10, 12, 24 h. The mycelia from liquid culture and solid culture were collected and dry at 40°C for 2 h, and then at the weight of 100 mg mycelia were polished with liquid nitrogen for 5 min. For riboflavin measurements, samples were diluted to arrive at the linear range of the spectrophotometer with 0.05 M NaOH. The chlorophyll was determined according to the assay kits of chlorophyll (Nanjing Jiancheng Bioengineering Institute, Nanjing, China). The OD444 was immediately measured, the titer of riboflavin is calculated according to the following formula: $y = 0.0105x + 0.0089$, $R^2 = 0.9953$ (**Supplementary Figure 1**; Zhang et al., 2021).

RESULTS

Genome Assembly and Annotation

The whole genome data of *F. luteovirens* were reported in previous studies (Gan et al., 2020). By comparing with 357 species-specific gene families from KEGG database, we found 1,648 genes in the whole genome of *F. luteovirens*. Among them, a total of 205 genes were annotated, which were categorized into three levels: 193 signal transduction genes (94.14%), one membrane transport gene (0.49%) and 11 environmental adaptation genes (5.37%), respectively (**Figure 1A**).

[5]https://primer3.ut.ee/

Transcriptome Sequencing of *Floccularia luteovirens* and *de novo* Assembly

A total of 44,897,648, 53,152,546, and 46,470,082 high-quality sequence reads were obtained from the VM, YFB, and FB samples, respectively (**Table 2**). These reads were then assembled into 89962 extended transcripts with an average length of 2028.56 bp and a N50 length of 3559 bp (N50 indicates that at least half of the resulting transcripts have a base length of no less than 50 bp). The resulting extended transcripts were used to generate a transcriptome database by using Trinity (see text footnote 3). These extended transcripts consisted of 23823 unigenes, with an average unigene length of 1023.6 bp and a N50 length of 2447 bp (**Table 3**). The length of transcripts ranged from 200 to ≥2000 bp (**Supplementary Figure 2**).

Analysis of Differentially Expressed Genes

A total of 11,871 significant differently expressed genes (DEGs) were identified between the VM, YFB, and FB stages, of which 247 DEGs that were mainly involved in the growth and development of *F. luteovirens* co-existed in all three stages (**Supplementary Table 2**). A total of 4,444 DEGs were identified between the VM and YFB stages, 4,996 DEGs were identified between the VM and FB stages, and only 2,431 DEGs genes were identified between the YFB stage and FB stages ($q \leq 0.05$) (**Figure 2**). Furthermore, cluster analysis showed the DEGs of YFB and FB belonged to the same branch, but the DEGs of VM formed a separate branch (**Figure 2C**), suggesting that the expression profiles of the YFB and FB were similar.

Functional Analysis of Differentially Expressed Genes Under Strong Ultraviolet Radiation and External Environment Factors

A total of 225 DEGs were identified to play a regulatory role in adapting to the changes of external environmental factors

TABLE 3 | Functional annotation statistics of the *Floccularia luteovirens* assembly data.

Data	NO.	Total Len	Min Len	Max Len	Average	N50[c]
Transcript[a]	89962	182493102	201	18266	2028.56	3559
Unigene[b]	23823	24385122	201	18266	1023.6	2447

[a] *Total number of transcripts assembled using k-mer 51.*
[b] *Transcripts of multi-copy genes are collapsed into a single sequence.*
[c] *Half of all bases are in transcript at least as long as N50.*

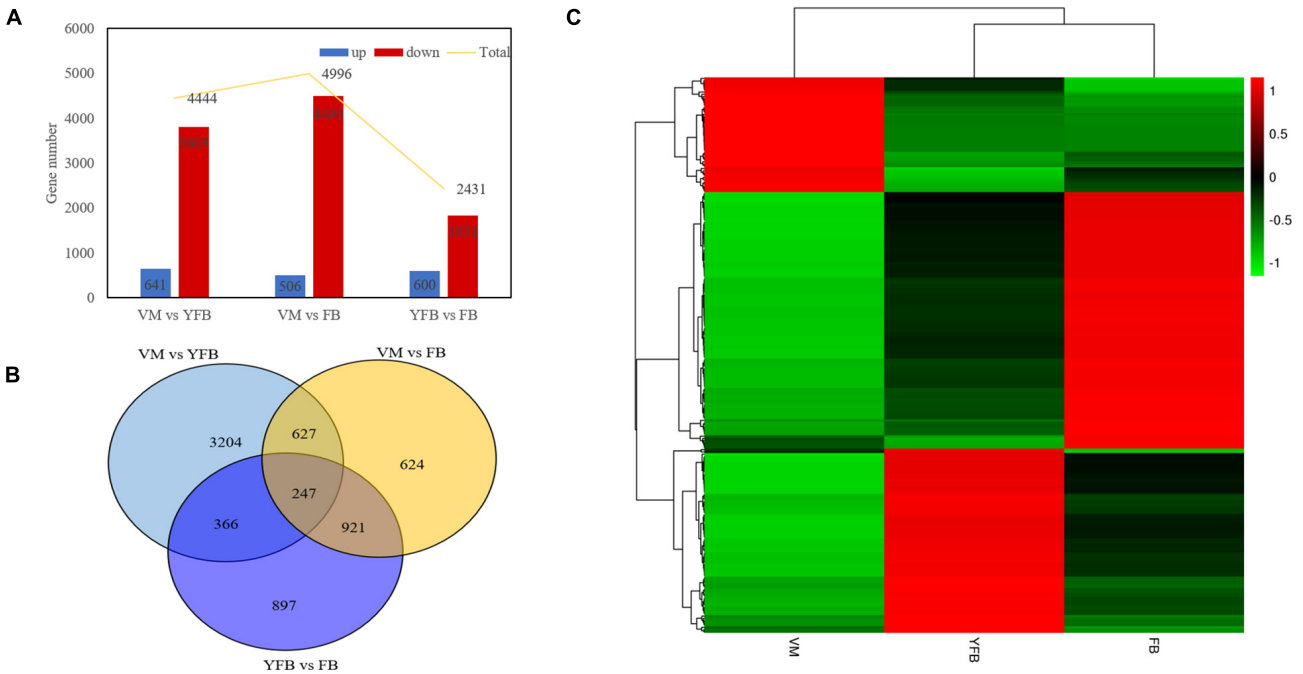

FIGURE 2 | Bar plot, Venn diagram, and heatmap showing co-differentially expressed genes. **(A)** Bar plot of the differentially expressed genes (DEGs). **(B)** Venn diagram showing the DEGs exclusive to VM vs. YFB (light blue circle), YFB vs. FB (dark blue circle), and VM vs. FB (yellow circle). **(C)** Heatmap of co-differentially genes. Red and green colors in the heat-maps represent down- and up- regulated expression levels, respectively.

and UV radiation. The functions of these DEGs included signal transduction, biochemical reaction preparation and effect stress (**Figure 1B** and **Supplementary Table 3**). Among these identified DEGs, calmodulin and G proteins play important roles in signal transduction of *F. luteovirens*. Five calmodulin signaling genes that were up-regulated in the cells of *F. luteovirens* at the FB stage were identified, and they were calmodulin-binding motif protein (DN6933), calmodulin (DN255, DN3162) and Calcium/calmodulin-dependent protein (DN8891, DN3857). The expression of nine G protein coding genes were significantly up-regulated from the VM stage to the FB stage. Secondly, kinase genes are the key genes regulating the biochemical reaction in *F. luteovirens*. The expression of five mitogen-activated protein kinase genes were significantly up-regulated in the cells at the VM stage compared with those at the FB stage, the expression of two cAMP-dependent protein kinase genes, three casein kinase genes and cAMP-dependent protein kinase (DN6015) and casein kinase (DN15337) genes were significantly upregulated in the cells at the FB stage, compared with that in the VM stage. In addition, ubiquitin ligase, RING-box protein, glycogen synthase, and F-box protein were involved in the regulation of effector stress. In the present study, genes for ubiquitin ligases, glycogen synthase, and F-box protein were all expressed at a much higher level in the cells at the FB stage than that that of VM state. In addition, heat shock protein and WD40 repeat-like protein play vital role in oxidative stress of *F. luteovirens* under UV radiation and environmental factors. For instance, a large number of heat shock proteins were up-regulated in the cells at the FB growth stage. Most of the WD40 repeat-like protein genes of *F. luteovirens* were significantly upregulated in the cells at both YFB and FB stages (**Figure 3**).

Metabolic Pathways Indicated by Differentially Expressed Genes

Two metabolic pathways including chlorophyll and riboflavin metabolisms, related to pigment synthesis were differentially regulated in *F. luteovirens*. Several DEGs were enriched in the metabolisms of chlorophyll and riboflavin pathways. The chlorophyll metabolic pathway may affect the accumulation of photosynthetic pigments and the production of photochromes (**Supplementary Figure 3**). The gene expression of the core enzymes of the chlorophyll metabolic pathway was higher at the FB stage than at the VM stage (**Supplementary Table 4**). Such core enzyme included the genes of uroporphyrinogen decarboxylase (*HemE*, 21.24-fold), 5-aminolevulinate synthase (*ALAS*, 22.29-fold), ferrochelatase (*FECH*, 21.94-fold), glutamyl-tRNA synthetase (*EARS*, 21.41-fold), cytochrome c heme-lyase (*CYC*, 21.40-fold), oxygen-dependent protoporphyrinogen oxidase (*HemY*, 21.15-fold). In the riboflavin metabolism pathway, the expression levels of tyrosinase (*TYR*, 27.81-fold) and GTP cyclohydrolase II (*ribA*, 21.62-fold) genes were much higher than those in the FB stage than in the VM stage (**Supplementary Table 5** and **Supplementary Figure 4**). Another gene for 3,4-dihydroxy 2-butanone 4-phosphate synthase (*ribB*) and 6,7-dimethyl-8-ribityllumazine synthase (*ribH*) was differentially expressed only in the FB stage (**Figure 4B**). The expression of these enzymes may result in the accumulation of riboflavin

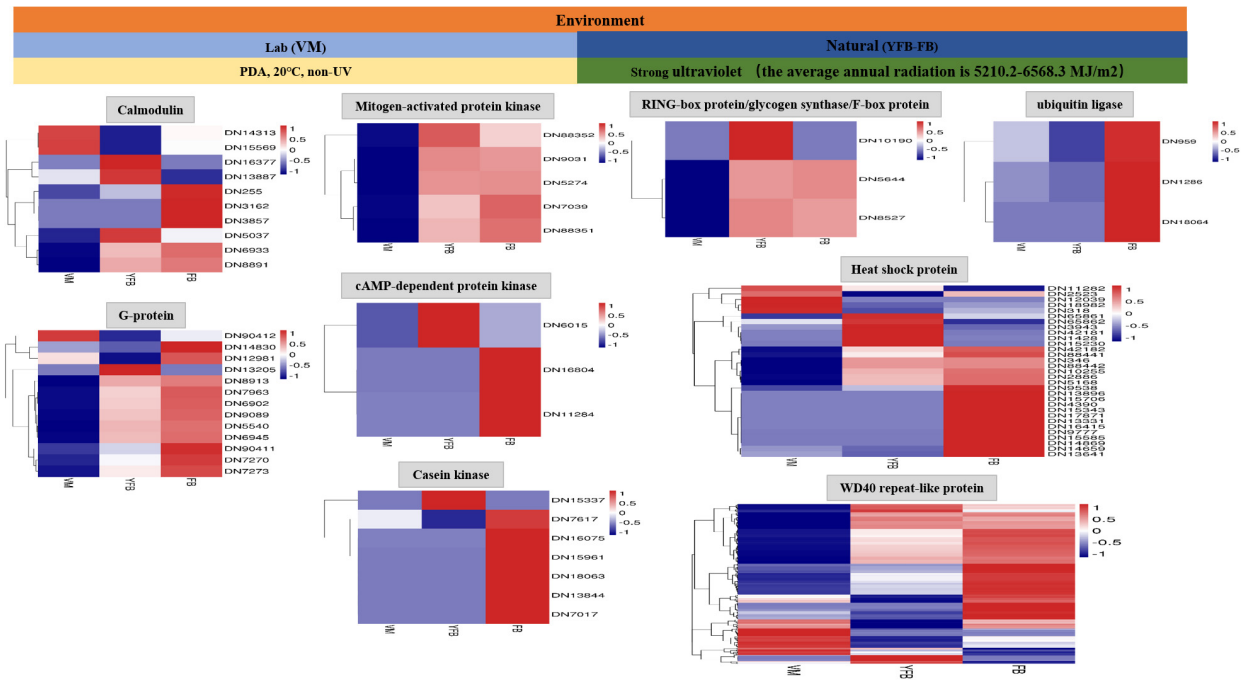

FIGURE 3 | The 255 differential genes were annotated in response to UV radiation of *F. luteovirens*.

in *F. luteovirens* in the FB stage. In general, there were more differential regulation genes and specific genes of pigment synthesis under strong UV than without UV radiation, which was consistent with the fact that the fruiting body of *F. luteovirens* obtained long-term sunlight radiation and a large amount of UV radiation in the late stage of development.

In addition, the cell-cycle pathway of *F. luteovirens* was associated with its cell growth, proliferation, and development. The expression of the genes related to cell-cycle pathway in the cells of *F. luteovirens* was greatly up-regulated, and such genes included the S phase-related *Mcm1* (21.01-fold), *Pho81* (22.31-fold), *Pho85* (21.58-fold), *Grr1* (21.73-fold), *Cdc4* (21.42-fold), and *Cdc7* (23.88-fold); the G2 phase-related *Mps1* (21.70-fold), *Cak1* (22.02-fold), and *Cdh1* (21.67-fold) (**Supplementary Figure 5**); and the M phase-related *Rad53* (21.61-fold) and *Scc2* (21.46-fold), were higher in the FB stage than in the VM stage (**Supplementary Table 6**). However, the expression of *Cdc7* and *Cyc8* were significantly down-regulated, which were considered to depress the growth and development of *F. luteovirens* cells. Moreover, there were 34 DEGs that may be mainly involved in DNA damage repair of *F. luteovirens*, and they showed higher expression at the FB stage than at the VM stage (**Figure 4C**).

Validation of RNA-Seq Results by qRT-PCR

Twenty-two DEGs from *F. luteovirens* that were significantly expressed at all the three stages (VM, YFB, and FB) were randomly selected, and their differential expression was confirmed by qRT-PCR (**Supplementary Table 7**). Among them, 11 environment-related DEGs, eight growth and development-related DEGs, and three sex-related DEGs were investigation, all of which have different expression patterns similar to those in the RNA-Seq (**Figure 5**), indicating the reliability and accurately of the RNA-Seq data of *F. luteovirens*.

Effect of Ultraviolet on Riboflavin and Chlorophyll Production in *Floccularia luteovirens* Mycelium

Under UV irradiation for 8–10 h, the riboflavin concentration of mycelium reached the concentration of 42.35–47.21 ug/mL (**Figure 6**). Meanwhile, the chlorophyll content reached the 1.56–2.10 mg/g after UV stress for 4–6 h. Both DTS 10 and F18-3 of *F. luteovirens* reached the highest concentration after simultaneous exposure to UV radiation of 5400 mW m^{-2}, although they were cultured and exposed in different states. The highest of riboflavin concentration occurred at UV radiation of 8–10 h, which was consistent with the daytime illumination time of *F. luteovirens*.

DISCUSSION

UV radiation affected the biochemical process and physiological characteristics of organisms. In this study, 205–225 DEGs potentially involved in coping with external strong UV radiation stress were obtained from *F. luteovirens* living on the Qinghai-Tibet Plateau. The genome environmental adaptation and information processing genes of these DEGs were basically consistent with the transcriptome genes of their environment-related genes. When *F. luteovirens* cells received signals of

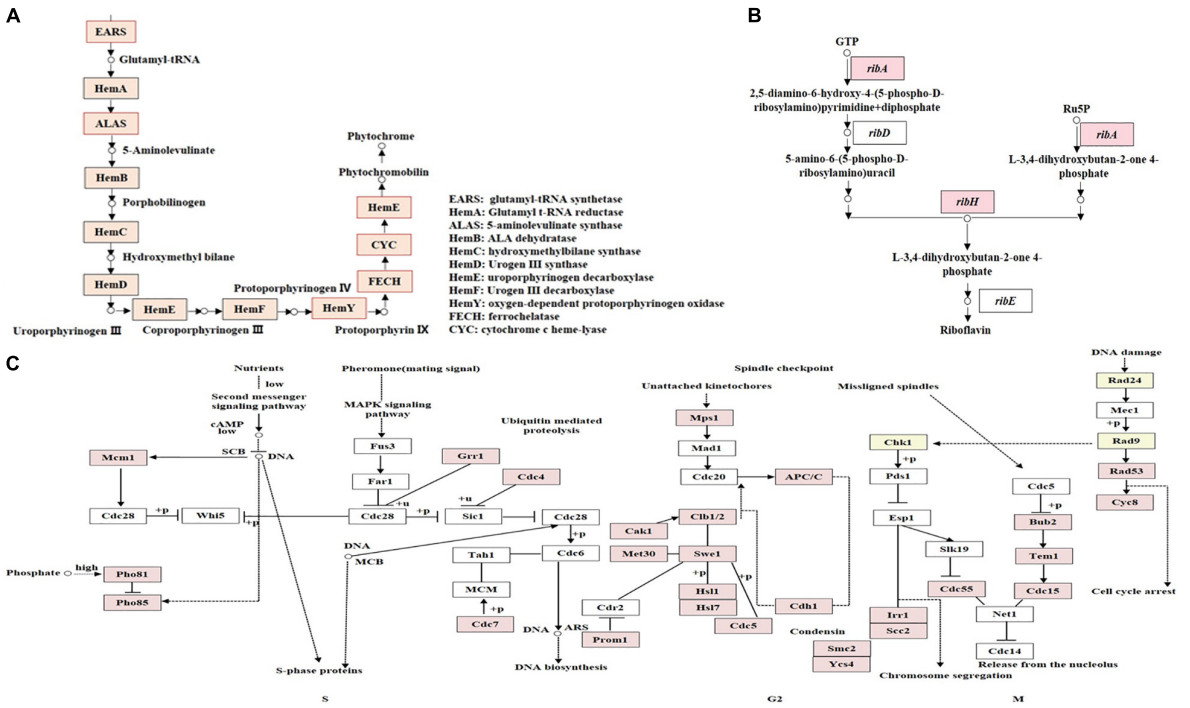

FIGURE 4 | KEGG annotation of DEGs involved in different metabolism pathways. **(A)** KEGG annotation of proteins encoded by DEGs involved in the phytochrome biosynthesis pathway. The genes whose products are highlighted in red are up-regulated during the FB stages. **(B)** KEGG annotation of DEGs involved in riboflavin metabolism pathways. Genes highlighted in red are up-regulated during the FB stages. **(C)** KEGG annotation of DEGs involved in the cell-cycle. DEGs between VM and FB are shown in the cell-cycle pathway at the S, G2, and M phases. Genes whose products are highlighted in red are up-regulated during the FB stages.

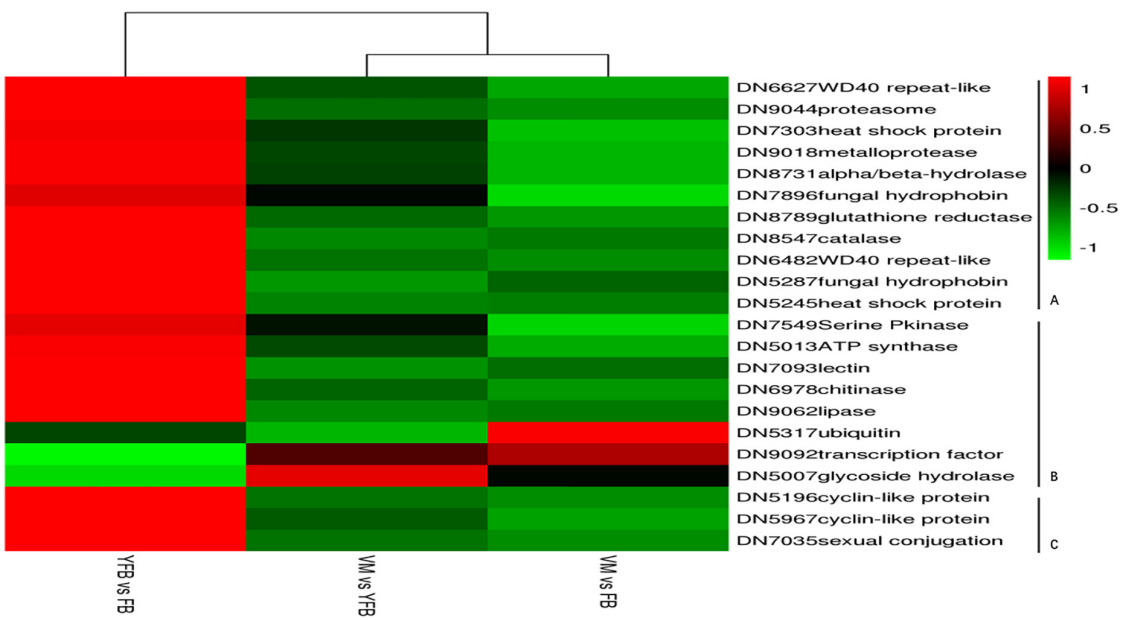

FIGURE 5 | qRT-PCR validation of DEGs. The 18S gene was selected as the internal control in this study. The expression patterns determined by qRT-PCR were consistent with those obtained by RNA-Seq, thus confirming the reliability of our RNA-Seq data. **(A)** Eleven environment-related DEGs were analyzed by qRT-PCR. **(B)** Eight growth and development-related DEGs were analyzed by qRT-PCR. **(C)** Three sex-related DEGs were analyzed by qRT-PCR.

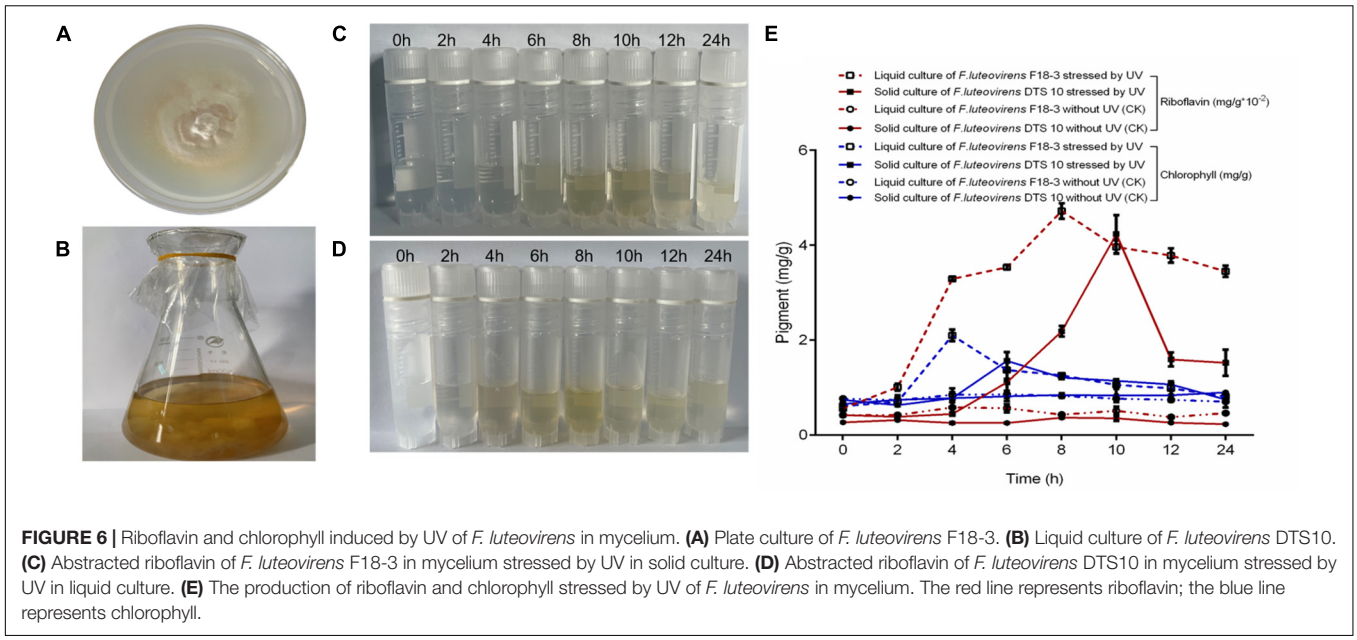

FIGURE 6 | Riboflavin and chlorophyll induced by UV of *F. luteovirens* in mycelium. **(A)** Plate culture of *F. luteovirens* F18-3. **(B)** Liquid culture of *F. luteovirens* DTS10. **(C)** Abstracted riboflavin of *F. luteovirens* F18-3 in mycelium stressed by UV in solid culture. **(D)** Abstracted riboflavin of *F. luteovirens* DTS10 in mycelium stressed by UV in liquid culture. **(E)** The production of riboflavin and chlorophyll stressed by UV of *F. luteovirens* in mycelium. The red line represents riboflavin; the blue line represents chlorophyll.

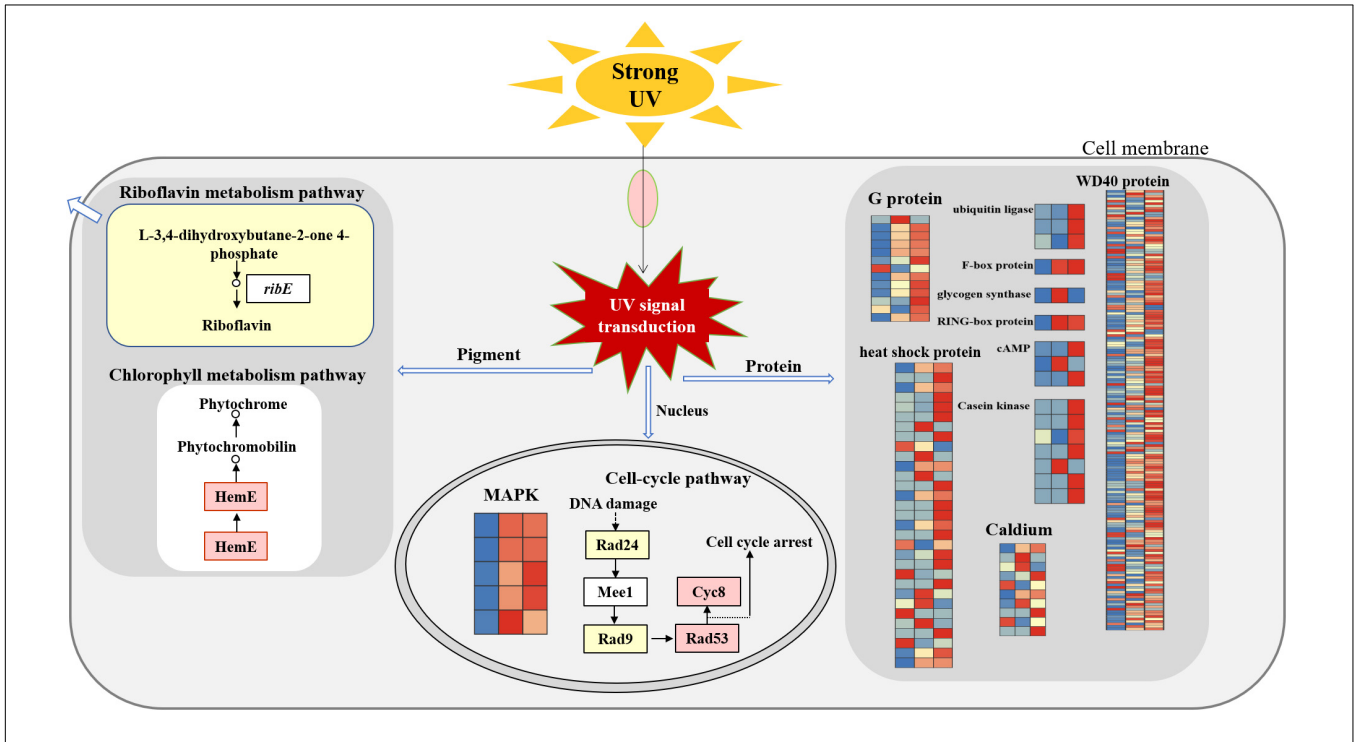

FIGURE 7 | The molecular regulation mode of *F. luteovirens* under UV radiation.

UV and external stimuli, G protein and calmodulin were activated as signal molecules. G protein interacted directly with downstream enzymes or ion channels and was involved in regulating cell-specific changes caused by UV and external stimuli (Smrcka and Fisher, 2019; Wang et al., 2019; Patel et al., 2020). Calmodulin, as a ubiquitous sensor protein and calcium receptor in eukaryotic cells, was involved in regulating the response of organisms to various environmental stresses and transmitting stimulation signals (Kiselev et al., 2021; Li et al., 2021). Our results showed that the significantly upregulated genes of DN255 and DN90411 were considered as candidate genes that played a crucial role in coping with UV stress and signal transduction in response to external factors. This finding was consistent with the expression trend of signal transduction genes of *CaM* and *CML* in *Vitis amurensis* under abiotic stress (Kiselev et al., 2021).

In addition, phosphorylation pathway is a key biological process in signal transduction, and can regulate the expression of kinase genes. When the kinase genes sense stimulation signals, cAMP-dependent protein kinase was the core enzyme that regulated the protein phosphorylation pathway (Wu Z. et al., 2019), and MAPK transduced signals through the phosphorylation pathway of downstream targets (Li C. et al., 2018). DEGs of DN7039 and DN88351 were found to be involved in the regulation of UV and external stress response of *F. luteovirens* and showed differential expression patterns. Furthermore, casein kinase is another gene essential for cell proliferation. It is an evolutionarily conserved Ser/Thr protein kinase and is also pivotal in signal transduction (Li Y. et al., 2018). Nagatoshi et al. (2018) reported that casein kinase is a pleiotropic enzyme involved in a variety of developmental and stress response processes. Our results suggested that casein kinase may be independently involved in signal transduction of *F. luteovirens* on the Qinghai-Tibet Plateau.

The cells of *F. luteovirens* often undergo post-translational modifications of proteins they sense and transmit internal or external UV stimulation signals (Han et al., 2019; Jiao and Duan, 2019; Yu et al., 2021). In *F. luteovirens*, RING-box protein, ubiquitin ligase, F-box protein, and glycogen synthase were involved in the post-translational modification of proteins under UV and external stimulation: on the one hand, RING-box proteins and ubiquitin ligases were identified as key regulators of basic cellular processes and participated in plant growth and development (Abd-Hamid et al., 2020); On the other hand, F-box protein and glycogen synthase depended on the regulation of protein stability under abiotic stress, and participated in the regulation of antioxidant system after translational modification (Rameneni et al., 2018; Jiao and Duan, 2019). Thus it is reasonable to speculate that RING-box protein and ubiquitin ligase may mediate the ubiquitination of key factors in the process of UV and external stress, and then regulate the adaptability of *F. luteovirens* to strong UV radiation and external factors.

Heat shock protein and WD40-repeat like protein were important molecular regulators involved in controlling cellular processes in response to stresses (Guz et al., 2021; Kim et al., 2021). The former helped to maintain the folding of damaged and newly formed proteins under stress conditions, and also responded to environmental stress by regulating the expression dynamics of numerous genes involved in maintaining intracellular homeostasis (Guz et al., 2021; Kim et al., 2021); while the latter mainly regulated signal transduction, transcriptional regulation, and immune response (Jain and Pandey, 2018). Our results suggested that under UV the stimulation and external factors, *F. luteovirens* cells produced denatured peptides and new proteins, so the genes of DN13641 and DN7704 were significantly upregulated.

Chlorophyll metabolism includes chlorophyll biosynthesis, chlorophyll cycle, and chlorophyll degradation. The produced chlorophyll can regulate the host's defense response and survival under different extreme environmental conditions (Wang et al., 2020). In this study, 20 candidate genes related to porphyrin and chlorophyll metabolic pathway were analyzed. It is found that the core genes of *HemE*, *ALAS*, *FECH*, *EARS*, *CYC*, *HemY* were involved in the synthesis of phytochrome and cytochrome in *F. luteovirens* under strong UV radiation. Previous studies showed that *ALAS* can promote plant growth under abiotic stress and participate in the regulation of plant photosynthesis, nutrient absorption, antioxidant properties and osmotic balance (Wu Y. et al., 2019). Therefore, *ALAS* may mediate the color change of *F. luteovirens* to adapt to the strong UV radiation on the Qinghai-Tibet Plateau. The role of *ALAS* in *F. luteovirens* may be consistent with that of HY5 in regulating the color change of *Brassica campestris L.* leaf under cold stress (Yuan et al., 2021).

In addition to chlorophyll, riboflavin also participated in the response to UV radiation and the other external environment stimuli in the Qinghai-Tibet Plateau. The coding genes of FXN and BLVRA, the main derivatives of riboflavin, were other genes that mainly regulate plant growth and color rendering (Bai et al., 2019; Rouault, 2019; Britti et al., 2021). We found that the coding genes of FXN and BLVRA were involved in controlling the growth and division of *F. luteovirens* under strong UV radiation, and regulated its yellow color at the later growth stage of *F. luteovirens* (**Figure 4A**). FMN and FAD, the main riboflavin derivatives, were cofactors of enzymes that mediated many redox reactions in cells, and riboflavin operon *ribA* gene encoded GTP, which was the first step of riboflavin biosynthesis (Cisternas et al., 2017; Liu et al., 2020; Zhao G. et al., 2021). Accordingly, we found that *F. luteovirens* may have the capability of *de novo* riboflavin biosynthesis, and the *ribA* and *ribH* genes were directly involved in riboflavin synthesis. Their differential expression patterns may be related to the regulation of redox reaction and electron respiratory chain transmission under UV radiation. This is similar to the role of the anthocyanins of *Lycium ruthenicum* on Qinghai-Tibet Plateau (Qi et al., 2021). These results suggested that the metabolic pathway of fungal pigment synthesis was closely related to the response to UV radiation.

Furthermore, fungi have evolved complex signal transduction pathways to repair direct DNA damage. DNA damage checkpoints transmit signals of damaged DNA to effector molecules, thereby regulating cell cycle pathways to repair DNA oxidative damages (Zhou et al., 2016; Gkouskou et al., 2020). In the cell cycle pathway of *F. luteovirens*, the key genes *Rad53*, *Pho85*, *Pho81*, and *Cdh1* were significantly upregulated in the FB stage under strong UV radiation. The *Rad53* gene was responsible for the transduction of UV stimulated signals and was significantly upregulated under strong UV radiation to regulate DNA damage repair, replication, bifurcation stability, cell cycle progression, and transcription (Gkouskou et al., 2020). *Pho81* and *Pho85* gene were significantly upregulated in *F. luteovirens*, indicating that their encoded enzymes may play a key role in maintaining phosphate homeostasis under UV stimulation; *Pho85* controlled the cell cycle by regulating phosphate metabolism when it binds to the *Pho80* family of cyclins, while the CDK inhibitor *Pho81* regulated the cell cycle by inhibiting thePho80-Pho85 complex (Zhou et al., 2016; Zheng et al., 2020). The *Cdh1* gene encoded cell division cycle 20-like protein 1, which was highly upregulated in the FB stage under strong UV radiation. This result suggested that *Cdh1* may be a key regulatory gene in the cell cycle of the fruiting body of *F. luteovirens* from the S phase to G2 phase, which may be

consistent with the role of *Chl1p* as G1/S phase checkpoint and its role in the damage checkpoint pathway in budding yeast (Katheeja et al., 2021).

CONCLUSION

Floccularia luteovirens can adapt to the changes of external environmental factors, especially it can respond to UV radiation in three ways by regulating key genes and obtain the ability to deal with UV radiation (as shown in the conceptual scheme **Figure 7**). Firstly, at the nuclear level, cell cycle was regulated to repair DNA oxidative damage of ultraviolet radiation to cells. Secondly, at the cytoplasmic level, differentially expressed genes of environmental signal transduction, biochemical reaction preparation and stress response involved in maintaining intracellular homeostasis, and the metabolic pathways of chlorophyll and riboflavin were activated to involved in the pigment synthesis of ultraviolet radiation to cells. In addition, after metabolizing gene clusters at the fruiting body and mycelium levels, the pigment of yellowish brightness and sulfur color emerged in the cells of yellow mushroom, which contribute to the characteristic yellow color of ultraviolet radiation to cells. This regulation model can reveal the molecular mechanism of *F. luteovirens* to deal with the strong UV radiation, which is of great significance for us to understand the environmental adaptation mechanism of fungi on the Qinghai-Tibet Plateau.

DATA AVAILABILITY STATEMENT

The datasets presented in this study can be found in online repositories. The names of the repository/repositories and accession number(s) can be found below: NCBI–RPFY00000000.1, SRP279887.

AUTHOR CONTRIBUTIONS

JG: conceptualization, methodology, and writing-original draft. ZX: supervision, validation, and writing-review and editing. HJ: writing-review and editing. HX: investigation. BL: supervision. QM: visualization. All authors contributed to the article and approved the submitted version.

FUNDING

This study was supported by funding from the Natural Science Planning Project of Qinghai Province (grant no. 2021-HZ-802).

SUPPLEMENTARY MATERIAL

The Supplementary Material for this article can be found online at: https://www.frontiersin.org/articles/10.3389/fmicb.2022.918491/full#supplementary-material

REFERENCES

Abd-Hamid, N. A., Ahmad-Fauzi, M. I., Zainal, Z., and Ismail, I. (2020). Diverse and dynamic roles of F-box proteins in plant biology. *Planta* 251:68.

Azarafshan, M., Peyvandi, M., Abbaspour, H., Noormohammadi, Z., and Majd, A. (2020). The effects of UV-B radiation on genetic and biochemical changes of *Pelargonium graveolens* L'Her. *Physiol. Mol. Biol. Plants* 26, 605–616. doi: 10.1007/s12298-020-00758-6

Bai, D. P., Lin, X. Y., Wu, Y., Zhou, S. Y., Huang, Z. B., Huang, Y. F., et al. (2019). Isolation of blue-green eggshell pigmentation-related genes from Putian duck through RNA-seq. *BMC Genomics.* 20:66. doi: 10.1186/s12864-019-5436-4

Braga, G. U., Rangel, D. E., Fernandes, E. K., Flint, S. D., and Roberts, D. W. (2015). Molecular and physiological effects of environmental UV radiation on fungal conidia. *Curr. Genet.* 61, 405–425. doi: 10.1007/s00294-015-0483-0

Britti, E., Delaspre, F., Tamarit, J., and Ros, J. (2021). Calpain-inhibitors protect frataxin-deficient dorsal root Ganglia Neurons from loss of mitochondrial Na (+)/Ca (2+) exchanger, NCLX, and apoptosis. *Neurochem. Res.* 46, 108–119. doi: 10.1007/s11064-020-03020-3

Chen, H., Huang, K., Liu, S., and Lu, S. (2021). Effects of ultraviolet (UV) radiation on outdoor- and indoor-cultured *Prorocentrum lima*, a toxic benthic dinoflagellate. *J. Ocean Univ. China* 20, 619–628.

Cisternas, I. S., Torres, A., Flores, A. F., and Angulo, V. A. G. (2017). Differential regulation of riboflavin supply genes in *Vibrio cholerae*. *Gut Pathog.* 9:10. doi: 10.1186/s13099-017-0159-z

Gan, X. L., Bao, X. M., Liu, B. L., Li, Y., Cao, D., Zhang, H., et al. (2022). Chemical constituents and molecular mechanisms of the yellow phenotype of yellow mushroom (*Floccularia luteovirens*). *J. Fungi* 8:314. doi: 10.3390/jof8030314

Gan, X., Cao, D., Zhang, Z., Cheng, S., Wei, L., Li, S., et al. (2020). Draft genome assembly of *Floccularia luteovirens*, an edible and symbiotic mushroom on Qinghai-Tibet Plateau. *G3 (Bethesda)* 10, 1167–1173. doi: 10.1534/g3.120.401037

Gkouskou, K., Fragiadakis, G. S., Voutsina, A., and Alexandraki, D. (2020). Distinct associations of the *Saccharomyces cerevisiae* Rad9 protein link Mac1-regulated transcription to DNA repair. *Curr. Genet.* 66, 531–548. doi: 10.1007/s00294-019-01047-w

Gmoser, R., Ferreira, J., Lennartsson, P., and Taherzadeh, M. (2017). Filamentous ascomycetes fungi as a source of natural pigments. *Fungal Biol. Biotechnol.* 4:4. doi: 10.1186/s40694-017-0033-2

Guz, N., Dageri, A., Altincicek, B., and Aksoy, S. (2021). Molecular characterization and expression patterns of heat shock proteins in *Spodoptera littoralis*, heat shock or immune response? *Cell Stress Chaperon.* 26, 29–40.

Han, P. L., Dong, Y. H., Gu, K. D., Yu, J. Q., Hu, D. G., and Hao, Y. J. (2019). The apple U-box E3 ubiquitin ligase MdPUB29 contributes to activate plant immune response to the fungal pathogen *Botryosphaeria dothidea*. *Planta* 249, 1177–1188.

Huarte-Bonnet, C., Pereira-Junior, R. A., Paixão, F. R. A., Braga, G. U. L., Roberts, D. W., Luz, C., et al. (2020). *Metarhizium robertsii* and *M. acridum* conidia produced on riboflavin-supplemented medium have increased UV-A tolerance and upregulated photoprotection and photoreactivation genes. *BioControl* 65, 211–222.

Jain, B. P., and Pandey, S. (2018). WD40 repeat proteins: signalling scaffold with diverse functions. *Protein J.* 37, 391–406. doi: 10.1007/s10930-018-9785-7

Jiao, C., and Duan, Y. (2019). The role of glycogen synthase kinase-3 in Gibberellic acid-induced chilling tolerance and defense response in postharvest peach fruit. *Food Bioprocess Tech.* 12, 1733–1740.

Katheeja, M. N., Das, S. P., and Laha, S. (2021). The budding yeast protein Chl1p is required for delaying progression through G1/S phase after DNA damage. *Cell Div.* 16:4. doi: 10.1186/s13008-021-00072-x

Kim, T., Samraj, S., Jimenez, J., Gomez, C., Liu, T., and Begcy, K. (2021). Genome-wide identification of heat shock factors and heat shock proteins in response to UV and high intensity light stress in lettuce. *BMC Plant Biol.* 21:185. doi: 10.1186/s12870-021-02959-x

Kiselev, K. V., Aleynova, O. A., Ogneva, Z. V., Suprun, A. R., Ananev, A. A., Nityagovsky, N. N., et al. (2021). The effect of stress hormones, UV-C, and stilbene precursors on calmodulin (CaM) and calmodulin-like gene (CML) expression in *Vitis amurensis* Rupr. *Plant Cell Tiss Org.* 146, 59–68.

Li, C., Kong, F., Sun, P., Bi, G., Li, N., Mao, Y., et al. (2018). Genome-wide identification and expression pattern analysis under abiotic stress of mitogen-activated protein kinase genes in *Pyropia yezoensis*. *J. Appl. Phycol.* 30, 2561–2572.

Li, H., Gao, D., and Yan, X. (2021). Identification and expression analysis of a calmodulin gene in *Phycocalida chauhanii* (Rhodophyceae, Bangiales). *J. Appl. Phycol.* 33, 1915–1923.

Li, X., Huang, L., He, Y., Xie, C., Zhan, F., Zu, Y., et al. (2019a). Effects of enhanced UV-B radiation on the interaction between rice and *Magnaporthe oryzae* in Yuanyang terrace. *Photochem. Photobiol.* 18, 2965–2976. doi: 10.1039/c8pp00556g

Li, X., Wang, F., Liu, Q., Li, Q., Qian, Z., Zhang, X., et al. (2019b). Developmental transcriptomics of Chinese cordyceps reveals gene regulatory network and expression profiles of sexual development-related genes. *BMC Genomics* 20:337. doi: 10.1186/s12864-019-5708-z

Li, Y., Min, L., Zhang, L., Hu, Q., Wu, Y., Li, J., et al. (2018). Promoters of Arabidopsis casein kinase I-like 2 and 7 confer specific high-temperature response in anther. *Plant Mol. Biol.* 98, 33–49.

Liu, S., Hu, W., Wang, Z., and Chen, T. (2020). Production of riboflavin and related cofactors by biotechnological processes. *Microb. Cell Fact.* 19:31. doi: 10.1186/s12934-020-01302-7

Mapari, S., Nielsen, K., Larsen, T., Frisvad, J., Meyer, A., and Thrane, U. (2005). Exploring fungal biodiversity for the production of water-soluble pigments as potential natural food colorants. *Curr. Opin. Biotechnol.* 16, 231–238. doi: 10.1016/j.copbio.2005.03.004

Mortazavi, A., Williams, B. A., McCue, K., Schaeffer, L., and Wold, B. (2008). Mapping and quantifying mammalian transcriptomes by RNA-Seq. *Nat. Methods* 5, 621–628. doi: 10.1038/nmeth.1226

Nagatoshi, Y., Fujita, M., and Fujita, Y. (2018). Casein kinase 2 alpha and beta subunits inversely modulate ABA signal output in *Arabidopsis protoplasts*. *Planta* 248, 571–578. doi: 10.1007/s00425-018-2919-5

Ozel, H. B., Abo Aisha, A. E. S., Cetin, M., Sevik, H., and Zeren Cetin, I. (2021). The effects of increased exposure time to UV-B radiation on germination and seedling development of Anatolian black pine seeds. *Environ. Monit. Assess.* 193:388. doi: 10.1007/s10661-021-09178-9

Patel, J. S., Selvaraj, V., Gunupuru, L. R., Kharwar, R. N., and Sarma, B. K. (2020). Plant G-protein signaling cascade and host defense. *3 Biotech.* 10:219. doi: 10.1007/s13205-020-02201-9

Qi, Y., Wei, H., Gu, W., Shi, W., Jiang, L., Deng, L., et al. (2021). Transcriptome profiling provides insights into the fruit color development of wild *Lycium ruthenicum* Murr. from Qinghai-Tibet Plateau. *Protoplasma* 258, 33–43. doi: 10.1007/s00709-020-01542-9

Qiao, Q., Wang, Q., Han, X., Guan, Y. L., Sun, H., Zhong, Y., et al. (2016). Transcriptome sequencing of *Crucihimalaya himalaica* Brassicaceae reveals how Arabidopsis close relative adapt to the Qinghai-Tibet Plateau. *Sci. Rep.* 6:21729. doi: 10.1038/srep21729

Rameneni, J. J., Dhandapani, V., Paul, P., Devaraj, S. P., Choi, S. R., Yi, S. Y., et al. (2018). F-Box genes in *Brassica rapa*: genome-wide identification, structural characterization, expressional validation, and comparative analysis. *Plant Mol. Biol. Rep.* 36, 500–517.

Rouault, T. A. (2019). The indispensable role of mammalian iron sulfur proteins in function and regulation of multiple diverse metabolic pathways. *Biometals* 32, 343–353. doi: 10.1007/s10534-019-00191-7

Smrcka, A. V., and Fisher, I. (2019). G-protein betagamma subunits as multi-functional scaffolds and transducers in G-protein-coupled receptor signaling. *Cell Mol. Life Sci.* 76, 4447–4459. doi: 10.1007/s00018-019-03275-2

Song, H. Y., Kim, D. H., and Kim, J. M. (2018). Comparative transcriptome analysis of dikaryotic mycelia and mature fruiting bodies in the edible mushroom *Lentinula edodes*. *Sci. Rep.* 8:8983. doi: 10.1038/s41598-018-27318-z

Wang, M., Chen, L., Liang, Z., He, X., Liu, W., Jiang, B., et al. (2020). Metabolome and transcriptome analyses reveal chlorophyll and anthocyanin metabolism pathway associated with cucumber fruit skin color. *BMC Plant Biol.* 20:386. doi: 10.1186/s12870-020-02597-9

Wang, Y., Wang, Y., and Deng, D. (2019). Multifaceted plant G protein: interaction network, agronomic potential, and beyond. *Planta* 249, 1259–1266. doi: 10.1007/s00425-019-03112-7

Wu, Y., Liao, W., Dawuda, M. M., Hu, L., and Yu, J. (2019). 5-Aminolevulinic acid (ALA) biosynthetic and metabolic pathways and its role in higher plants: a review. *Plant Growth Regul.* 87, 357–374.

Wu, Z., Jin, Y., Chen, B., Gugger, M. K., Wilkinson-Johnson, C. L., Tiambeng, T. N., et al. (2019). Comprehensive characterization of the recombinant catalytic subunit of cAMP-Dependent protein Kinase by Top-down mass spectrometry. *J. Am. Soc. Mass Spectrom.* 30, 2561–2570. doi: 10.1007/s13361-019-02341-0

Xing, R., Gao, Q. B., Zhang, F. Q., Fu, P. C., Wang, J. L., Yan, H. Y., et al. (2017). Genetic variation and phylogenetic relationships of the ectomycorrhizal *Floccularia luteovirens* on the Qinghai-Tibet Plateau. *J. Microbiol.* 55, 600–606. doi: 10.1007/s12275-017-7101-4

Xu, H. Y., Xie, Z. L., Jiang, H. C., Guo, J., Meng, Q., Zhao, Y., et al. (2021). Transcriptome analysis and expression profiling of molecular responsed to Cd toxicity in morchella spongiola. *Mycobiology* 49, 421–433. doi: 10.1080/12298093.2021.1937882

Yu, Y., Yang, S., Bian, L., Yu, K., Meng, X., Zhang, G., et al. (2021). Identification of C3H2C3-type RING E3 ubiquitin ligase in grapevine and characterization of drought resistance function of VyRCHC114. *BMC Plant Biol.* 21:422. doi: 10.1186/s12870-021-03162-8

Yuan, L., Zhang, L., Wu, Y., Zheng, Y., Nie, L., Zhang, S., et al. (2021). Comparative transcriptome analysis reveals that chlorophyll metabolism contributes to leaf color changes in wucai (*Brassica campestris* L.) in response to cold. *BMC Plant Biol.* 21:438. doi: 10.1186/s12870-021-03218-9

Zhang, M. X., Zhao, X. C., Chen, X., Li, M. Y., and Wang, X. D. (2021). Enhancement of riboflavin production in Bacillus subtilis via in vitro and in vivo metabolic engineering of pentose phosphate pathway. *Biotechnol. Lett.* 43, 2209–2216. doi: 10.1007/s10529-021-03190-2

Zhao, G., Dong, F., Lao, X., and Zheng, H. (2021). Strategies to increase the production of biosynthetic riboflavin. *Mol. Biotechnol.* 63, 909–918. doi: 10.1007/s12033-021-00318-7

Zhao, Y. T., Pu, Y. F., Lin, H. L., and Tang, R. (2021). Examining soil erosion responses to grassland conversation policy in three-river headwaters, China. *Sustainability* 13, 1–14.

Zheng, Q., Guan, G., Cao, C., Li, Q., and Huang, G. (2020). The PHO pathway regulates white-opaque switching and sexual mating in the human fungal pathogen *Candida albicans*. *Curr Genet.* 66, 1155–1162. doi: 10.1007/s00294-020-01100-z

Zhou, Y., Yuikawa, N., Nakatsuka, H., Maekawa, H., Harashima, S., Nakanishi, Y., et al. (2016). Core regulatory components of the PHO pathway are conserved in the methylotrophic yeast *Hansenula polymorpha*. *Curr. Genet.* 62, 595–605. doi: 10.1007/s00294-016-0565-7

Zhu, L., Huang, R., Zhou, L., Xi, Y., and Xiang, X. (2021). Responses of the ecological characteristics and antioxidant enzyme activities in *Rotaria rotatoria* to UV-B radiation. *Hydrobiologia* 848, 4749–4761.

Conflict of Interest: The authors declare that the research was conducted in the absence of any commercial or financial relationships that could be construed as a potential conflict of interest.

Publisher's Note: All claims expressed in this article are solely those of the authors and do not necessarily represent those of their affiliated organizations, or those of the publisher, the editors and the reviewers. Any product that may be evaluated in this article, or claim that may be made by its manufacturer, is not guaranteed or endorsed by the publisher.

frontiers | Frontiers in Microbiology

ORIGINAL RESEARCH
published: 23 June 2022
doi: 10.3389/fmicb.2022.924447

Deletion of the Loop Linking Two Domains of Exo-Inulinase InuAMN8 Diminished the Enzymatic Thermo-Halo-Alcohol Tolerance

Xiaolong Cen[1,2,3,4], *Rui Zhang*[1,2,3,4], *Limei He*[1,2,3,4], *Xianghua Tang*[1,2,3,4], *Qian Wu*[1,2,3,4], *Junpei Zhou*[1,2,3,4]* *and Zunxi Huang*[1,2,3,4]*

[1] *Engineering Research Center of Sustainable Development and Utilization of Biomass Energy, Ministry of Education, Yunnan Normal University, Kunming, China,* [2] *College of Life Sciences, Yunnan Normal University, Kunming, China,* [3] *Key Laboratory of Biomass Energy and Environmental Biotechnology, Yunnan Normal University, Kunming, China,* [4] *Key Laboratory of Yunnan Provincial Education Department for Plateau Characteristic Food Enzymes, Yunnan Normal University, Kunming, China*

Inulin is the rich water-soluble storage polysaccharide after starch in nature, and utilization of inulin through hydrolysis of exo-inulinases has attracted much attention. Thermo-halo-alcohol tolerance is essential for exo-inulinase applications, while no report reveals the molecular basis involved in halo-alcohol tolerance of exo-inulinases *via* experimental data. In this study, two loops of exo-inulinase InuAMN8, including the loop built with ^{360}GHVRLGPQP^{368} linking domains of Glyco_hydro_32N and Glyco_hydro_32C and another loop built with ^{169}GGAG^{172} in the catalytic domain, were deleted to generate mutants MutG360Δ9 and MutG169Δ4, respectively. After heterologous expression, purification, and dialysis, InuAMN8, MutG169Δ4, and MutG360Δ9 showed half-lives of 144, 151, and 7 min at 50°C, respectively. InuAMN8 and MutG169Δ4 were very stable, while MutG360Δ9 showed a half-life of approximately 60 min in 5.0% (w/v) NaCl, and they showed half-lives of approximately 60 min in 25.0, 25.0, and 5.0% (w/v) ethanol, respectively. Structural analysis indicated that two cation-π bonds, which contributed to thermal properties of InuAMN8 at high temperatures, broke in MutG360Δ9. Four basic amino acid residues were exposed to the structural surface of MutG360Δ9 and formed positive and neutral electrostatic potential that caused detrimental effects on halo-alcohol tolerance. The study may provide a better understanding of the loop-function relationships that are involved in thermo-halo-alcohol adaptation of enzymes in extreme environment.

Keywords: inulinase, loop, thermostability, salt, alcohol, structure, mechanism, mutagenesis

OPEN ACCESS

Edited by:
Li Liao,
Polar Research Institute of China, China

Reviewed by:
Mustafa Germeç,
Akdeniz University, Turkey
Wujun Liu,
Dalian Medical University, China

***Correspondence:**
Junpei Zhou
junpeizhou@ynnu.edu.cn;
junpeizhou@126.com
Zunxi Huang
huangzunxi@163.com

Specialty section:
This article was submitted to Extreme Microbiology, a section of the journal Frontiers in Microbiology

Received: *20 April 2022*
Accepted: *31 May 2022*
Published: *23 June 2022*

Citation:
Cen X, Zhang R, He L, Tang X, Wu Q, Zhou J and Huang Z (2022) Deletion of the Loop Linking Two Domains of Exo-Inulinase InuAMN8 Diminished the Enzymatic Thermo-Halo-Alcohol Tolerance. Front. Microbiol. 13:924447. doi: 10.3389/fmicb.2022.924447

INTRODUCTION

Jerusalem artichoke is widely cultivated in China, even in saline-alkaline soils or coastal shoals, as a non-grain crop and also widely distributed in tropical and temperate countries across the world, since the crop has the advantages of rapid growth as well as the high resistance to pets, cold, drought, salt, and alkali conditions (Qiu et al., 2018; Singh et al., 2019). Tuberous roots of Jerusalem artichoke store inulin with an abundant content as high as 80% of the carbohydrates (Qiu et al., 2018). Inulin is well-known as the rich storage polysaccharide after starch in nature, thus, its utilization has attracted much attention (Singh et al., 2019).

Inulin is a hot-water-soluble polyfructan with a linear structure linked by β-D-(2→1) fructosides and ended by a (1→2) α-D-glucose unit (Qiu et al., 2018; Singh et al., 2019). Compared with other renewable biomass such as lignin, cellulose, hemicellulose, and chitin, biotransformation of inulin is easier on account of the higher water solubility and lower structure heterogeneity and complexity (Saha, 2003; Geib et al., 2008; Stoykov et al., 2015; Singh et al., 2019).

Hydrolysis of inulin using exo-inulinases is a convenient and efficacious biotransformation way owing to that a high-content (90–95%) fructose syrup, which is more than 2-fold fructose concentration produced *via* conventional multienzymatic transformation of starch, is directly produced through the single-step hydrolysis process (Singh et al., 2018a). Fructose syrup is a generally recognized as safe (GRAS) food ingredient and has been widely used as a sweetener in various food and beverage such as Coca-Cola and Pepsi (Singh et al., 2018a). Fructose is also being used in pharmaceutical industries as the capsule formulation and infusion or injection solution and used as fermentable sugar to produce various valuable chemicals such as butanol, ethanol, single-cell oils, sorbitol, lactic acid, succinic acid, and poly-(γ-glutamic acid) (Qiu et al., 2018; Singh et al., 2019, 2022).

Thermo-halo-alcohol tolerance is essential for enzyme applications in various biotechnology industries. For example, enzymes with good thermal tolerance usually show the advantages of a high reaction rate and solubility of substrates at a high temperature (Xu et al., 2020); salt-tolerant enzymes usually show the ability of processing high salt and marine food such as marine algae, pickles, and sauces, yielding biochemicals and biofuel using sea water (Warden et al., 2015; Cao et al., 2021); alcohol-tolerant enzymes suit for simultaneous saccharification and fermentation using microorganisms to transform biomass to butanol, ethanol, acetone, and other useful chemicals (Li et al., 2018; Singh et al., 2022).

Exo-inulinases are classified in family 32 of glycoside hydrolases (GH32), which usually consist of two domains, with the N-terminal catalytic domain belonging to Glyco_hydro_32N (PF00251) and the C-terminal domain belonging to Glyco_hydro_32C (PF08244) (Mistry et al., 2021). To date, studies on thermal properties and substrate recognition, as well as related mechanisms of exo-inulinases, have been reported (Nagem et al., 2004; Arjomand et al., 2016; Zhou S. H. et al., 2016; Singh et al., 2018b; Germec and Turhan, 2019, 2020; Ma et al., 2019, 2020; He et al., 2020, 2022; Zhang et al., 2020; Wang et al., 2021). Among these studies, deletion of loops at the N-terminal tail and catalytic domain influences the thermal performance of exo-inulinases (Arjomand et al., 2016; He et al., 2020, 2022). However, the effects of loops, especially the loop in the linking region, on the thermo-halo-alcohol tolerance of exo-inulinases remain unclear.

Previously, the low-temperature-active and salt-tolerant exo-inulinase InuAMN8 was isolated in our lab from *Arthrobacter* sp. MN8, which was a cold-adapted bacterium harbored in lead-zinc-rich soil (Zhou et al., 2015a). To the best of our knowledge, only InuAMN8 shows an optimal exo-inulinase activity at 35°C (Zhou et al., 2015a), while others show optimal exo-inulinase activity at the temperature range of equal to or higher than 40°C (Kango and Jain, 2011; Singh et al., 2017). In this study, the loop linking domains of Glyco_hydro_32N and Glyco_hydro_32C of InuAMN8 were deleted, and the effects of the loop deletion on the thermo-halo-alcohol tolerance and structural properties were investigated. The study may provide a better understanding of the loop-function relationships that are involved in thermo-halo-alcohol adaptation of enzymes in extreme environment.

MATERIALS AND METHODS

Chemicals, Plasmids, and Strains

The commercial reagents include Mut Express II Fast Mutagenesis Kit for enzyme mutagenesis (Vazyme Biotech, Nanjing, China), isopropyl-β-D-1-thiogalactopyranoside for recombinant enzyme induction (Amresco, Solon, OH, United States), *Escherichia coli* BL21 (DE3) for recombinant enzyme expression (TransGen, Beijing, China), nickel-NTA agarose for recombinant enzyme purification (Qiagen, Valencia, CA, United States), dialysis bag with a molecular weight cutoff of 44 kDa for removing the elution reagent of enzyme purification (Biosharp, Hefei, China), substrate inulin for enzymatic reaction (Thermo Fisher Scientific, Waltham, MA, United States), microplate for enzymatic assay (Corning, NY, United States), and silica gel G plate for thin-layer chromatography (Haiyang, Qingdao, China). Other commercial reagents are of analytical grade and purchased from regular suppliers.

Previously, exo-inulinase InuAMN8 (accession number AGC01505) was isolated from *Arthrobacter* sp. MN8 deposited in the Strains Collection of the Yunnan Institute of Microbiology under registration no. YMF 4.00006, and InuAMN8-encoding gene (accession number JQ863111) was ligated to vector *pEASY*-E1 (TransGen) and heterologously expressed in *E. coli* BL21 (DE3) (Zhou et al., 2015a).

Multiple Amino Acid Sequences Alignment and Structure Modeling

Representative amino acid sequences of GH32 from the Pfam database (Mistry et al., 2021) and InuAMN8 were aligned using Clustal X (Chenna et al., 2003), then manually adjusted. The tertiary structures of InuAMN8 and its mutants were homologously modeled using SwissModel (Guex et al., 2009), and model quality was evaluated using Verify3D (Eisenberg et al., 1997) and PROCHECK (Laskowski et al., 1993) programs ran on the SAVES server of the UCLA-DOE Institute for Genomics and Proteomics. Structures of InuAMN8 and its mutants were visualized using the Discovery Studio software (Accelrys, San Diego, CA, United States).

Vectors of Mutants Construction

Primer sets for mutagenesis were designed using the CE Design software (Vazyme Biotech), with the expression plasmid (*pEASY-inuAMN8*) of wild-type InuAMN8 as a sequence template, which was constructed previously (Zhou et al., 2015a). The primer set for mutant MutG169Δ4 (deletion of residues ^{169}GGAG^{172}) was

TGGTACGACAGTTACTGGGTGATGGTCGCCGTC and CCAGTAACTGTCGTACCAAAAAACCTTTGGATC. The primer set for mutant MutG360Δ9 (deletion of residues ^{360}GHVRLGPQP^{368}) was AGCGGGAAACATTGGCGTCCGGCGTTCTG and ACGCCAATGTTTCCCGCTCCGGCAA. The primer set for mutant MutV376Δ5 (deletion of residues ^{376}VPAAA^{380}) was GTTCTGGACTCCGTGGCGCGGATCGAC and CGCCACGGAGTCCAGAACGCCGGACGC.

According to the manufacturer's instructions of Mut Express II Fast Mutagenesis Kit V2, mutated vectors were obtained *via* amplification with polymerase chain reaction, digestion with restriction enzyme *Dpn*I, and homologous recombination with the enzyme Exnase.

Recombinant Enzyme Induction and Heterologous Expression

The *E. coli* BL21 (DE3) competent cells were $CaCl_2$-heat-shocked for the transformation of the mutated vectors. After that, mutated vectors were methylated in *E. coli* BL21 (DE3) cells. Positive transformants harboring the mutated sequences were individually confirmed by DNA sequencing of plasmids (Tsingke, Beijing, China).

Details of mutated enzyme induction and heterologous expression are the same as that of wild-type InuAMN8 and have been described previously (Zhou et al., 2015a). Briefly, the induction and expression of recombinant enzyme were performed using isopropyl-β-D-1-thiogalactopyranoside as an induction reagent, Luria-Bertani broth with 100 mg ml^{-1} ampicillin as culture medium, and shaking at 200 rpm and 20°C for approximately 20 h as induction conditions.

Recombinant Enzyme Purification and Dialysis

Wild-type InuAMN8 and its mutants were expressed inside the cells of *E. coli* BL21 (DE3). The host cells were harvested by centrifugation at 12,000 × *g* for 10 min at 20°C and then disrupted by sonication (20–24 kHz) on ice, as described previously (Zhou et al., 2015a). Recombinant enzymes in the sonication-disrupted solution were purified using immobilized His_6-tag affinity chromatography, with the purification reagents containing 20 mM Tris–HCl (pH 7.2), 0.5 M NaCl, 10% (w/v) glycerol, and 300 mM imidazole.

With regard to the effects of NaCl and glycerol on exo-inulinase property (Zhou et al., 2014, 2015a), the elution of affinity chromatography, which contained purified enzymes, were dialyzed with the dialysis bag against McIlvaine buffer (pH 7.0) at 12°C, shaking at 60 rpm for an appropriate time.

The purity of purified wild-type InuAMN8 and its mutants were evaluated by sodium dodecyl sulfate-polyacrylamide gel electrophoresis (SDS-PAGE) experiments.

Recombinant Enzyme Characterization

Exo-inulinase activity of purified wild-type InuAMN8 and its mutants were determined by the classic 3,5-dinitrosalicylic acid (DNS) method (Miller, 1959), with 450 μl of 0.5% (w/v) inulin solution used as the substrate. After the substrate preheat at the reaction temperature, 50 μl of purified wild-type InuAMN8 or the mutated enzyme was pipetted into the substrate solution to initiate the catalytic activity. To stop the catalytic activity, 750 μl of the DNS reagent was pipetted into the reaction mixture. The hydrolytic products, including fructose and a small amount of glucose, reacted with DNS to show a reddish-brown product in a boiling water bath. The absorption of the reddish-brown product was measured at 540 nm using a microplate reader. One unit of exo-inulinase activity was defined as the amount of enzyme releasing 1 μmol of fructose per minute. Experiments of enzyme characterization were performed in triplicate.

Activity determination of purified wild-type InuAMN8 and its mutants was individually carried out in pH 7.0 McIlvaine buffer at 0–60°C, 5.0–25.0% (w/v) NaCl, or 3.0–25.0% (v/v) ethanol. Stability determination was to measure the residual activity at 37°C in pH 7.0 McIlvaine buffer after individually incubating these purified enzymes at 50°C for 10–60 min, 5.0–25.0% (w/v) NaCl for 60 min, or 3.0–25.0% (v/v) ethanol for 60 min in the absence of inulin. More details have been described in the previous study (Zhou et al., 2015a). Half-lives of enzymes at 50°C ($t_{1/2}$) were calculated according to the stability data using the equation: Half-life = $\ln 0.5/(-k_d)$, where k_d is the slope plotted with ln(activity) vs. time.

The thin-layer chromatography method, performed as described previously (Zhou et al., 2015a), was employed to visualize the hydrolysis products of purified wild-type InuAMN8 and its mutants toward inulin, after enzymatic reactions carried out at 37°C, pH 7.0 for 4 h.

Structural Analyses of Enzymes

Intraprotein interactions of InuAMN8 and its mutants, including salt bridges (oxygen-nitrogen distance cutoff: 3.2Å) and energetically significant cation-π interactions (distance cutoff: 6.0 Å), were predicted using VMD (Humphrey et al., 1996) and CaPTURE (Gallivan and Dougherty, 1999), respectively, and visualized using the Discovery Studio software (Accelrys).

RESULTS

Multiple Amino Acid Sequences Alignment and Structure Modeling

The homology model of InuAMN8 ranking first in the SwissModel modeling results was selected for the study. The model used the exo-inulinase from *Aspergillus awamori* var. 2250 (PDB ID 1Y4W) as template (Arand et al., 2002), with an amino acid sequence identity of 42.1%. The Ramachandran plot of the InuAMN8 model generated with PROCHECK showed 99% residues in allowed regions (**Supplementary Figure 1**). VERIFY3D results of the InuAMN8 model indicated that 99.39% of the residues had an averaged 3D-1D score equal to or higher than 0.2 (**Supplementary Figure 2**).

To identify the suitable mutagenesis region, multiple amino acid sequences alignment and structure model were combined to analyze. The alignment of InuAMN8 with representative amino acid sequences of GH32 showed an unconserved region from residues P355–I385 of InuAMN8 (**Figure 1**). The InuAMN8

model indicated that two loops were built with residues P355–I385, including one loop built with ^{360}GHVRLGPQP^{368} linking domains of Glyco_hydro_32N and Glyco_hydro_32C, as well as another loop built with ^{376}VPAAA^{380} (**Figure 2**). Thus, the deletion of ^{360}GHVRLGPQP^{368} and ^{376}VPAAA^{380} was performed to generate mutants MutG360Δ9 and MutV376Δ5, respectively. Furthermore, domains of Glyco_hydro_32N and Glyco_hydro_32C of InuAMN8 were also linked by a 3_{10}-helix plus β-strands structure built with residues N312–I351 (designated as LK1) and a 3_{10}-helix structure built with residues D352–T359 (designated as LK2) (**Figure 2**).

Nine **Ω**-loops were observed in the catalytic domain of Glyco_hydro_32N of exo-inulinases (Arjomand et al., 2016). Two of the nine **Ω**-loops have been deleted previously and resulted in thermostability loss of exo-inulinases (Arjomand et al., 2016; He et al., 2022). To compare the effects between the deletion of the **Ω**-loop in the catalytic domain and the loop built with ^{360}GHVRLGPQP^{368} in the linking region on thermo-halo-alcohol tolerance, the **Ω**-loop built with ^{169}GGAG^{172} in the catalytic domain was also deleted to generate the mutant MutG169Δ4 (**Figure 2**).

Enzyme Expression in *Escherichia coli*

The expression vectors for mutants MutG169Δ4, MutG360Δ9, and MutV376Δ5 were successfully constructed using the Mut Express II Fast Mutagenesis Kit V2 and then transformed to *E. coli* BL21 (DE3) competent cells separately. After induction of positive transformants with isopropyl-β-D-1-thiogalactopyranoside, enzymatic activities of MutG169Δ4 and MutG360Δ9 toward inulin were observed in the supernatant of disrupted cells solution. In contrast, the enzymatic activity of MutV376Δ5 was not observed.

Crude MutG169Δ4, MutG360Δ9, and MutV376Δ5, as well as the wild-type InuAMN8 in the supernatant of disrupted cells solution, were individually loaded onto nickel-NTA agarose gel columns and eluted with the purification reagents containing 20 mM Tris–HCl (pH 7.2), 0.5 M NaCl, 10% (w/v) glycerol, and 300 mM imidazole. Elutions were dialyzed against McIlvaine buffer (pH 7.0) on account of the effects of NaCl and glycerol in the elution on exo-inulinase property (Zhou et al., 2014, 2015a). As shown in **Figure 3**, SDS-PAGE analysis indicated that the wild-type InuAMN8 and its mutants MutG169Δ4 and MutG360Δ9 were successfully heterologously expressed and purified to electrophoretic purity, while the band of mutant MutV376Δ5 was not observed. SDS-PAGE and enzymatic activity assay indicated that the mutant MutV376Δ5 was not expressed in *E. coli* BL21 (DE3). Thus, thermo-halo-alcohol characteristics of MutV376Δ5 were not determined.

Thermo-Halo-Alcohol Characteristics of Purified Enzymes

The thermal activity assay indicated that purified wild-type InuAMN8 and its mutants MutG169Δ4 and MutG360Δ9 were maximally active at 35, 40, and 35°C, respectively (**Figure 4A**). All of the three enzymes showed approximately 15% relative activity at 0°C, while InuAMN8, MutG169Δ4, and MutG360Δ9 showed 40.0, 52.1, and 11.6% relative activities at 50°C, respectively (**Figure 4A**). The thermostability assay indicated that purified wild-type InuAMN8 showed 88.3–82.4% residual activities after incubation of the enzyme at 50°C for 10–60 min (**Figure 4B**). At the same incubation conditions, MutG169Δ4 showed 97.9–76.2% residual activities, while MutG360Δ9 showed only 12.9–0% residual activities (**Figure 4B**). Values of $t_{1/2}$ at 50°C were 144, 151, and 7 min for InuAMN8, MutG169Δ4, and MutG360Δ9, respectively. Thus, the above results revealed that the thermal tolerance of exo-inulinase InuAMN8 was affected slightly after ^{169}GGAG^{172} deletion while that diminished greatly after ^{360}GHVRLGPQP^{368} deletion.

The halo tolerance and alcohol tolerance of exo-inulinase InuAMN8 were also affected slightly after ^{169}GGAG^{172} deletion, while that were diminished greatly after ^{360}GHVRLGPQP^{368} deletion. Adding 5.0–20.0% (w/v) NaCl to the reaction mixture, InuAMN8, MutG169Δ4, and MutG360Δ9 showed 79.1–28.7%, 75.7–24.6%, and 55.8–16.2% of the initial activity, respectively (**Figure 4C**). After incubation of purified enzymes in 5.0–25.0% (w/v) NaCl for 60 min, InuAMN8 and MutG169Δ4 were very stable as activity loss was not observed, while MutG360Δ9 showed only 47.0–20.5% residual activities, with a half-life value of approximately 60 min in 5.0% (w/v) NaCl (**Figure 4D**). Adding 3.0–10.0% (v/v) ethanol to the reaction mixture, InuAMN8, MutG169Δ4, and MutG360Δ9 showed 70.8–32.9, 79.6–33.6, and 53.8–14.6% of the initial activity, respectively (**Figure 4E**). After incubation of purified enzymes in 3.0–25.0% (w/v) ethanol for 60 min, InuAMN8, MutG169Δ4, and MutG360Δ9 showed 96.3–57.4, 97.0–58.7, and 74.3–12.2% residual activities, respectively (**Figure 4F**). Half-life values of InuAMN8, MutG169Δ4, and MutG360Δ9 were approximately 60 min in 25.0, 25.0, and 5.0% (w/v) ethanol, respectively.

Regarding the unclear mechanisms of exo-action and endo-action of GH 32 exo-inulinases, thin-layer chromatography was performed. It showed that fructose was the end-product of inulin hydrolysis by InuAMN8, MutG169Δ4, and MutG360Δ9. The results revealed that the deletion of ^{169}GGAG^{172} and ^{360}GHVRLGPQP^{368} did not change the exo-action mode of the enzyme.

Structural Characteristics

To compare structural characteristics between wild-type InuAMN8 and its mutants, the homology models of MutG169Δ4 and MutG360Δ9 were also successfully built using the exo-inulinase from *A. awamori* var. 2250 (PDB ID 1Y4W) as a template. The Ramachandran plot of MutG169Δ4 and MutG360Δ9 models generated with PROCHECK showed 99.0 and 98.8% residues in allowed regions, respectively (**Supplementary Figure 1**). VERIFY3D results of MutG169Δ4 and MutG360Δ9 models indicated that 99.8 and 92.7% of the residues had an averaged 3D-1D score equal to or higher than 0.2, respectively (**Supplementary Figure 2**).

The numbers of salt bridges detected in the tertiary structures of InuAMN8, MutG169Δ4, and MutG360Δ9 were 27, 26, and 27, respectively. The numbers of energetically significant cation-π interactions detected in the tertiary structures of InuAMN8, MutG169Δ4, and MutG360Δ9 were 6, 7, and 4, respectively.

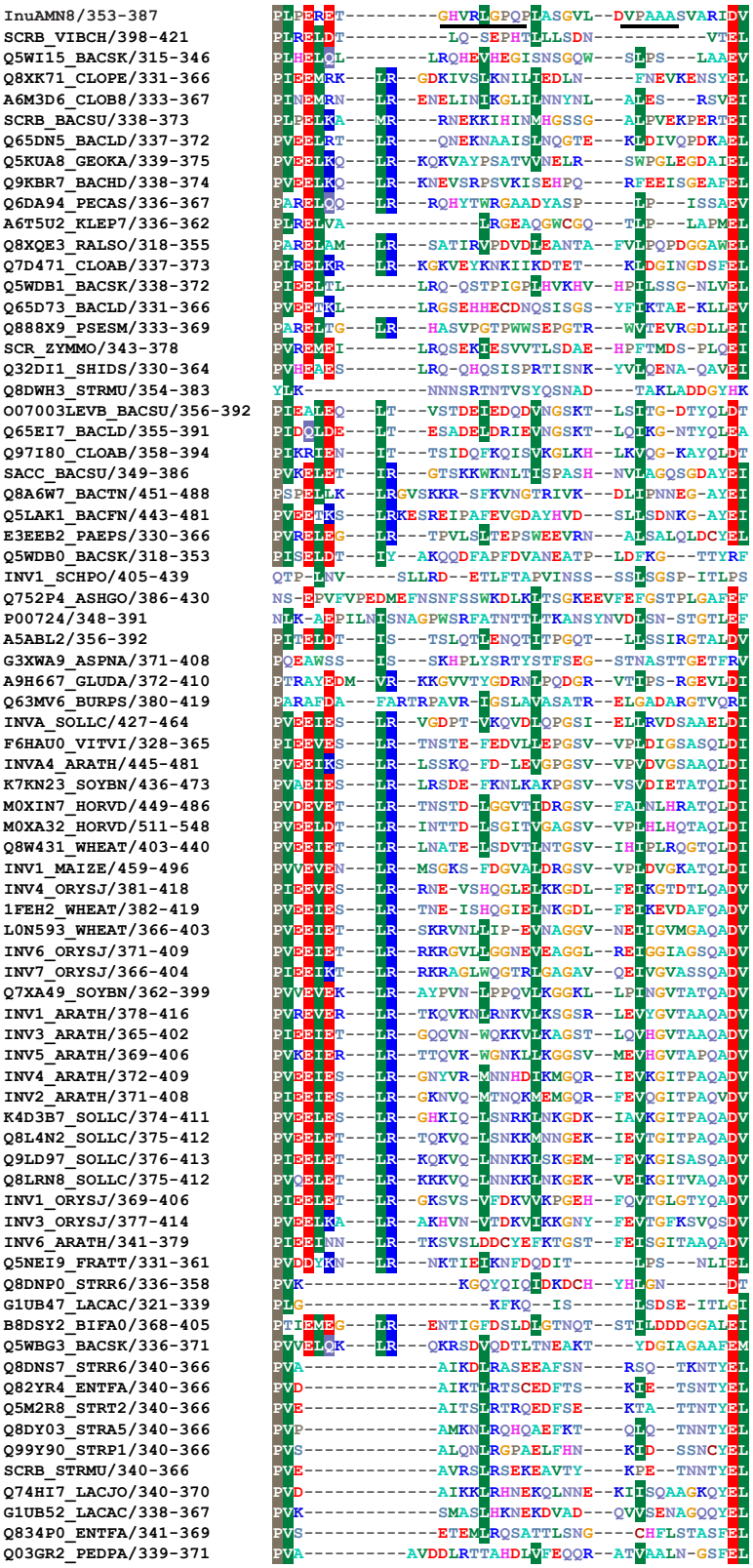

FIGURE 1 | Partial alignment of amino acid residues of InuAMN8 with seed sequences of GH 32 from Pfam database (Mistry et al., 2021). Residues ^{360}GHVRLGPQP^{368} and ^{376}VPAAA^{380} selected for mutagenesis are underlined.

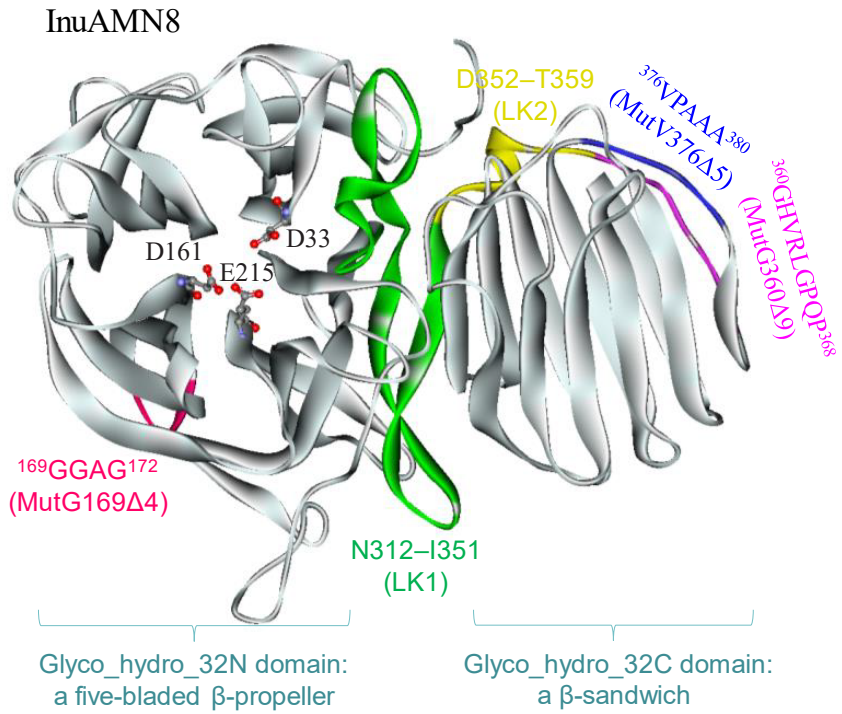

FIGURE 2 | The tertiary structure of InuAMN8. Catalytic amino acid residues are shown in ball and stick form.

Notably, two cation-π interactions formed by amino acid residues F22 with R357 and F436 with R424 in InuAMN8 broke in MutG360Δ9 (**Figure 5**).

After removing ^{360}GHVRLGPQP^{368}, LK2 changed from a 3_{10}-helix structure into a loop structure (**Figure 6**), and the residue R357 in LK2 was too far away from F22 to form a cation-π bond (**Figure 5**). The change of LK2 and break of the cation-π bond showed a Tamino domino effect on the Glyco_hydro_32C structure and the linking region: (1) the cation-π bond formed by F436 with R424 far from LK2 broke in the mutant MutG360Δ9 (**Figure 5**); (2) two basic amino acid residues R19 and R450 were exposed to the structural surface and changed the corresponding surface from negative electrostatic potential to positive electrostatic potential (**Figure 6A**); and (3) another two basic amino acid residues R339 and K343 in LK1 were also exposed to the structural surface and changed the corresponding surface from negative electrostatic potential to positive and neutral electrostatic potential (**Figure 6B**). However, the removal of ^{169}GGAG^{172} did not expose any basic residue and changed surface potential (**Figure 6C**).

DISCUSSION

Loop structure plays an important role in the thermal performance of enzymes because it is usually located on the structural surface and has high flexibility that reduces the thermostability of enzymes (Vieille and Zeikus, 2001; Yu and Huang, 2014; Pucci and Rooman, 2017). To improve the thermostability of enzymes, loop structure is usually substituted, deleted, or shortened, such as in the studies for the effects of loops on the mannanase Man1312 from *Bacillus subtilis* B23 (Zhou H. Y. et al., 2016), the phospholipase D from *Streptomyces antibioticus* PLD (Damnjanovic et al., 2014), and the acylphosphatase from human muscle (Dagan et al., 2013). Loop structure also affected the thermal performance of exo-inulinases (Arjomand et al., 2016; He et al., 2022). Previously, Ω-loop 3 formed by ^{74}YGSDVT^{79} of the exo-inulinase from *Aspergillus niger* 5012 was deleted and resulted in the optimum temperature decrease by 12°C and $t_{1/2}$ decrease by 32 h at 60°C compared with the wild-type enzyme (Arjomand et al., 2016); Ω-loop 5 formed by ^{137}EEDRK^{141} of the exo-inulinase InuAGN25 from *Sphingobacterium* sp. GN25 was deleted and resulted in the optimum temperature decrease by 10°C and $t_{1/2}$ decrease by 31.7 min at 50°C compared with the wild-type

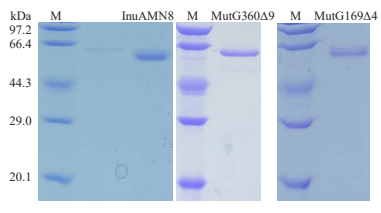

FIGURE 3 | Sodium dodecyl sulfate-polyacrylamide gel electrophoresis analysis of purified wild-type InuAMN8 and its mutants. Lane M, protein molecular weight marker.

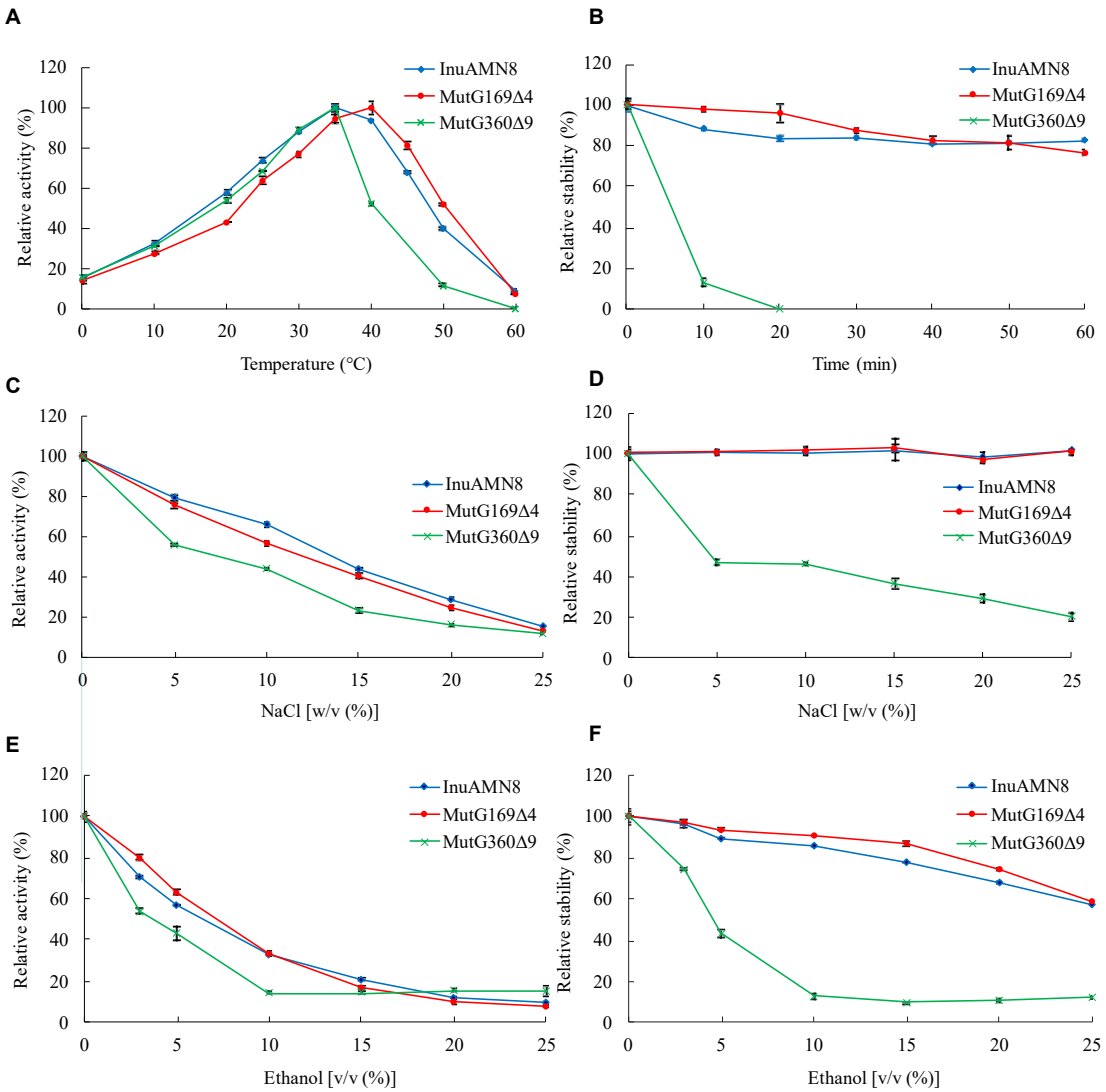

FIGURE 4 | Thermo-halo-alcohol characteristics of purified wild-type InuAMN8 and its mutants. **(A,C,E)** indicate activity assay; **(B,D,F)** indicate stability assay. The error bars represent the means ± SD (n = 3).

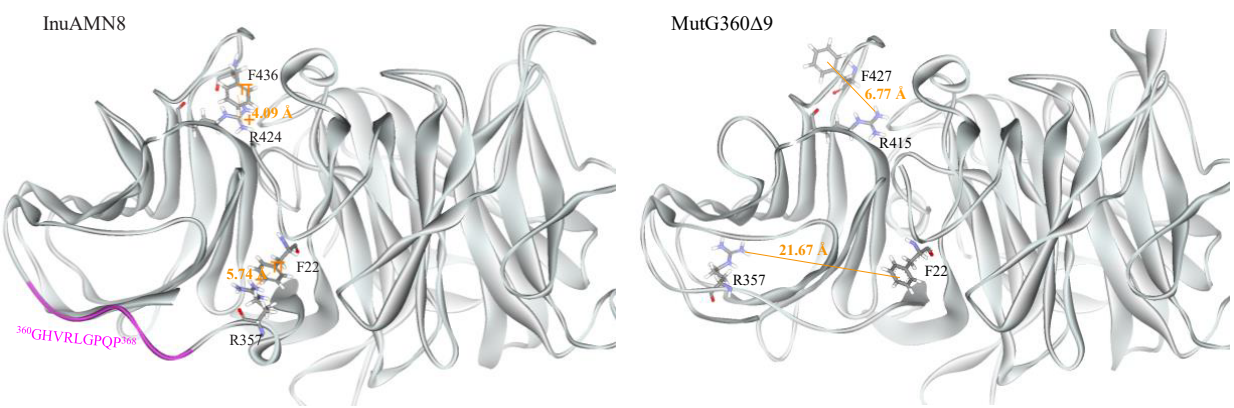

FIGURE 5 | Comparisons of cation-π interactions between wild-type InuAMN8 and MutG360Δ9. Residues involved in cation-π interactions are shown in *stick* form.

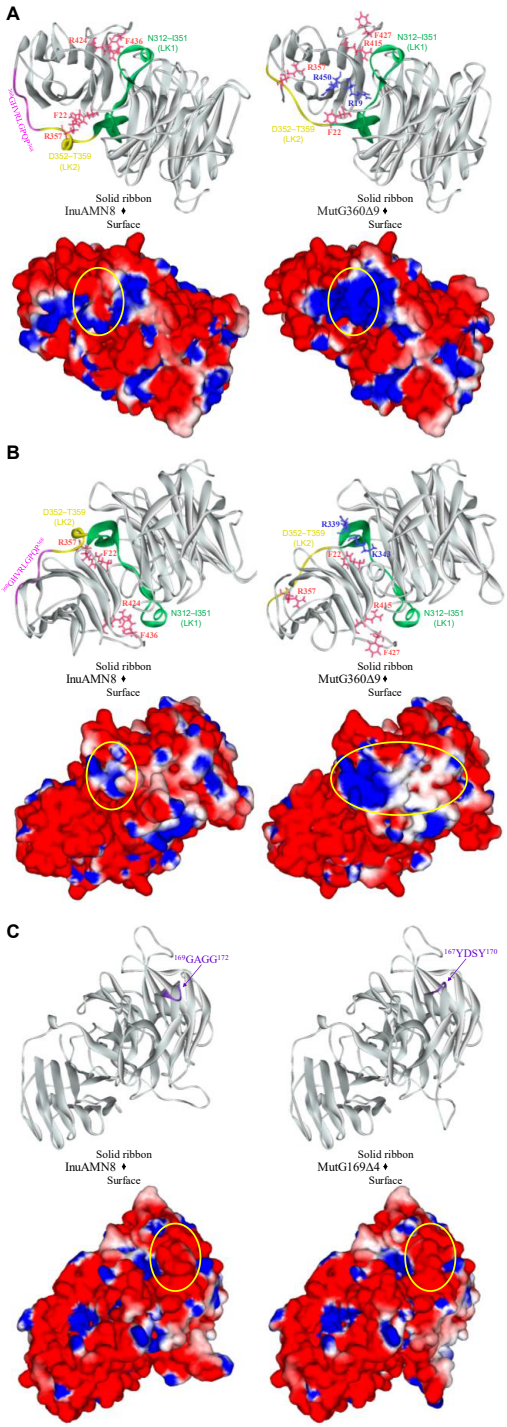

FIGURE 6 | Comparisons of structures and charge distributions between wild-type InuAMN8 and its mutants. **(A)** Comparisons of structures and charge distributions between wild-type InuAMN8 and MutG360Δ9; **(B)** 180 degree rotation view of panel **(A)**; **(C)** comparisons of structures and charge distributions between wild-type InuAMN8 and MutG169Δ4. Positive charges are shown in *blue*, and negative charges are shown in *red*. The charge-changed surfaces are *circled*. Residues involved in charge-changed surfaces are shown in *blue* and *stick* form. Residues involved in cation-π interactions are shown in *peach* and *stick* form.

enzyme (He et al., 2022). Both Ω-loop 3 and Ω-loop 5 are in the catalytic Glyco_hydro_32N domain. In this study, deletion of the Ω-loop formed by ^{360}GHVRLGPQP^{368} in the linking region led similar thermal tolerance loss to previous studies for exo-inulinases; however, deletion of the Ω-loop formed by ^{169}GGAG^{172} in the catalytic Glyco_hydro_32N domain did not lead thermal tolerance loss.

Thermal characteristics of enzymes are usually engineered through mutation for unconserved amino acid residue sites involved in intraprotein interactions (Vieille and Zeikus, 2001; Yu and Huang, 2014; Pucci and Rooman, 2017). Intraprotein interactions, including salt bridges and cation–π interactions, usually help to improve global and local rigidity of enzyme structure that hampers thermal denaturation of enzymes (Vieille and Zeikus, 2001; Pucci and Rooman, 2017; Siddiqui, 2017). A decrease in intraprotein interactions after loop deletion led to thermostability loss of exo-inulinases from *A. niger* 5012 and *Sphingobacterium* sp. GN25 (Arjomand et al., 2016; He et al., 2020, 2022). On the contrary, an increase in intraprotein interactions resulted in the thermostability enhancement of the exo-inulinase from *Sphingobacterium* sp. GN25 (He et al., 2020; Zhang et al., 2020). Therefore, the close numbers of salt bridges and cation-π interactions should be responsible for similar thermal characteristics of InuAMN8 and its mutant MutG169Δ4. In contrast, the loss of two cation-π interactions in MutG360Δ9 compared with InuAMN8 should play an important role for thermostability loss of the mutant.

In recent years, salt-tolerant enzymes have attracted much attention owing to their commercial and environmental values (Cao et al., 2021). The exo-inulinases from *Arthrobacter* strains HJ7 and MN8 and *Sphingomonas* sp. JB13 were observed to exhibit considerable salt tolerance, without a clear elucidation of structural characteristics and mechanisms regarding salt tolerance (Shen et al., 2015; Zhou et al., 2015a,b). Comparisons of biochemical and structural properties among InuAMN8 and its mutants MutG169Δ4 and MutG360Δ9 in this study revealed that salt tolerance showed a positive correlation with the negatively charged surface. Few studies also increased the negatively charged surfaces of enzymes through site-directed mutagenesis and caused the activity or stability enhancement of enzymes in salts (Warden et al., 2015) and vice versa (Li et al., 2019). To the best of our knowledge, most salt-tolerant enzymes have a structural characteristic of a larger negatively charged surface than their salt-sensitive counterparts, owing to that the negative electrostatic potential is capable of competing with salt ions for water molecules to form a stable hydration sphere that separates the protein molecules from each other in solution to avoid aggregating and collapsing (Warden et al., 2015; Cai et al., 2018; Cao et al., 2021).

Ethanol production using inulin is affected by ethanol tolerance of microbial strains and enzymes (Guo et al., 2013). However, alcohol-tolerant inulinases and related structural characteristics and mechanisms have not been reported. The molecular basis for enhanced tolerance of enzymes in organic solvents is very complex (Klibanov, 2001; Cui et al., 2020, 2021). Structural flexibility allows conformational mobility in increased

intraprotein electrostatic interactions caused by organic solvents and then plays an important role in maintaining enzymatic activities (Klibanov, 2001; Li et al., 2018). The charged surface also contributes to the organic-solvent tolerance of enzymes. Some studies indicated that the activities or stabilities of enzymes improved, after that structural surfaces were substituted with charged electrostatic potential (Cui et al., 2020, 2021). For example, Cui et al. (2021) reported that the mutant M4 (I12R/Y49R/E65H/N98R/K122E/L124K) of *B. subtilis* lipase A was introduced charged amino acids to the structural surface and showed 2.1-fold activity increase in 30% (v/v) ethanol, in comparison with the wild-type enzyme. Therefore, the similar structural surface electrostatic potential resulted in similar alcohol-tolerant characteristics of InuAMN8 and its mutant MutG169Δ4, while the decrease in charged surface, especially negatively charged surface, in MutG360Δ9 compared with InuAMN8 accounted for the alcohol-tolerant loss of the mutant.

CONCLUSION

The study revealed that the loop, which was constructed by ^{360}GHVRLGPQP^{368} for linking domains of Glyco_hydro_32N and Glyco_hydro_32C of InuAMN8, affected thermo-halo-alcohol tolerance and structural properties. The loop was involved in the formation of two energetically significant cation-π bonds, which contributed to thermal properties of InuAMN8 at high temperatures. The loop was also involved in burying four basic amino acid residues with the ability to change the surface from negative electrostatic potential to positive and neutral electrostatic potential that caused detrimental effects on halo-alcohol tolerance. In the future, the loop in the linking region may be given attention for protein engineering in improving enzymatic properties in harsh environments.

DATA AVAILABILITY STATEMENT

The datasets presented in this study can be found in online repositories. The names of the repository/repositories and accession number(s) can be found in the article/ **Supplementary Material**.

AUTHOR CONTRIBUTIONS

JZ and ZH: conceptualization. XC, RZ, and LH: data curation. XC and LH: formal analysis. JZ: funding acquisition, writing – review and editing, and methodology. ZH: project administration. XT, QW, and ZH: resources. RZ: writing – original draft. All authors contributed to the article and approved the submitted version.

FUNDING

This research was funded by the National Natural Science Foundation of China, grant numbers 31660445 and 31960459; the Yunnan Fundamental Research Projects, grant number 202001AS070022; and the Yunnan Ten Thousand Talents Plan Young & Elite Talents Project, grant number YNWR-QNBJ-2018-383. The APC was funded by 31660445.

SUPPLEMENTARY MATERIAL

The Supplementary Material for this article can be found online at: https://www.frontiersin.org/articles/10.3389/fmicb.2022.924447/full#supplementary-material

REFERENCES

Arand, M., Golubev, A. M., Neto, J. R. B., Polikarpov, I., Wattiez, R., Korneeva, O. S., et al. (2002). Purification, characterization, gene cloning and preliminary X-ray data of the exo-inulinase from *Aspergillus awamori*. *Biochem. J.* 362, 131–135. doi: 10.1042/0264-6021:3620131

Arjomand, M. R., Habibi-Rezaei, M., Ahmadian, G., Hassanzadeh, M., Karkhane, A. A., Asadifar, M., et al. (2016). Deletion of loop fragment adjacent to active site diminishes the stability and activity of exo-inulinase. *Int. J. Biol. Macromol.* 92, 1234–1241. doi: 10.1016/j.ijbiomac.2016.08.039

Cai, Z. W., Ge, H. H., Yi, Z. W., Zeng, R. Y., and Zhang, G. Y. (2018). Characterization of a novel psychrophilic and halophilic β-1, 3-xylanase from deep-sea bacterium, *Flammeovirga pacifica* strain WPAGA1. *Int. J. Biol. Macromol.* 118, 2176–2184. doi: 10.1016/j.ijbiomac2018.07.090

Cao, L., Zhang, R., Zhou, J. P., and Huang, Z. X. (2021). Biotechnological aspects of salt-tolerant xylanases: a review. *J. Agr. Food Chem.* 69, 8610–8624. doi: 10.1021/acs.jafc.1c03192

Chenna, R., Sugawara, H., Koike, T., Lopez, R., Gibson, T. J., Higgins, D. G., et al. (2003). Multiple sequence alignment with the clustal series of programs. *Nucleic Acids Res.* 31, 3497–3500. doi: 10.1093/nar/gkg500

Cui, H. Y., Jaeger, K. E., Davari, M. D., and Schwaneberg, U. (2021). CompassR yields highly organic-solvent-tolerant enzymes through recombination of compatible substitutions. *Chem. Eur. J.* 27, 2789–2797. doi: 10.1002/chem.202004471

Cui, H. Y., Zhang, L. L., Eltoukhy, L., Jiang, Q. J., Korkunc, S. K., Jaeger, K. E., et al. (2020). Enzyme hydration determines resistance in organic cosolvents. *ACS Catal.* 10, 14847–14856. doi: 10.1021/acscatal.0c03233

Dagan, S., Hagai, T., Gavrilov, Y., Kapon, R., Levy, Y., and Reich, Z. (2013). Stabilization of a protein conferred by an increase in folded state entropy. *Proc. Natl. Acad. Sci. U.S.A.* 110, 10628–10633. doi: 10.1073/pnas.1302284110

Damnjanovic, J., Nakano, H., and Iwasaki, Y. (2014). Deletion of a dynamic surface loop improves stability and changes kinetic behavior of phosphatidylinositol-synthesizing *Streptomyces phospholipase* D. *Biotechnol. Bioeng.* 111, 674–682. doi: 10.1002/bit.25149

Eisenberg, D., Luthy, R., and Bowie, J. U. (1997). VERIFY3D: assessment of protein models with three-dimensional profiles. *Methods Enzymol.* 277, 396–404. doi: 10.1016/s0076-6879(97)77022-8

Gallivan, J. P., and Dougherty, D. A. (1999). Cation-π interactions in structural biology. *Proc. Natl. Acad. Sci. U.S.A.* 96, 9459–9464. doi: 10.1073/pnas.96.17.9459

Geib, S. M., Filley, T. R., Hatcher, P. G., Hoover, K., Carlson, J. E., Jimenez-Gasco, M. D., et al. (2008). Lignin degradation in wood-feeding insects. *Proc. Natl. Acad. Sci. U.S.A.* 105, 12932–12937. doi: 10.1073/pnas.0805257105

Germec, M., and Turhan, I. (2019). Evaluation of carbon sources for the production of inulinase by *Aspergillus niger* A42 and its characterization. *Bioprocess Biosyst. Eng.* 42, 1993–2005. doi: 10.1007/s00449-019-02192-9

Germec, M., and Turhan, I. (2020). Thermostability of *Aspergillus niger* inulinase from sugar beet molasses in the submerged fermentation and determination of its kinetic and thermodynamic parameters. *Biomass Convers. Bior.* 1–9. doi: 10.1007/s13399-020-00809-8

Guex, N., Peitsch, M. C., and Schwede, T. (2009). Automated comparative protein structure modeling with SWISS-MODEL and Swiss-PdbViewer: a historical perspective. *Electrophoresis* 30, S162–S173. doi: 10.1002/elps.200900140

Guo, L. H., Zhang, J., Hu, F. X., Ryu, D. D., and Bao, J. (2013). Consolidated bioprocessing of highly concentrated Jerusalem artichoke tubers for simultaneous saccharification and ethanol fermentation. *Biotechnol. Bioeng.* 110, 2606–2615. doi: 10.1002/bit.24929

He, L. M., Zhang, R., Shen, J. D., Miao, Y., Tang, X. H., Wu, Q., et al. (2020). Removal of N-terminal tail changes the thermostability of the low-temperature-active exo-inulinase InuAGN25. *Bioengineered* 11, 921–931. doi: 10.1080/21655979.2020.1809921

He, L. M., Zhang, R., Shen, J. D., Miao, Y., Zeng, C. Y., Tang, X. H., et al. (2022). Improving the low-temperature properties of an exo-inulinase via the deletion of a loop fragment located in its catalytic pocket. *Electron. J. Biotechn.* 55, 1–8. doi: 10.1016/j.ejbt.2021.09.004

Humphrey, W., Dalke, A., and Schulten, K. (1996). VMD: visual molecular dynamics. *J. Mol. Graphics* 14, 33–38. doi: 10.1016/0263-7855(96)00018-5

Kango, N., and Jain, S. C. (2011). Production and properties of microbial inulinases: recent advances. *Food Biotechnol.* 25, 165–212. doi: 10.1080/08905436.2011.590763

Klibanov, A. M. (2001). Improving enzymes by using them in organic solvents. *Nature* 409, 241–246. doi: 10.1038/35051719

Laskowski, R. A., MacArthur, M. W., Moss, D. S., and Thornton, J. M. (1993). PROCHECK: a program to check the stereochemical quality of protein structures. *J. Appl. Cryst.* 26, 283–291. doi: 10.1107/S0021889892009944

Li, N., Han, X. W., Xu, S. J., Li, C. Y., Wei, X., Liu, Y., et al. (2018). Glycoside hydrolase family 39 β-xylosidase of *Sphingomonas* showing salt/ethanol/trypsin tolerance, low-pH/low-temperature activity, and transxylosylation activity. *J. Agr. Food Chem.* 66, 9465–9472. doi: 10.1021/acs.jafc.8b03327

Li, Z., Li, X., Liu, T., Chen, S., Liu, H., Wang, H., et al. (2019). The critical roles of exposed surface residues for the thermostability and halotolerance of a novel GH11 xylanase from the metagenomic library of a saline-alkaline soil. *Int. J. Biol. Macromol.* 133, 316–323. doi: 10.1016/j.ijbiomac.2019.04.090

Ma, J., Li, T., Tan, H., Liu, W., and Yin, H. (2020). The important roles played in substrate binding of aromatic amino acids in exo-inulinase from *Kluyveromyces cicerisporus* CBS 4857. *Front. Mol. Biosci.* 7:569797. doi: 10.3389/fmolb.2020.569797

Ma, J. Y., Li, Q., Tan, H. D., Jiang, H., Li, K. K., Zhang, L. H., et al. (2019). Unique N-glycosylation of a recombinant exo-inulinase from *Kluyveromyces cicerisporus* and its effect on enzymatic activity and thermostability. *J. Biol. Eng.* 13:81. doi: 10.1186/s13036-019-0215-y

Miller, G. L. (1959). Use of dinitrosalicylic acid reagent for determination of reducing sugar. *Anal. Chem.* 31, 426–428. doi: 10.1021/ac60147a030

Mistry, J., Chuguransky, S., Williams, L., Qureshi, M., Salazar, G. A., Sonnhammer, E. L. L., et al. (2021). Pfam: the protein families database in 2021. *Nucleic Acids Res.* 49, D412–D419. doi: 10.1093/nar/gkaa913

Nagem, R. A. P., Rojas, A. L., Golubev, A. M., Korneeva, O. S., Eneyskaya, E. V., Kulminskaya, A. A., et al. (2004). Crystal structure of exo-inulinase from *Aspergillus awamori*: the enzyme fold and structural determinants of substrate recognition. *J. Mol. Biol.* 344, 471–480. doi: 10.1016/j.jmb.2004.09.024

Pucci, F., and Rooman, M. (2017). Physical and molecular bases of protein thermal stability and cold adaptation. *Curr. Opin. Struct. Biol.* 42, 117–128. doi: 10.1016/j.sbi.2016.12.007

Qiu, Y. B., Lei, P., Zhang, Y. T., Sha, Y. Y., Zhan, Y. J., Xu, Z. Q., et al. (2018). Recent advances in bio-based multi-products of agricultural Jerusalem artichoke resources. *Biotechnol. Biofuels* 11:151. doi: 10.1186/s13068-018-1152-6

Saha, B. C. (2003). Hemicellulose bioconversion. *J. Ind. Microbiol. Biot.* 30, 279–291. doi: 10.1007/s10295-003-0049-x

Shen, J. D., Zhang, R., Li, J. J., Tang, X. H., Li, R. X., Wang, M., et al. (2015). Characterization of an exo-inulinase from *Arthrobacter*: a novel NaCl-tolerant exo-inulinase with high molecular mass. *Bioengineered* 6, 99–105. doi: 10.1080/21655979.2015.1019686

Siddiqui, K. S. (2017). Defying the activity-stability trade-off in enzymes: taking advantage of entropy to enhance activity and thermostability. *Crit. Rev. Biotechnol.* 37, 309–322. doi: 10.3109/07388551.2016.1144045

Singh, R. S., Chauhan, K., and Kennedy, J. F. (2017). A panorama of bacterial inulinases: production, purification, characterization and industrial applications. *Int. J. Biol. Macromol.* 96, 312–322. doi: 10.1016/j.ijbiomac.2016.12.004

Singh, R. S., Chauhan, K., Pandey, A., and Larroche, C. (2018a). Biocatalytic strategies for the production of high fructose syrup from inulin. *Bioresource Technol.* 260, 395–403. doi: 10.1016/j.biortech.2018.03.127

Singh, R. S., Chauhan, K., Pandey, A., Larroche, C., and Kennedy, J. F. (2018b). Purification and characterization of two isoforms of exoinulinase from *Penicillium oxalicum* BGPUP-4 for the preparation of high fructose syrup from inulin. *Int. J. Biol. Macromol.* 118, 1974–1983. doi: 10.1016/j.ijbiomac.2018.07.040

Singh, R. S., Singh, T., Hassan, M., and Larroche, C. (2022). Biofuels from inulin-rich feedstocks: a comprehensive review. *Bioresource Technol.* 346:126606. doi: 10.1016/j.biortech.2021.126606

Singh, R. S., Singh, T., and Larroche, C. (2019). Biotechnological applications of inulin-rich feedstocks. *Bioresource Technol.* 273, 641–653. doi: 10.1016/j.biortech.2018.11.031

Stoykov, Y. M., Pavlov, A. I., and Krastanov, A. I. (2015). Chitinase biotechnology: production, purification, and application. *Eng. Life Sci.* 15, 30–38.

Vieille, C., and Zeikus, G. J. (2001). Hyperthermophilic enzymes: sources, uses, and molecular mechanisms for thermostability. *Microbiol. Mol. Biol. Rev.* 65, 1–43.

Wang, C. H., Xiong, W. P., Huang, C., Li, X. M., Wang, Q. Y., and Huang, R. B. (2021). Engineering better catalytic activity and acidic adaptation into *Kluyveromyces marxianus* exoinulinase using site-directed mutagenesis. *J. Sci. Food Agric.* 101, 2472–2482. doi: 10.1002/jsfa.10873

Warden, A. C., Williams, M., Peat, T. S., Seabrook, S. A., Newman, J., Dojchinov, G., et al. (2015). Rational engineering of a mesohalophilic carbonic anhydrase to an extreme halotolerant biocatalyst. *Nat. Commun.* 6:10278. doi: 10.1038/ncomms10278

Xu, Z., Cen, Y. K., Zou, S. P., Xue, Y. P., and Zheng, Y. G. (2020). Recent advances in the improvement of enzyme thermostability by structure modification. *Crit. Rev. Biotechnol.* 40, 83–98. doi: 10.1080/07388551.2019.1682963

Yu, H. R., and Huang, H. (2014). Engineering proteins for thermostability through rigidifying flexible sites. *Biotechnol. Adv.* 32, 308–315. doi: 10.1016/j.biotechadv.2013.10.012

Zhang, R., He, L. M., Shen, J. D., Miao, Y., Tang, X. H., Wu, Q., et al. (2020). Improving low-temperature activity and thermostability of exo-inulinase InuAGN25 on the basis of increasing rigidity of the terminus and flexibility of the catalytic domain. *Bioengineered* 11, 1233–1244. doi: 10.1080/21655979.2020.1837476

Zhou, S. H., Liu, Y., Zhao, Y. J., Chi, Z., Chi, Z. M., and Liu, G. L. (2016). Enhanced exo-inulinase activity and stability by fusion of an inulin-binding module. *Appl. Microbiol. Biot.* 100, 8063–8074. doi: 10.1007/s00253-016-7587-4

Zhou, H. Y., Yong, J., Gao, H., Yuan, Z. H., Yang, W. J., Tian, Y., et al. (2016). Loops adjacent to catalytic region and molecular stability of Man1312. *Appl. Biochem. Biotech.* 180, 122–135. doi: 10.1007/s12010-016-2087-7

Zhou, J. P., Gao, Y. J., Zhang, R., Mo, M. H., Tang, X. H., Li, J. J., et al. (2014). A novel low-temperature-active exo-inulinase identified based on molecular-activity strategy from *Sphingobacterium* sp. GN25 isolated from feces of *Grus nigricollis*. *Process Biochem.* 49, 1656–1663. doi: 10.1016/j.procbio.2014.06.013

Zhou, J. P., Lu, Q., Peng, M. Z., Zhang, R., Mo, M. H., Tang, X. H., et al. (2015a). Cold-active and NaCl-tolerant exo-inulinase from a cold-adapted *Arthrobacter* sp. MN8 and its potential for use in the production of fructose at low temperatures. *J. Biosci. Bioeng.* 119, 267–274. doi: 10.1016/j.jbiosc.2014.08.003

Zhou, J. P., Peng, M. Z., Zhang, R., Li, J. J., Tang, X. H., Xu, B., et al. (2015b). Characterization of *Sphingomonas* sp. JB13 exo-inulinase: a novel detergent-, salt-, and protease-tolerant exo-inulinase. *Extremophiles* 19, 383–393. doi: 10.1007/s00792-014-0724-z

Conflict of Interest: The authors declare that the research was conducted in the absence of any commercial or financial relationships that could be construed as a potential conflict of interest.

Publisher's Note: All claims expressed in this article are solely those of the authors and do not necessarily represent those of their affiliated organizations, or those of the publisher, the editors and the reviewers. Any product that may be evaluated in this article, or claim that may be made by its manufacturer, is not guaranteed or endorsed by the publisher.

frontiers | Frontiers in Microbiology

ORIGINAL RESEARCH
published: 12 July 2022
doi: 10.3389/fmicb.2022.957473

Cytotoxic Indolocarbazoles From a Marine-Derived *Streptomyces* Sp. OUCMDZ-5380

Tongxu Cui[1†], Simin Lin[1†], Zizhen Wang[1], Peng Fu[1,2], Cong Wang[3] and Weiming Zhu[1,2*]*

[1] Key Laboratory of Marine Drugs, Ministry of Education of China, School of Medicine and Pharmacy, Ocean University of China, Qingdao, China, [2] Laboratory for Marine Drugs and Bioproducts, Pilot National Laboratory for Marine Science and Technology, Qingdao, China, [3] Key Laboratory of Chemistry and Engineering of Forest Products, State Ethnic Affairs Commission, School of Chemistry and Chemical Engineering, Guangxi Minzu University, Nanning, China

Under the guidance of global natural product social molecular networking, three new indolocarbazoles named streptocarbazoles F–H (**1**-**3**), along with staurosporine (**4**) were isolated from the marine-derived *Streptomyces* sp. OUCMDZ-5380. Structures of streptocarbazoles F–H were, respectively, determined as *N*-demethyl-*N*-hexanoylstaurosporine (**1**), *N*-demethyl-*N*-(2-methyl-3-methoxypyridin-4-yl) staurosporine staurosporine (**2**), and 4-(*N*-demethylstaurosporine-*N*-yl)-1,2-dimethyl-3-methoxypyridinium (**3**) by spectroscopic analysis and electronic circular dichroism comparison with staurosporine. Compared with staurosporine (**4**), streptocarbazoles F–H (**1**-**3**) showed a selective antiproliferation of the acute myeloid leukemia cell line MV4-11 with the IC_{50} values of 0.81, 0.55, and 1.88 μM, respectively.

Keywords: indolocarbazoles, streptocarbazoles F–H, antiproliferatory activity, marine microorganism, *Streptomyces* sp.

OPEN ACCESS

Edited by:
Xian-Wen Yang,
Third Institute of Oceanography, Ministry of Natural Resources, China

Reviewed by:
Wen-Jian Lan,
Sun Yat-sen University, China
Huajie Zhu,
Hebei University of Science and Technology, China

***Correspondence:**
Cong Wang
wangcong@gxun.edu.cn
Weiming Zhu
weimingzhu@ouc.edu.cn

[†] These authors have contributed equally to this work

Specialty section:
This article was submitted to Extreme Microbiology, a section of the journal Frontiers in Microbiology

Received: *31 May 2022*
Accepted: *20 June 2022*
Published: *12 July 2022*

Citation:
Cui T, Lin S, Wang Z, Fu P, Wang C and Zhu W (2022) Cytotoxic Indolocarbazoles From a Marine-Derived Streptomyces Sp. OUCMDZ-5380. Front. Microbiol. 13:957473. doi: 10.3389/fmicb.2022.957473

INTRODUCTION

Staurosporine and its analogs are a special family of natural products with an indolo[2,3-*a*]pyrrolo[3,4-*c*]carbazole-12,13-diyl *N*-2-deoxy-1,5-glucopyranoside framework, which have attracted great attention because of the interesting structures and diverse bioactivities (Bergman et al., 2001; Sánchez et al., 2006; Janosik et al., 2008, 2018; Zenkov et al., 2020; Chambers et al., 2021). Since the first indolocarbazole, staurosporine was reported in 1977 (Ômura et al., 1977), more than 55 staurosporine derivatives have been isolated and identified from different organisms, namely, bacteria, clams, ascidia, slugs, and tunicates (Zenkov et al., 2020). Moreover, midostaurin (Stone et al., 2018), a staurosporine derivative, had been developed as the antitumor drug for the treatment of acute myeloid leukemia (AML). In recent years, the discovery of new compounds has been hampered due to the repeated isolation of known compounds. Therefore, dereplication becomes critical to finding new bioactive molecules. The LC-MS/MS-based global natural product social (GNPS) molecular networking can provide guidance and improve efficiency in the discovery of new and bioactive natural products within complex mixtures by analyzing and visualizing the spectral similarity of MS/MS data (Guthals et al., 2012; Watrous et al., 2012; Quinn et al., 2017). Molecular networking plays a significant role in exploring correlations of chemical structures among the known compounds, their analogs, and new compounds, which can guide the separation of the unreported compounds (Cheng et al., 2018).

We previously identified a staurosporine-producing strain, *Streptomyces* sp. OUCMDZ-5380 (originally numbered as MDCW-126), from a marine driftwood sample (Wang et al., 2019). To discover new indolocarbazoles cytotoxic to MV4-11, a human AML cell line with internal

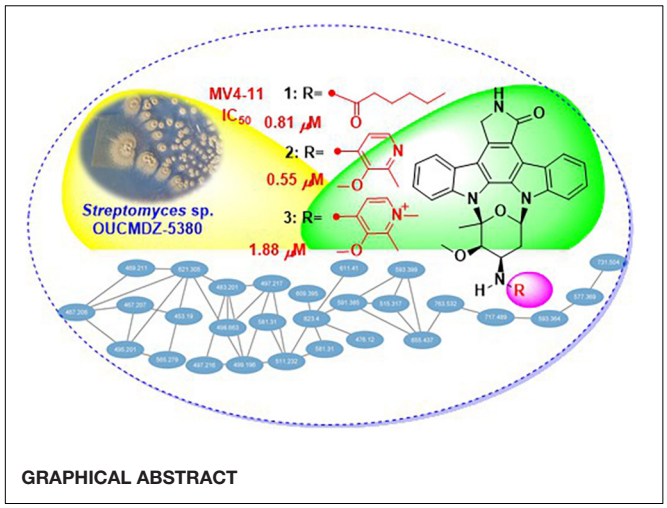

GRAPHICAL ABSTRACT

tandem duplication (ITD) mutation, we carried out the optimization of fermentation conditions for *Streptomyces* sp. OUCMDZ-5380 in different media. The ethyl acetate (EtOAc) or acetone extracts of the fermentation broth in different media were first analyzed by HPLC-UV at λ_{max} 290 nm (**Supplementary Figure 1**) to evaluate the chemodiversity of staurosporine analogs and assayed the cytotoxic activity against MV4-11 cells. Kazuo medium was selected as the optimal medium for the EtOAc extract containing more variety of staurosporine analogs and showing the most effective inhibition (99.2%) against the proliferation of MV-4-11 cells at 0.1 mg/ml (**Supplementary Figure 1**).

Thus, 113 L scale fermentation of *Streptomyces* sp. OUCMDZ-5380 in Kazuo medium was subsequently performed and the fermentation broth was extracted with acetone and EtOAc to give an organic extract. The organic extract was subjected to LC-MS/MS analysis which was then converted and generated a visualized GNPS molecular networking (**Figure 1**; Quinn et al., 2017). Compound **4** with *m/z* 467.20 $[M+H]^+$ (**Supplementary Figure 2**) could be proposed as staurosporine ($C_{28}H_{27}N_4O_3$), which was confirmed by the follow-up isolation and identification (**Supplementary Table 1** and **Supplementary Figures 3, 4**). Two of the 28 nodes visualized in the cluster of indolocarbazole family, that is, *m/z* 591.3 $[M+NH_4]^+$ (**Supplementary Figure 12**) for **2** and *m/z* 611.4 $[M+Na]^+$ (**Supplementary Figure 20**) for **3**, could be new indolocarbazoles. Chemical isolation guided by molecular networking and LC-MS provided compounds **1**-**4** from the fermentation extract. Compounds **1**-**3** were identified as new staurosporine derivatives that we named streptocarbazoles F–H, while compound **4** was the known staurosporine (Fu et al., 2012).

MATERIALS AND METHODS

General Experimental Procedures

Ultraviolet (UV) spectra were recorded on a Thermofisher NanoDrop OneC microvolume UV-Vis spectrophotometer. Experimental electronic circular dichroism (ECD) spectra in MeOH were recorded on a Chirascan circular dichroism spectrometer. IR spectra were obtained on a Nicolet Nexus 470 spectrophotometer using KBr disks. NMR spectroscopic data were recorded on Bruker Avance NEO 400 MHz, Agilent DD2-500, and JEOL JNM-ECP600 spectrometers, where chemical shifts were referenced to the corresponding residual solvent signal ($\delta_{H/C}$ 2.50/39.52 for DMSO-d_6). High-resolution ESI-TOF mass spectra were recorded using a Waters Q-TOF Ultima Global GAA076 LC mass spectrometer. LC-MS/MS was performed on an Agilent Infinity 1290 HPLC instrument, coupled with a Thermo Electron LTQ-Orbitrap XL mass spectrometer, with a C_{18} column (YMC-Triart C_{18} column, 150 mm × 4.6 mm, 3-5 μm). Low-resolution LC/ESI-MS data were measured using a Waters ACQUITY SQD 2 UPLC/MS system with a reversed-phase C_{18} column (ACQUITY UPLC BEH C_{18}, 2.1 mm × 50 mm, 1.7 μm) at a flow rate of 0.4 ml/min. Semipreparative HPLC was performed using an ODS column (YMC-park ODS-A, 10 mm × 250 mm, 5 μm). TLC was performed on plates precoated with silica gel GF254 (10-40 μm, Marine Chemical Factory of Qingdao). Silica gel (200-300 or 100-200 mesh, Marine Chemical Factory of Qingdao) was used for vacuum-liquid chromatography (VLC). RP-18 silica gel (YMC ODS-A, 50 μm) and Toyopearl HW-40F (Tosoh Bioscience) were used for column chromatography. Natural seawater was collected from the Huanghai Sea in the Jiaozhou Bay (Qingdao, China) without treatment.

Strain and Fermentation Optimization Experiments

Streptomyces sp. OUCMDZ-5380 (originally numbered as MDCW-126) was isolated from a driftwood sample collected at the Beibu Gulf nearby Guangxi (21°44′39″N and 108°35′22″E) and identified by the 16S rRNA gene sequence (GenBank accession no. MK615749; Wang et al., 2019). *Streptomyces* sp. OUCMDZ-5380 was seeded in 500 ml Erlenmeyer flasks each containing 150 ml of ISP2 medium (pH 7.3) prepared by dissolving malt extract (10 *g*), yeast extract (2 *g*), and D-glucose (4 *g*) in 1 L of natural seawater and shaken for 3 days at 28°C and 180 rpm, which was used as the seed culture. Then the seed liquid (5 ml) was transferred to a 500 ml Erlenmeyer flask containing 150 ml of Kazuo medium (pH 7.5) that was prepared by dissolving soluble starch (25 *g*), yeast extract (2 *g*), soybean meal (15 *g*), $CaCO_3$ (2 *g*), and Amberlite XAD-16 N (10 *g*) in 1 L natural seawater and was shaken on a rotary shaker at 180 rpm and 28°C for 9 days. The seed liquid (5 ml) was also aseptically transferred to rice solid medium and corn solid medium which were, respectively, prepared by adding rice (100 *g*) and corn (100 *g*) in 80 ml ISP2 medium, both of which were statically cultured at 28°C for 2 months. The fermentation broth in the Kazuo medium was filtrated into supernate and residue-containing resin and mycelia. The supernate was extracted three times with three volumes of EtOAc to give the EtOAc extract, and the residue was extracted three times with three volumes of acetone to give the acetone extract. The EtOAc and acetone extracts were combined and concentrated in a vacuum to give extract A. While fermentation on rice and corn solid media were

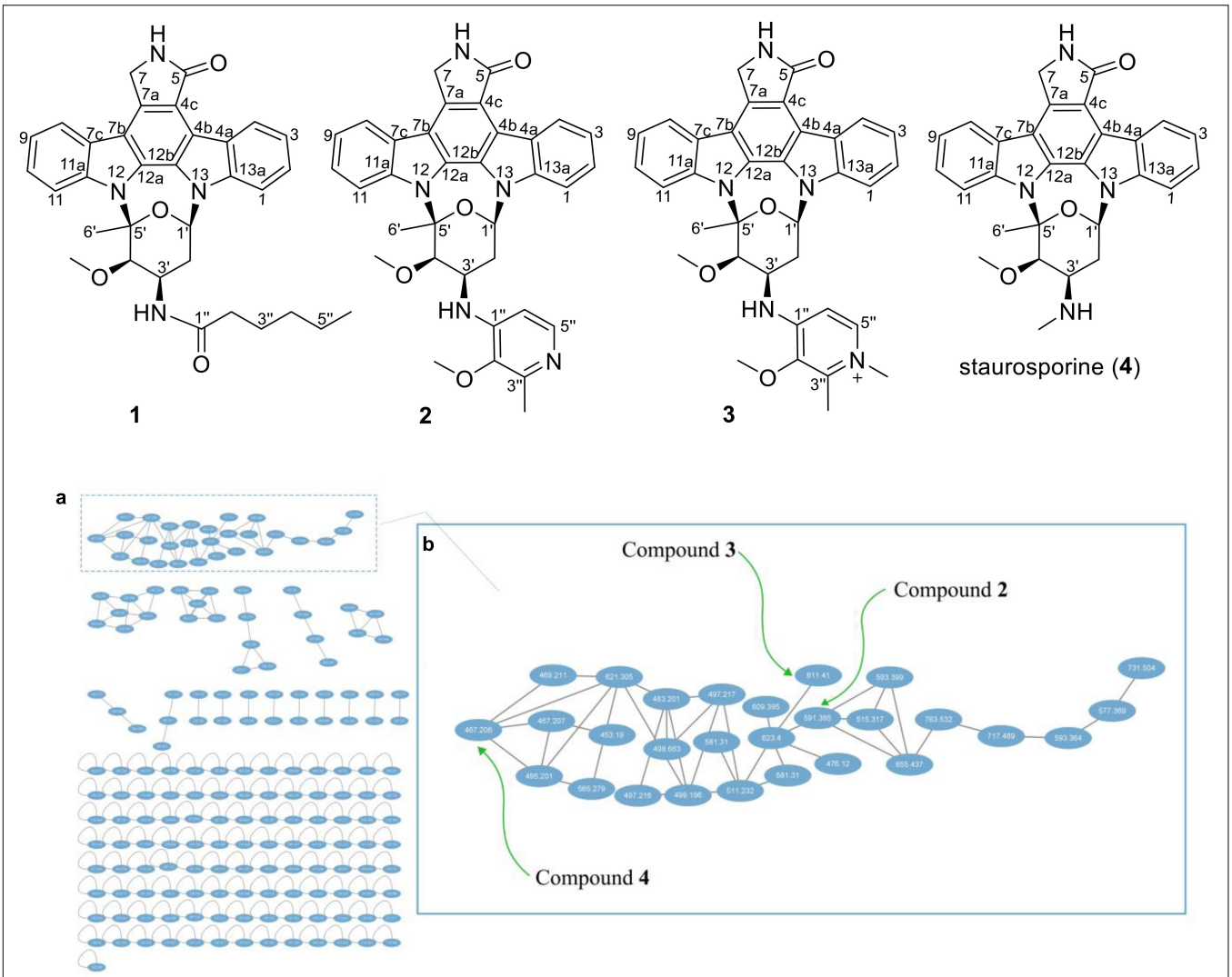

FIGURE 1 | Structures **1**–**4** and the molecular networking of the extract (MeOH layer) from *Streptomyces* sp. OUCMDZ-5380 (a) and the compound cluster of indolocarbazole family observed in the molecular networking (b).

extracted three times with three volumes of EtOAc to give extracts B and C, respectively.

Scale Fermentation and Extraction

Streptomyces sp. OUCMDZ-5380 was seeded in an ISP2 medium and shaken for 3 days at 28°C and 180 rpm, which was used as the seed culture. Then the seed liquid (5 ml) was transferred to 500 ml Erlenmeyer flasks each containing 150 ml of Kazuo medium and shaken for 9 days at 28°C and 180 rpm. A total of 113.25 L cultivation was performed and extracted with acetone and EtOAc. By the same separation procedure, the fermentation liquor was extracted with EtOAc and acetone. The EtOAc and acetone extracts were combined and concentrated in a vacuum to give 242.12 *g* extract, which was partitioned between 90% MeOH/H_2O and petroleum ether (PE) to give the MeOH/H_2O layer (46.46 *g*).

Molecular Networking Analysis and Its Application

The MeOH/H_2O layer was dissolved in MeCN to prepare a 5 mg/ml solution and analyzed by LC-MS/MS. The sample was injected and eluted with a gradient program of MeCN-H_2O containing 0.1% formic acid (0-20 min 10–100%; 0.5 ml/min; MS scan 200-2,000 Da). Mass spectra were obtained in positive ESI mode and with an automated full-dependent MS/MS scan. The MS/MS data were converted digitally to.mzXML file that was recognized by the GNPS using CompassXport software. The molecular networking was performed using the GNPS data analysis workflow. The spectral networks were imported into Cytoscape (version 3.9.1) and visualized using the force-directed layout.

As shown in **Figure 1**, each ellipse represented a compound with an *m/z* value. The connection lines indicated that the

MS/MS fragments of the compounds were correlated, which could be used to identify the structural similarity of the compounds. From the complete molecular network, it could be seen that there were several compound clusters, and the one with the most nodes contained the reported staurosporine (Fu et al., 2012; *m/z* 467.2 $[M+H]^+$). This compound cluster was thus useful for recognition of the indolocarbazole family, which contained new LC-MS peaks at *m/z* 591.3 and 611.4 corresponding to streptocarbazoles G (**2**; *m/z* 591.3 $[M+NH_4]^+$) and H (**3**; *m/z* 611.4 $[M+Na]^+$), respectively. Similarly, the LC-MS/MS-based GNPS molecular networking could be used as guidance for isolating the new compounds from the extracts.

Isolation and Purification

The MeOH layer (46.5 *g*) was subjected to a silica gel VLC column using step gradient elution with CH_2Cl_2-PE (0–100%) and then with MeOH-CH_2Cl_2 (0–100%) to yield eight fractions (Fr.1–Fr.8). Fr.3 (9.0 *g*) was re-chromatographed on a silica gel VLC column with a step gradient of MeOH-CH_2Cl_2 (0–100%) to provide nine fractions (Fr.3.1–Fr.3.9). Fr.3.5 (182.0 mg) was fractionated by Toyopearl HW-40F column eluting with MeOH-CH_2Cl_2 (1:1) to give ten fractions (Fr.3.5.1–Fr.3.5.10). Fr.3.5.1 (9.8 mg) was purified by semipreparative HPLC (ODS column, 44% MeCN-H_2O with 0.05% TFA, 3 ml/min) to yield compound **1** (2.0 mg, t_R 77.0 min). Fr.8 (669.2 mg) was fractionated by Toyopearl HW-40F column eluting with MeOH-CH_2Cl_2 (1:1), to give three fractions (Fr.8.1-Fr.8.3). Fr.8.3 (342.8 mg) was subjected to an RP-silica gel column eluting with a step gradient of MeOH-H_2O (20–100%) to afford four fractions (Fr.8.3.1–Fr.8.3.4). Fr.8.3.2 (15.6 mg) was purified by semipreparative HPLC [ODS column, 30% MeCN-H_2O containing 0.05% trifluoroacetic acid (TFA), 4 ml/min] to yield compound **2** (3.0 mg, t_R 37.3 min). Fr.8.3.3 (18.3 mg) was purified by semipreparative HPLC (ODS column, 35% MeCN-H_2O containing 0.05% TFA, 4 ml/min) to yield compound **3** (3.0 mg, t_R 35.5 min). Fr.4 (15.85 *g*) was purified by refluxing with acetone to afford compound **4** (8.0 *g*).

Streptocarbazole F (**1**): pale yellow powder; $[\alpha]_D^{19}$ +42.5 (*c* 0.05, MeOH); UV (MeOH) λ_{max} (log ε) 372 (3.43), 354 (3.39), 334 (3.59), 318 (3.60), 291 (4.17), and 238 (3.88) nm; IR (KBr) ν_{max} 3,433, 2,953, 2,359, 1,680, 1,520, 1,458, and 1,316 cm^{-1}; ECD (0.45 mM, MeOH) λ_{max} 206 (Δε −9.57), 234 (Δε +3.73), 245 (Δε +1.41), 250 (Δε +1.83), 264 (Δε −0.28), and 295 (Δε +3.53) nm; ^1H and ^{13}C NMR, **Table 1**; and HRESIMS *m/z* 551.2651 $[M+H]^+$ (calculated for $C_{33}H_{35}N_4O_4$, 551.2653).

Streptocarbazole G (**2**): pale yellow powder; $[\alpha]_D^{17}$ +6.6 (*c* 0.05, MeOH); UV (MeOH) λ_{max} (log ε) 371 (3.46), 354 (3.42), 334 (3.63), 319 (3.58), 290 (4.25), and 243 (3.92) nm; IR (KBr) ν_{max} 3,403, 2,932, 2,370, 1,684, 1,541, 1,458, 1,384, 1,210, 1,136, and 1,025 cm^{-1}; ECD (0.44 mM, MeOH) λ_{max} 204 (Δε −6.67), 223 (Δε +4.00), 240 (Δε −3.42), 260 (Δε −0.31), 276 (Δε −2.37), and 295 (Δε +4.74) nm; ^1H and ^{13}C NMR, **Table 1**; and HRESIMS *m/z* 574.2440 $[M + H]^+$ (calculated for $C_{34}H_{32}N_5O_4$, 574.2449).

Streptocarbazole H (**3**): brown oily liquid; $[\alpha]_D^{17}$ +18.5 (*c* 0.05, MeOH); UV (MeOH) λ_{max} (log ε) 371 (3.89), 354 (3.86), 333 (4.10), 318 (4.08), 290 (4.70), and 243 (4.32) nm; IR (KBr) ν_{max} 3,484, 2,927, 2,359, 1,682, 1,635, 1,557, 1,458, 1,384, 1,317, 1,201, 1,131, and 1,028 cm^{-1}; ECD (0.43 mM, MeOH) λ_{max} 204 (Δε −8.89), 224 (Δε +5.86), 240 (Δε −4.64), 266 (Δε −0.28), 279 (Δε −3.04), and 297 (Δε +7.22) nm; ^1H and ^{13}C NMR, **Table 1**; and HRESIMS *m/z* 588.2607 M^+ (calculated for $C_{35}H_{34}N_5O_4^+$, 588.2605).

Antiproliferatory Activity Assay

The antiproliferatory activity of compounds **1**–**3** was evaluated against 12 human cancer cell lines (lung adenocarcinoma cell line A549, lung adenocarcinoma cell line PC-9 with EGFR mutation, gastric cancer cell line MKN-45, colorectal carcinoma cell line HCT-116, acute promyelocytic leukemia cell line HL-60, erythroleukemic cell line K562, acute myeloid leukemia cell line MV4-11 with ITD mutation, acute human leukemia monocytic cell line THP-1 to constitutively express most TLRs, acute T lymphocyte cell line Jurkat, pancreatic cancer cell line PATU8988T, hepatocellular carcinoma cell line HepG2, and hepatoma cell line HuH-7) and one human cell line L-02 (embryo liver cell line) using the CCK-8 assay (Tominaga et al., 1999). These cells were, respectively, prepared into single-cell suspension with the RPMI1640 or MEDM medium containing 10% FBS, and the 96 well plates were inoculated with 100 μl cell culture medium (adherent cell viewed 5×10^4/ml and suspension cell viewed 9×10^4/ml) per well, then cultured at 5% CO_2 and 37°C for 24 h before being exposed to each compound at eight concentration gradients. Then the 96 well plates adding the compounds were cultured for 48 h. The old culture medium and drug solution of adherent cells were sucked out, then 100 μl of CCK-8 solution (diluted ten times with the basic medium) was added and the suspension cells were directly added to 10 μl of CCK-8 stock solution. After incubation at 37°C with 5% CO_2 for 4 h away from light, the cell culture measured the absorbance at 450 nm. The IC_{50} was calculated by the software GraphPad Prism 8 (version 8.0.2, from GraphPad Software Inc). Staurosporine (**4**) was used as the positive control. By the same procedure, the inhibitory rates of extracts A–C on MV4-11 cells were also tested at the final concentration of 0.1 mg/ml.

RESULTS AND DISCUSSION

Streptocarbazole F (**1**) was obtained as a pale-yellow powder. Its molecular formula was determined as $C_{33}H_{35}N_4O_4$ based on the HRESIMS data at *m/z* 551.2651 $[M+H]^+$ (**Supplementary Figure 5**). Careful comparison of its ^1H (**Supplementary Figure 6**) and ^{13}C (**Supplementary Figure 7**) NMR data (**Table 1**) with those of staurosporine (**4**; **Supplementary Table 1** and **Supplementary Figures 3**, **4**) indicated an *N*-demethyl staurosporine unit that was confirmed by ^1H-^1H COSY (**Supplementary Figure 9**) of H-1/H-2/H-3/H-4, H-8/H-9/H-10/H-11, HN-6/H-7, H-1′/H-2′/H-3′/H-4′, and H-3′/HN-3′ and the HMBC (**Supplementary Figure 10**) correlations of H-1 to C-3 and C-4a, H-2 to C-4 and C-13a, H-3 to C-1 and C-4a, H-4 to C-2 and C-4b, HN-6 to C-4c and C-7a, H-7 to C-5 and C-7b, H-8 to C-11a and C-7b, H-9 to C-7c and C-11, H-10 to C-8 and C-11a, H-11 to C-9 and C-7c, H-1′ to C-12b and C-5′, H-2′ to C-4′, H-4′ to C-2′ and

TABLE 1 | ^{1}H (500 MHz) and ^{13}C NMR (125 MHz) data for compounds **1**–**3** in DMSO-d_6.

No.	1		2		3[a]	
	δ_C, type	δ_H, mult. (*J* in Hz)	δ_C, type	δ_H, mult. (*J* in Hz)	δ_C, type	δ_H, mult. (*J* in Hz)
1	108.9, CH	7.59, *d* (8.2)	109.1, CH	7.64, *d* (8.3)	109.1, CH	7.64, *d* (8.4)
2	125.3, CH	7.48, overlapped	125.5, CH	7.49, overlapped	125.2, CH	7.48, overlapped
3	119.4, CH	7.29, *t* (7.5)	119.7, CH	7.29, *t* (7.4)	119.8, CH	7.30, *t* (7.3)
4	125.7, CH	9.28, *d* (7.9)	125.7, CH	9.24, *d* (7.9)	125.7, CH	9.24, *d* (8.1)
4a	122.6, C	–	122.6, C	–	122.6, C	–
4b	114.9, C	–	115.1, C	–	115.1, C	–
4c	119.6, C	–	119.9, C	–	119.9, C	–
5	171.8, C	–	171.7, C	–	171.7, C	–
6	–	8.63, s	–	8.68, s	–	8.67, s
7	45.4, CH_2	5.01, *d* (17.8); 4.96, d (17.8)	45.4, CH_2	5.04, *d* (17.8); 4.99, d (17.8)	45.4, CH_2	5.04, *d* (17.9); 4.99, d (17.9)
7a	132.3, C	–	132.6, C	–	132.6, C	–
7b	114.1, C	–	114.9, C	–	115.0, C	–
7c	123.9, C	–	124.3, C	–	124.3, C	–
8	121.3, CH	8.05, *d* (8.3)	121.2, CH	8.08, *d* (8.3)	121.3, CH	8.08, *d* (8.3)
9	120.4, CH	7.36, *t* (7.4)	120.8, CH	7.38, *t* (7.5)	120.9, CH	7.39, *t* (7.6)
10	125.1, CH	7.48, overlapped	125.2, CH	7.49, overlapped	125.5, CH	7.48, overlapped
11	114.3, CH	8.05, *d* (8.3)	115.6, CH	8.08, *d* (8.3)	115.6, CH	8.08, *d* (8.3)
11a	138.9, C	–	139.6, C	–	139.6, C	–
12a	128.8, C	–	125.3, C	–	125.0, C	–
12b	125.4, C	–	125.1, C	–	125.0, C	–
13a	136.3, C	–	136.7, C	–	136.7, C	–
1'	80.9, CH	6.87, *dd* (7.6, 3.3)	79.9, CH	6.92, *d* (6.2)	79.8, CH	6.92, *d* (6.2)
2'	29.5, CH_2	2.41, *m*; 2.73, *m*	30.8, CH_2	2.96, *m*; 2.71, *m*	30.7, CH_2	2.95, *m*; 2.74, *d* (15.2)
3'	42.5, CH	4.43, *m*	44.5, CH	4.68, *m*	44.5, CH	4.67, brs
4'	81.2, CH	4.13, *d* (3.3)	79.7, CH	4.36, *d* (4.1)	79.6, CH	4.38, brs
4'-OCH_3	59.1, CH_3	2.87, s	58.1, CH_3	3.23, s	58.0, CH_3	3.26, s
5'	92.7, C	–	91.9, C	–	91.9, C	–
6'	29.0, CH_3	2.39, s	28.8, CH_3	2.36, s	28.8, CH_3	2.36, s
3'-NH	–	6.77, *d* (6.8)	–	5.99, brs	–	5.98, *d* (7.2)
1"	171.9, C	–	150.9, C	–	149.9, C	–
2"	35.2, CH_2	1.47, *m*; 1.61, *m*	139.6, C	–	140.2, C	–
2"-OCH_3			59.1, CH_3	2.43, s	59.4, CH_3	2.36, s
3"	24.2, CH_2	0.85, overlapped	143.0, C	–	145.5, C	
3"-CH_3			13.9, CH_3	2.10, s	12.7, CH_3	2.11, s
4"	30.5, CH_2	0.83, overlapped				
4"-CH_3					42.8, CH_3	3.68, s
5"	21.6, CH_2	1.00, *d* (7.3); 0.98, d (7.0)	137.7, CH	8.01, *d* (6.9)	142.3, CH	8.14, *d* (7.4)
6"	13.7, CH_3	0.69, *t* (7.3)	104.3, CH	7.03, *d* (6.9)	104.1, CH	7.08, *d* (7.4)

[a]*Recorded in 600 and 150 MHz for ^{1}H and ^{13}C NMR, respectively.*

CH_3O-4′, CH_3O-4′ to C-4′, and H-6′ to C-4′ and C-5′ (**Figure 2**). In addition to the signals of the *N*-demethyl staurosporine unit, compound **1** also included the signals of a carbonyl (δ_C 171.9, C-1″), four sp^3-methylene groups ($\delta_{H/C}$ 1.47 and 1.61/35.2, CH_2-2″; 0.85/24.2, CH_2-3″; 0.83/30.5, CH_2-4″; and 0.98 and 1.00/21.6, CH_2-5″), and a methyl group ($\delta_{H/C}$ 0.69/13.7, CH_3-6″; **Supplementary Figure 8**). ^{1}H-^{1}H COSY (**Supplementary Figure 9**) of H-2″/H-3″/H-4″/H-5″/H-6″ and the HMBC (**Supplementary Figure 10**) correlations of H-2″ to C-1″, C-3″, and C-4″, and H-6″ to C-4″ and C-5″ (**Figure 2**) suggested that these groups connected as a hexanoyl moiety. The key HMBC (**Supplementary Figure 10**) correlations from H-3′ (δ_H 4.43) and HN-3′ (δ_H 6.77) to C-1″ attached the hexanoyl group to the N-3′ position. The relative configuration of **1** was elucidated by the NOESY (nuclear Overhauser effect spectroscopy) experiment which showed correlations of H-1′ (δ_H 6.87) to H-4′ (δ_H 4.13) and H-6′ (δ_H 2.39) and H-3′ (δ_H 4.43) to H-6′ (**Figure 3** and **Supplementary Figure 11**), suggesting the same relative configuration to staurosporine (**4**). Moreover, compound **1** displayed similar ECD Cotton effects to staurosporine at λ_{max} 206 ($\Delta\varepsilon$ −9.57), 234 ($\Delta\varepsilon$ +3.73), and 295 ($\Delta\varepsilon$ +3.53) nm (**Figure 4** and **Supplementary Figure 28**),

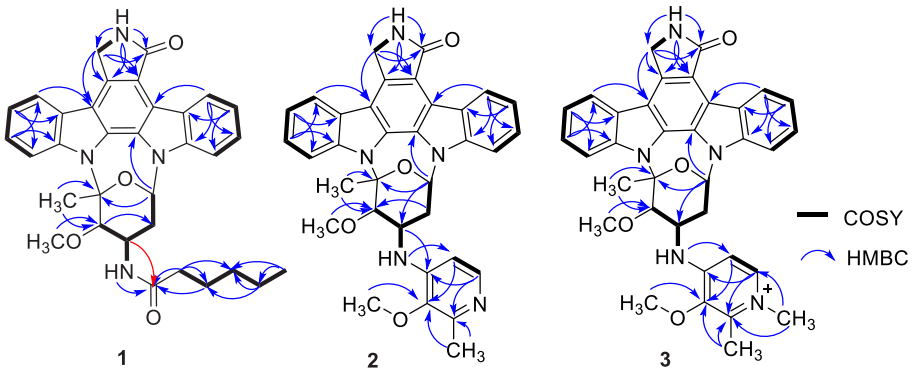

FIGURE 2 | ^{1}H-^{1}H COSY and HMBC correlations of compounds **1**–**3**.

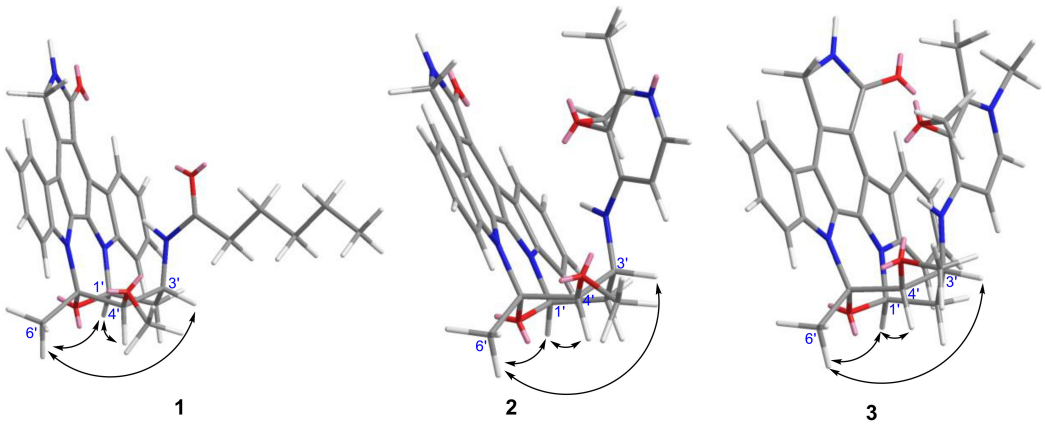

FIGURE 3 | Key NOESY correlations of compounds **1**–**3**.

indicating that compound **1** and staurosporine shared the same (1′*R*, 3′*R*, 4′*R*, and 5′*S*)—configuration (Funato et al., 1994; Fu et al., 2012). To further confirm the absolute configuration, the predicted ECD spectrum of compound **1** was obtained by the TDDFT [B3LYP/6-31G(d)] method (Stephens et al., 2001). The measured ECD spectrum of compound **1** matches with the calculated ECD curve of (1′*R*, 3′*R*, 4′*R*, and 5′*S*)-**1** (**Supplementary Figure 28**). Thus, streptocarbazole F (**1**) was identified as *N*-demethyl-*N*-hexanoyl staurosporine.

Streptocarbazole G (**2**) was obtained as a pale-yellow powder. Its molecular formula was determined as $C_{34}H_{32}N_5O_4$ based on the HRESIMS data at *m/z* 574.2440 $[M+H]^+$ (**Supplementary Figure 12**). The comparison of the ^{1}H (**Supplementary Figure 13**) and ^{13}C NMR (**Supplementary Figure 14**) data of compound **2** (**Table 1**) with staurosporine (**4**; **Supplementary Figures 3, 4**) indicated the lack of 3′-*N*-methyl signals at $\delta_{H/C}$ 1.46/33.3 (**Supplementary Table 1**), showing an *N*-demethyl staurosporine unit in compound **2**. The rest signals included those for a methyl ($\delta_{H/C}$ 2.10/13.9, CH_3-3″), a methoxy ($\delta_{H/C}$ 2.43/59.1, CH_3O-2″), two sp^2 methines ($\delta_{H/C}$ 8.01/137.7, CH-5″ and 7.03/104.3, CH-6″), and three sp^2 nonhydrogen carbons (δ_C 150.9, C-1″; 139.6, C-2″; and 143.0, C-3″; **Table 1**; and **Supplementary Figures 15, 16**). Combined with the molecular formula, the ^{1}H-^{1}H COSY correlations of H-5″/H-6″ (**Supplementary Figure 17**) and the HMBC correlations (**Supplementary Figure 18**) from the olefinic protons H-5″ to

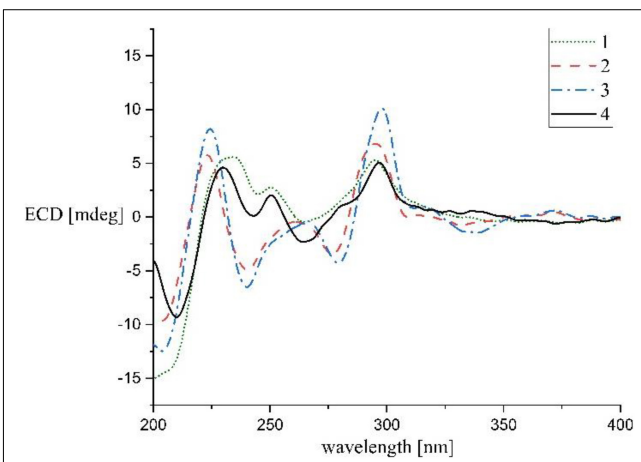

FIGURE 4 | Experimental ECD spectra of compounds **1**–**4**.

C-1″ and C-3″, and H-6″ to C-2″ (**Figure 2**) presented a pyridine moiety. The HMBC (**Supplementary Figure 18**) correlations from the methoxy proton (δ_H 2.43) to C-2″ (δ_C 139.6) and the methyl proton (δ_H 2.10) to C-2″ and C-3″ (δ_C 143.0) indicated that the methoxy and methyl groups, respectively, linked to C-2″ and C-3″, forming a 2-methyl-3-methoxypyridine moiety. The key HMBC (**Supplementary Figure 18**) correlations of H-3′ (δ_H 4.68) to C-1″ (δ_C 150.9) and HN-3′ (δ_H 5.99) to C-6″ (δ_C 104.3) suggested that 2-methyl-3-methoxypyridine moiety and the *N*-demethylstaurosporine moiety were connected by a C–N σ-bond between N-3′ and C-1″ (**Figure 2**). The NOESY (**Supplementary Figure 19**) experiment showed correlations of H-1′ (δ_H 6.92) to H-4′ (δ_H 4.36) and H-6′ (δ_H 2.36) and H-3′ (δ_H 4.68) to H-6′ (**Figure 3**), suggesting the same relative configuration of **2** to staurosporine. Meantime, compound **2** displayed ECD Cotton effects at λ_{max} 204 (Δε −6.67), 223 (Δε +4.00), and 295 (Δε +4.74) nm (**Figure 4**) similar to those of staurosporine (Fu et al., 2012), indicating that compound **2** and staurosporine have the same absolute configuration. The 3D structure of compound **2** indicated that CH_3O-2″ protons were shielded by the indolocarbazole framework (**Figure 3**), leading to an unusual chemical shift of 2″-methoxy protons (δ_H 2.43). Therefore, streptocarbazole G (**2**) was convincingly elucidated as *N*-demethyl-*N*-(2-methyl-3-methoxypyridin-4-yl) staurosporine.

Streptocarbazole H (**3**) was obtained as a brown oil. Its molecular formula was determined as $C_{35}H_{34}N_5O_4^+$ based on the HRESIMS data at *m/z* 588.2607 $[M]^+$ (**Supplementary Figure 20**), within a 15 amu more than **2**. Its ^1H (**Supplementary Figure 21**) and ^{13}C NMR (**Supplementary Figure 22**) data were very similar to those of **2** except for an additional methyl signal at $\delta_{C/H}$ 42.8/3.68 (**Table 1** and **Supplementary Figures 23–25**). The HMBC (**Supplementary Figure 26**) correlations of this methyl proton signal (δ_H 3.68) to C-3″ (δ_C 145.5) and C-5″ (δ_C 142.3; **Figure 3**) located this methyl at the nitrogen atom of the pyridine ring, that is, 4″-position. Thus, compound **3** was deduced as the *N*-methyl pyridinium of compound **2** and was further evidenced by NOESY (**Supplementary Figure 27**) and ECD experiments. Compound **3** displayed the same NOE pattern from H-1′ (δ_H 6.92) to H-4′ (δ_H 4.38) and H-6′ (δ_H 2.36) and H-3′ (δ_H 4.67) to H-6′ (**Figure 2**), and the similar ECD Cotton effects to compound **2** (**Figure 4**), indicating that they share the same absolute configuration. Therefore, streptocarbazole H (**3**) was convincingly identified as the *N*-methyl pyridinium of **2**, that is 4-(*N*-demethyl staurosporine-*N*-yl)-1,2-dimethyl-3-methoxypyridinium.

Compounds **1**–**4** were assayed for their antiproliferative effects on twelve human cancer cell lines (A549, PC-9, MKN-45, HCT-116, HL-60, K562, MV4-11, THP-1, Jurkat, PATU8988T, HepG2, and HuH-7) and one human normal cell line (fetal hepatocyte line L-02) by CCK-8 method (Tominaga et al., 1999). The results showed that new compounds **1**-**3** exhibited a selective inhibitory activity against the growth of MV4-11 cancer cells with the IC_{50} values of 0.81 ± 0.007, 0.55 ± 0.04, and 1.88 ± 0.11 μM, respectively, while no activity against the other cell lines was not observed ($IC_{50} \geq 10$ μM). The IC_{50} values for the positive control, staurosporine (**4**), were 0.12 ± 0.006, 13.58 ± 0.68, 0.0029 ± 0.0008, 0.062 ± 0.0006, 0.17 ± 0.018, 0.64 ± 0.073, 0.0014 ± 0.0001, 0.16 ± 0.038, >1, 0.12 ± 0.014, 0.18 ± 0.034, and 0.11 ± 0.016 μM against A549, PC-9, MKN-45, HCT-116, HL-60, K562, MV4-11, THP-1, Jurkat, PATU8988T, HepG2, HuH-7, and L-02 cell lines, respectively.

CONCLUSION

In summary, three new indolocarbazoles, streptocarbazoles F–H (**1**-**3**), were identified from the marine-derived *Streptomyces* sp. OUCMDZ-5380 by spectroscopic analysis and ECD comparison. It is different from the broad-spectrum antiproliferative activity of staurosporine that streptocarbazoles F–H displayed a selective antiproliferation for the Flt3-ITD mutation AML cell line, MV4-11 with the IC_{50} values of 0.55–1.88 μM.

DATA AVAILABILITY STATEMENT

The original contributions presented in the study are included in this article/**Supplementary Material**, further inquiries can be directed to the corresponding authors.

AUTHOR CONTRIBUTIONS

All authors listed have made a substantial, direct, and intellectual contribution to the work, and approved it for publication.

FUNDING

This work was financially supported by the NSFC-Shandong Union Foundation (No. U1906213) and NSFC (No. 41876172).

SUPPLEMENTARY MATERIAL

The Supplementary Material for this article can be found online at: https://www.frontiersin.org/articles/10.3389/fmicb.2022.957473/full#supplementary-material

REFERENCES

Bergman, J., Janosik, T., and Wahlstrom, N. (2001). Indolocarbazoles. *Adv. Heterocycl. Chem.* 80, 1–17. doi: 10.1016/S0065-2725(01)80012-X

Chambers, G. E., Sayan, A. E., and Brown, R. C. D. (2021). The synthesis of biologically active indolocarbazole natural products. *Nat. Prod. Rep.* 38, 1794–1820. doi: 10.1039/d0np00096e

Cheng, T. F., Jin, H. Z., Liu, C. X., and Zhang, W. D. (2018). LC-MS/MS-based molecular networking producing enlighten study of Chinese materia medica. *Zhong Cao Yao* 49, 265–273. doi: 10.7501/j.issn.0253-2670.2018.02.001

Fu, P., Zhuang, Y., Wang, Y., Liu, P., Qi, X., Gu, K., et al. (2012). New indolocarbazoles from a mutant strain of the marine-derived actinomycete *Streptomyces fradiae* 007M135. *Org. Lett.* 14, 6194–6197. doi: 10.1021/ol302940y

Funato, N., Takayanagi, H., Konda, Y., Toda, Y., and Harigaya, Y. (1994). Absolute configuration of staurosporine by X-ray analysis. *Tetrahedron Lett.* 35, 1251–1254. doi: 10.1016/0040-4039(94)88036-0

Guthals, A., Watrous, J. D., Dorrestein, P. C., and Bandeira, N. (2012). The spectral networks paradigm in high throughput mass spectrometry. *Mol. Biosyst.* 8, 2535–2544. doi: 10.1039/c2mb25085c

Janosik, T., Rannug, A., Rannug, U., Wahlström, N., Slätt, J., and Bergman, J. (2018). Chemistry and Properties of Indolocarbazoles. *Chem. Rev.* 118, 9058–9128. doi: 10.1021/acs.chemrev.8b00186

Janosik, T., Wahlström, N., and Bergman, J. (2008). Recent progress in the chemistry and applications of indolocarbazoles. *Tetrahedron* 64, 9159–9180. doi: 10.1016/j.tet.2008.06.101Get

Ômura, S., Iwai, Y., Hitano, A., Nakaga, A., Awaya, J., Tsuchiya, H., et al. (1977). A new alkaloid AM-2282 of *Streptomyces origin* taxonomy, fermentation, isolation and preliminary characterization. *J. Antibiot.* 30, 275–282. doi: 10.7164/antibiotics.30.275

Quinn, R. A., Nothias, L.-F., Vining, O., Meehan, M., Esquenazi, E., and Dorrestein, P. C. (2017). Molecular networking as a drug discovery, drug metabolism, and precision medicine strategy. *Trends Pharmacol. Sci.* 38, 143–154. doi: 10.1016/j.tips.2016.10.011

Sánchez, C., Méndez, C., and Salas, J. A. (2006). Indolocarbazole natural products: occurrence, biosynthesis, and biological activity. *Nat. Prod. Rep.* 23, 1007–1045. doi: 10.1039/b601930g

Stephens, P. J., Pan, J.-J., and Devlin, F. J. (2001). Determination of the absolute configurations of natural products via density functional theory calculations of vibrational circular dichroism, electronic circular dichroism and optical rotation: the schizozygane alkaloid schizozygine. *J. Org. Chem.* 72, 2508–2524. doi: 10.1021/np060112p

Stone, R. M., Manley, P. W., Larson, R. A., and Capdeville, R. (2018). Midostaurin: its odyssey from discovery to approval for treating acute myeloid leukemia and advanced systemic mastocytosis. *Blood Adv.* 2, 444–453. doi: 10.1182/bloodadvances.2017011080

Tominaga, H., Ishiyama, M., Ohseto, F., Sasamoto, K., Hamamoto, T., Suzuki, K., et al. (1999). A water-soluble tetrazolium salt useful for colorimetric cell viability assay. *Anal. Commun.* 36, 47–50. doi: 10.1039/A809656B

Wang, C., Wang, K., Jiang, M. G., Tan, X. C., Lei, F. H., Du, F. K., et al. (2019). Isolation and screening of actinomycetes to produce antibiotic metabolites from Beibu Gulf nearby Guangxi. *Nat. Prod. Res. Dev.* 31, 1170–1176. doi: 10.16333/j.1001-6880.2019.7.008

Watrous, J., Roach, P., Alexandrov, T., Heath, B. S., Yang, J. Y., Kersten, R. D., et al. (2012). Mass spectral molecular networking of living microbial colonies. *Proc. Natl. Acad. Sci. U S A.* 109, E1743–E1752. doi: 10.1073/pnas.1203689109

Zenkov, R. G., Ektova, L. V., Vlasova, O. À, Belitskiy, G. À, Yakubovskaya, M. G., and Kirsanov, I. (2020). Indolo[2,3-a]carbazoles: diversity, biological properties, application in antitumor therapy. *Chem. Heterocycl. Comp.* 56, 644–658. doi: 10.1007/s10593-020-02714-4

Conflict of Interest: The authors declare that the research was conducted in the absence of any commercial or financial relationships that could be construed as a potential conflict of interest.

Publisher's Note: All claims expressed in this article are solely those of the authors and do not necessarily represent those of their affiliated organizations, or those of the publisher, the editors and the reviewers. Any product that may be evaluated in this article, or claim that may be made by its manufacturer, is not guaranteed or endorsed by the publisher.

frontiers | Frontiers in Microbiology

ORIGINAL RESEARCH
published: 22 July 2022
doi: 10.3389/fmicb.2022.943452

Pro-angiogenic New Chloro-Azaphilone Derivatives From the Hadal Trench-Derived Fungus *Chaetomium globosum* YP-106

Yaqin Fan[1†], Chunjiao Jiang[1†], Yan Zhang[1], Zhiheng Ma[1], Peihai Li[2], Lizhong Guo[1], Ting Feng[3], Liman Zhou[3] and Lili Xu[1*]*

[1] Shandong Provincial Key Laboratory of Applied Mycology, School of Life Sciences, Qingdao Agricultural University, Qingdao, China, [2] Shandong Provincial Engineering Laboratory for Biological Testing Technology, Key Laboratory for Biosensor of Shandong Province, Engineering Research Center of Zebrafish Models for Human Diseases and Drug Screening of Shandong Province, Biology Institute, Qilu University of Technology (Shandong Academy of Sciences), Jinan, China, [3] Key Laboratory of Chemistry and Engineering of Forest Products, State Ethnic Affairs Commission, Guangxi Key Laboratory of Chemistry and Engineering of Forest Products, Guangxi Collaborative Innovation Center for Chemistry and Engineering of Forest Products, School of Chemistry and Chemical Engineering, Guangxi Minzu University, Nanning, China

OPEN ACCESS

Edited by:
Junfeng Wang,
South China Sea Institute of Oceanology (CAS), China

Reviewed by:
Fei Cao,
Hebei University, China
Bin-Gui Wang,
Institute of Oceanology (CAS), China

***Correspondence:**
Liman Zhou
zhouliman88@126.com
Lili Xu
Ellyxu@163.com

[†] These authors have contributed equally to this work

Specialty section:
This article was submitted to Extreme Microbiology, a section of the journal Frontiers in Microbiology

Received: 13 May 2022
Accepted: 23 June 2022
Published: 22 July 2022

Citation:
Fan Y, Jiang C, Zhang Y, Ma Z, Li P, Guo L, Feng T, Zhou L and Xu L (2022) Pro-angiogenic New Chloro-Azaphilone Derivatives From the Hadal Trench-Derived Fungus Chaetomium globosum YP-106. Front. Microbiol. 13:943452. doi: 10.3389/fmicb.2022.943452

Five new chloro-azaphilones, chaetofanixins A–E (1–5), and five known analogs (6–10) were isolated and identified from the hadal trench-derived fungus *Chaetomium globosum* YP-106. The structure of chaetofanixin E (5) is unique and interesting, bearing a highly rigid 6/6/5/3/5 penta-cyclic ring system, which is first encountered in natural products. The structures of these compounds, including absolute configurations, were determined based on the spectroscopic analysis, electronic circular dichroism (ECD) calculations, and analysis of biogenetic origins. Compounds 1–7 significantly promoted angiogenesis in a dose-dependent manner, and thus, these compounds might be used as promising molecules for the development of natural cardiovascular disease agents.

Keywords: hadal trench-derived fungus, metabolites, chloro-azaphilones, pro-angiogenic activity, *Chaetomium globosum*

INTRODUCTION

The prevention and treatment of cardiovascular diseases (CVDs) is an important project in the field of medicine and food. CVD has emerged as one of the major diseases endangering human health, causing more than 17 million deaths worldwide every year (Virani et al., 2020). Insufficient angiogenesis is one of the most common causes of CVD, accompanied by symptoms, such as myocardial ischemia, cerebral ischemia, vasculitis obliterans, peripheral vascular disease, etc. (Jude et al., 2010; Kurusamy et al., 2017). In recent years, pro-angiogenesis has been highly valued as a new target for the development of cardiovascular drugs, and various therapeutic angiogenesis studies have been carried out in animal models and clinical practice (Li et al., 2021; Zhou et al., 2021). Clinical therapeutic angiogenesis approaches are diverse, such as cytokine therapy, endothelial progenitor cell therapy, stem cell therapy, gene therapy, and mechanical therapy. However, the above-mentioned methods have shortcomings, including transient efficacy, strong

toxic side effects, and low success rate (Potz et al., 2017). Food prevention and drug treatment are important methods to prevent and treat cardiovascular diseases. The extraction of CVD drugs from microbial natural products has been considered an effective strategy for the prevention and treatment of CVDs. In the past 50 years, about 20,000 natural products have been reported from marine microorganisms, but the number of natural products reported from deep-sea microorganisms is very low, less than 2%, and hadal trench (>6,000 m) microorganisms are hardly reported (Skropeta and Wei, 2014; Carroll et al., 2021). In recent years, with the rapid development of sample collection, identification, and culture techniques of microorganisms, the chemical study of deep-sea fungi has shown a dramatic increase, and researchers have found a wealth of novel active secondary metabolites with pro-angiogenic (Fan et al., 2015; Yan et al., 2022), antibacterial (Wang et al., 2016; Chi et al., 2020b), anti-inflammatory (Guo et al., 2021), anticancer (Chi et al., 2020a), and other biological activities (Wang et al., 2020) from deep-sea microorganisms.

In our continuous efforts for discovering structurally novel bioactive natural compounds from marine-derived microorganisms inhabiting unique environments, a fungal strain YP-106, identified as *Chaetomium globosum*, was isolated from the hadal zone seawater collected at a depth of 6,215 m from Yap Trench in the western Pacific Ocean. A subsequent chemical investigation of this fungus led to the identification of five new chloro-azaphilone derivatives, chaetofanixins A–E (1–5), and five related known azaphilones, chaetomugilin D (6) (Qin et al., 2009), chaetomugilin Q (7) (Yamada et al., 2011), chaetoviridin J (8) (Youn et al., 2015), chaetoviridin I (9) (Borges et al., 2011), and chaetomugilin E (10) (Youn et al., 2015) (**Figure 1**). Chaetofanixin E (5) is a novel chloro-azaphilone bearing a unique 6/6/5/3/5 penta-cyclic ring system. Compounds 1-7 exhibited the noteworthy pro-angiogenic effect in a dose-dependent manner. Herein, the isolation, structure identification, and bioactivity of these compounds are reported.

MATERIALS AND METHODS

General Experimental Procedures

The ^{1}H, ^{13}C NMR, DEPT, and 2D NMR spectra were recorded on a Bruker Avance 600 spectrometer (Bruker). HRESIMS were measured on a Q-TOF Ultima Global GAA076 LC mass spectrometer. UV spectra were recorded on a 2487 detector of Waters. Electronic circular dichroism (ECD) spectra were measured on a JASCO J-815 spectrometer. Optical rotations were recorded with a JASCO P-1020 digital polarimeter. Sephadex LH-20 (Pharmacia Biotec AB, Uppsala, Sweden) and reverse-phase C18 silica gel (Merck, Darmstadt, Germany) were used for column chromatography (CC). Thin-layer chromatography (TLC) was performed on plates precoated with silica gel GF 254 (10–40 μm) and silica gel (200–300 mesh) (Qingdao Haiyang Chemical Co., Qingdao, China). Vacuum-liquid chromatography (VLC) used silica gel H (Qingdao Marine Chemical Factory). All solvents used were of analytical grade (Sinopharm Chemical Reagent Co., Shanghai, China). Semipreparative HPLC was performed using an ODS column (YMC-pack ODS-A, 10 × 250 mm, 5 μm, 4.0 mL/min).

Collection and Phylogenetic Analysis of Strain YP-106

The fungus YP-106 was originally obtained from a seawater sample collected from the Yap Trench of the Pacific Ocean at a depth of 6,215 m in 2017. The sample (2 g) was diluted to

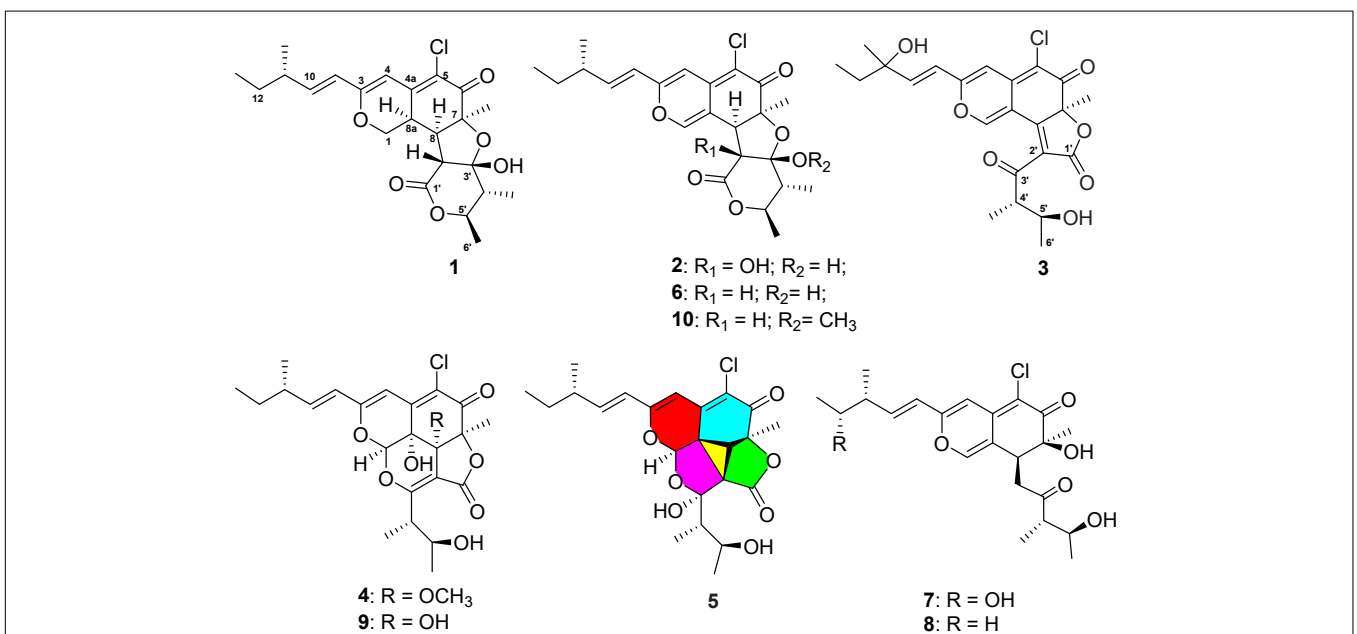

FIGURE 1 | Structures of compounds 1–10.

10^{-3} g/mL, and 100 μL of this solution was dispersed across a solid-phase agar plate (potato dextrose agar/PDA agar media) and incubated at 28°C for 4 days. A single colony was transferred to PDA agar media. The fungus was identified using a molecular biological protocol by DNA amplification and sequencing of the ITS and β-tubulin regions (Wang et al., 2006), as both showed a 99% identity to *Chaetomium globosum*. The sequence is deposited in GenBank under accession no. OL872214.

Fermentation, Extraction, and Isolation

The fungus *Chaetomium globosum* YP-106 was aseptically transferred and grown under static conditions at 28°C for 30 days in fifty 1,000 mL conical flasks containing liquid nutrition medium (300 mL/flask) composed of malt extract (17 g/L), glucose (3 g/L), peptone (3 g/L), and sea salt (33 g/L), and tap water was added later. After the completion of the fermentation period, the whole fermentation broth (60 L) was filtered, and the broth media was extracted with ethyl acetate (EtOAc), while the solid mycelia were extracted by 85% (v/v) aqueous acetone. The combined extracts (105 g) of the fermentation broth and mycelia were eluted with a stepwise gradient of petroleum ether (PE):ethyl acetate (EtOAc) (80:1, 50:1, 20:1, 10:1, 8:1, 4:1, 2:1, and 1:1, v/v, 2 L each) and chloroform ($CHCl_3$) : methyl alcohol (MeOH) (50:1, 20:1, 10:1, 5:1, 1:1, and 0:1, v/v, 2 L each) and fractionated into six fractions (Fr.1-Fr.6) over a silica gel (200-300 mesh) vacuum-liquid chromatography (VLC) column. Fr. 2 (25.8 g) was further purified by column chromatography (CC) on Sephadex LH-20 (1:1, v/v, $CHCl_3$:MeOH) to obtain nine subfractions (Fr.2.1–2.9). Subfraction 2.5 was further subjected to HPLC purification using octadecylsilyl (ODS) silica gel column (MeOH-H_2O, 75:25, v/v) to yield compounds 6 (34.2 mg) and 10 (33.5 mg). Fraction 3 (36.8 g) was further separated into four subfractions by Sephadex LH-20 CC using 100% MeOH. Subfraction 3.2 was further purified using HPLC on ODS (MeCN-H_2O, 35:65, v/v) to yield 4 (1.1 mg), 3 (2.1 mg), and Fr.3.2.3. Subfraction 3.2.3 was further purified using preparative thin-layer chromatography (TLC) (PE–EtOAc, 1:1) to get 5 (1.1 mg) and 1 (7.8 mg). Fr. 4 (28.1 g) was subjected to CC on Sephadex LH-20 by eluting with 100% MeOH to yield six subfractions (Fr. 4.1–4.6). Subfraction 4.3 was further purified using HPLC on ODS (MeCN-H_2O, 45:55, v/v) to get 9 (4.3 mg) and Fr.4.3.2. Subfraction 4.3.2 was further purified using preparative TLC (PE–EtOAc, 1:1) to get 2 (5.3 mg) and 8 (9.5 mg). Fr.5 (9.8 g) was disposed of reverse-phase silica gel (ODS) using stepwise gradient elution with MeOH/H_2O (10–100%) to obtain four subfractions (Fr.5.1–Fr.5.4). Subfraction 5.3 was further purified by Sephadex LH-20 CC using 100% MeOH and then followed by HPLC (MeCN-H_2O, 35:65, v/v) to yield 7 (1.2 mg).

Chaetofanixin A (1). This is a yellow amorphous powder; [α]25 D −47 (*c* 0.1, $CHCl_3$); UV (MeOH) λ_{max} 217 (4.58), 238 (4.82), 282 (4.26), and 373 (5.50) nm; CD (*c* 0.1, MeOH) λ_{max} (Δε) 205 (−3.14), 223 (+3.89), 242 (−1.87), 320 (+0.63), and 377 (−3.38); ^{1}H and ^{13}C NMR data, see **Table 1**; HRESIMS m/z 437.1729 $[M+H]^+$ (calcd for $C_{23}H_{30}O_6Cl$, 437.1725).

Chaetofanixin B (2). This is a yellow amorphous powder; [α]25 D −28 (*c* 0.1, $CHCl_3$); UV (MeOH) λ_{max} 225 (4.69), 252 (3.88), 294 (4.58), 336 (4.28), and 392 (4.81) nm; CD (*c* 0.1, MeOH) λ_{max} (Δε) 218 (−4.6), 261 (+0.61), and 326 (−0.98); ^{1}H and ^{13}C NMR data, see **Table 1**; HRESIMS m/z 449.1368 $[M-H]^-$ (calcd for $C_{23}H_{32}O_5Cl$, 449.1373).

Chaetofanixin C (3). This is a yellow amorphous powder; [α]25 D +30 (*c* 0.1, $CHCl_3$); UV (MeOH) λ_{max} 219 (4.19), 247 (3.77), 307 (3.48), 386 (4.41), and 455 (2.80) nm; CD (*c* 0.1, MeOH) λ_{max} (Δε) 215 (−3.15), 256 (+1.85), 271 (+0.33), 300 (+1.64), 366 (−2.72), and 448 (+0.66) nm; ^{1}H and ^{13}C NMR data, see **Table 1**; HRESIMS m/z 449.1362 $[M+H]^+$ (calcd for $C_{23}H_{32}O_5Cl$, 449.1362).

Chaetofanixin D (4). This is a yellow amorphous powder; [α]25 D −107 (*c* 0.19, $CHCl_3$); UV (MeOH) λ_{max} 216 (3.80), 249 (4.22), 307 (3.50), 386 (4.45), and 455 (2.83) nm; CD (*c* 0.1, MeOH) λ_{max} (Δε) 229 (−3.50), 261 (+3.16), 370 (−3.31), and 455 (+0.04) nm; ^{1}H and^{13}C NMR data, see **Table 1**; HRESIMS m/z 481.1613 $[M+H]^+$ (calcd for $C_{24}H_{30}O_8Cl$, 481.1624).

Chaetofanixin E (5). This is a yellow amorphous powder; [α]25 D −25 (*c* 0.2, $CHCl_3$); UV (MeOH) λ_{max} 210 (5.06), 228 (4.92), 249 (5.05), 270 (4.57), 384 (5.60), and 456 (3.98) nm; CD (*c* 0.1, MeOH) λ_{max} (Δε) 200 (+2.97), 219 (−0.24), 236 (+0.24), 271 (−3.63), 303 (−1.92), 337 (−3.59) and 392 (+4.68) nm; ^{1}H and ^{13}C NMR data, see **Table 1**; HRESIMS m/z 473.1345 $[M+Na]^+$ (calcd for $C_{23}H_{27}O_7ClNa$, 473.1338).

Pro-angiogenic Activity Experiment

Transgenic zebrafish [Transgenic zebrafish:Tg (flk1:EGFP)] were maintained under conditions of a 14/10-h light/dark cycle at a temperature of 28°C to ensure normal spawning. Healthy male and female mature zebrafish were placed in the breeding tank at a ratio of 1:1. In the next morning, the fertilized eggs were obtained and transferred to zebrafish embryo culture water (containing 5.0 mM NaCl, 0.17 mM KCl, 0.4 mM $CaCl_2$, and 0.16 mM $MgSO_4$). The zebrafish embryos that have been fertilized for 24 h were treated with 1 mg/mL pronase E solution to remove the egg membrane. Then, they were randomly divided into 12 groups: the normal control group, the model group (vatalanib, PTK787), the positive control group (Danhong injection), and the experimental group (test compounds). Each group has 10 zebrafish embryos, and each group has two parallel repeats. The model group was built based on a significant inhibition of the growth of intersegmental blood vessels (ISVs) by treating zebrafish embryos with vatalanib (0.2 μg/mL PTK787). The test compounds 1–10 (20, 40, and 80 μg/mL) and 10 μl/mL Danhong were added to the 24-well plates with model zebrafish embryos (n = 10/well). After incubation in a light-operated incubator at 28 °C for 24 h, the number of ISVs was collected using a fluorescence microscope (SZX16 Tokyo, Japan) (Fan et al., 2015).

ECD Calculation of Compounds 1–5

Conformational searches were carried out via molecular mechanics with the MM+ method in HyperChem 8.0 software, and the geometries were optimized at the gas-phase B3LYP/6-31G(d) level in Gaussian09 software (Version D.01; Gaussian, Inc.: Wallingford, CT, United States) (Frisch et al., 2013) to afford the energy-minimized conformers. Then, the optimized conformers were subjected to the calculations of ECD spectra

TABLE 1 | NMR data of compounds 1–5 in DMSO-d_6 (600 MHz for ^{1}H and 150 MHz for ^{13}C, δ in ppm, *J* in Hz).

No.	1		2		3		4		5	
	δ_C	δ_H	δ_C	δ_H	δ_C	δ_H	δ_C	δ_H	δ_C	δ_H
1	68.5, CH_2	4.41 (1H, dd, 11.4, 5.0); 4.15 (1H, dd, 13.6,11.4)	144.4, CH	7.25 (1H, s)	150.8, CH	8.62 (1H, s)	96.2, CH	6.00 (1H, s)	99.2, CH	5.74 (1H, s)
3	161.7, C		156.0, C		157.2, C		155.8, C		160.5, C	
4	101.3, CH	6.11 (1H, s)	104.6, CH	6.54 (1H, s)	105.7, CH	6.88 (1H, s)	101.4, CH	6.20 (1H, s)	100.0, CH	6.09 (1H, s)
4a	144.5, C		141.7, C		140.2, C		144.1, C		141.0, C	
5	119.0, C		109.4, C		107.4, C		123.0, C		117.3, C	
6	188.9, C		188.1, C		183.2, C		186.2, C		183.9, C	
7	83.6, C		81.9, C		87.3, C		85.9, C		80.5, C	
8	48.9, CH	2.83 (1H, overlap)	52.4, CH	3.35 (1H, overlap)	160.5, C		77.2, C		39.1, CH	2.93 (1H, s)
8a	33.3, CH	3.39 (1H, ddd, 13.6, 5.0, 2.0)	112.0, C		110.0, C		65.3, C		39.2, C	
9	122.8, CH	6.19 (1H, d, 15.6)	120.9, CH	6.35 (1H, d, 15.8)	118.4, CH	6.54 (1H, d, 15.7)	123.0, CH	6.28 (1H, d, 15.2)	123.9, CH	6.19 (1H, d, 15.7)
10	144.8, CH	6.39 (1H, dd, 15.6, 7.8)	145.2, CH	6.43 (1H, dd, 15.8,7.6)	148.5, CH	6.74 (1H, d, 15.7)	146.4, CH	6.52 (1H, dd, 15.2, 6.7)	146.1, CH	6.39 (1H, dd, 15.7,7.9)
11	37.8 CH	2.23 (1H, m)	38.0, CH	2.25 (1H, m)	72.0, C		38.4, CH	2.27 (1H, m)	38.5, CH	2.22 (1H, m)
12	28.6, CH_2	1.36 (2H, m)	28.6, CH_2	1.39 (2H, m)	34.4, CH_2	1.54 (1H, dd, 14.9, 7.4) 1.53 (1H, dd, 14.9, 7.4)	29.1, CH_2	1.40 (2H, m)	29.2, CH_2	1.37 (2H, m)
13	11.6, CH_3	0.85 (3H, t,7.4)	11.6, CH_3	0.85 (3H, t,7.4)	8.2, CH_3	0.82 (3H, t, 7.4)	12.1, CH_3	0.85 (3H, t,7.4)	12.3, CH_3	0.85 (3H, t, 7.4)
7-Me	21.5, CH_3	1.39 (3H, s)	24.2, CH_3	1.26 (3H, s)	25.2, CH_3	1.63 (3H, s)	18.3, CH_3	1.61 (3H, s)	20.0, CH_3	1.55 (3H, s)
11-Me	19.2, CH_3	1.01 (3H, d, 6.7)	19.4, CH_3	1.02 (3H, d,6.9)	27.3, CH_3	1.23 (3H, s)	19.4, CH_3	1.04 (3H, d, 6.7)	19.7, CH_3	1.02 (3H, d, 6.8)
1′	171.4, C		170.7, C		168.0, C		166.7, C		167.7, C	
2′	54.3, CH	2.82 (1H, overlap)	81.7, C		125.9, C		98.3, C		55.0, C	
3′	104.2, C		104.6, C		200.9, C		169.6, C		107.8, C	
4′	45.3, CH	1.64 (1H, dq, 9.4, 6.9)	46.2, CH	1.65 (1H, dq, 9.2, 6.7)	50.5, CH	3.41 (1H, dq, 8.6, 6.3)	40.9, CH	3.38 (1H, dq, 10.9, 6.7)	47.9, CH	1.64(1H, dq, 9.2, 7.1)
5′	76.1, CH	4.27 (1H, dq, 9.4, 6.4)	75.3, CH	4.37 (1H, dq, 9.2, 6.2)	69.6, CH	3.56 (1H, m)	68.0, CH	3.40 (1H, dq, 10.9, 6.7)	66.3, CH	3.70 (1H, ddq, 9.2, 3.8, 6.6)
6′	18.3, CH_3	1.24 (3H, d, 6.4)	18.5, CH_3	1.27 (3H, d, 6.2)	21.5, CH_3	0.98 (3H, d, 6.2)	20.9, CH_3	0.92 (3H, d, 6.7)	22.1, CH_3	1.03 (3H, d, 6.6)
4′-Me	8.8, CH_3	0.95 (3H, d, 6.9)	9.5, CH_3	1.01 (3H, d, 6.7)	12.7, CH_3	0.99 (3H, d, 6.3)	13.4, CH_3	1.00 (3H, d, 6.7)	11.3, CH_3	0.93 (3H, d, 7.1)
1′-OH		6.25, s								
3′-OH										7.12 (1H, s)
5′-OH						4.66 (1H, d, 6.2)				4.79 (1H, d, 3.8)
11-OH						4.85 (1H, br, s)				
OCH_3							53.1, CH_3	3.29 (3H, s)		

using the TD-DFT at BH&HLYP/TZVP, CAM-B3LYP/TZVP, and PEB0/TZVP, and solvent effects of the MeOH solution were evaluated at the same DFT level using the SCRF/PCM method.

RESULTS AND DISCUSSION

Chaetofanixin A (1) was obtained as a yellow amorphous powder. The molecular formula of compound 1 was determined to be $C_{23}H_{29}O_6Cl$ by HRESIMS (**Supplementary Figure 1**). The ^1H and ^{13}C NMR data (**Table 1**), assigned by HSQC, COSY, and HMBC correlations (**Figure 2** and **Supplementary Figures 4–6**), indicated the presence of 23 carbon atoms, which were clarified into five methyls, two methylenes (including one oxygenated), nine methines (including three olefinic and one oxygenated), and seven quaternary carbons (containing two oxygenated, three olefinic, and two carbonyls). Compound 1 has a chlorine atom, which was determined by the HRESIMS spectrum (**Supplementary Figure 1**) of two isotope peak intensities for $[M+H]^+/[M+H+2]^+$ at a rate of 3:1. Extensive comparison of its 1D and 2D NMR data with those of chaetomugilin D (6) (Qin et al., 2009), a co-metabolite also found in this fungus, revealed that the structures of the two compounds (1 and 6) are very similar, except for the absent double bond ($\Delta^{1,8a}$) in 1. Instead, resonances for a methylene group (CH_2-1, $\delta_{H/C}$ 4.41, 4.15/68.5) and a methine group (CH-8a, $\delta_{H/C}$ 3.39/33.3) were observed in the NMR spectra of 1. The above observation indicated that compound 1 was the double-bond hydrogenated derivative of chaetomugilin D (6). Meanwhile, the key COSY correlation (**Figure 2** and **Supplementary Figure 5**) of H_2-1/H-8a and the HMBC correlations (**Figure 2** and **Supplementary Figure 6**) from H_2-1 to C-4a and C-8a, H-8a to C-4a and C-5, and H-4 and H-8 to C-8a further confirmed the above deduction. The overall planar structure of 1 was finally defined by the HMBC and COSY correlations (**Supplementary Figures 5, 6**) as shown in **Figure 2**. The configuration of the Δ^9 double bond was assigned as *E* by the coupling constant (15.6 Hz) of H-9/H-10. The large coupling constant (13.6 Hz) of H_β-1/H-8a indicated their *trans*-diaxial relationship. NOESY correlation (**Figure 3** and **Supplementary Figure 7**) of H_β-1/H-2′ suggested their same orientation, while correlation of H-8a/CH_3-7 indicated that they were in the face opposite to H_β-1. NOESY correlations (**Supplementary Figure 7**) of H_α-1/H-8/H-5′ suggested their cofacial relationship. The opposite direction of H-4′ to H-5′ was determined by their large coupling constant (9.4 Hz). From a biosynthetic viewpoint, compound 1 should possess the same absolute configuration at C-11 as 6. The absolute configuration of 1 was assigned as (7*S*,8*R*,8a*R*,11*S*,1′*R*,2′*R*,4′*R*,5′*R*) by its similar ECD curve to that of 6. This was further confirmed by ECD calculation (**Figure 4**) of (7*S*,8*R*,8a*R*,11*S*,1′*R*,2′*R*,4′*R*,5′*R*)-1, the result of which matched well with the experimental result.

Chaetofanixin B (2) was obtained as a yellow amorphous powder. The molecular formula of compound 2 was established as $C_{23}H_{27}O_7Cl$ by HRESIMS (**Supplementary Figure 8**) peak at m/z 449.1368 $[M-H]^-$, as well as ^1H and ^{13}C-DEPTQ NMR data (**Table 1** and **Supplementary Figures 9, 10**), which indicated 10 degrees of unsaturation. A comparison of its ^1H and ^{13}C NMR spectra (**Table 1** and **Supplementary Figures 9, 10**) with those of 6 revealed that their NMR data were very similar. The main difference between them was that signal for a hydroxylated sp^3 non-protonated carbon of 2 replaced signals for CH-2′ of 6, which indicated that 2 was a hydroxylated derivative of 6 at C-2′. The large *J* value (15.8 Hz) of H-9/H-10 assigned the *E* configuration of the Δ^9 double bond. The NOESY (**Figure 3** and **Supplementary Figure 14**) correlations of H-8 with CH_3-7 and H-5′ suggested the cofacial relationship of these protons. The large *J* value (9.2 Hz) of H-4′/H-5′ suggested their *trans*-diaxial relationship. The experimental ECD curve of 2 was similar to that of 6, indicating the (7*S*,8*R*,11*S*,1′*R*,2′*S*,4′*R*,5′*R*) configuration of 2. The ECD calculations (**Figure 4**) further confirmed this deduction.

Chaetofanixin C (3) was obtained as yellow amorphous powder and was determined to be $C_{23}H_{25}O_7Cl$ by HRESIMS

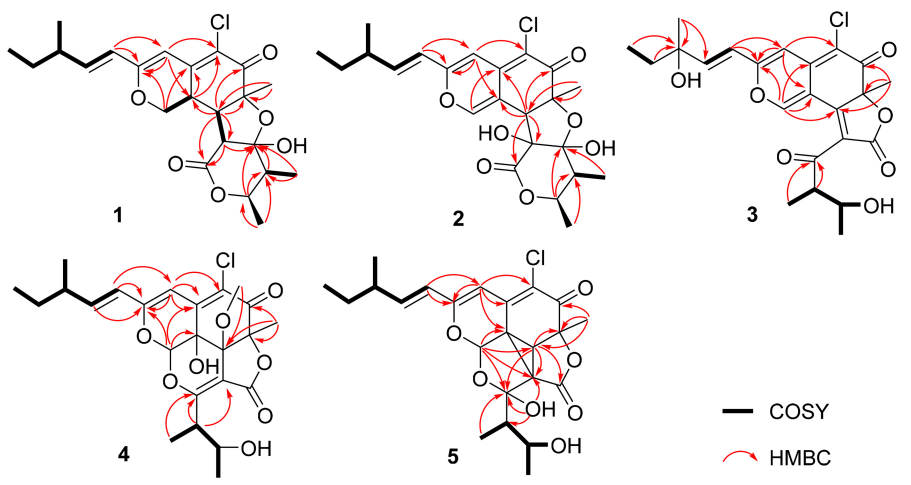

FIGURE 2 | Key ^1H–^1H COSY and HMBC correlations of 1–5.

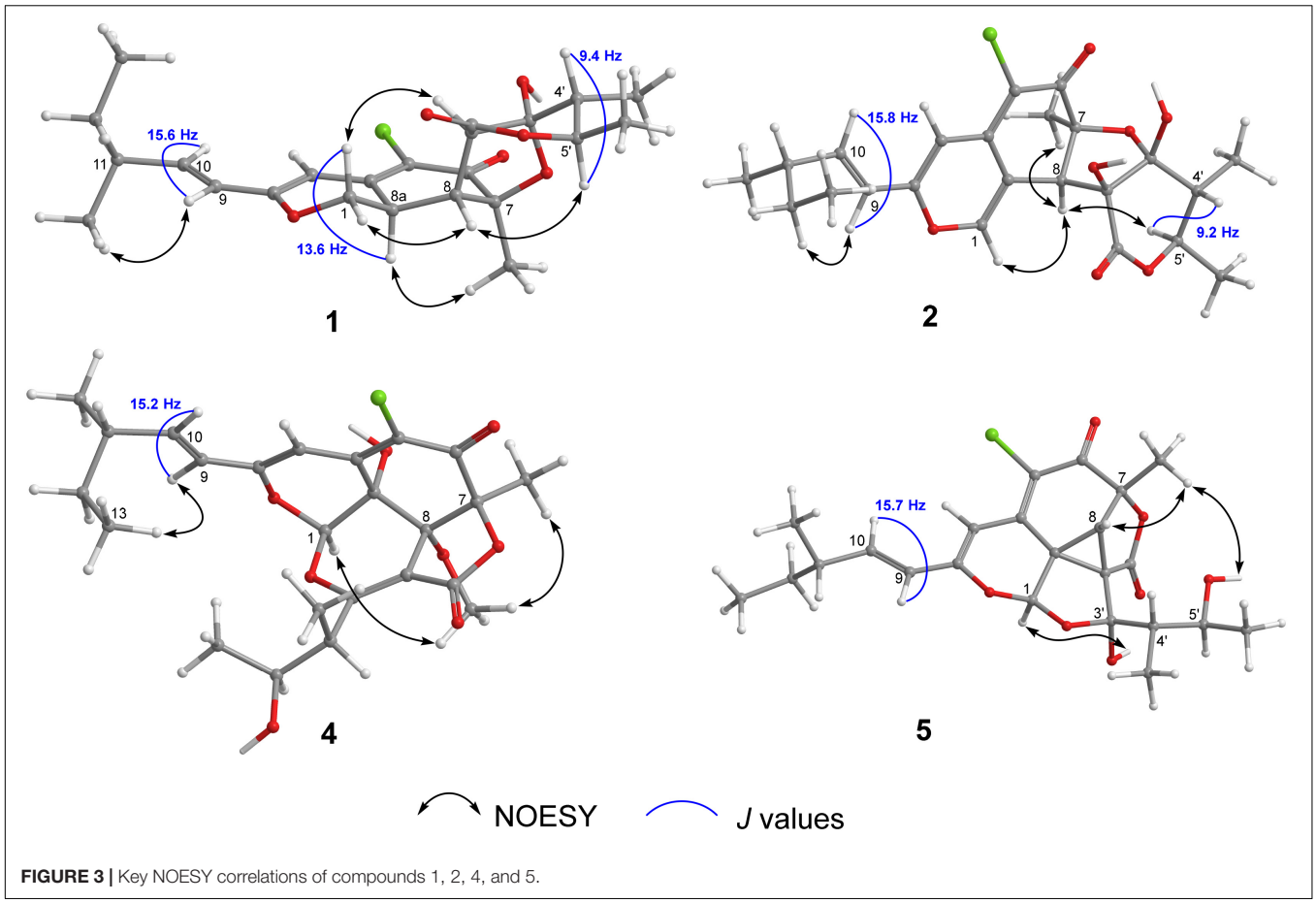

FIGURE 3 | Key NOESY correlations of compounds 1, 2, 4, and 5.

(**Supplementary Figure 15**) peak at m/z 449.1362 $[M+H]^+$. The ^1H and ^{13}C-DEPTQ NMR data (**Supplementary Figures 16, 17** and **Supplementary Table 1**), with the aid of HSQC spectra (**Supplementary Figure 18**), indicated the presence of 23 carbon atoms, which were clarified into five methyls, one methylene, six methines (including four olefinic and one oxygenated), and eleven quaternary carbons (containing two oxygenated, six olefinic, and three carbonyls). An extensive comparison of the above data with those of *epi*-chaetoviridin A (Phonkerd et al., 2008) revealed that the structures of these two compounds are very similar, except that the signals for CH-11 ($\delta_{H/C}$ 2.29/38.9) in *epi*-chaetoviridin A were absent in the NMR spectra of 3. Instead, a hydroxy group (δ_H 4.85) and one oxygenated quaternary carbon (δ_C 72.0) were observed. The above observation indicated that compound 3 was the 11-OH derivative of *epi*-chaetoviridin A. The overall planar structure of 3 was finally defined by the HMBC and COSY correlations (**Supplementary Figures 19, 20**) as shown in **Figure 2**. The *J* value (8.6 Hz) of H-4′/H-5′ was similar to those of the two known compounds chaetomugilin Q (7) (Yamada et al., 2011) and chaetoviridin J (8) (Youn et al., 2015), suggesting that the relative configuration of the two chiral centers C-4′ and C-5′ was the same as those of 7 and 8. The absolute configurations of C-7, C-4′, and C-5′ of 3 were proposed to be the same as its cometabolites 1, 2, and 6–8 from biosynthetic considerations, and were further confirmed by ECD calculations (**Figure 4**). However, the absolute configuration of C-11 remains unassigned.

Chaetofanixin D (4) was obtained as a yellow amorphous powder. The molecular formula of compound 4 was established as $C_{24}H_{29}O_8Cl$ by HRESIMS (**Supplementary Figure 21**) peak at m/z 481.1613 $[M+H]^+$, as well as ^1H and ^{13}C-DEPTQ NMR data (**Table 1** and **Supplementary Figures 22, 23**), which indicated 10 degrees of unsaturation. The ^{13}C-DEPTQ and HSQC NMR spectra (**Supplementary Figures 23, 24**) revealed the presence of 24 carbons, which were clarified into six methyls (including one oxygenated), one methylene, seven methines (including three olefinic and two oxygenated), and ten quaternary carbons (containing five olefinic, three oxygenated, and two carbonyls). Comparison of its ^1H and ^{13}C NMR spectra (**Table 1** and **Supplementary Figures 22, 23**) with those of the known azaphilone, chaetoviridin I (9) (Borges et al., 2011), which was also isolated from the culture broth of YP-6, revealed that their NMR data were very similar, except that additional signals for an oxygenated methyl (CH_3O-8, $\delta_{H/C}$ 3.29/53.1) were observed in the NMR spectra of 4. The key HMBC correlation (**Figure 2** and **Supplementary Figure 26**) of CH_3O-8 to C-8 revealed the location of this oxygenated methyl at C-8 in 4. The similarity of the coupling constants and chemical shifts between 4 and 9,[17] as well

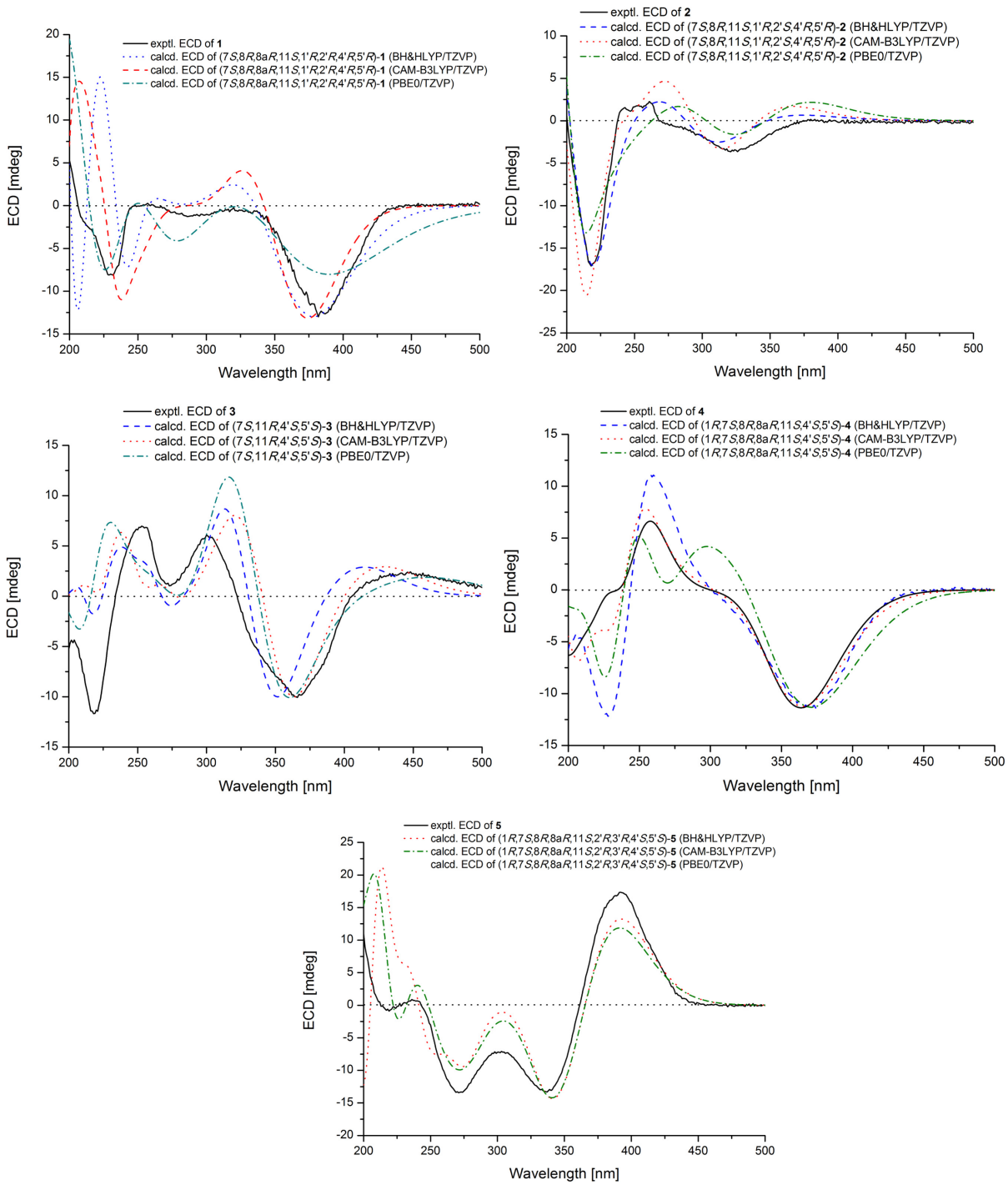

FIGURE 4 | Experimental and calculated ECD spectrum of 1–5.

as NOESY (**Figure 3**) correlations from CH_3O-8 to CH_3-7 and H-1, indicated their same relative configuration. The optical rotation value (–107) and experimental ECD curve were very similar to those of 9 (–37), suggesting their same (1*R*,7*S*,8*R*,8a*R*,11*S*,4′*S*,5′*S*) absolute configuration. The calculated ECD spectrum for the (1*R*,7*S*,8*R*,8a*R*,11*S*,4′*S*,5′*S*)-4 matched well with the experimental curve, further confirming the above deduction (**Figure 4**).

Chaetofanixin E (5) was obtained as a yellow amorphous powder. Its molecular formula was determined as $C_{23}H_{27}O_7Cl$ based on the HRESIMS peak at m/z 473.1345 $[M+Na]^+$ (**Supplementary Figure 28**) and ^1H and ^{13}C-DEPTQ NMR data

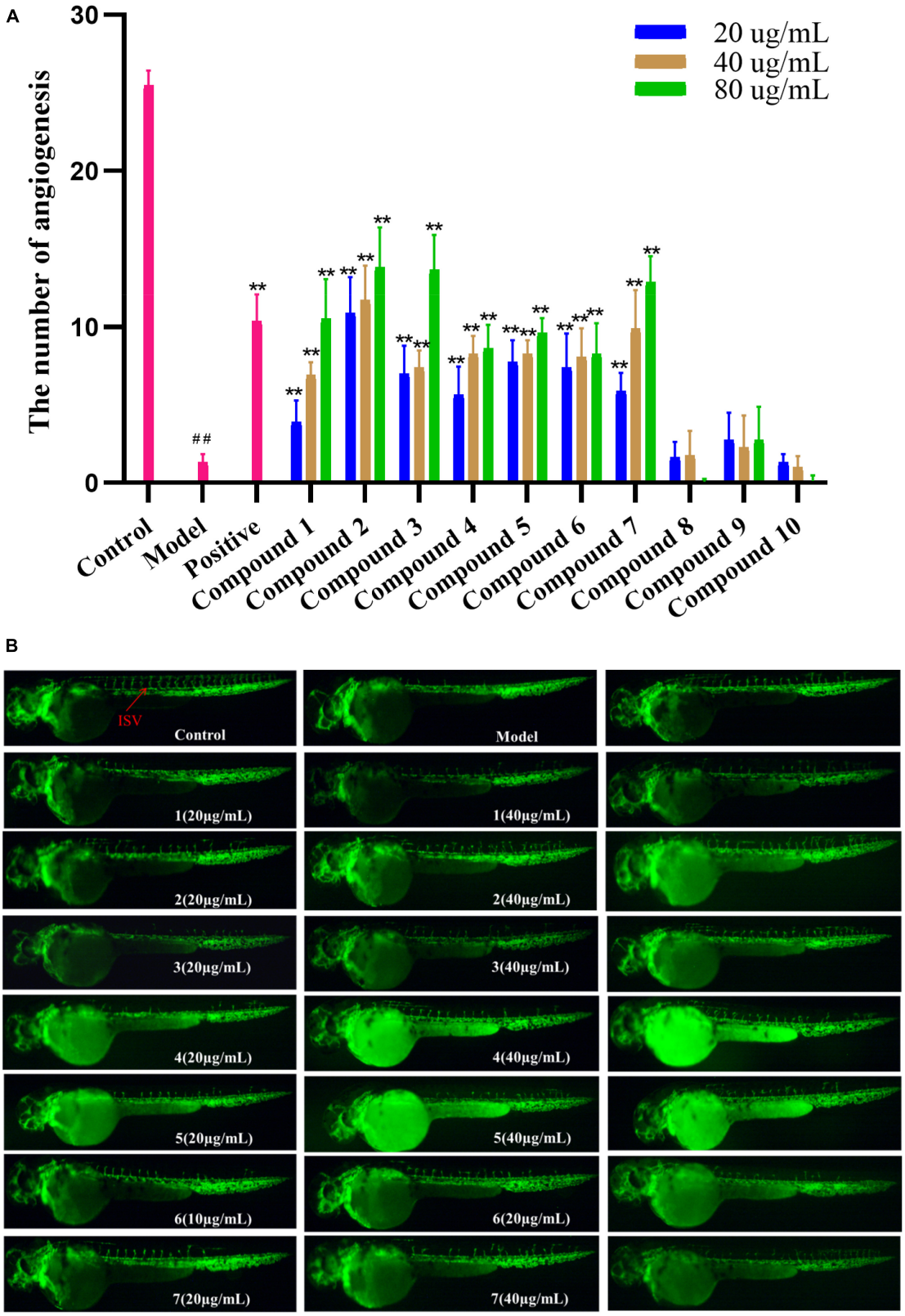

FIGURE 5 | (A) Vasculogenesis activity of compounds 1–10 (20, 40, and 80 μg/mL). $^{\#\#}P < 0.01$, compared with the normal control group; $^{**}P < 0.01$, compared with the model control group. **(B)** Images of intersomitic vessels (ISV) in transgenic fluorescent zebrafish.

(**Table 1** and **Supplementary Figures 29, 30**), which indicated 10 degrees of unsaturation. Two isotope peak intensities for $[M+H]^+/[M+H+2]^+$ at a rate of 3:1 indicated the presence of chlorine atom in compound 5. The ^{13}C NMR spectrum showed 23 signals that were classified by HSQC (**Supplementary Figure 31**) as nine non-protonated carbons (two keto carbonyls, three olefinic carbons, and two oxygenated ones), two sp^2-methine carbons, six sp^3-methine carbons (two oxygenated ones), one methylene carbon, and five methyl carbons. The ^1H-NMR spectrum showed five methyl signals at δ_H 0.85 (d, J = 7.4 Hz), 0.93 (d, J = 7.1 Hz), 1.55 (s), 1.02 (d, J = 6.8 Hz), and 1.03 (d, J = 6.6 Hz); three olefin signals at δ_H 6.09 (s), 6.19 (d, J = 15.7 Hz), and 6.39 (dd, J = 15.6, 7.9 Hz); and two oxygenated signals at δ_H 5.74 (s) and 3.70 (m). Further analysis of its NMR data suggested that chaetofanixin E (5) is similar to chaetoviridin I (9). The comparison of NMR data with those of 9 revealed that two oxygenated non-protonated carbons (C-8/C-8a) and a double bond ($\Delta^{2',3'}$) of chaetoviridin I (9) were replaced by an sp^3-methine carbon (CH-8, $\delta_{H/C}$ 2.93/39.1), two non-protonated sp^3 carbons (C-8a, δ_C 39.2; C-2′, δ_C 55.0), and an oxygenated non-protonated carbon (C-3′, δ_C 107.8) of compound 5. In the HMBC spectrum (**Figure 2** and **Supplementary Figure 33**), both H-1 and H-8 correlated with two quaternary carbons C-8a at δ_C 39.2 and C-2′ at δ_C 55.0, indicating the presence of a direct linkage between C-8a and C-2′. HMBC correlations (**Figure 2** and **Supplementary Figure 33**) from CH_3-4′ to C-4′, C-5′, and the deoxygenated non-protonated carbon C-3′ indicated the presence of a hydroxy group at C-3. Thus, compound 5 was assigned to be a novel member of the chloro-azaphilone family, the structure of which bears a highly rigid 6/6/5/3/5 penta-cyclic ring system. The large coupling constant ($J_{9/10}$ = 15.7 Hz) in the ^1H-NMR data (**Table 1** and **Supplementary Figure 29**) deduced the configuration of a double bond at C-9/C-10 as *trans* form. The NOESY (**Figure 3** and **Supplementary Figure 34**) correlations from H-8/CH_3-7/OH-5′ and H-1/OH-3′, with the aid of biosynthetic analysis from other cometabolites, led to the assignment of the relative configuration of 5 as shown in **Figure 1**. The calculated ECD spectrum (**Figure 4**) for the (1*R*,7*S*,8*R*,8a*R*,11*S*,2′*R*,3′*R*,4′*S*,5′*S*)-5 matched well with that of the experimental curve, allowing the establishment of the absolute configuration of 5 (**Figure 1**). Therefore, the chiral centers of compound 5 were tentatively assigned as (1*R*,7*S*,8*R*,8a*R*,11*S*,2′*R*,3′*R*,4′*S*,5′*S*).

Compounds 1–10 were evaluated for pro-angiogenic activity in the zebrafish models at concentrations of 20, 40, and 80 μg/mL. Compared with the model group, 1–7 significantly promoted angiogenesis in a dose-dependent manner. Among them, compounds 2, 3, and 7 showed potent pro-angiogenic activities at the concentration of 80 μg/mL, while compounds 8-10 did not show relevant activities (**Figure 5**). In addition, the activity of compound 2 was stronger than those of 6 and 10, suggesting that hydroxylation at C-2′ and C-3′ might contribute to the pro-angiogenic activity. Compound 4 exhibited much higher activity than that of 9, implying that methylation at 8-OH might increase the activity. Furthermore, compound 7 showed stronger activities than 8, indicating that oxidation at C-12 could increase the activity. The results suggested that compounds 1–7 could be promising candidates for the development of lead drugs against cardiovascular diseases.

In summary, five new chloro-azaphilone derivatives, including a structurally unique one, and five related known analogs were isolated from the culture extract of *Chaetomium globosum* YP-106, a fungus obtained from the hadal trench-derived seawater. Compounds 1–7 showed excellent pro-angiogenic activities in a dose-dependent manner, possessing the potential to be developed as natural cardiovascular disease agents. These results further demonstrated the great potential for the development and utilization of deep-sea microbial resources for drug research.

DATA AVAILABILITY STATEMENT

The original contributions presented in this study are included in the article/**Supplementary Material**, further inquiries can be directed to the corresponding authors.

ETHICS STATEMENT

The animal study was reviewed and approved by Ethics Committee of the Biology Institute of Shandong Academy of Science. Written informed consent was obtained from the owners for the participation of their animals in this study.

AUTHOR CONTRIBUTIONS

YF conceived and designed the experiments and wrote the manuscript. CJ, YZ, and ZM contributed to the isolation of compounds. PL and TF contributed to the bioactivity assay. LG revised the manuscript. LZ and LX supervised the work. All authors contributed to the article and approved the submitted version.

FUNDING

This work was financially supported by the National Natural Science Foundation of China (42006096), the Natural Science Foundation of Shandong Province (ZR2020QD098), the China Postdoctoral Science Foundation (2020M682266), the Talents of High-Level Scientific Research Foundation of Qingdao Agricultural University (Grant 6651120031), Specific Research Project of Guangxi for Research Bases and Talents (AD18126005), and Technical Demonstration and Application of Wood Segment Cultivation of Rare Edible Fungi in the Undergrowth (Grant 6602419059).

SUPPLEMENTARY MATERIAL

The Supplementary Material for this article can be found online at: https://www.frontiersin.org/articles/10.3389/fmicb.2022.943452/full#supplementary-material

REFERENCES

Borges, W. S., Mancilla, G., Guimarães, D. O., Durán-Patrón, R., Collado, I. G., and Pupo, M. T. (2011). Azaphilones from the endophyte *Chaetomium globosum*. *J. Nat. Prod.* 74, 1182–1187. doi: 10.1021/np200110f

Carroll, A. R., Copp, B. R., Davis, R. A., Keyzers, R. A., and Prinsep, M. R. (2021). Marine natural products. *Nat. Prod. Rep.* 38, 362–413. doi: 10.1039/D0NP00089B

Chi, L. P., Li, X. M., Wan, Y. P., Li, X., and Wang, B. G. (2020b). Ophiobolin sesterterpenoids and farnesylated phthalide derivatives from the deep sea cold-seep-derived fungus *Aspergillus insuetus* SD-512. *J. Nat. Prod.* 83, 3652–3660. doi: 10.1021/acs.jnatprod.0c00860

Chi, L. P., Li, X. M., Li, L., Li, X., and Wang, B. G. (2020a). Cytotoxic thiodiketopiperazine derivatives from the deep sea-derived fungus *Epicoccum nigrum* SD-388. *Mar. Drugs* 18:160. doi: 10.3390/md18030160

Fan, Y. Q., Li, P. H., Chao, Y. X., Chen, H., Du, N., He, Q. X., et al. (2015). Alkaloids with cardiovascular effects from the marine-derived fungus *Penicillium expansum* Y32. *Mar. Drugs* 13, 6489–6504. doi: 10.3390/md13106489

Frisch, M. J., Trucks, G. W., Schlegel, H. B., Scuseria, G. E., Robb, M. A., Cheeseman, J. R., et al. (2013). *Gaussian 09, Version D. 01*.

Guo, X., Meng, Q., Niu, S., Liu, J., Guo, X., Sun, Z., et al. (2021). Epigenetic manipulation to trigger production of guaiane-type sesquiterpenes from a marine-derived *Spiromastix* sp. fungus with antineuroinflammatory effects. *J. Nat. Prod.* 84, 1993–2003. doi: 10.1021/acs.jnatprod.1c00293

Jude, E. B., Eleftheriadou, I., and Tentolouris, N. (2010). Peripheral arterial disease in diabetes-a review. *Diabetic Med.* 27, 4–14. doi: 10.1111/j.1464-5491.2009.02866.x

Kurusamy, S., López-Maderuelo, D., Little, R., Cadagan, D., Savage, A. M., Ihugba, J. C., et al. (2017). Selective inhibition of plasma membrane calcium ATPase 4 improves angiogenesis and vascular reperfusion. *J. Mol. Cell. Cardiol.* 109, 38–47. doi: 10.1016/j.yjmcc.2017.07.001

Li, P., Zhang, M., Xie, D., Zhang, X., Zhang, S., Gao, F., et al. (2021). Characterization and bioactivities of phospholipids from squid viscera and gonads using ultra-performance liquid chromatography-Q-exactive orbitrap/mass spectrometry-based lipidomics and zebrafish models. *Food Funct.* 12, 7986–7996. doi: 10.1039/D1FO00796C

Phonkerd, N., Kanokmedhakul, S., Kanokmedhakul, K., Soytong, K., Prabpai, S., and Kongsearee, P. (2008). Bis-spiro-azaphilones and azaphilones from the fungi *Chaetomium cochliodes* VTh01 and C. cochliodes CTh05. *Tetrahedron* 64, 9636–9645. doi: 10.1016/j.tet.2008.07.040

Potz, B. A., Parulkar, A. B., Abid, R. M., Sodha, N. R., and Sellke, F. W. (2017). Novel molecular targets for coronary angiogenesis and ischemic heart disease. *Coronary Artery Dis.* 28, 605–613. doi: 10.1097/MCA.0000000000000516

Qin, J. C., Zhang, Y. M., Gao, J. M., Bai, M. S., Yang, S. X., Laatsch, H., et al. (2009). Bioactive metabolites produced by *Chaetomium globosum*, an endophytic fungus isolated from *Ginkgo biloba*. *Bioorg. Med. Chem. Lett.* 19, 1572–1574. doi: 10.1016/j.bmcl.2009.02.025

Skropeta, D., and Wei, L. (2014). Recent advances in deep-sea natural products. *Nat. Prod. Rep.* 31, 999–1025. doi: 10.1039/B808743A

Virani, S. S., Alonso, A., Benjamin, E. J., Bittencourt, M. S., Callaway, C. W., Carson, A. P., et al. (2020). Heart disease and stroke statistics—2020 update: a report from the American heart association. *Circulation* 141, e139–e596. doi: 10.1161/CIR.0000000000000757

Wang, J., He, W., Huang, X., Tian, X., Liao, S., Yang, B., et al. (2016). Antifungal new oxepine-containing alkaloids and xanthones from the deep-sea-derived fungus *Aspergillus versicolor* SCSIO 05879. *J. Agric. Food Chem.* 14, 2910–2916. doi: 10.1021/acs.jafc.6b00527

Wang, S., Li, X. M., Teuscher, F., Li, D. L., Diesel, A., Ebel, R., et al. (2006). Chaetopyranin, a benzaldehyde derivative, and other related metabolites from *Chaetomium globosum*, an endophytic fungus derived from the marine red alga *Polysiphonia urceolata*. *J. Nat. Prod.* 69, 1622–1625. doi: 10.1021/np060248n

Wang, Y. N., Meng, L. H., and Wang, B. G. (2020). Progress in research on bioactive secondary metabolites from deep-sea derived microorganisms. *Mar. Drugs* 18:614. doi: 10.3390/md18120614

Yamada, T., Muroga, Y., Jinno, M., Kajimoto, T., Usami, Y., Numata, A., et al. (2011). New class azaphilone produced by a marine fish-derived *Chaetomium globosum*. the stereochemistry and biological activities. *Bioorg. Med. Chem.* 19, 4106–4113. doi: 10.1016/j.bmc.2011.05.008

Yan, L. H., Li, P. H., Li, X. M., Yang, S. Q., Liu, K. C., Wang, B. G., et al. (2022). Chevalinulins A and B, proangiogenic alkaloids with a spiro[bicyclo[2.2.2]octane-diketopiperazine] skeleton from deep sea cold-seep-derived fungus *Aspergillus chevalieri* CS-122. *Org. Lett.* 24, 2684–2688. doi: 10.1021/acs.orglett.2c00781

Youn, U. J., Sripisut, T., Park, E. J., Kondratyuk, T. P., Fatima, N., Simmons, C. J., et al. (2015). Determination of the absolute configuration of chaetoviridins and other bioactive azaphilones from the endophytic fungus *Chaetomium globosum*. *Bioorg. Med. Chem. Lett.* 25, 4719–4723. doi: 10.1016/j.bmcl.2015.08.063

Zhou, F., Dai, O., Peng, C., Xiong, L., Ao, H., Liu, F., et al. (2021). Pro-angiogenic effects of essential oil from perilla frutescens and its main component (perillaldehyde) on zebrafish embryos and human umbilical vein endothelial cells. *Drug Des. Dev. Ther.* 15, 4985–4999. doi: 10.2147/DDDT.S336826

Conflict of Interest: The authors declare that the research was conducted in the absence of any commercial or financial relationships that could be construed as a potential conflict of interest.

Publisher's Note: All claims expressed in this article are solely those of the authors and do not necessarily represent those of their affiliated organizations, or those of the publisher, the editors and the reviewers. Any product that may be evaluated in this article, or claim that may be made by its manufacturer, is not guaranteed or endorsed by the publisher.

frontiers | Frontiers in Microbiology

TYPE Original Research
PUBLISHED 29 August 2022
DOI 10.3389/fmicb.2022.976399

OPEN ACCESS

EDITED BY
Liao Li,
Polar Research Institute of China, China

REVIEWED BY
Huang Riming,
South China Agricultural University, China
Fu Peng,
Ocean University of China, China
Yang Fan,
Shanghai Jiao Tong University, China

*CORRESPONDENCE
Xiaowei Luo
luoxiaowei1991@126.com
Yonghong Liu
yonghongliu@scsio.ac.cn
Peng Guo
guopeng_chcip@163.com

†These authors have contributed equally to this work

SPECIALTY SECTION
This article was submitted to Extreme Microbiology a section of the journal Frontiers in Microbiology

RECEIVED 23 June 2022
ACCEPTED 21 July 2022
PUBLISHED 29 August 2022

CITATION
Ren X, Chen C, Ye Y, Xu Z, Zhao Q, Luo X, Liu Y and Guo P (2022) Anti-inflammatory compounds from the mangrove endophytic fungus *Amorosia* sp. SCSIO 41026.
Front. Microbiol. 13:976399.
doi: 10.3389/fmicb.2022.976399

Anti-inflammatory compounds from the mangrove endophytic fungus *Amorosia* sp. SCSIO 41026

Xue Ren[1†], Chunmei Chen[2,3†], Yuxiu Ye[4], Ziying Xu[1], Qingliang Zhao[5], Xiaowei Luo[4*], Yonghong Liu[2,3,4,6*] and Peng Guo[1*]

[1]Capital Institute of Pediatrics, Beijing, China, [2]CAS Key Laboratory of Tropical Marine Bio-resources and Ecology/Guangdong Key Laboratory of Marine Materia Medica, South China Sea Institute of Oceanology, Chinese Academy of Sciences, Guangzhou, China, [3]University of Chinese Academy of Sciences, Beijing, China, [4]Institute of Marine Drugs, Guangxi University of Chinese Medicine, Nanning, China, [5]State Key Laboratory of Molecular Vaccinology and Molecular Diagnostics, Center for Molecular Imaging and Translational Medicine, Department of Laboratory Medicine, School of Public Health, Xiamen University, Xiamen, China, [6]Southern Marine Science and Engineering Guangdong Laboratory, Guangzhou, China

Three new chlorinated compounds, including two propenylphenol derivatives, chlorophenol A and B (**1** and **2**), and one benzofuran derivative, chlorophenol C (**3**), together with 16 known compounds, were isolated from the mangrove endophytic fungus *Amorosia* sp. SCSIO 41026. 7-Chloro-3,4-dihydro-6,8-dihydroxy-3-methylisocoumarine (**4**) and 2,4-dichloro-3-hydroxy-5-methoxy-toluene (**5**) were obtained as new natural products. Their structures were elucidated by physicochemical properties and extensive spectroscopic analysis. Compounds **1**, **4**, **7**, **9**, **13**, **15**, **16**, and **19** possessed inhibitory effects against the excessive production of nitric oxide (NO) and pro-inflammatory cytokines in lipopolysaccharide (LPS)-challenged RAW264.7 macrophages without obvious cytotoxicity. Moreover, 5-chloro-6-hydroxymellein (**13**) further alleviated the pathological lung injury of LPS-administrated mice and protected RAW264.7 macrophages against LPS-induced inflammation through PI3K/AKT pathway *in vivo*. Our research laid the foundation for the application of compound **13** as a potential anti-inflammatory candidate.

KEYWORDS

marine fungi, *Amorosia* sp., chlorinated compounds, anti-inflammatory activity, acute lung injury mice

Introduction

As an adaptive response, inflammation is triggered by harmful stimuli and conditions that prompt the host to produce pro-inflammatory cytokines including interferon, interleukin, chemokines, and tumor necrosis factor against pathogens (Al-Lamki et al., 2001). A controlled inflammatory response is generally thought to be beneficial, in providing protection against infection for example, but it can become harmful or even fatal if it is maladjusted (e.g., rheumatoid arthritis, systemic infection, and septic shock). Nitric

oxide (NO) is synthesized by inducible nitric oxide synthase type 2 (NOS-2) in many cells involved in immunity and inflammation. Studies have shown that overproduction of NO is rapidly oxidized to reactive nitrogen oxides (RNOs; Coleman, 2001), which are able to modify key signal molecules such as kinases and transcription factors. In addition, RNOs restrain crucial enzymes in mitochondrial respiration, resulting in intra-cellular ATP depletion. In addition, a high concentration of NO inhibited the activity of antigen-presenting cells and T-cell proliferation (Kim et al., 2002; Hortelano et al., 2003). Therefore, targeting the reduction of these pro-inflammatory mediators can be an effective way to control and prevent chronic inflammatory diseases to some extent.

Lipopolysaccharide (LPS) is a virulence factor of the outer membrane of gram-negative bacterial cell wall, of which lipid A is the immunologically active component and can cause an inflammatory response. LPS induces the translocation of the transcription factor NF-κB into the nucleus by binding to cells expressing toll-like receptor 4 (TLR4), resulting in dephosphorylation of phosphorylated interferon regulatory factor 3 (IRF3) and stimulating the production of type I interferons, which causes subsequent inflammatory response (Yoo et al., 2014; Peerapornratana et al., 2019; Zhuo et al., 2019). Although NF-κB signaling has been historically considered a classic LPS-induced inflammatory pathway, it is of great significance to enthusiastically search for the in-depth understanding of the inflammatory response mechanism and the development of target drugs.

Halogenated organic molecules are generally rare in nature and could simply be classified as fluorinated, chlorinated, brominated, or iodinated compounds (Wang et al., 2013). Over 5,000 halogenated natural products had been reported as of 2011 with structural and functional diversity (Gribble, 2015; Zeng and Zhan, 2019). As a key part of halogenated molecules, chlorinated compounds have demonstrated a broad range of remarkable activities (Gribble, 2015), including antibacterial activity (Bracegirdle et al., 2021; Saetang et al., 2021) and anticancer activity (Luo et al., 2018). Recently, three new natural chlorinated 3-phenylpropanoic acid derivatives were found with significant and selective inhibitory activities toward *Escherichia coli* and *Staphylococcus aureus* (Shaala et al., 2020).

Naturally occurring chlorinated compounds were mainly isolated from the marine environment and microorganisms (Wang et al., 2013, 2021a,b). Mangrove forests are complex ecosystems with the frequent tide, which contained a high concentration of chloride ions. Therefore, mangrove-derived fungi are proved to be a promising source of novel and unique chlorine-containing bioactive secondary metabolites (Xu, 2015; Chen et al., 2021a). As part of our continuous efforts to discover structurally novel and bioactive secondary metabolites from mangrove endophytic fungi (Chen et al., 2021b,d), three new chlorine-containing compounds, chlorophenol A – C (**1**–**3**), and two new natural products (**4** and **5**), together with 14 known compounds, were isolated from the mangrove-derived fungus *Amorosia* sp. SCSIO 41026. Herein, the isolation, structure elucidation, and biological effects of compounds **1**–**19** (Figure 1) are described.

Materials and methods

General experimental procedures

The UV and IR spectra were recorded on a Shimadzu UV-2600 PC spectrometer (Shimadzu) and an IR Affinity-1 spectrometer (Shimadzu). Optical rotations were determined with an Anton Paar MPC 500 polarimeter. HRESIMS spectra were recorded with a Bruker maXis Q-TOF mass spectrometer. The NMR spectra were recorded on a Bruker Avance-500 or 700 spectrometers (Bruker BioSpin International AG, Switzerland) using tetramethylsilane as internal standard, and chemical shifts were recorded as δ-values. Semipreparative high-performance liquid chromatography (HPLC) was performed on the Hitachi Primaide with a DAD detector, using an ODS column (YMC-pack ODS-A, 10 mm × 250 mm, 5 μm). Thin-layer chromatography analysis (TLC) and column chromatography (CC) were performed on plates precoated with silica gel GF254 (10–40 μm) and over silica gel (200–300 mesh; Qingdao Marine Chemical Factory) and Sephadex LH-20 (Amersham Biosciences, Uppsala, Sweden), respectively. Spots were detected on TLC (Qingdao Marine Chemical Factory) under 254 nm UV light. All solvents employed were of analytical grade (Tianjin Fuyu Chemical and Industry Factory).

Fungal material

The endophytic fungal strain SCSIO 41026 was isolated from the leaf of *Avicennia marina* (Forsk.) Vierh. collected from the mangrove wetland in Zhanjiang, Guangdong province, China (21.235° N, 110.451° E). The strain was stored on MB agar (malt extract 15 g, sea salt 10 g, agar 16 g, H_2O 1 l, and pH 7.4–7.8) slants at 4°C and deposited at the Key Laboratory of Tropical Marine Bio-resources and Ecology, Chinese Academy of Sciences. The ITS1-5.8S-ITS4 sequence region (GenBank accession No. OL826791) of strain SCSIO 41026 was amplified by PCR. The DNA sequencing showed it shared significant homology to the sequence of *Amorosia littoralis* (accession No. AM292047.1), so it was designated as *Amorosia* sp. SCSIO 41026.

Fermentation and extraction

A large-scale fermentation of fungal strain SCSIO 41026 was incubated at 28°C for 14 days on a rotating shaker (180 rpm) in 1 L conical flasks containing the liquid medium (300 ml/flask) composed of mannitol (2%), yeast extract (0.3%), $MgSO_4{\cdot}7H_2O$

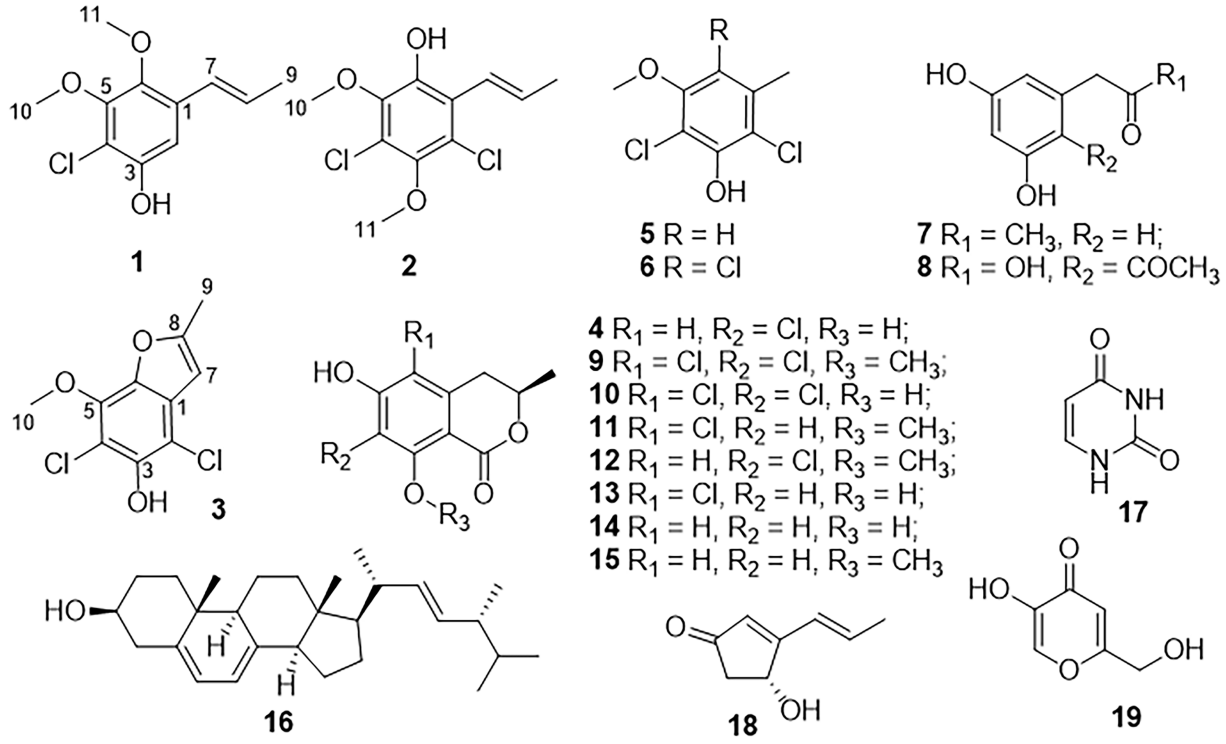

FIGURE 1
Structures of compounds **1**–**19**.

(0.03%), sodium glutamate (1%), glucose (1%), KH_2PO_4 (0.05%), sucrose (2%), corn steep liquor (0.1%), artificial sea salt (3.3%), and tap water after adjusting its pH to 7.5. The whole fermented broth (33 L) was overlaid with EtOAc, sonicated for 15 min, and extracted with EtOAc three times to afford a brown extract (22.0 g).

Isolation and purification

The organic extract was subjected to silica gel CC using step gradient elution with petroleum ether/CH_2Cl_2 (0–100%, *v*/*v*) and CH_2Cl_2/CH_3OH (0–100%, *v*/*v*) to obtain 10 subfractions (Frs. 1–10) based on TLC properties.

Fraction 1 was separated by semipreparative reverse-phase HPLC (74% CH_3OH/H_2O, 2 ml/min) to afford **5** (4.5 mg, t_R = 12.5 min), **3** (5.9 mg, t_R = 17.7 min), **6** (7.8 mg, t_R = 26.0 min), and **2** (8.2 mg, t_R = 28.8 min). Fraction 2 was also subjected to semipreparative HPLC eluting with 62% CH_3OH/H_2O to give **10** (13.3 mg, t_R = 22.3 min) and **1** (2.6 mg, t_R = 27.5 min). Fraction 3 was divided into a white solid (16, 51.5 mg) and a methanol solution (Fr.3–2) by filtration. Fr. 3–2 was further subjected to a Sephadex LH-20 column eluting with CH_3OH, followed by semipreparative HPLC (58% CH_3OH/H_2O, 2 ml/min) to afford **12** (83.5 mg, t_R = 11.5 min), **14** (20.1 mg, t_R = 13.2 min), **4** (10.8 mg, t_R = 16.8 min), **9** (17.6 mg, t_R = 18.8 min), and **13** (10.6 mg, t_R = 22.5 min). Fraction 6 was purified by semipreparative HPLC (35% CH_3CN/H_2O, 2 ml/min) to offer **18** (6.7 mg, t_R = 11.3 min), **15** (7.1 mg, t_R = 15.0 min), and **11** (6.3 mg, t_R = 22.0 min). **7** (6.2 mg, t_R = 16.0 min) was obtained from fraction 8 by semipreparative HPLC eluting with 15% CH_3CN/H_2O (2 ml/min). Fraction 10 was separated by semipreparative HPLC (30% CH_3OH/H_2O, 2 ml/min) to afford **17** (6.3 mg, t_R = 7.0 min), **19** (70.5 mg, t_R = 8.5 min), and **8** (11.0 mg, t_R = 17.5 min).

Spectroscopic data of compounds

The specifications are as follows:

Chlorophenol A (**1**): colorless oil; UV (CH_3OH) λ_{max} (log ε) 206 (4.04), 254 (3.53), and 320 (3.29) nm; IR (film)ν_{max} 3,385, 2,929, 1,680, 1,458, 1,411, 1,205, 1,141, 1,070, 1,012, 844, 802, and 725 cm^{-1}; ^1H and ^{13}C NMR data, Table 1; and HRESIMS *m*/*z* 227.0476 $[M-H]^-$ (calcd for $C_{11}H_{12}ClO_3^-$, 227.0480).

Chlorophenol B (**2**): colorless oil; UV (CH_3OH) λ_{max} (log ε) 211 (4.12), 261 (3.62), and 298 (3.33) nm; IR (film)ν_{max} 3,394, 2,937, 1,680, 1,454, 1,408, 1,348, 1,205, 1,143, 1,083, 985, 798, and 723 cm^{-1}; ^1H and ^{13}C NMR data, Table 1; and HRESIMS *m*/*z* 261.0092 $[M-H]^-$ (calcd for $C_{11}H_{11}Cl_2O_3^-$, 261.0091).

Chlorophenol C (**3**): brown oil; UV (CH_3OH) λ_{max} (log ε) 216 (4.08), 261 (3.76), and 292 (3.19) nm; IR (film)ν_{max} 2,926,

TABLE 1 ^{1}H (500MHz) and ^{13}C (125MHz) NMR data for 1–3 (δ in ppm, DMSO-d_6).

Pos.	1		2		3	
	δ_C type	δ_H (J in Hz)	δ_C type	δ_H (J in Hz)	δ_C type	δ_H (J in Hz)
1	129.8, C		122.8, C		128.3, C	
2	106.9, CH	6.83 (s)	122.4, C		110.4, C	
3	150.0, C		144.5, C		145.5, C	
4	113.0, C		120.0, C		104.9, C	
5	150.0, C		143.3, C		139.6, C	
6	143.1, C		146.1, C		138.7, C	
7	124.3, CH	6.53 (dd, 16.0, 1.5)	123.1, CH	6.42 (dd, 16.0, 1.5)	101.7, CH	6.61 (d, 1.0)
8	127.3, CH	6.19 (dq, 16.0, 6.5)	133.5, CH	6.58 (dq, 16.0, 6.5)	157.7, C	
9	18.7, CH_3	1.88 (dd, 6.5, 1.5)	19.6, CH_3	1.89 (dd, 6.5, 1.5)	13.8, CH_3	2.47 (d, 1.0)
10	60.5, CH_3	3.80 (s)	60.4, CH_3	3.73 (s)	60.6, CH_3	4.12 (s)
11	61.1, CH_3	3.68 (s)	60.7, CH_3	3.72 (s)		
OH		9.97 (s)		9.63 (s)		9.75 (s)

2,854, 1,683, 1,472, 1,437, 1,375, 1,339, 1,209, 1,142, 1,005, 980, 947, 910, and 723 cm^{-1}; ^{1}H and ^{13}C NMR data, Table 1; and HRESIMS m/z 244.9786 $[M-H]^-$ (calcd for $C_{10}H_7Cl_2O_3^-$, 244.9778).

X-ray crystallographic analysis

The clear light colorless crystals of **4** and **12** were obtained in MeOH by slow evaporation. Crystallographic data for the structures have been deposited in the Cambridge Crystallographic Data Centre. Copies of the data can be obtained, free of charge, on application to CCDC, 12 Union Road, Cambridge CB21EZ, United Kingdom [fax: +44(0)-1,223–336,033 or e-mail: deposit@ccdc.cam.ac.uk].

Crystal data for **4**: $2C_{10}H_9ClO_4{\cdot}2CH_3OH$, $M_r = 521.33$, crystal size $0.18 \times 0.09 \times 0.08\ mm^3$, monoclinic, $a = 7.17000$ (10) Å, $b = 15.1731$ (2) Å, $c = 10.73390$ (10) Å, $\alpha = 90°$, $\beta = 90.9170$ (10)°, $\gamma = 90°$, $V = 1167.60$ (2) Å3, $Z = 2$, $T = 100.00$ (10) K, space group $P2_1$, μ(Cu Kα) = 1.54184 mm^{-1}, $D_{calc} = 1.483\ g/cm^3$, 11,652 reflections measured ($8.238° \leq 2\Theta \leq 148.702°$), and 4,588 unique ($R_{int} = 0.0251$, $R_{sigma} = 0.0301$). The final R_1 values were 0.0274 [$I > 2\sigma(I)$]. The final $wR(F^2)$ values were 0.0745 [$I > 2\sigma(I)$]. The final R_1 values were 0.0279 (all data). The final $wR(F^2)$ values were 0.0748 (all data). The goodness of fit on F^2 was 1.069. The flack parameter was 0.005 (5) (CCDC 2133225).

Crystal data for **12**: $4C_{11}H_{11}ClO_4$, $M_r = 970.59$, crystal size $0.19 \times 0.15 \times 0.04\ mm^3$, triclinic, $a = 7.5028$ (2) Å, $b = 10.4928$ (4) Å, $c = 14.5209$ (4) Å, $\alpha = 105.964$ (3)°, $\beta = 90.259$ (2)°, $\gamma = 96.779$ (2)°, $V = 1090.57$ (6) Å3, $Z = 1$, $T = 100.00$ (10) K, space group $P1$, μ(Cu Kα) = 1.54184 mm^{-1}, $Dc_{alc} = 1.478\ g/cm^3$, 10,467 reflections measured ($8.834° \leq 2\Theta \leq 149.016°$), and 5,572 unique ($R_{int} = 0.0559$, $R_{sigma} = 0.0601$). The final R_1 values were 0.0551 [$I > 2\sigma(I)$]. The final $wR(F^2)$ values were 0.1339 [$I > 2\sigma(I)$]. The final R_1 values were 0.0624 (all data). The final $wR(F^2)$ values were 0.1373 (all data). The goodness of fit on F^2 was 1.062. The flack parameter was 0.000 (16) (CCDC 2133224).

RAW264.7 cell culture and LPS-induced inflammation cell model

RAW264.7 macrophages were obtained from Peking Union Medical College. Cells were maintained in Dulbecco's modified Eagle's medium (DMEM) with high glucose (Corning, Corning, NY, United States) supplemented with 10% (v/v) fetal bovine serum (FBS, Gibco, Grand Island, NY, United States), penicillin (100 U/ml), and streptomycin (100 mg/ml; Thermo Scientific, Waltham, MA, United States) in a 100% humidified incubator with 5% CO_2 at 37°C. The culture medium was changed every 2 days.

For LPS induction, RAW264.7 cells were cultured in a 24-well plate at a density of 1×10^5 cells/well (1 ml medium/well) overnight. After 24 h of exposure to 0.1 μg/ml LPS (#L2630, Merck, Shanghai, China) and being separately co-treated with the compounds (final concentration was maintained at 10 μM), the culture supernatant was collected to measure the production of NO, IL-6, TNF-α, and MCP-1, and cells were digested and harvested for RNA extraction.

Cell viability assay

3×10^4 cells/well (100 μl medium/well) were seeded in a 96-well plate overnight; then, they were exposed to DMEM supplemented with the compounds (final concentration was maintained at 10 μM) for 24 h, respectively. At the same time, the wells without cells were set as blank group and the drug-free cells as control group. Whereafter, 10 μl CCK-8 solution (#C0037, Beyotime Institute of Biotechnology, Shanghai, China) was added to each well and incubated at 37°C for 1 h. The absorbance was read at 450 nm with a microplate reader (Thermo, Waltham, MA, United States). Cell viability was calculated by the formula (experimental group absorbance value/control group absorbance value) × 100%.

Nitric oxide production assay

Nitric oxide production was assessed by a Nitric Oxide Assay Kit (#S0021, Beyotime Institute of Biotechnology, Shanghai, China) according to the manufacturer's instructions; in the meanwhile, L-NMMA was used as a positive control of compound treatment since it is the total NOS inhibitor.

Briefly, after 24 h of LPS induction, 50 µl cell culture supernatant was transferred to another 96-well plate, and then, 50 µl Griess reagents I and Griess reagents II were successively added. The absorbance was read at 540 nm with a microplate reader. The calibration curve was contained in the Supplementary Figure 24.

Cytokine detection

After 24 h of LPS induction, the cell culture supernatant was collected to measure the release of tumor necrosis factor α (TNF-α), interleukin 6 (IL-6), and monocyte chemoattractant protein 1 (MCP-1). Cytokine levels were quantified in the samples using an automatic ELISA (ELLA, protein simple).

Quantitative real-time PCR analysis

Total RNA was isolated from cells using TRIzol® reagent (Ambion, Austin, Texas, United States) and was reverse-transcribed into cDNA using EasyScript® One-Step gDNA Removal and cDNA Synthesis SuperMix (TransGen Biotech, Beijing, China). Gene transcript levels of IL-6, TNF-α, MCP-1, IL-10, IL-4, and Arg-1 were quantified using the TransStart Top Green qPCR SuperMix (TransGen Biotech, Beijing, China) according to the manufacturer's protocol. β-actin was used as housekeeping control. Primers used for quantitative PCR are listed in Supplementary Table 1.

Animal experimental protocol

All animal experiments have been approved by the Medical Ethics Committee of Peking Union Medical College and comply with the regulations of the National Institutes of Health regarding the care and use of animals in research. The experiment programs on animals are shown in Supplementary Figure 28. Briefly, 6-week-old male BALB/c mice were purchased from Vital River Laboratories Co., Ltd. (Beijing, China). Animals were randomly divided into three groups ($n = 6$): the control group (Group B), the model group (5 mg/kg LPS; Group M), and LPS (5 mg/kg) + compound **13** (20 mg/kg) group (Group A). After 6 h of LPS administration, animals were killed for the bronchoalveolar lavage fluid (BALF) and lung tissue collection. Cytokine levels in BALF were detected by ELISA, and the upper left lungs from each group ($n = 6$ per group) were fixated with 4% buffered formalin solution and stained with hematoxylin and eosin (*H&E*).

RNA sequencing

After 24 h of co-treatment of LPS and compound **13**, RAW264.7 macrophages were collected for RNA extraction and transcriptome sequencing. RNA sequencing was performed on the Annoroad Illumina-HiSeq platform. Differentially expressed genes were defined as values of $p < 0.01$. Pathway enrichment analysis using Gene Set Enrichment Analysis (GSEA).

Western blot

The concentration was detected with BCA kit before total protein was extracted from RAW264.7 cells. The samples mixed with the loading buffer were separated on an 8% SDS-PAGE gel. After transferring to polyvinylidene fluoride membranes by electro-transfer, the membranes were blocked with 5% BSA at room temperature for 1 h. Next, the PVDF membranes were incubated with primary antibody overnight at 4°C and then incubated with peroxidase-conjugated secondary antibodies at room temperature for 1 h. The protein brands were captured in a gel imaging system. ImageJ was used to analyze the value of the brands.

Statistical analysis

Statistical analyses were performed with GraphPad Prism (version 8.4.3). Independent Student's *t*-tests were used to compare the means of numerical variables. Data were presented as the mean ± SD. Statistical significance was defined as $p < 0.05$.

Results and discussion

Structural characterization of these isolated compounds

Chlorophenol A (**1**) was obtained as a colorless oil and had the molecular formula $C_{11}H_{13}ClO_3$ as determined by HRESIMS spectrum, which showed a cluster of deprotonated ion peaks at *m/z* 227.0476/229.0422 ($[M-H]^-$) with a ratio of 3:1, indicative of a monochlorinated compound (Luo et al., 2018). The 1D NMR (Table 1) and HSQC spectrum of **1** showed signals of five non-protonated sp^2 carbons (δ_C 150.0, 150.0, 143.1, 129.8, and 113.0), one aromatic methine ($\delta_{H/C}$ 6.83/106.9), two olefinic methines ($\delta_{H/C}$ 6.53/124.3 and 6.19/127.3), two oxygenated methyls ($\delta_{H/C}$ 3.80/60.5 and 3.68/61.1), one methyl ($\delta_{H/C}$ 1.88/18.7), and one phenolic hydroxyl group (δ_H 9.97). The aforementioned data combined with five degrees of unsaturation (DOU) suggested that compound **2** presented a benzene ring skeleton, and the ^{1}H-^{1}H COSY correlations (Figure 2) between H-7/H-8 and H-8/H_3-9 showed the existence of a propenyl group. Besides, the HMBC correlations (Figure 2) from H-7 to C-1, C-2, and C-6, and from H_3-11 to C-6, revealed that the propenyl group

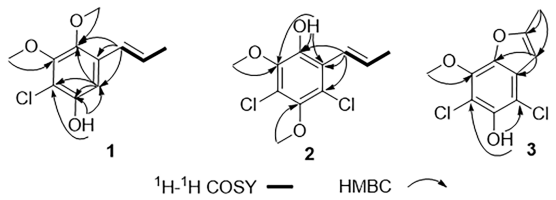

FIGURE 2
Key ^{1}H-^{1}H COSY and HMBC correlations of **1**–**3**.

and one methoxy group were located at C-1 and C-6, respectively. The HMBC correlations from 3-OH to C-2, C-3, and C-4 indicated the location of the phenolic hydroxyl group (C-3). The chemical shift of C-4 (δ_C 113.0) revealed that the chlorine substituent instead of the oxygenated methyl was attached at C-4. The other methoxy group was deduced to link with C-5 by the HMBC signal of H_3-10/C-5 and the chemical shift of C-5 (δ_C 150.0). The aforementioned NMR characteristics showed great similarity to those of the co-isolated 2,4-dichloro-3-hydroxy-5-methoxy-toluene (**5**), which was reported as a synthetic chlorinated phenolic compound (Calam and Oxford, 1939). The main differences were the appearances of a propenyl group at C-1, a methoxy group at C-6, an aromatic hydrogen at C-2 in **1** instead of a methyl at C-1, an aromatic hydrogen at C-6, and a chlorine atom at C-2 in **5**, respectively. This deduction was further supported by the above 2D NMR data. Therefore, the structure of **1** was determined, as shown in Figure 1.

Chlorophenol B (**2**) was obtained as a colorless oil, and its molecular formula was deduced to be $C_{11}H_{12}Cl_2O_3$ by the HRESIMS peak at *m/z* 261.0092 $[M-H]^-$ (calcd. For $C_{11}H_{11}Cl_2O_3^-$ 261.0091), suggesting five DOU. The 9:6:1 (*m/z* 261.0092/263.0065/265.0033) isotopic distribution pattern suggested the presence of two chlorine atoms (El-Kashef et al., 2020). The ^{1}H, ^{13}C (Table 1) NMR, and HSQC spectra of **2** showed signals of six non-protonated sp^2 carbons (δ_C 146.1, 144.5, 143.3, 122.8, 122.4, and 120.0), two olefinic methines ($\delta_{H/C}$ 6.42/123.1 and 6.58/133.5), two methoxy groups ($\delta_{H/C}$ 3.73/60.4 and 3.72/60.7), one methyl ($\delta_{H/C}$ 1.89/19.6), and one phenolic hydroxyl group (δ_H 9.63). The above NMR data were highly similar to those of compound **1**. The main differences were the appearances of a chlorine atom at C-2, a methoxy group at C-3, and a hydroxyl group at C-6 in **2** instead of an aromatic hydrogen at C-2, a hydroxyl group at C-3, and a methoxy group at C-6 in **1**, respectively. This deduction was further supported by the 2D NMR data. The HMBC spectrum of **2** showed correlations from H-7 to C-1, C-2, and C-6, and from 6-OH to C-1 and C-6, which implied that the propenyl and the hydroxyl groups were located at C-1 and C-6, respectively. Besides, the HMBC correlations from 6-OH and H_3-10 (δ_H 3.73) to C-5 (δ_C 143.3) suggested that the methoxy group ($\delta_{H/C}$ 3.73/60.4) was located at C-5. The chemical shift of C-2 (δ_C 122.4) indicated one of the chlorine atoms was attached to C-2. Besides, the HMBC correlation from H_3-11 (δ_H 3.72) to C-3 (δ_C 144.5) verified that the remained one methoxy group ($\delta_{H/C}$ 3.72/60.4) was located at C-3. The above-detailed analysis of the NMR data allowed the assignment of all carbon and proton resonances of **2**. Consequently, the structure of **2** was elucidated, as shown in Figure 1.

Chlorophenol C (**3**) was obtained as brown oil. Analysis of the deprotonated molecule at *m/z* 244.9786 in the HRESIMS spectrum indicated a molecular formula of $C_{10}H_8Cl_2O_3$ (six DOU), and the 9:6:1 (*m/z* 244.9786/246.9759/248.9616) isotopic distribution also confirmed the presence of two chlorine atoms (El-Kashef et al., 2020). The ^{1}H and ^{13}C NMR data (Table 1) displayed signals of seven non-protonated sp^2 carbons (δ_C 157.7, 145.5, 139.6, 138.7, 128.3, 110.4, and 104.9), one olefinic methine ($\delta_{H/C}$ 6.61/101.7), one oxygenated methyl ($\delta_{H/C}$ 4.12/60.6), one methyl ($\delta_{H/C}$ 2.47/13.8), and one phenolic hydroxyl group (δ_H 9.75). The above data and the HMBC correlations from 3-OH to C-2 and C-4, from H_3-10 to C-5 implied that **3** was structurally related to the co-isolated 2,4-dichloro-3-hydroxy-5-methoxy-toluene (**5**), except the different substituents at C-1 and C-6. The above functional groups accounted for five DOU, and the remaining one DOU suggested that **3** possessed one ring. Furthermore, a methyl-furan ring linked to the benzene *via* C-1 and C-6 was deduced from the HMBC correlations from H-7 to C-1 and C-6, and from H_3-9 to C-7 and C-8. Consequently, the structure of **3** was assigned as 4,6-dichloro-5-hydroxy-3-methoxy-10-methyl-benzofuran (Figure 1), which was similar to a synthetic compound, 4-chloro-7-hydroxy-5-methoxy-2-methyl-benzofuran (Lousberg and Tirilly, 1976). Compound **3** was finally characterized as shown in Figure 1 and was given the trivial name chlorophenol C.

Both 7-chloro-3,4-dihydro-6,8-dihydroxy-3-methylisocoumarin (**4**; Henderson and Hill, 1982a,b) and 2,4-dichloro-3-hydroxy-5-methoxy-toluene (**5**; Calam and Oxford, 1939) were obtained as new natural products. Compound **4** was reported as a synthetic product (Henderson and Hill, 1982a) and has been suggested as an intermediate in the biosynthesis of cryptosporiopsinol-type secondary metabolites (Henderson and Hill, 1982a). Compound **5** was also known as a synthetic product without reported bioactive data (Calam and Oxford, 1939). Meanwhile, the other 14 known compounds were identified as 2,4,6-trichloro-3-hydroxy-5-methoxy-toluene (**6**; Monde et al., 1998), *α*-acetylorcinol (**7**; Leyte-Lugo et al., 2020), *O*-methylcurvulinic acid (**8**; Ying et al., 2014), (*S*)-5,7-dichloro-6-methoxy-2-methyl-2,3-dihydrobenzofuran-4-carboxylic acid (**9**; Richardson et al., 2015), pericochlorosin A (**10**; Liu et al., 2020), palmaerones F and G (**11** and **12**; Zhao et al., 2018), 5-chloro-6-hydroxymellein (**13**; Krohn et al., 1997), (*R*)-6-hydroxymellein (**14**; Quang et al., 2013), 3-methyl-6-hydroxy-8-methoxy-3,4-dihydroisocoumarin (**15**; Dethoup et al., 2007), (22*E*, 24*R*)-ergosta-5,7,22-trien-3*β*-ol (**16**; Liu et al., 2012), uracil (**17**; Liu et al., 2009), cyclohelminthol I (**18**; Honmura et al., 2016), and kojic acid (**19**; Li et al., 2003), respectively, by comparison of their NMR data with

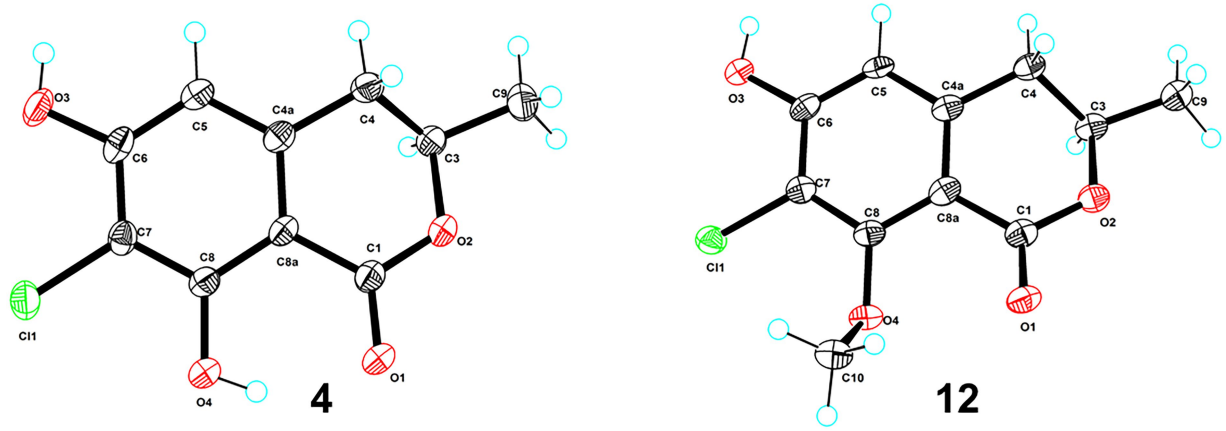

FIGURE 3
ORTEP diagrams of compounds **4** and **12**.

those reported ones. Besides, the X-ray crystal structures of **4** (CDCC 2133225, Figure 3) and **12** (CDCC 2133224, Figure 3) were reported herein for the first time with flack parameters of 0.005 (5) and 0.000 (16), respectively, which further unambiguously confirmed their absolute configurations.

Compounds 1, 4, 7, 9, 13, 15, 16, and 19 inhibited LPS-induced inflammation in RAW264.7 macrophages *via* promoting M2-type macrophage polarization

These compounds were primarily evaluated with no cytotoxicity against RAW264.7 cells (Supplementary Figure 25). Next, RAW264.7 cells were exposed to 0.1 μg/ml LPS and were co-treated with the same dose of the compounds (10 μM) for 24 h to evaluate their anti-inflammation activities. Compounds **1**, **4**, **7**, **9**, **13**, **15**, **16**, and **19** suppressed LPS-induced NO accumulation in a dose-dependent manner (Figure 4A), while others showed no reduction (Supplementary Figure 26). By comparison with the structural characteristics among them, a preliminary structure–activity relationship is discussed. The chlorine atom at C-5 and hydrogen atom at C-7, together with hydroxy group at C-8 in **13**, would probably increase the inflammatory activity, and the chlorine atom at C-7 may decrease the activity. Moreover, compounds **1**, **4**, **7**, **9**, **13**, **15**, **16**, and **19** suppressed both the mRNA expression and release of pro-inflammatory factors, including IL-6, TNF-α (Li et al., 2021), and MCP-1 (Matsuzawa-Ishimoto et al., 2018; Figures 4B,C). In addition, anti-inflammatory genes (IL-4, IL-10, and Arg-1; Georgakis et al., 2019) were also significantly upregulated in response to compound treatment (Figure 4D). These investigations indicate that these eight bioactive compounds could block the expression of pro-inflammatory factors *via* promoting the M2-type macrophage polarization to fight against LPS-induced inflammation.

Compound 13 alleviated the pathological lung injury of LPS-administrated mice

These anti-inflammatory activity results suggested that these marine natural products possessed excellent suppression on nitric oxide and pro-inflammatory cytokines. In addition, compound **13** showed the greatest anti-inflammatory potential among these chlorinated compounds; thus, its inhibitory effect was subsequently inspected *in vivo* (Yang et al., 2020). In brief, BALB/c mice were orally administrated with compound **13** at a dose of 20 mg/kg for 24 h before the LPS treatment, and mice were killed 6 h after intratracheal injection of LPS (5 mg/kg). Lung histopathology was performed with *H&E* staining, which demonstrated that the physiological lung tissue of mice treated with compound **13** was relatively intact with less inflammatory cell infiltration compared with the model group. Besides, the alveoli were clearly delineated and demarcated, and no proliferation of alveolar epithelial cells was observed (Figures 5A,B, as shown by the arrow). These results indicated that compound **13** attenuated the acute lung injury (ALI) caused by LPS-induced inflammation. Furthermore, "cytokine storm" is well characterized in ALI (Chen et al., 2021c). The cytokine detection in the bronchoalveolar lavage fluid (BALF) revealed that the levels of pro-inflammatory factors, such as IL-6, TNF-α, and MCP-1, in compound **13** administrated group were generally lower (Figure 6C) than those of the model group. Taken together, our results prompted that compound **13** effectively alleviated inflammation levels in mice with acute lung injury pneumonia (Figure 5C).

10.3389/fmicb.2022.976399

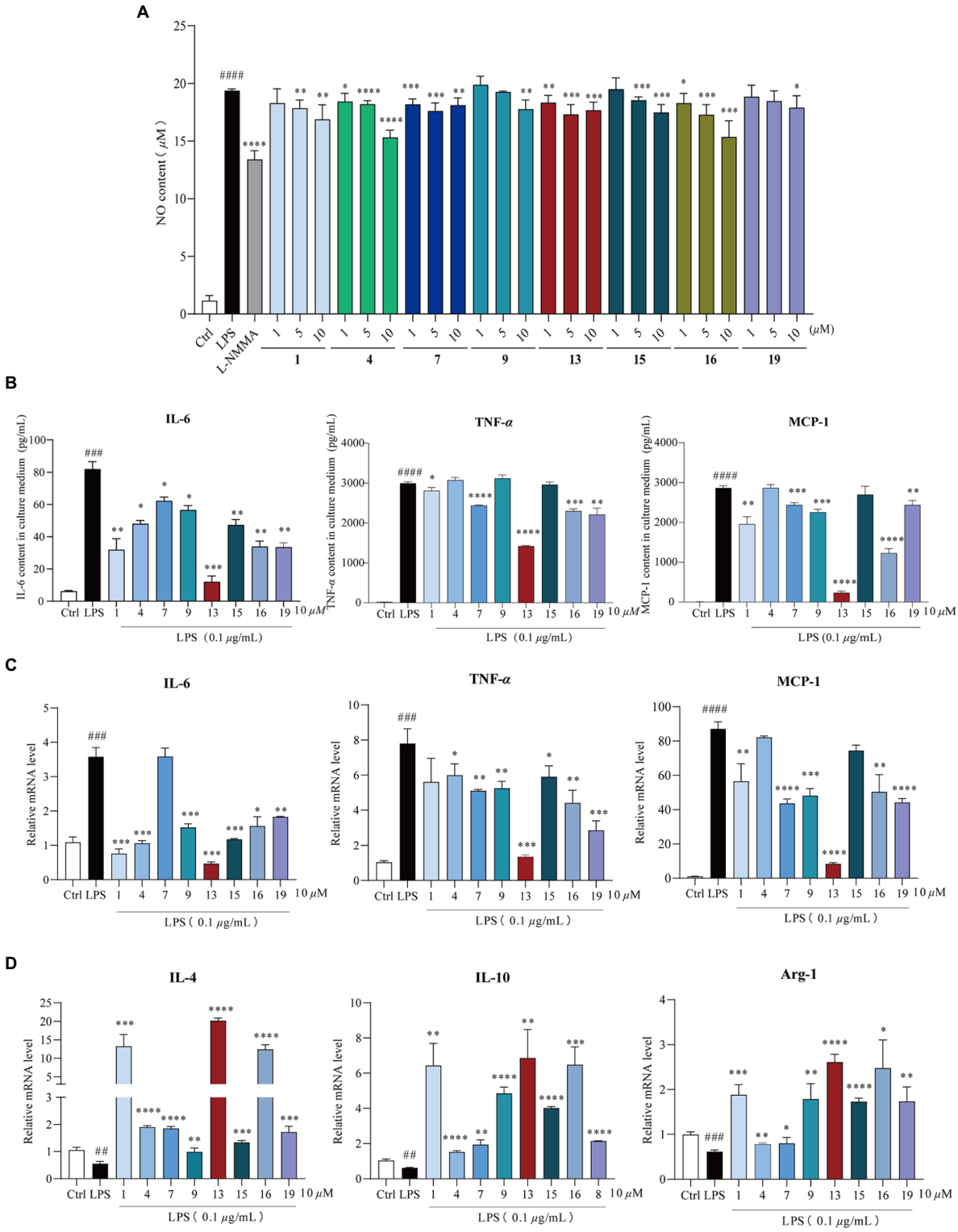

FIGURE 4
Anti-inflammation activity of compounds **1**, **4**, **7**, **9**, **13**, **15**, **16**, and **19**. Cells were exposed to 0.1μg/ml lipopolysaccharide (LPS) and co-treated with **1**, **4**, **7**, **9**, **13**, **15**, **16**, and **19** (1, 5, and 10μM) for 24h, respectively. **(A)** Nitric oxide (NO) production in the supernatant after 24h of LPS induction, n=5. L-NMMA was used as the positive control; **(B)** compounds **1**, **4**, **7**, **9**, **13**, **15**, **16**, and **19** reduced LPS-induced IL-6, TNF-α, and MCP-1 release, n=3; **(C)** qPCR analysis of M1-type macrophage genes (IL-6, TNF-α, and MCP-1) normalized by β-actin, n=3; **(D)** qPCR analysis of M2-type macrophage genes (IL-4, IL-10, and Arg-1) normalized by β-actin, n=3. All data were presented as the mean±SD of three independent experiments. ns, p>0.05, *p<0.05, **p<0.01, ***p<0.005, ****p<0.001 vs. LPS group; $^{\#\#}p$<0.01, $^{\#\#\#}p$<0.005, $^{\#\#\#\#}p$<0.001 vs. control group, n=3. p value was assessed by two-tailed Student's t-test.

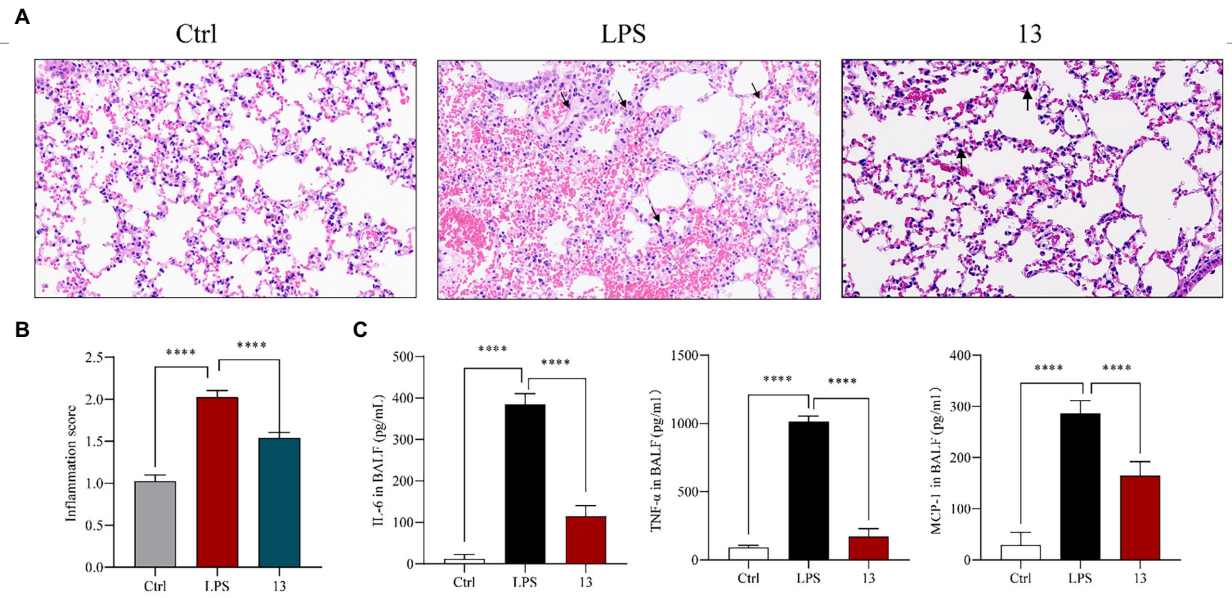

FIGURE 5
Compound **13** weakens the pathological lung injury of LPS-challenged mice. BALB/c mice were intragastric injected with compound **13** for 24h before the LPS administration. Mice were killed after 6h of LPS injection (5mg/kg), and lung histopathology was performed with *H&E* staining **(A)**. Inflammation score was measured independently by three pathologists blinded to the experiment (**B**, $n=6$). The levels of anti-inflammation cytokines in BALF were assayed **(C)**. ****$p<0.001$ vs. control group, $n=6$. p value was assessed by two-tailed Student's t-test.

Compound 13 protected RAW264.7 macrophages against LPS-induced inflammation through PI3K/AKT pathway

To further explore the mechanism of compound **13** in ameliorating LPS-induced inflammation, high-throughput sequencing of RNAs from RAW264.7 macrophages was conducted. The results of the GO enrichment analysis indicated that chemokine activity and nitric oxide synthase regulatory activity may play key roles in inflammation induced by LPS (Figure 6A and Supplementary Figure 27). Furthermore, combining the results of the KEGG pathway analysis uncovered that the PI3K/AKT signaling pathway was significantly activated, indicating that it might be a potential key pathway in mediating inflammatory responses in the current cell model (Figure 6B). Consistent with this hypothesis, our subsequent research displayed that compound **13** could effectively restrain the expression levels of PI3K and AKT upregulated by LPS (Figures 6C,D), proving that the PI3K/AKT signaling pathway was involved in this procedure regulated by compound **13**, which is in accordance with another research (Zhong et al., 2016). In this study, we found that compounds **4**, **9**, **13**, and **15** could effectively inhibit the synthesis of NO and overproduction of pro-inflammatory cytokines induced by LPS. Especially, compound **13** also exhibited an outstanding anti-inflammatory activity *in vivo*, suggesting the most active compound.

Mitochondria are key organelles involved in metabolic regulation, and their dysfunction is closely related to metabolic inflammatory diseases. Although the gene expression heat map showed that genes related to mitochondrial function and transcription factors were largely enriched (Supplementary Figure 27), whether they participated in LPS-induced inflammatory response of compound **13** still needs further investigation.

Conclusion

In summary, the chemical investigation of the mangrove endophytic fungus *Amorosia* sp. SCSIO 41026 resulted in the isolation and identification of 19 secondary metabolites, including three new chlorine-containing fungal metabolites and two new natural products. Our results demonstrated that compounds **1**, **4**, **7**, **9**, **13**, **15**, **16**, and **19** inhibited LPS-induced overproductions of NO and pro-inflammatory cytokines including IL-6, TNF-α, and MCP-1 both in mRNA and protein levels with a premise that none of these compounds showed significant cytotoxicity. Among these metabolites, compound **13** was identified as the most active compound with an outstanding ability of anti-LPS-induced inflammation in RAW264.7 macrophages and in ALI mice, probably by inhibiting the PI3K/AKT signaling pathway. Thus, this study demonstrates the potential value of mangrove endophytic fungus as a promising source of bioactive compounds.

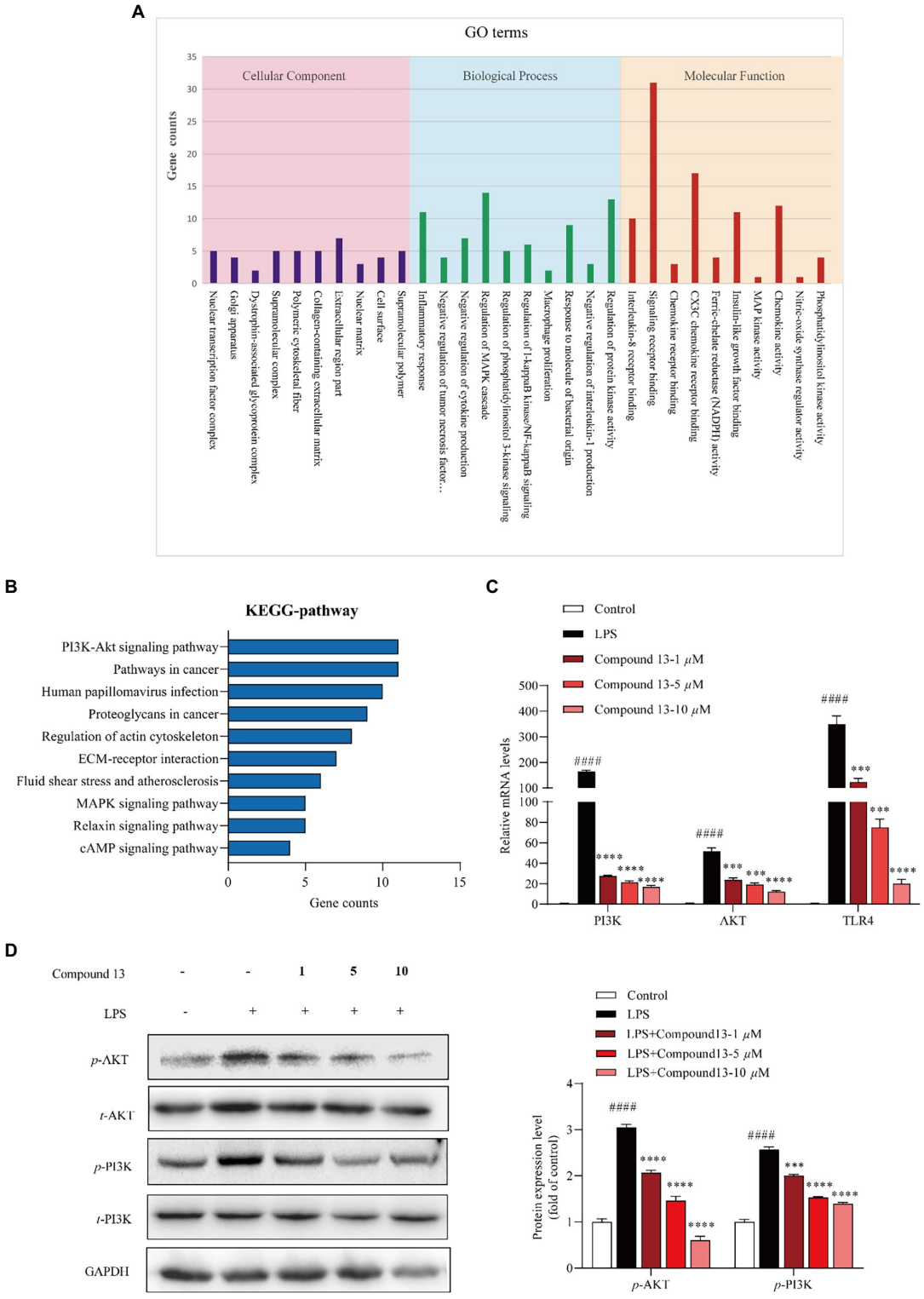

FIGURE 6
PI3K/AKT signaling pathway was involved in the regulation of LPS-induced inflammation by compound **13** in RAW264.7 macrophages. **(A)** Inflammation-related GO terms enriched from differentially expressed genes (DEGs) between compound **13**-treated and model RAW264.7 macrophages. **(B)** Inflammation-related KEGG pathways enriched from DEGs. **(C)** qPCR analysis of PI3K, AKT, and TLR4 genes normalized by β-actin. All data were presented as the mean±SD of three independent experiments. $p>0.05$, ns; $^{***}p<0.005$, $^{****}p<0.001$ vs. LPS group; $^{\#\#\#\#}p<0.001$ vs. control group, $n=3$. p value was assessed by two-tailed Student's t-test. **(D)** Immunoblotting against the PI3K, AKT proteins, $n=3$. All data were presented as the mean±SD of three independent experiments. $^{***}p<0.005$, $^{****}p<0.001$ vs. LPS group; $^{\#\#\#\#}p<0.001$ vs. control group, $n=3$. p value was assessed by two-tailed Student's t-test.

Data availability statement

The data presented in the study are deposited in the NCBI repository, accession number GSE207442 (https://www.ncbi.nlm.nih.gov/sra/PRJNA855018), CDCC Nos: 2133225 and 2133224.

Ethics statement

The animal study was reviewed and approved by the Medical Ethics Committee of Peking Union Medical College. Written informed consent was obtained from the owners for the participation of their animals in this study.

Author contributions

XR and CC performed the experiments and wrote the paper. YY, ZX, and XL helped with the analysis of the data. PG, XL, and YL designed and supervised the experiments. All authors contributed to the article and approved the submitted version.

Funding

This research was funded by CXYJ-2022-01 from the Research Foundation of Capital Institute of Pediatrics (China), Guangdong-Joint Foundation of Shenzhen (2021B1515120046), and the Special Fund for Bagui Scholars of Guangxi (YL).

Acknowledgments

We are grateful to Z. Xiao, X. Zheng, A. Sun, Y. Zhang, and X. Ma in the analytical facility at SCSIO for recording spectroscopic data.

Conflict of interest

The authors declare that the research was conducted in the absence of any commercial or financial relationships that could be construed as a potential conflict of interest.

Publisher's note

All claims expressed in this article are solely those of the authors and do not necessarily represent those of their affiliated organizations, or those of the publisher, the editors and the reviewers. Any product that may be evaluated in this article, or claim that may be made by its manufacturer, is not guaranteed or endorsed by the publisher.

Supplementary material

The Supplementary material for this article can be found online at: https://www.frontiersin.org/articles/10.3389/fmicb.2022.976399/full#supplementary-material

References

Al-Lamki, R. S., Wang, J., Skepper, J. N., Thiru, S., Pober, J. S., and Bradley, J. R. (2001). Expression of tumor necrosis factor receptors in normal kidney and rejecting renal transplants. *Lab. Investig.* 81, 1503–1515. doi: 10.1038/labinvest.3780364

Bracegirdle, J., Stevenson, L. J., Sharrock, A. V., Page, M. J., Vorster, J. A., Owen, J. G., et al. (2021). Hydrated rubrolides from the New Zealand tunicate *Synoicum kuranui*. *J. Nat. Prod.* 84, 544–547. doi: 10.1021/acs.jnatprod.0c01248

Calam, C. T., and Oxford, A. E. (1939). Halogen derivatives of the methyl ethers of orcinol, *p*-orsellinic acid and phloroglucinolcarboxylic acid. *J. Chem. Soc.* 60, 280–284. doi: 10.1039/jr9390000280

Chen, S., Cai, R., Liu, Z., Cui, H., and She, Z. (2021b). Secondary metabolites from mangrove-associated fungi: source, chemistry and bioactivities. *Nat. Prod. Rep.* 39, 560–595. doi: 10.1039/d1np00041a

Chen, C. M., Chen, W. H., Pang, X. Y., Liao, S. R., Wang, J. F., Lin, X. P., et al. (2021d). Pyrrolyl 4-quinolone alkaloids from the mangrove endophytic fungus *Penicillium steckii* SCSIO 41025: chiral resolution, configurational assignment, and enzyme inhibitory activities. *Phytochemistry* 186:112730. doi: 10.1016/j.phytochem.2021.112730

Chen, C. M., Chen, W. H., Tao, H. M., Yang, B., Zhou, X. F., Luo, X. W., et al. (2021c). Diversified polyketides and nitrogenous compounds from the mangrove endophytic fungus *Penicillium steckii* SCSIO 41025. *Chin. J. Chem.* 39, 2132–2140. doi: 10.1002/cjoc.202100226

Chen, C., Li, X., Li, C., Jin, J., Wang, D., Zhao, Y., et al. (2021a). CD39+ regulatory T cells attenuate lipopolysaccharide-induced acute lung injury via autophagy and the ERK/FOS pathway. *Front. Immunol.* 11:602605. doi: 10.3389/fimmu.2020.602605

Coleman, J. W. (2001). Nitric oxide in immunity and inflammation. *Int. Immunopharmacol.* 1, 1397–1406. doi: 10.1016/s1567-5769(01)00086-8

Dethoup, T., Manoch, L., Kijjoa, A., Pinto, M., Gales, L., Damas, A. M., et al. (2007). Merodrimanes and other constituents from *Talaromyces thailandiasis*. *J. Nat. Prod.* 70, 1200–1202. doi: 10.1021/np0680578

El-Kashef, D. H., Youssef, F. S., Hartmann, R., Knedel, T. O., Janiak, C., Lin, W., et al. (2020). Azaphilones from the red sea fungus *Aspergillus falconensis*. *Mar. Drugs* 18:204. doi: 10.3390/md18040204

Georgakis, M. K., Gill, D., Rannikmäe, K., Traylor, M., Anderson, C. D., Lee, J. M., et al. (2019). Genetically determined levels of circulating cytokines and risk of stroke. *Circulation* 139, 256–268. doi: 10.1161/CIRCULATIONAHA.118.035905

Gribble, G. W. (2015). Biological activity of recently discovered halogenated marine natural products. *Mar. Drugs* 13, 4044–4136. doi: 10.3390/md13074044

Henderson, G. B., and Hill, R. A. (1982a). Synthesis of chlorinated isocoumarin derivatives. *J. Chem. Soc. Perkin Trans.* 1, 1111–1115. doi: 10.1039/P19820001111

Henderson, G. B., and Hill, R. A. (1982b). The biosynthesis of chlorine-containing metabolites of *Periconia macrospinosa*. *J. Chem. Soc. Perkin Trans.* 12, 3037–3039. doi: 10.1039/P19820003037

Honmura, Y., Uesugi, S., Maeda, H., Tanaka, K., Nehira, T., Kimura, K. I., et al. (2016). Isolation, absolute structures, and biological properties of cyclohelminthols I–IV from *Helminthosporium velutinum* yone96. *Tetrahedron* 72, 1400–1405. doi: 10.1002/chin.201625219

Hortelano, S., Través, P. G., Zeini, M., Alvarez, A. M., and Boscá, L. (2003). Sustained nitric oxide delivery delays nitric oxide-dependent apoptosis in macrophages: contribution to the physiological function of activated macrophages. *J. Immunol.* 171, 6059–6064. doi: 10.4049/jimmunol.171.11.6059

Kim, P. K., Kwon, Y. G., Chung, H. T., and Kim, Y. M. (2002). Regulation of caspases by nitric oxide. *Ann. N. Y. Acad. Sci.* 962, 42–52. doi: 10.1111/j.1749-6632.2002.tb04054.x

Krohn, K., Bahramsari, R., Flsrke, U., Ludewig, K., Kliche-Spory, C., Michel, A., et al. (1997). Dihydroisocoumarins from fungi: isolation, structure elucidation, circular dichroism and biological activity. *Phytochemistry* 45, 313–320. doi: 10.1016/s0031-9422(96)00854-0

Leyte-Lugo, M., Richomme, P., Poupard, P., and Pena-Rodriguez, L. M. (2020). Identification and quantification of a phytotoxic metabolite from *Alternaria dauci*. *Molecules* 25, 2108–2112. doi: 10.3390/molecules25174003

Li, X., Jeong, J. H., Lee, K. T., Rho, J. R., and Son, B. W. (2003). γ-Pyrone derivatives, kojic acid methyl ethers from a marine-derived *Fungusaltenaria* sp. *Arch. Pharm. Res.* 26, 532–534. doi: 10.1007/BF02976876

Li, T. X., Liang, J. X., Liu, L. L., Shi, F. C., Jia, X. W., Li, M. H., et al. (2021). Novel kojic acid derivatives with anti-inflammatory effects from *Aspergillus versicolor*. *Fitoterapia* 154:105027. doi: 10.1016/j.fitote.2021.105027

Liu, J., Chen, M., Chen, R., Xie, K., Chen, D., Si, S., et al. (2020). Three new compounds from endophytic fungus *Periconia* sp. F-31. *Aust. J. Pharm.* 29, 244–251. doi: 10.5246/jcps.2020.04.023

Liu, R. H., Luo, H., Li, Y. L., Ming, Y., Xu, X. K., and Li, H. L. (2009). *N*-containing compounds from the traditional Chinese medicine ChanSu. *Chem. Nat. Compd.* 45, 599–600. doi: 10.1007/s10600-009-9380-4

Liu, T., Zhang, L., Li, Z., Wang, Y., Tian, L., Pei, Y., et al. (2012). A new sulfoxanthone from the marine-derived fungus *penicillium sacculum*. *Chem. Nat. Compd.* 48, 771–773. doi: 10.1080/14786419.2015.1101693

Lousberg, R., and Tirilly, Y. (1976). Structure of furasterin, a chlorinated metabolite from the fungus *Phialophora asteris* (downson) burge et isaac. *Experientia* 32, 1394–1395. doi: 10.1007/BF01937395

Luo, X. W., Lin, X. P., Tao, H. M., Wang, J. F., Li, J. Y., Yang, B., et al. (2018). Isochromophilones A–F, cytotoxic chloroazaphilones from the marine mangrove endophytic fungus *Diaporthe sp.* SCSIO 41011. *J. Nat. Prod.* 81, 934–941. doi: 10.1021/acs.jnatprod.7b01053

Matsuzawa-Ishimoto, Y., Hwang, S., and Cadwell, K. (2018). Autophagy and inflammation. *Annu. Rev. Immunol.* 36, 73–101. doi: 10.1146/annurev-immunol-042617-053253

Monde, K., Satoh, H., Nakamura, M., Tamura, M., and Takasugi, M. (1998). Organochlorine compounds from a terrestrial higher plant: structures and origin of chlorinated orcinol derivatives from diseased bulbs of *Lilium maximowiczii*. *J. Nat. Prod.* 61, 913–921. doi: 10.1021/np980062r

Peerapornratana, S., Manrique-Caballero, C. L., Gómez, H., and Kellum, J. A. (2019). Acute kidney injury from sepsis: current concepts, epidemiology, pathophysiology, prevention and treatment. *Kidney Int.* 96, 1083–1099. doi: 10.1016/j.kint.2019.05.026

Quang, D. N., Lam, D. M., Hanh, N. T. H., and Que, D. D. (2013). Cytotoxic constituents from the fungus *Daldinia concentrica* (Xylariaceae). *Nat. Prod. Res.* 27, 486–490. doi: 10.1080/14786419.2012.698411

Richardson, S. N., Nsiama, T. K., Walker, A. K., McMullin, D. R., and Miller, J. D. (2015). Antimicrobial dihydrobenzofurans and xanthenes from a foliar endophyte of *Pinus strobus*. *Phytochemistry* 117, 436–443. doi: 10.1016/j.phytochem.2015.07.009

Saetang, P., Rukachaisirikul, V., Phongpaichit, S., Preedanon, S., Sakayaroj, J., Hadsadee, S., et al. (2021). Antibacterial and antifungal polyketides from the fungus *Aspergillus unguis* PSU-MF16. *J. Nat. Prod.* 84, 1498–1506. doi: 10.1021/acs.jnatprod.0c01308

Shaala, L. A., Youssef, D. T. A., Alzughaibi, T. A., and Elhady, S. S. (2020). Antimicrobial chlorinated 3-phenylpropanoic acid derivatives from the red sea marine actinomycete *Streptomyces coelicolor* LY001. *Mar. Drugs* 18:450. doi: 10.3390/md18090450

Wang, C., Du, W., Lu, H., Lan, J., Liang, K., and Cao, S. (2021a). A review: halogenated compounds from marine actinomycetes. *Molecules* 26:2754. doi: 10.3390/molecules26092754

Wang, B. G., Gloer, J. B., Ji, N. Y., and Zhao, J. C. (2013). Halogenated organic molecules of Rhodomelaceae origin: chemistry and biology. *Chem. Rev.* 113, 3632–3685. doi: 10.1021/cr9002215

Wang, C., Lu, H., Lan, J., Zaman, K., and Cao, S. (2021b). A review: halogenated compounds from marine fungi. *Molecule* 26:458. doi: 10.3390/molecules26020458

Xu, J. (2015). Bioactive natural products derived from mangrove-associated microbes. *RSC Adv.* 5, 841–892. doi: 10.1039/c4ra11756e

Yang, H. H., Duan, J. X., Liu, S. K., Xiong, J. B., Guan, X. X., Zhong, W. J., et al. (2020). A COX-2/sEH dual inhibitor PTUPB alleviates lipopolysaccharide-induced acute lung injury in mice by inhibiting NLRP3 inflammasome activation. *Theranostics* 10, 4749–4761. doi: 10.7150/thno.43108

Ying, Y. M., Zhang, L. W., Shan, W. G., and Zhan, Z. J. (2014). Secondary metabolites of *Peyronellaea* sp. XW-12, an endophytic fungus of *Huperzia serrata*. *Chem. Nat. Compd.* 50, 723–725. doi: 10.1007/s10600-014-1063-0

Yoo, H., Ku, S. K., Han, M. S., Kim, K. M., and Bae, J. S. (2014). Anti-septic effects of fisetin *in vitro* and *in vivo*. *Inflammation* 37, 1560–1574. doi: 10.1007/s10753-014-9883-4

Zeng, J., and Zhan, J. (2019). Chlorinated natural products and related halogenases. *Isr. J. Chem* 59, 387–402. doi: 10.1002/ijch.201800175

Zhao, M., Yuan, L. Y., Guo, D. L., Ye, Y., Da-Wa, Z. M., Wang, X. L., et al. (2018). Bioactive halogenated dihydroisocoumarins produced by the endophytic fungus *Lachnum palmae* isolated from *Przewalskia tangutica*. *Phytochemistry* 148, 97–103. doi: 10.1016/j.phytochem.2018.01.018

Zhong, W., Qian, K., Xiong, J., Ma, K., Wang, A., and Zou, Y. (2016). Curcumin alleviates lipopolysaccharide induced sepsis and liver failure by suppression of oxidative stress-related inflammation via PI3K/AKT and NF-κB related signaling. *Biomed. Pharmacother.* 83, 302–313. doi: 10.1016/j.biopha.2016.06.036

Zhuo, Y., Li, D., Cui, L., Li, C., Zhang, S., Zhang, Q., et al. (2019). Treatment with 3,4-dihydroxyphenylethyl alcohol glycoside ameliorates sepsis-induced ALI in mice by reducing inflammation and regulating M1 polarization. *Biomed. Pharmacother.* 116:109012. doi: 10.1016/j.biopha.2019.109012

frontiers | Frontiers in Microbiology

TYPE Original Research
PUBLISHED 12 October 2022
DOI 10.3389/fmicb.2022.1008053

OPEN ACCESS

EDITED BY
Xian-Wen Yang,
Third Institute of Oceanography, China

REVIEWED BY
Xiaowei Luo,
Guangxi University of Chinese Medicine, China
Huizi Jin,
Tongji University, China
Junmin Zhang,
Lanzhou University, China
Sara De Martin,
University of Padua, Italy

*CORRESPONDENCE
Yongxia Zhu
yongxia_zhu0409@uestc.edu.cn
Li Liu
liuli@swmu.edu.cn
Xia Xiong
xiongxia789@126.com

†These authors have contributed equally to this work and share first authorship

SPECIALTY SECTION
This article was submitted to Extreme Microbiology, a section of the journal Frontiers in Microbiology

RECEIVED 31 July 2022
ACCEPTED 20 September 2022
PUBLISHED 12 October 2022

CITATION
Xia T, Lei H, Wang J, He Y, Wang H, Gao L, Qi T, Xiong X, Liu L and Zhu Y (2022) Identification of an ergosterol derivative with anti-melanoma effect from the sponge-derived fungus *Pestalotiopsis* sp. XWS03F09. *Front. Microbiol.* 13:1008053. doi: 10.3389/fmicb.2022.1008053

Identification of an ergosterol derivative with anti-melanoma effect from the sponge-derived fungus *Pestalotiopsis* sp. XWS03F09

Tong Xia[1†], Hui Lei[2†], Jianv Wang[1], Yijing He[3], Hailan Wang[4], Lanyang Gao[3], Tingting Qi[5], Xia Xiong[1*], Li Liu[1*] and Yongxia Zhu[5*]

[1]Department of Dermatology, The Affiliated Hospital of Southwest Medical University, Luzhou, China, [2]School of Pharmacy, Southwest Medical University, Luzhou, China, [3]Department of Science and Technology, The Affiliated Hospital of Southwest Medical University, Luzhou, China, [4]School of Public Health, Southwest Medical University, Luzhou, China, [5]Department of Clinical Pharmacy, Sichuan Cancer Hospital and Institute, Sichuan Cancer Center, School of Medicine, University of Electronic Science and Technology of China, Chengdu, China

It is difficult to treat malignant melanoma because of its high malignancy. New and effective therapies for treating malignant melanoma are urgently needed. Ergosterols are known for specific biological activities and have received widespread attention in cancer therapy. Here, **LH-1**, a kind of ergosterol from the secondary metabolites of the marine fungus *Pestalotiopsis* sp., was extracted, isolated, purified, and further investigated the biological activities against melanoma. *In vitro* experiments, the anti-proliferation effect on tumor cells was detected by MTT and colony formation assay, and the anti-metastatic effect on tumor cells was investigated by wound healing assay and transwell assay. Subcutaneous xenograft models, histopathology, and immunohistochemistry have been used to verify the anti-tumor, toxic, and side effect *in vivo*. Besides, the anti-tumor mechanism of **LH-1** was studied by mRNA sequencing. *In vitro*, **LH-1** could inhibit the proliferation and migration of melanoma cells A375 and B16-F10 in a dose-dependent manner and promote tumor cell apoptosis through the mitochondrial apoptosis pathway. *In vivo* assays confirmed that **LH-1** could suppress melanoma growth by inducing cell apoptosis and reducing cell proliferation, and it did not have any notable toxic effects on normal tissues. **LH-1** may play an anti-melanoma role by upregulating *OBSCN* gene expression. These findings suggest that **LH-1** may be a potential for the treatment of melanoma.

KEYWORDS

melanoma, ergosterol, antitumor, mitochondrial apoptosis, *OBSCN*

Introduction

Malignant melanoma is a kind of cancer with a high incidence, high degree of malignancy, and poor prognosis. It is one of the most difficult to cure malignant tumors in the world. Although it accounts for only 4% of skin cancer cases, it accounts for 75% of skin cancer deaths. The 5-year survival rate is less than 10% (Garbe et al., 2016; Dimitriou et al., 2018; Davis et al., 2019; Suhonen et al., 2021). In China, there are about 20,000 cases of melanoma every year. Compared with Europe and the United States, the incidence rate is slightly lower and has not attracted people's attention. Most of the newly diagnosed patients have reached the middle and late stages. Subsequently, cancer cells have spread to important organs such as the liver, lung, and brain through blood vessels or lymphatic vessels, of which lung metastasis is the most common site of metastasis (Whiteman et al., 2016; Gershenwald et al., 2017). The treatment for advanced melanoma is limited, in addition to traditional surgical treatment, radiotherapy, and chemotherapy, it also includes targeted therapy and immunotherapy. Although these drugs are still used extensively in clinical treatment, their effect is not satisfactory due to drug resistance and toxic side effects (Ouellet et al., 2016; Grimaldi et al., 2017; Rozeman et al., 2018; Ny et al., 2020; Ziogas et al., 2021). Hence, innovative agents against melanoma are urgently needed. Therefore, the exploration of new drugs for tumor cells that have little effect on normal cells will be beneficial to the treatment of melanoma in the future.

In the last few years, a growing interest in microbial secondary metabolites reflects the importance of microbial secondary metabolites in the discovery and development of new drugs which might be associated with their rich chemical structure (Shen and Thorson, 2012; Wright, 2019; Maglangit et al., 2021). At present, a large number of natural products have been isolated from microbial secondary metabolites and have shown significant biological activities (Yi et al., 2020; Ramirez-Rendon et al., 2022). Among them, marine microorganisms play a major role in the research of natural products, inhabiting environments with extremely high salinity, high pressure, low temperature, and low oxygen for a long time, resulting in a wide variety of secondary metabolites and novel structures. For instance, aspulvinone H isolated from a marine-derived *Aspergillus terreus* showed strong anti-tumor activity in an SW1990-cell-induced xenograft model. Asperphenin A, a lipopeptidyl benzophenone from marine-derived *Aspergillus* sp., has an anti-tumor effect on colon cancer (Cruz et al., 2006; Liu et al., 2016; Bae et al., 2020; Shams Ul Hassan et al., 2021; Yan et al., 2021). As one of the secondary metabolites of fungi, ergosterol analogs have been shown to have anti-tumor, antioxidant, and anti-bacterial properties, and can promote the apoptosis of tumor cells, such as gastric cancer, lung cancer, liver cancer, and breast cancer cells (Shimizu et al., 2016; Tan et al., 2017; Wu et al., 2018; Bu et al., 2019; Zhou et al., 2019). However, the application of ergosterol analogs in anti-melanoma has not been reported in the literature.

OBSCN is primarily a gene necessary for the assembly and organization of sarcomere and sarcoplasmic reticulum in the myocardium and skeletal muscle (Young et al., 2001). Obscurins are giant cytoskeletal proteins with structural and regulatory roles which are encoded by the *OBSCN* gene that spans ∼170 kb on human chromosome 1q42 (Young et al., 2001; Ackermann et al., 2014). Although obscurins were originally discovered in striated muscle cells, it is now thought that they are also expressed in non-muscle tissues and play a key role in maintaining cellular homeostasis. A pioneering study that sequenced 13,023 genes in breast and colorectal cancer identified *OBSCN* as one of 189 candidate genes for displaying high-frequency somatic mutations (Sjoblom et al., 2006). Further analysis of the *OBSCN* Gene Mutation Atlas revealed the presence of missense *OBSCN* mutations in melanoma (Balakrishnan et al., 2007). It has been reported that the deletion of the *OBSCN* gene can promote the proliferation and migration of tumor cells in pancreatic cancer and breast cancer (Shriver et al., 2015; Tuntithavornwat et al., 2022).

In this study, our investigations on the ethyl acetate (EtOAc) extract of the sponge-derived fungus *Pestalotiopsis* sp. XWS03F09 resulted in the isolation of one compound 4,4-dimethyl-5α-ergosta-8,24(28)-dien-3β-ol (1) (*named* ***LH-1***) (**Figure 1A**), which was consistent with the compound previously extracted in *Marasmius oreades* (Fattorusso et al., 1992) and *Phycomyces blakesleeanus* (Barrero et al., 1998). However, they only separated, extracted, and identified the compounds, and did not further study the activity and mechanism of the compounds.

LH-1 was screened for the *in vitro* anticancer activity against various cancer cell lines by the 3-(4,5-dimethyl-2-thiazolyl)-2,5-diphenyltetrazolium bromide (MTT) assay method. We found that melanoma cells were more sensitive to **LH-1** (The IC_{50} value of **LH-1** on B16-F10 melanoma cells was 16.57 μM at 72 h) than other cancer cell lines (IC_{50} values > 60 μM at 72 h). Therefore, we further investigated the biological activities against melanoma *in vitro* and *in vivo*. Our data provided that **LH-1** could inhibit proliferation and migration, induce apoptosis *via* the mitochondria apoptotic pathway, and upregulate *OBSCN* gene expression in melanoma cells. In addition, we also evaluated the anti-tumor activity of **LH-1** in the B16-F10 tumor-bearing xenograft mice model. These results indicate that **LH-1** could be a promising new anti-melanoma drug that is worth further investigation.

Materials and methods

Reagents and instruments

AV400MHZ nuclear magnetic resonance spectrometer (Bruker, Germany); BSZ-100 collector (Shanghai Jiapeng

Technology Co., Ltd., Shanghai, China); Nmur1300 rotary evaporation instrument (Shanghai Ailang Instrument Co., Ltd., Shanghai, China); ZF-20D dark box ultraviolet spectrometer (Shanghai Baoshan Gucun Electro-Optic Instrument Factory, Shanghai, China); DLSB-5/20 cryogenic coolant circulation instrument (Zhengzhou Science and Technology Industry and Trade Co., Ltd., Zhengzhou, China.); Sephadex-LH-20 (GE Healthcare Bio-sciences AB, Uppsala, Sweden); SW-CJ-2D double purification table (Zhejiang Sujing purification equipment Co., Ltd., Zhejiang, China). Silicone (Anhui Liangchen Silicon Source material Co., Ltd., Anhui, China). 3-(4,5-dimethyl-2-thiazolyl)-2,5-diphenyltetrazolium bromide (MTT, Shanghai Yuan Ye Bio-Technology Co., Ltd., Shanghai, China). Hoechst 33342 solutions (Shanghai Yuanye Technology Co., Ltd.). PI solutions (Beyotime Biotechnology, Shanghai, China). The fluorescence images of cells were obtained by the Nikon Ts2R-FL fluorescence microscope (Tokyo, Japan). The absorbance was determined by SpectraMAX M5 microplate spectrophotometer (Molecular device); Western blot analyses and immunohistochemistry were performed using primary antibodies against Cleaved Caspase 3 antibody, β-actin antibody, and Bcl-2 antibody (Chengdu Zhengneng Biotechnology Co., Ltd., Chengdu, China); Ki-67 antibody, Bax antibody (Cell Signaling Technology, Boston, USA); Cleaved Caspase 9 antibody (Abcam, Shanghai, China).

Fungal material

The strain was provided by the Yonghong Liu Research Group of the South China Sea Institute of Oceanography, Chinese Academy of Sciences and the preservation number is XWS03F09. The strain was isolated from the sponge *Phakellia fusca* in Xisha Islands and identified as *Pestalotiopsis* sp. by morphological and Internally Transcribed Spacer (ITS) sequence systematic analysis. The strain was preserved in the School of Pharmacy of Southwest Medical University and stored in an MB slant medium at 4°C (**Supplementary Table 2**).

Fermentation and isolation

After the strain *Pestalotiopsis* sp. XWS03F09 was activated, and it was inoculated into the plate medium, cultured at 28°C for 5–7 days, inoculated to the liquid medium, and cultured on the 180RPM shaker at 28°C for 2 days, and the seed solution was obtained. A total of 10% concentration was inoculated into the rice solid medium containing 1% crude sea salt and cultured at 28°C for 36 days. The solid strain at the end of fermentation was soaked in acetone, mashed and soaked overnight, filtered with gauze, then extracted with ethyl acetate, concentrated, and the crude substance was obtained. The crude extract of ethyl acetate was eluted by silica gel column chromatography (CH_2Cl_2-MeOH) (50:1, 10:1, 5:1, 1:1) to obtain five components of Fr.1∼Fr.5. Three components of Fr.2 were eluted by dextran gel chromatography (Sephadex LH-20 C.C) and eluted with MeOH. The Fr.2.1∼Fr.2.3; Fr.2.2 was eluted by silica gel column chromatography P.E.-EtOAc (Fr.2.1∼Fr.2.3; Fr.2.2 E) (20:1), and the target compound was obtained and named **LH-1**. (220.0 mg).

4,4-dimethyl-5α-ergosta-8,24(28)-dien-3β-ol (***LH-1***), White solid; $[\alpha]_D^{25}$ 15.9 (c 0.1, MeOH); HRESIMS *m/z* 449.3849 $[M+Na]^+$ (**Supplementary Figure 1**). ^1H NMR (400 MHz, $CDCl_3$) and ^{13}C NMR data, see **Supplementary Table 3**.

Cell culture

A375, B16-F10, and 293T cells were purchased from the American Type Culture Collection (ATCC, Rockville, MD, USA). They were cultured in DMEM supplemented with 10% heat-inactivated FBS (Gibco, Auckland, New Zealand) and 1% penicillin/streptomycin solution at 37°C in a water-saturated 5% CO_2 incubator.

Cell viability assay

Cell viability assay was determined by MTT assay. A375 and B16-F10 cells were seeded overnight in 96-well plates. The cells were treated with different concentrations of **LH-1** (60, 50, 40, 30, 20, 10, 5, 2.5, and 1.25 μM) for 24, 48, and 72 h, respectively. After treatments, 20 μL of 5 mg/mL MTT was added to each well and incubated for 2–4 h. MTT formazan crystals were dissolved in 100 μL DMSO and incubated for 15–20 min. The absorbance at 570 nm was measured by SpectraMAX M5 microplate spectrophotometer (Molecular Devices) and the cell growth survival rate was calculated. Each experiment was performed at least three times.

Colony formation assay

The A375 and B16-F10 cells were seeded in 6-well plates at 200–500 cells/well and treated with various concentrations of **LH-1** (40, 20, 10, and 2 μM) after 24 h. The cells were incubated for 10 days, and the medicated medium was changed every 3 days. Finally, the cells were fixed with methanol and stained with 0.5% crystal violet for 20 min, and the colonies containing >50 cells were counted. The colony formation numbers were analyzed using Image J software. Each experiment was performed at least three times.

Wound healing assay

The A375 and B16-F10 cells were seeded in 6-well plates at 3×10^5 cells/well overnight. And the cells were

scratched by micro-pipette tips and then washed with PBS twice. And cells were treated with various concentrations of **LH-1** (20, 10, and 2 μM) after 24 h. Then the cells were washed with PBS to remove non-adherent cells and cell debris in the medium. And the migration distance was taken by the microscope and analyzed using Image J software. Each experiment was performed at least three times.

Transwell migration assay

The migration ability of B16-F10 cells was measured using transwell chambers. Cells in 200 μL serum-free medium with various concentrations of **LH-1** (20 and 2 μM) were added to the upper chamber at a density of 5×10^5/mL, while the lower chamber was filled with 500 μL medium containing 10% FBS. After being treated for 24 h at 37°C, the B16-F10 cells were fixed with methanol for 20 min and stained with crystal violet for 20 min. Finally, cells were viewed by the microscope and analyzed using Image J software. Each experiment was performed at least three times.

Propidium iodide staining

Propidium iodide (PI) staining was used to observe cell death. The B16-F10 cells (2×10^5 cells/well) were seeded in 6-well plates overnight. After being treated with different concentrations of **LH-1** for 24 h, the B16-F10 cells were washed with PBS and stained with PI solutions. After incubation, the staining effect was observed under the fluorescence microscope.

Morphological analysis by Hoechst staining

The morphological changes related to apoptosis were observed by Hoechst 33342 staining, and the apoptosis-inducing effect of **LH-1** was detected. After incubating with **LH-1** (40, 20, 10, and 2 μM) for 24 h, the A375 and B16-F10 cells were washed with PBS and stained with Hoechst 33342 solutions (2 μg/mL). Then, the nuclear morphology of cells was observed by fluorescence microscopy.

Western blot analysis

Collection, lysis, and quantification of B16-F10 cells (BCA Protein Assay Kit; Beyotime, China). Western blot analysis was performed with the indicated antibody. Protein density was analyzed by ImageJ software. The monoclonal antibody against β-actin was used as a control. Data were described as multiple differences from untreated controls.

Subcutaneous xenograft models

All animal experiments were approved by the Southwest Medical University in China (Permit Number: 201903-38) (**Supplementary Table 4**), and all protocols were carried out following approved guidelines. Female C57BL/6 mice 4–6 weeks of age were obtained. 5×10^5 cells (100 μL cell suspension) were subcutaneously implanted into the lumbosacral region of C57BL/6 mice to prepare the B16-F10 tumor xenograft model. When the tumors reached an average volume of 100 mm^3, the mice were randomly divided into three groups ($n = 6$). **LH-1** (10 and 40 mg/kg) or vehicle was administered intraperitoneally once every 2 days for 15 days, and the tumor and body weights were measured every 2 days. The tumor volume was calculated as follows: volume = $0.5 \times a \times b^2$, among them a (mm) is the length of the tumor, and b (mm) is the width of the tumor. Tumor inhibition rate = (average volume of the control group–average volume of the experimental group)/average volume of the control group ×100%.

Histopathology and immunohistochemistry

Tumor tissues fixed in formalin were subjected to hematoxylin and eosin (H&E) to detect whether there are any toxic and side effects on normal organs and immunohistochemistry analysis to detect anti-Ki67 and cleaved caspase-3 (Liu et al., 2022).

mRNA sequencing and bioinformatics analysis

B16-F10 cells treated with **LH-1** for 24 h were sequenced by Shenzhen Huada Genome Co., Ltd., Shenzhen, China. The concentration of **LH-1** was 20 μM. Total RNA was extracted from the cells using Trizol (Invitrogen, Carlsbad, CA, USA) according to manual instruction, qualified and quantified using a NanoDrop and Agilent 2100 bioanalyzer (Thermo Fisher Scientific, Waltham, MA, USA). The sequencing data was filtered with SOAPnuke (v1.5.2) (Li et al., 2008). The heatmap was drawn by heatmap (v1.0.8) according to the gene expression in different samples. Differential expressed genes (DEGs) was identified using DESeq2 package (v1.4.5) (Love et al., 2014) under the criterion of the adjusted $P < 0.05$ and $|\log_2 FC| > 1$. The clusterProfiler Bioconductor

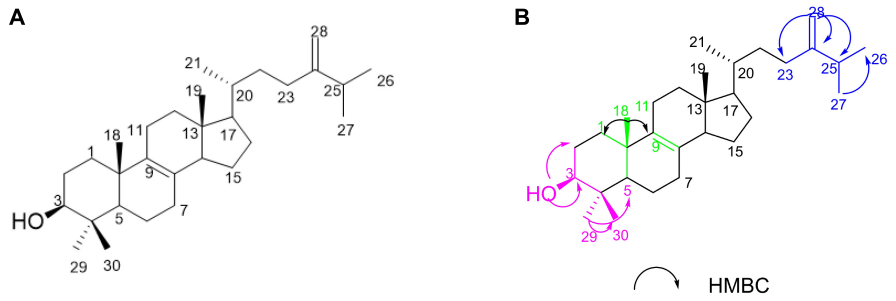

FIGURE 1
The structure of **LH-1** and the Key HMBC correlations of **LH-1**.

software was used to enrich gene ontologies (GO) and the Kyoto encyclopedia of genes and genomes (KEGG) (v4.2.2).

Quantitative real-time polymerase chain reaction

Cells were lysed with 1 mL of RNA-easy Isolation Reagent (Nanjing Novozan Biotechnology Co., Ltd., Nanjing, China), and cDNA was synthesized with the HiScript® III RT SuperMix for qPCR (+gDNA wiper) (Nanjing Nuowizan Biotechnology Co., Ltd.). QRT-PCR was performed by using Taq Pro Universal SYBR qPCR Master Mix (Nanjing Novozan Biotechnology Co., Ltd.). The Primers used are listed in **Supplementary Table 1** of the **Supplementary material**. Sequence data were submitted to the NCBI Sequence Read Archive under BioProject ID PRJNA866290.

Statistical analyses

All the results are shown as the mean ± standard deviation (SD), which were determined using GraphPad Prism 8.0 software (GraphPad, Inc., La Jolla, CA, USA). Comparisons between the treatment and negative control groups were conducted by the independent sample *t*-test. Statistically significant *P*-values were labeled as following: $^{*}P < 0.05$, $^{**}P < 0.01$, $^{***}P < 0.001$.

Results

Identification of 4,4-dimethyl-5α-ergosta-8,24(28)-dien-3β-ol (LH-1)

LH-1 was isolated as a white solid. The ^{1}H NMR (**Supplementary Figure 2**) data of **LH-1** displayed seven methyl signals at δ_H 0.61 (3H, s, H-18), δ_H 1.00 (3H, s, H-19), δ_H 0.96 (3H, d, J = 6.5 Hz, H-21), δ_H 0.99 (3H, d, J = 6.5 Hz, H-26), δ_H 0.95 (3H, d, J = 6.5 Hz, H-27), δ_H 0.81 (3H, s, H-29), δ_H 1.02 (3H, s, H-30). The ^{13}C NMR (**Supplementary Figure 3**), DEPT (**Supplementary Figure 4**), and HSQC (**Supplementary Figure 5**) data showed 30 carbon signals corresponding to seven methyls, 10 methylenes, 6 methines carbons, and 6 oxygenated carbons. A detailed analysis of the NMR data of **LH-1** revealed that it was a known compound, 4,4-dimethyl-5α-ergosta-8,24(28)-dien-3β-ol (**LH-1**), which was previously reported from *P. blakesleeanus*. This was proved by the HMBC (**Supplementary Figure 6**) correlation from 3-OH (δ_H 3.24) to C-29 (δ_C 15.4), C-2 (δ_C 28.5), C-4 (δ_C 39.0), and C-3 (δ_C 79.0), from Me-29 (δ_H 0.81) to C-30 (δ_C 27.9), C-5 (δ_C 50.2), C-4 (δ_C 39.0), and C-3 (δ_C 79.0), from H-25 (δ_H 2.21) to C-24 (δ_C 156.9), C-28 (δ_C 105.9), C-27 (δ_C 21.9), and C-26 (δ_C 19.9), from H-28 (δ_H 4.71) to C-24 (δ_C 156.9), C-23 (δ_C 31.1), and C-25 (δ_C 33.8) (**Figure 1B**). The planar structure of **LH-1** was determined by HSQC, HMBC, and COSY experiments (**Supplementary Figure 7**). The NOESY (**Supplementary Figures 8**, **9**) correlations observed between H-3/H-2α; H-1β/H_3-18; H_3-18/H-11β; H-H_3-19 and H-11β; and H-16α/H17α suggested that the hydroxy group on C-3 and the methyl on C-10 had a *cis*-relationship, and the hydroxy at C-3 was in the β-orientation (**Supplementary Figure 12**). According to the literature and comparison of the NMR data (Barrero et al., 1998), **LH-1** was identified as 4,4-dimethyl-5α-ergosta-8,24(28)-dien-3β-ol.

LH-1 inhibited the proliferation of melanoma cells

The MTT method was used to detect the anti-proliferative activity of **LH-1** on different tumor cells. It was found that **LH-1** had a selective inhibitory effect on melanoma cells and had no significant toxicity to human breast cancer cell MDA-MB-231 (IC_{50} > 60 μM at 72 h), human carcinoma cell A549

A

Cells	IC_{50} (μM)
A375	13.42
B16-F10	16.57
MDA-MB-231	>60
A549	>60
HEK-293T	>60

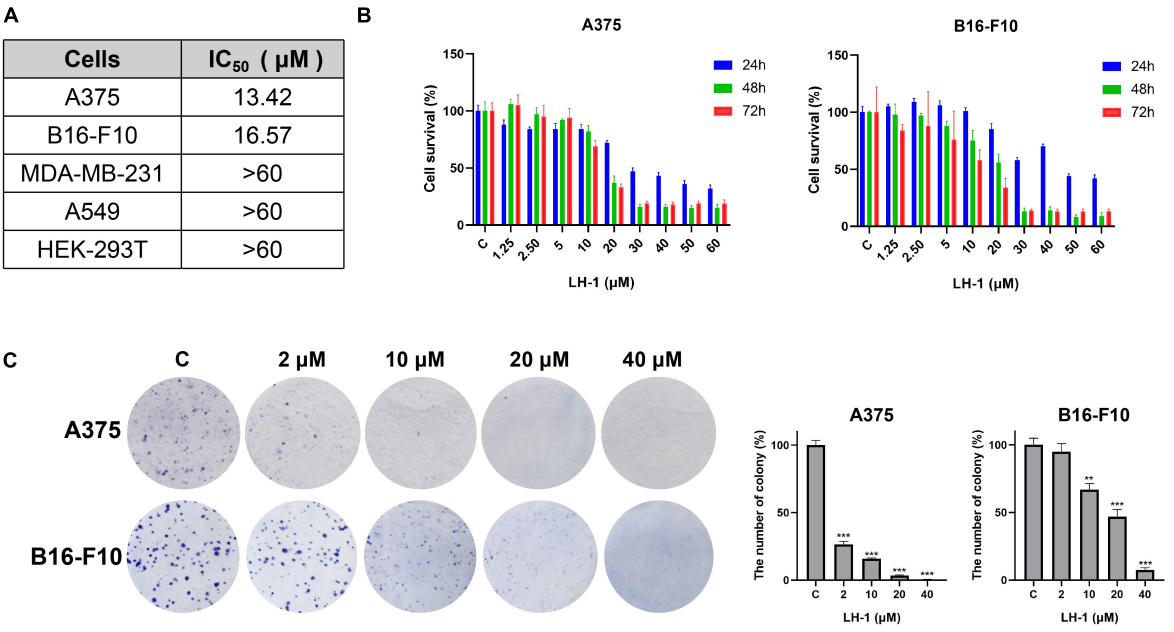

FIGURE 2
LH-1 inhibited melanoma cell viability. **(A)** IC_{50} of **LH-1** in melanoma cells A375, B16-F10, human breast cancer cells MDA-MB-231, human lung adenocarcinoma cells A549, and human renal epithelial cells HEK-293T for 72 h. **(B)** Melanoma cell lines A375 and B16-F10 were treated with different concentrations of **LH-1** for 24, 48, or 72 h, respectively. And the viability was measured by the MTT assay. **(C)** The effects of **LH-1** on colony formation in two melanoma cell lines for 10 days and the statistical data were shown on the right. All experiments were repeated at least three times. $^{**}P < 0.01$, $^{***}P < 0.001$ vs. control(C).

(IC_{50} > 60 μM at 72 h) and human renal epithelial cell HEK-293T (IC_{50} > 50 μM at 72 h) (Figure 2A and Supplementary Figure 10). The A375 and B16-F10 cells were treated with **LH-1** at different concentrations for 24, 48, and 72 h. As shown in Figure 2B, the inhibitory effect of **LH-1** on the proliferation of melanoma cells in a concentration and time-dependent manner. The IC_{50} values of **LH-1** on A375 and B16-F10 cells melanoma cells were 13.42 and 16.57 μM at 72 h, respectively. Furthermore, we did colony-forming assays to further investigate the effect of **LH-1** on the A375 and B16-F10 cells. After treatment with different concentrations of **LH-1**, the colony formation numbers of A375 and B16-F10 in the 10 μM group were 15.92 and 66.9% of those in the control group, and 0.55 and 7.46% in the 40 μM group, respectively (Figure 2C).

LH-1 inhibited the migration of melanoma cells

The colony formation results agree with the MTT data and indicated that **LH-1** selectively inhibited the growth of melanoma cells. In addition, the cell wound-healing, transwell assay, and western blot assay were performed to evaluate the anti-metastatic effect of **LH-1**. As shown in Figure 3A, the inhibitory effect increased with the increase in concentration. The migration capacity of A375 and B16-F10 in the 10 μM group was 74.79 and 88.76% of that in the control group, and 60.52 and 69.04% in the 20 μM group, respectively. The transwell assay results showed that the number of cells passing through the transwell chamber in the **LH-1** group was lower than that in the control group. **LH-1** significantly inhibited transwell migration in A375 and B16-F10 melanoma cells in a dose-dependent manner (Figure 3B). And the MMP-9 showed an apparent decrease after treatment of **LH-1** (Figure 3C). To sum up, this finding suggested that **LH-1** could inhibit the proliferation and migration of melanoma cells.

LH-1 induced apoptosis by the mitochondrial apoptotic pathway in melanoma cells

Avoiding apoptosis is one of the signs of cancer (Hanahan and Weinberg, 2011). Mitochondrial apoptosis is one of the main pathways of cancer cell death. Apoptosis is characterized by cell shrinkage, chromatin condensation, and nuclear and cell fragmentation. These characteristics lead to the formation of apoptotic bodies (Cotter, 2009). As shown in Figure 4A, with the increase in **LH-1** concentration, the number of remaining cells gradually decreased and the morphology changed significantly. At the same time, the number of PI-positive cells gradually increased. To evaluate whether **LH-1**

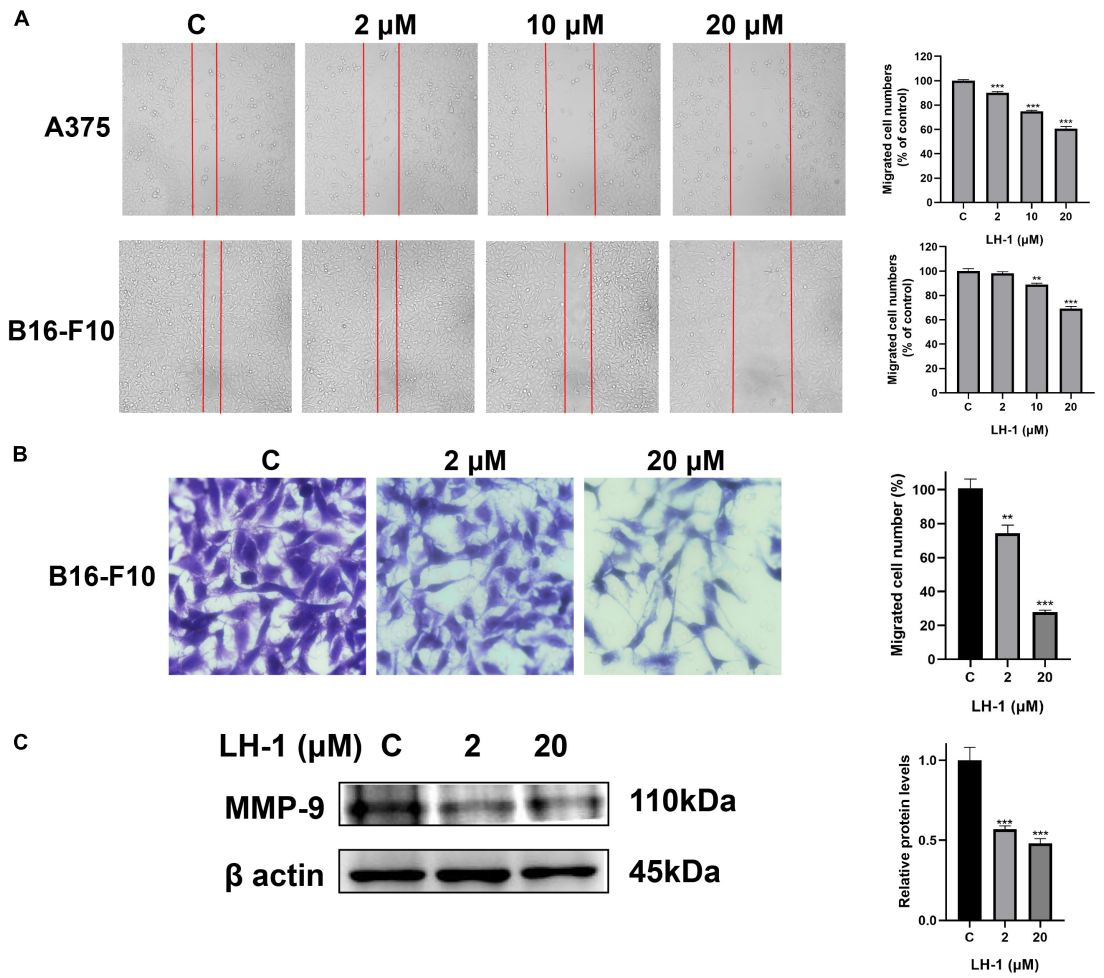

FIGURE 3
LH-1 inhibited melanoma cells A375 and B16-F10 migration. **(A)** A single scratch was created in the confluent monolayer of A375 and B16-F10 cells. The scratch was photographed at 24 h after **LH-1** treatment (left) and migrated cell numbers (right) were analyzed by Image J software. **(B)** Cells were allowed to migrate through the transwell chamber in the presence of an indicated concentration of **LH-1**. Representative photographs of migrated cells (left) and quantification of these cells (right) were shown. **(C)** Cells were treated with the indicated concentration of **LH-1** for 24 h, expression levels of MMP-9 were determined by the Western blot analysis (left), and relative expression levels were analyzed by Image J software (right). All experiments were repeated at least three times. $^{**}P < 0.01$, $^{***}P < 0.001$ vs. control.

can induce apoptosis, Hoechst 33342 staining was performed to visualize the formation of apoptotic bodies. As shown in Figure 4B and Supplementary Figure 11, apoptotic bodies and chromatin agglutination are significantly increased compared with control. Besides, these changes were concentration-dependent. Anti-apoptotic members of the Bcl-2 family such as pro-apoptotic proteins Bax and anti-apoptotic proteins Bcl-2 are representative markers of apoptosis (Cory et al., 2003). To further confirm the apoptosis-promoting effect of **LH-1**, the expression of apoptosis-related proteins was detected by western blot assay. We examined Bax, Bcl-2, Cleaved Caspase-3, and Cleaved Caspase-9 expression levels in B16-F10 cells after treatment with **LH-1** for 24 h. As shown in Figure 4C, the expression level of Bcl-2 was significantly decreased, whereas Bax, Cleaved Caspase-3, and Cleaved Caspase-9 were increased in a dose-dependent manner. These results suggested that the inhibitory effect of **LH-1** on melanoma cells is achieved by inducing the mitochondrial apoptotic pathway.

LH-1 inhibited melanoma tumor growth *in vivo*

To test the anti-tumor effect of **LH-1** *in vivo*, the xenograft model of B16-F10 cells in mice was established and the mice were injected intraperitoneally with 10 and 40 mg/kg every other day for 15 days. As shown in Figures 5A–D, compared with the vehicle group, **LH-1** treatment could inhibit tumor growth and tumor weight, and the inhibitory effect of the 40 mg/kg

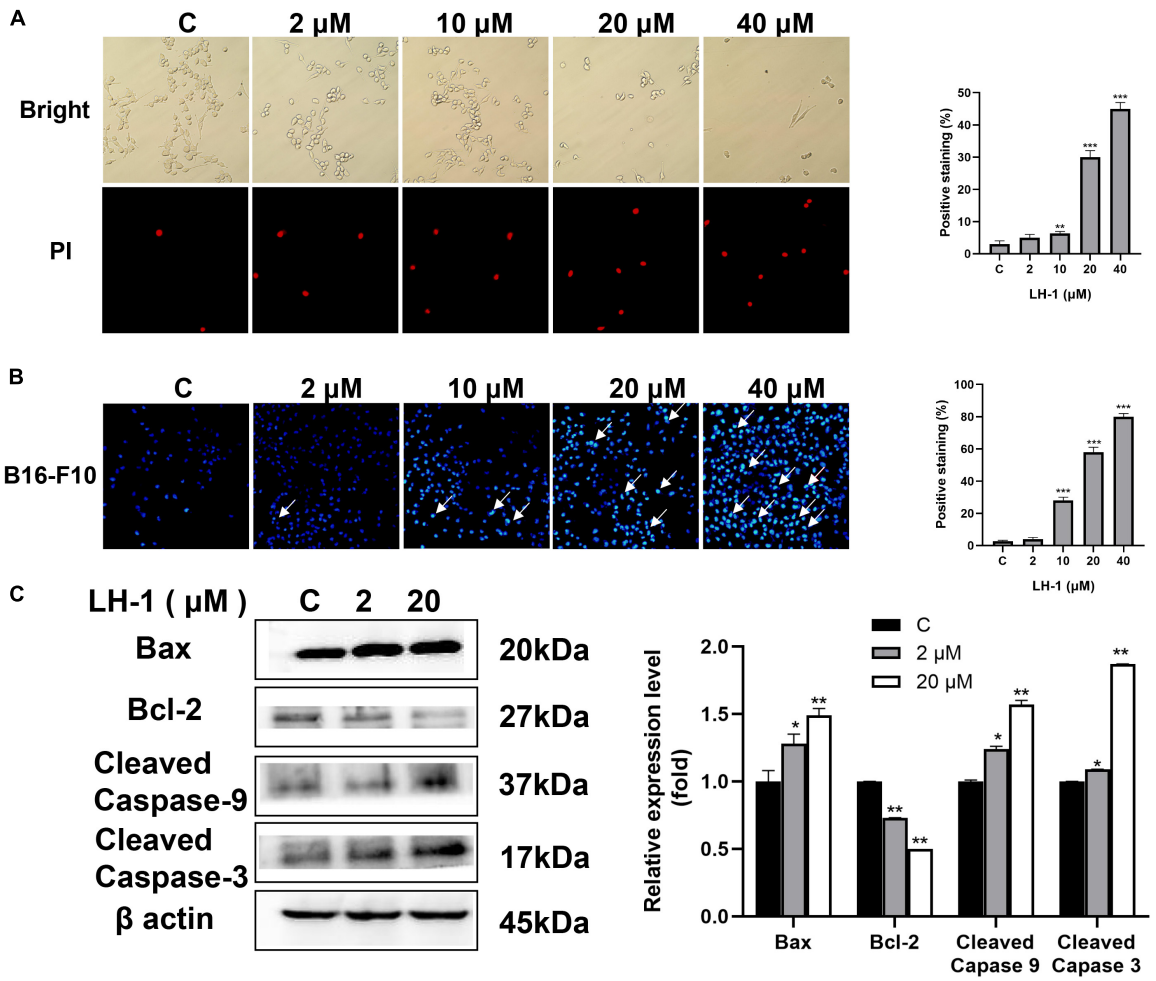

FIGURE 4
LH-1 induced cell apoptosis *via* mitochondria-mediated apoptosis. **(A)** B16-F10 cells were treated with the indicated concentration of **LH-1** for 24 h, and the morphology of cells and the cell with positive propidium iodide (PI) staining were under a fluorescence microscope. **(B)** Hoechst staining was used to stain apoptotic cells after treatment with **LH-1**. **(C)** Cells were treated with the indicated concentration of **LH-1** for 24 h, and the expression levels of Bax, Bcl-2, Cleaved Caspase-3, and Cleaved Caspase-9 were determined by the Western blot analysis (left), and relative expression levels were analyzed by Image J software (right). All experiments were repeated at least three times. $^{*}P < 0.05$, $^{**}P < 0.01$, $^{***}P < 0.001$ vs. control.

dose group was stronger than that of the 10 mg/kg dose group. The tumor inhibition rate of the low-dose group is 75.44%, and the high-dose group is 92.56%. Notably, during treatment, there was no significant change in the body weight of mice during the treatment (Figure 5E). The above data indicated that **LH-1** inhibited melanoma tumor growth *in vivo* and has no significant effect on the body weight of mice. To validate whether **LH-1** is toxic to normal organs of mice, the main organs were stained with hematoxylin and eosin (H&E) staining and observed under a light microscope. No histopathological abnormality was found in the treatment group (Figure 5F), these results indicated that **LH-1** had no significant toxic or side effects on the main organs of mice. To further understand the anti-tumor mechanism of **LH-1** *in vivo*, immunohistochemistry analysis was performed. As is shown in Figure 5G, after **LH-1** treatment, cell proliferation (Ki-67 positive) significantly decreased and apoptosis significantly increased (Cleaved Caspase-3 positive). Consequently, the **LH-1** inhibited tumor growth in the B16-F10 xenograft tumor model by inhibiting cell proliferation and inducing cell apoptosis.

LH-1 induces *OBSCN* expression

To further study the anti-melanoma mechanism of **LH-1**, mRNA sequencing was performed in B16-F10 cells treated with **LH-1**. As shown in Figure 6A, the total number of 6,130 genes was markedly altered in B16-F10 cells, a heatmap was generated to show **LH-1**-induced changes in gene expression in B16-F10 cells. The GO enrichment analysis indicated

10.3389/fmicb.2022.1008053

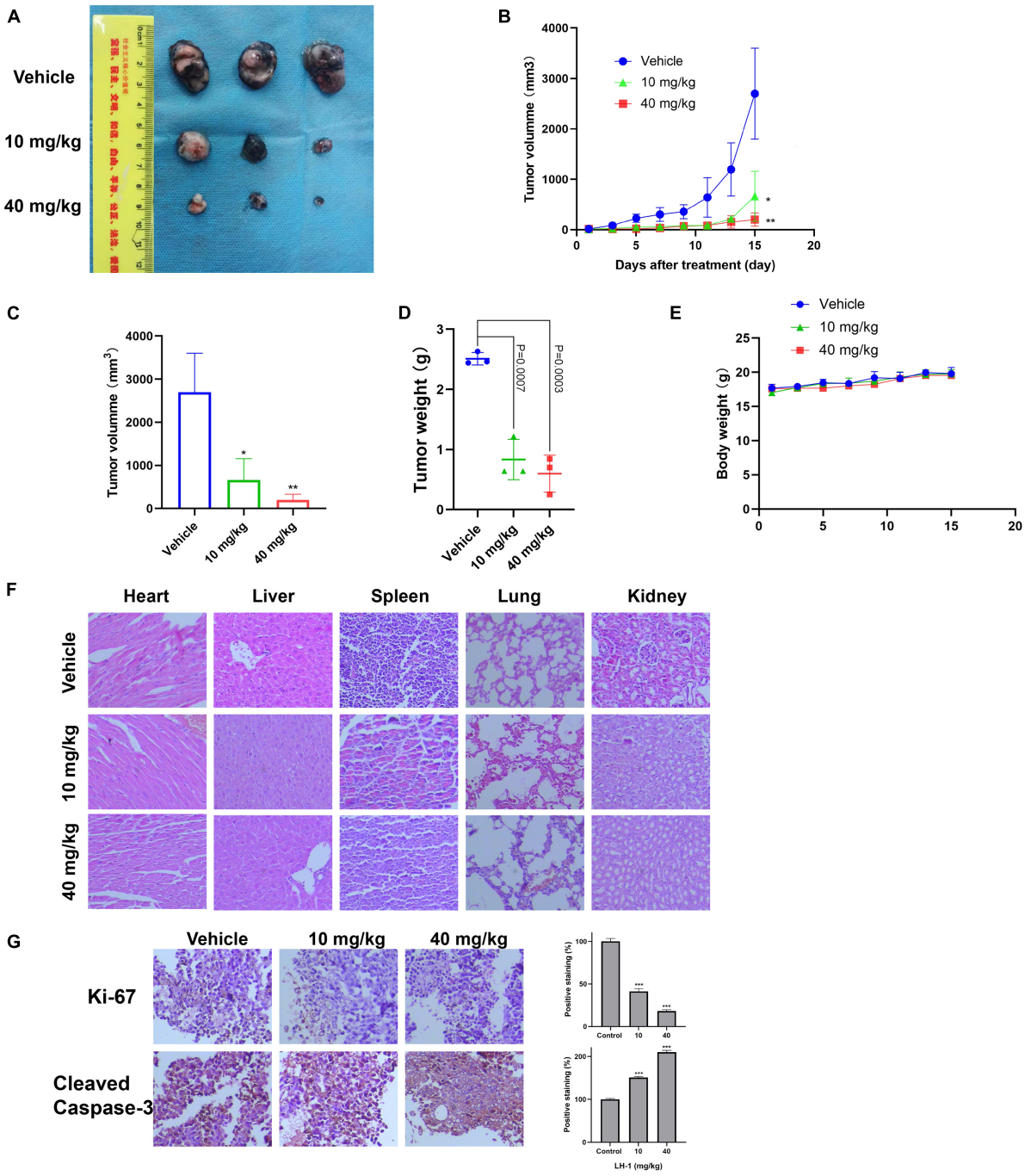

FIGURE 5

LH-1 inhibited tumor growth *in vivo*. In the B16-F10 xenograft model, the mice were treated with **LH-1** (10 and 40 mg/kg) or vehicle. **(A)** Tumors from mice treated with **LH-1** or vehicle on the final day. **(B)** Tumor volumes were measured every 2 days and were represented as the mean ± SD ($n = 6$, $^{*}P < 0.05$, $^{**}P < 0.01$ versus vehicle group). **(C)** Quantitative analysis of tumor volume changes on the final day (Day 15). **(D)** Represented the weight of tumors from mice in different groups when the mice were sacrificed at the endpoint. *P*-values for comparing two groups were determined using a two-tailed Student's *t*-test. **(E)** Body weights were measured every 2 days and were represented as the mean ± SD ($n = 3$, The difference was not statistically significant). **(F)** Histological observation of **LH-1** treated mice. Microscopic pathology of the heart, liver, spleen, lung, and kidney shows no evidence of adverse systemic toxicity following **LH-1** treatment in the mice. Slides were observed under a microscope (×200). **(G)** Tumor cell proliferation was evaluated through immunohistochemical analysis staining with Ki-67 and cleaved caspase-3, and the statistical data of positive staining were shown on the right. $^{*}P < 0.05$, $^{**}P < 0.01$, $^{***}P < 0.001$ vs. vehicle.

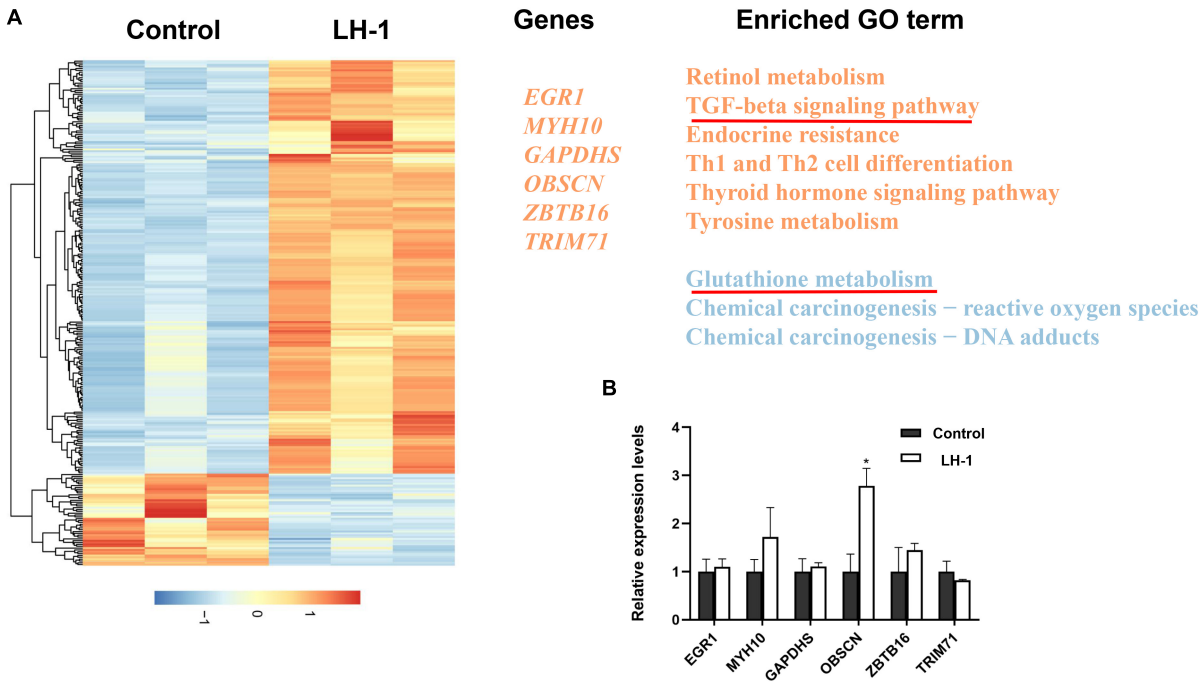

FIGURE 6
Gene expression changes induced by **LH-1** in melanoma cells. **(A)** Differential expressed genes (DEGs) expression profile and related functional term enrichments. Each row represents a single DEG and each column represents a sample. Heatmap values were normalized from −2 (blue; low expression counts) to +2 (red; high expression counts) (the left heatmap panel). Representative genes (middle panel) and enriched pathways (right panel) are then displayed. The upregulated genes and pathways are marked by orange, and the downregulated pathways are marked by blue. **(B)** The qRT-PCR validation of representative gene expression in B16-F10 cells. qRT-PCR was repeated at least three times. *$P < 0.05$ vs. control.

that the significant changes mainly focused on the "TGF-β signaling pathway" and "Glutathione transferase activity." As we all know, the transforming growth factor (TGF)-β signaling events are to control diverse processes and numerous responses, such as cell proliferation, differentiation, apoptosis, and migration (Xie et al., 2018). Among them, promoting apoptosis and mesenchymal transformation are the two most important functions of TGF-β (Song and Shi, 2018). Although our experimental results showed that the TGF-β signaling pathway was activated after **LH-1** treatment, the occurrence and development of the tumor is a complex process, not the result of the action of a single factor. In the future, the specific mechanisms of action can be studied by detecting key proteins in this pathway. In addition, γ-Glutamylcyclotransferase is one of the main enzymes in glutathione metabolism. It is upregulated in many cancers (breast, ovarian, cervical, lung, etc.) and promotes the progression of cancer. Its deletion leads to the inhibition of cancer cell proliferation, invasion, and migration (Kageyama et al., 2018). The experimental results suggested that **LH-1** may inhibit melanoma growth by downregulating glutathione metabolism. And then several genes related to carcinogenesis were selected from the top 20 mRNA-seq upregulated genes and were further verified by qRT-PCR. As shown in **Figure 6B**, the *OBSCN* gene was upregulated significantly. Our study suggested that **LH-1** may play an anti-melanoma role by upregulating *OBSCN* gene expression, activating the TGF-β signaling pathway, and inhibiting glutathione transferase activity.

Discussion

Human malignant melanoma is a highly invasive human cancer, and its incidence has increased faster than any other cancer in the past few decades (Sung et al., 2021). For advanced melanoma, targeted therapies (e.g., dabrafenib, ipilimumab) are now available in other countries but are costly (Gordon et al., 2016). Therefore, new anti-melanoma targeted therapies are urgently needed. In recent years, due to the wide sources of natural products, more and more studies have been conducted on their anti-tumor effects (Fontana et al., 2019). Especially, microbial secondary metabolites have become a rich source of new drugs, which have made great contributions to the discovery of new drugs (Lei et al., 2021; Ramirez-Rendon et al., 2022).

In this study, we extracted, isolated, and purified the target compound **LH-1** from the secondary metabolites of the marine fungus *Pestalotiopsis* sp. and its structure was identified

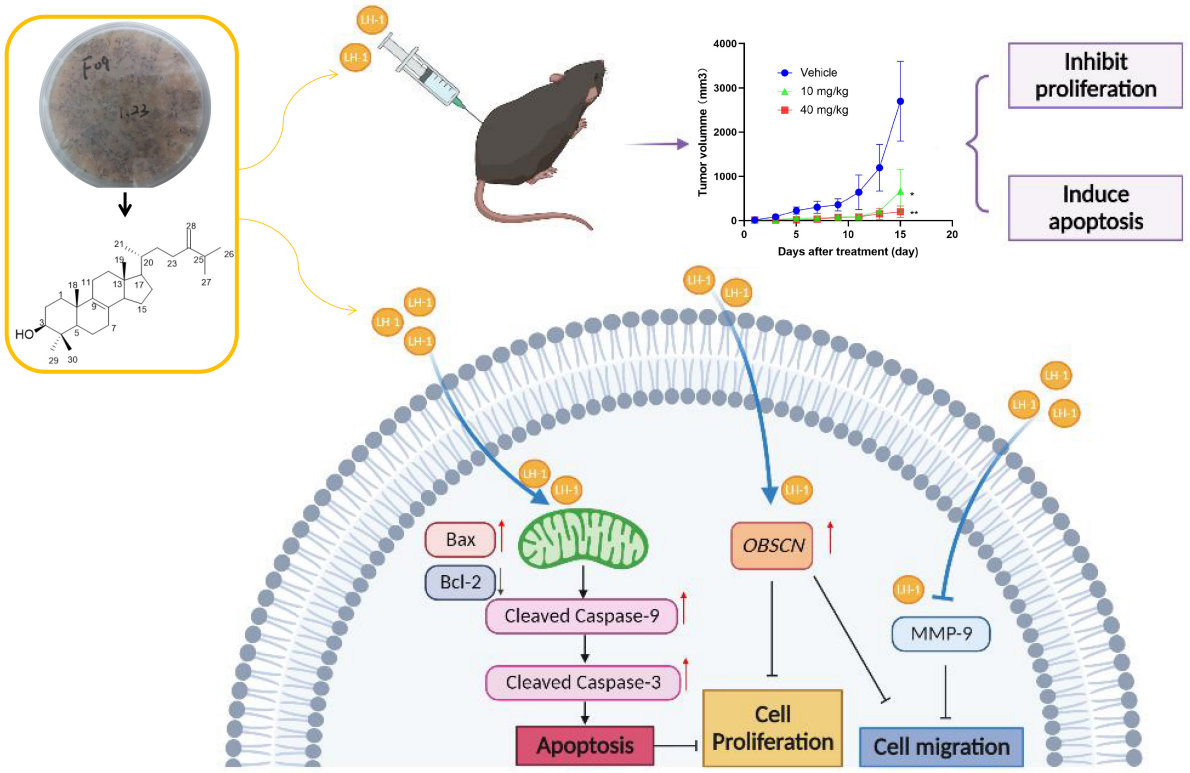

FIGURE 7
Diagram of the mechanism of LH-1 inhibiting melanoma.

as 4,4-dimethyl-5α-ergosta-8,24(28)-dien-3β-ol. Afterward, its biological activities against melanoma were explored for the first time. The inhibitory effect of **LH-1** on melanoma and its molecular mechanism was investigated *in vitro* and *in vivo* (**Figure 7**). First of all, **LH-1** inhibited the proliferation of two melanoma cell lines in a time-and concentration-dependent manner and had no significant inhibitory effect on normal cells. A sterol derived ergosterol peroxide (EP), extracted from medicinal mushrooms, has been reported to exert antitumor activity in several tumor types. The IC_{50} to ovarian cancer cells and lung cancer cells is about 50 and 23 μM, respectively (Tan et al., 2017; Wu et al., 2018). However, the IC_{50} value of **LH-1** on B16-F10 melanoma cells is 16.57 μM, which is better than that of EP. Furthermore, to explore the anti-proliferation mechanism of **LH-1**, Hoechst 33342 staining was performed, and we found that **LH-1** could induce apoptosis of melanoma cells in a dose-dependent manner. Apoptosis is an important way to destroy cancer cells, and the mitochondrial apoptosis pathway is the main signal pathway of apoptosis (Cotter, 2009). Bax, a member of the pro-apoptotic family, is a member of the BCL-2 family, which plays a central role in the permeability of the mitochondrial outer membrane and then induces apoptosis (Gibson and Davids, 2015). After **LH-1** treatment, the pro-apoptotic protein Bax, Cleaved Caspase-3, and Cleaved Caspase-9 were increased, while the anti-apoptotic proteins Bcl-2 were decreased. Summarizing these data, **LH-1** induced the apoptosis of melanoma cells through the mitochondrial apoptotic pathway. *In vivo*, the C57BL/6 mice tumor model of subcutaneous transplants showed that **LH-1** inhibited tumor growth and had no significant effect on the body weight of mice. We also found the activation of apoptosis (Cleaved Caspase-3 positive cells) and the decrease of cell proliferation (Ki-67 positive cells) by immunohistochemistry with mouse tumor tissue.

The main cause of melanoma death is the occurrence of metastases (Xia et al., 2021). Upregulation of MMP-9 is often associated with increased cancer cell migration, invasion, and metastasis (Zhu et al., 2019). Therefore, the inhibitory effect of **LH-1** on melanoma metastasis was evaluated by cell migration assay. Wound healing assay and transwell assay showed that **LH-1** could inhibit the migration of melanoma cells. In addition, **LH-1** downregulated the expression levels of MMP-9 in B16-F10. The above results have shown that **LH-1** inhibited the migration of melanoma *in vitro*.

Recently, *OBSCN* mutations have been found in many types of cancer, suggesting that the gene may play a key role in different cancers. It has been reported that giant obscurin regulates migration and metastasis in pancreatic cancer (Tuntithavornwat et al., 2022), and the loss of giant obscurins from breast epithelium promotes epithelial-to-mesenchymal

transition, tumorigenicity, and metastasis (Shriver et al., 2015). These results suggest that *OBSCN* may be a gene related to inhibiting the occurrence and development of cancer. Some studies have found that *OBSCN* has mutations in melanoma, suggesting that *OBSCN* may be related to the mechanism of melanoma progression (Balakrishnan et al., 2007). We found that the *OBSCN* was significantly increased after **LH-1** treatment in melanoma cells, and it was speculated that **LH-1** inhibited the proliferation and migration of melanoma by targeting *OBSCN*. However, how **LH-1** affects the upregulation of *OBSCN* requires further analysis. (Tan et al., 2017) reported that EP showed antitumor effects toward ovarian cancer cells through both β-catenin and STAT3 signaling pathways, and we speculate whether **LH-1**, which is similar to EP's structure, also acts through this pathway. We will study in this direction in follow-up experiments.

Due to the easy access and non-toxicity side effects, the use of marine natural products particularly marine fungi-derived biomolecules for inflammation, and cancer therapy has received much attention. This study paves the way for us to study anti-melanoma drugs of marine fungal secondary metabolites.

Conclusion

This study has extracted, isolated, purified the target compound **LH-1**, and evaluated the anti-melanoma activity of **LH-1** *in vivo* and *in vitro*. Our study verified that **LH-1** induced apoptosis through the mitochondrial apoptosis pathway and inhibited the migration *via* downregulated expression levels of MMP-9 in melanoma cells. In addition, **LH-1** showed anti-tumor activity in the xenograft model *in vivo* and had no significant toxicity. Altogether, **LH-1** is a promising candidate for treating melanoma growth and metastasis.

Data availability statement

The datasets presented in this study can be found in online repositories. The names of the repository/repositories and accession number(s) can be found below: PRJNA866290 (BioProject ID).

Ethics statement

The animal study was reviewed and approved by Southwest Medical University in China (Permit Number: 201903-38).

Author contributions

LL, HL, and TX designed the study. TX, HL, YZ, and LL wrote the manuscript. TX, HL, JW, and HW performed the experiments. TX, LG, and XX analyzed the data. TX, HL, and TQ revised the manuscript. All authors have read and agreed to the published version of the manuscript.

Funding

We are grateful to financial support from the National Natural Science Foundation of China (82003716), the Sichuan Science and Technology Department Project (2020YJ0191, 2021YFH0145, and 2021YJ0123), Natural Science Foundation of Sichuan Province (2022NSFSC0109), and Luzhou Municipal People's Government-Southwest Medical University Science and Technology Strategic Cooperation Project (2019LZXNYDJ08).

Conflict of interest

The authors declare that the research was conducted in the absence of any commercial or financial relationships that could be construed as a potential conflict of interest.

Publisher's note

Supplementary material

The Supplementary Material for this article can be found online at: https://www.frontiersin.org/articles/10.3389/fmicb.2022.1008053/full#supplementary-material

References

Ackermann, M. A., Shriver, M., Perry, N. A., Hu, L. Y., and Kontrogianni-Konstantopoulos, A. (2014). Obscurins: Goliaths and Davids take over non-muscle tissues. *PLoS One* 9:e88162. doi: 10.1371/journal.pone.0088162

Bae, S. Y., Liao, L., Park, S. H., Kim, W. K., Shin, J., and Lee, S. K. (2020). Antitumor activity of asperphenin A, a lipopeptidyl benzophenone from marine-derived *Aspergillus* sp. Fungus, by inhibiting tubulin polymerization in colon cancer cells. *Mar. Drugs* 18:110. doi: 10.3390/md18020110

Balakrishnan, A., Bleeker, F. E., Lamba, S., Rodolfo, M., Daniotti, M., Scarpa, A., et al. (2007). Novel somatic and germline mutations in cancer candidate genes in glioblastoma, melanoma, and pancreatic carcinoma. *Cancer Res.* 67, 3545–3550. doi: 10.1158/0008-5472.CAN-07-0065

Barrero, A. F., Oltra, J. E., Poyatos, J. A., Jiménez, D., and Oliver, E. (1998). Phycomysterols and other sterols from the fungus *Phycomyces blakesleeanus*. *J. Nat. Prod.* 61, 1491–1496. doi: 10.1021/np980199h

Bu, M., Li, H., Wang, H., Wang, J., Lin, Y., and Ma, Y. (2019). Synthesis of ergosterol peroxide conjugates as mitochondria targeting probes for enhanced anticancer activity. *Molecules* 24:3307. doi: 10.3390/molecules24183307

Cory, S., Huang, D. C., and Adams, J. M. (2003). The Bcl-2 family: Roles in cell survival and oncogenesis. *Oncogene* 22, 8590–8607. doi: 10.1038/sj.onc.1207102

Cotter, T. G. (2009). Apoptosis and cancer: The genesis of a research field. *Nat. Rev. Cancer* 9, 501–507. doi: 10.1038/nrc2663

Cruz, L. J., Insua, M. M., Baz, J. P., Trujillo, M., Rodriguez-Mias, R. A., Oliveira, E., et al. (2006). IB-01212, a new cytotoxic cyclodepsipeptide isolated from the marine fungus *Clonostachys* sp. ESNA-A009. *J. Org. Chem.* 71, 3335–3338. doi: 10.1021/jo051600p

Davis, L. E., Shalin, S. C., and Tackett, A. J. (2019). Current state of melanoma diagnosis and treatment. *Cancer Biol. Ther.* 20, 1366–1379. doi: 10.1080/15384047.2019.1640032

Dimitriou, F., Krattinger, R., Ramelyte, E., Barysch, M. J., Micaletto, S., Dummer, R., et al. (2018). The world of melanoma: Epidemiologic, genetic, and anatomic differences of melanoma across the globe. *Curr. Oncol. Rep.* 20:87. doi: 10.1007/s11912-018-0732-8

Fattorusso, E., Giovannitti, B., Lanzotti, V., Magno, S., and Violante, U. (1992). 4, 4-Dimethyl-5α-ergosta-8,24(28)dien-3β-ol from the fungus *Marasmius oreades*. *Steroids* 57, 119–121. doi: 10.1016/0039-128x(92)90069-l

Fontana, F., Raimondi, M., Di Domizio, A., Moretti, R. M., Montagnani Marelli, M., and Limonta, P. (2019). Unraveling the molecular mechanisms and the potential chemopreventive/therapeutic properties of natural compounds in melanoma. *Semin. Cancer Biol.* 59, 266–282. doi: 10.1016/j.semcancer.2019.06.011

Garbe, C., Peris, K., Hauschild, A., Saiag, P., Middleton, M., Bastholt, L., et al. (2016). Diagnosis and treatment of melanoma. European consensus-based interdisciplinary guideline - Update 2016. *Eur. J. Cancer* 63, 201–217. doi: 10.1016/j.ejca.2016.05.005

Gershenwald, J. E., Scolyer, R. A., Hess, K. R., Sondak, V. K., Long, G. V., Ross, M. I., et al. (2017). Melanoma staging: Evidence-based changes in the American Joint Committee on Cancer eighth edition cancer staging manual. *CA Cancer J. Clin.* 67, 472–492. doi: 10.3322/caac.21409

Gibson, C. J., and Davids, M. S. (2015). BCL-2 antagonism to target the intrinsic mitochondrial pathway of apoptosis. *Clin. Cancer Res.* 21, 5021–5029. doi: 10.1158/1078-0432.CCR-15-0364

Gordon, L. G., Elliott, T. M., Wright, C. Y., Deghaye, N., and Visser, W. (2016). Modelling the healthcare costs of skin cancer in South Africa. *BMC Health Serv. Res.* 16:113. doi: 10.1186/s12913-016-1364-z

Grimaldi, A. M., Simeone, E., Festino, L., Vanella, V., Strudel, M., and Ascierto, P. A. (2017). MEK inhibitors in the treatment of metastatic melanoma and solid tumors. *Am. J. Clin. Dermatol.* 18, 745–754. doi: 10.1007/s40257-017-0292-y

Hanahan, D., and Weinberg, R. A. (2011). Hallmarks of cancer: The next generation. *Cell* 144, 646–674. doi: 10.1016/j.cell.2011.02.013

Kageyama, S., Ii, H., Taniguchi, K., Kubota, S., Yoshida, T., Isono, T., et al. (2018). Mechanisms of tumor growth inhibition by depletion of gamma-glutamylcyclotransferase (GGCT): A novel molecular target for anticancer therapy. *Int. J. Mol. Sci.* 19:2054. doi: 10.3390/ijms19072054

Lei, H., Bi, X., Lin, X., She, J., Luo, X., Niu, H., et al. (2021). Heterocornols from the sponge-derived fungus pestalotiopsis heterocornis with anti-inflammatory activity. *Mar. Drugs* 19:585. doi: 10.3390/md19110585

Li, R., Li, Y., Kristiansen, K., and Wang, J. (2008). SOAP: Short oligonucleotide alignment program. *Bioinformatics* 24, 713–714. doi: 10.1093/bioinformatics/btn025

Liu, H., Li, X. M., Liu, Y., Zhang, P., Wang, J. N., and Wang, B. G. (2016). Chermesins A-D: Meroterpenoids with a drimane-type spirosesquiterpene skeleton from the marine algal-derived endophytic fungus *Penicillium chermesinum* EN-480. *J. Nat. Prod.* 79, 806–811. doi: 10.1021/acs.jnatprod.5b00893

Liu, Z., Wang, H., Sun, C., He, Y., Xia, T., Wang, J., et al. (2022). ZWZ-3, a fluorescent probe targeting mitochondria for melanoma imaging and therapy. *Front. Pharmacol.* 13:829684. doi: 10.3389/fphar.2022.829684

Love, M. I., Huber, W., and Anders, S. (2014). Moderated estimation of fold change and dispersion for RNA-seq data with DESeq2. *Genome Biol.* 15:550. doi: 10.1186/s13059-014-0550-8

Maglangit, F., Yu, Y., and Deng, H. (2021). Bacterial pathogens: Threat or treat (a review on bioactive natural products from bacterial pathogens). *Nat. Prod. Rep.* 38, 782–821. doi: 10.1039/d0np00061b

Ny, L., Hernberg, M., Nyakas, M., Koivunen, J., Oddershede, L., Yoon, M., et al. (2020). BRAF mutational status as a prognostic marker for survival in malignant melanoma: A systematic review and meta-analysis. *Acta Oncol.* 59, 833–844. doi: 10.1080/0284186X.2020.1747636

Ouellet, D., Kassir, N., Chiu, J., Mouksassi, M. S., Leonowens, C., Cox, D., et al. (2016). Population pharmacokinetics and exposure-response of trametinib, a MEK inhibitor, in patients with BRAF V600 mutation-positive melanoma. *Cancer Chemother. Pharmacol.* 77, 807–817. doi: 10.1007/s00280-016-2993-y

Ramirez-Rendon, D., Passari, A. K., Ruiz-Villafan, B., Rodriguez-Sanoja, R., Sanchez, S., and Demain, A. L. (2022). Impact of novel microbial secondary metabolites on the pharma industry. *Appl. Microbiol. Biotechnol.* 106, 1855–1878. doi: 10.1007/s00253-022-11821-5

Rozeman, E. A., Dekker, T. J. A., Haanen, J., and Blank, C. U. (2018). Advanced melanoma: Current treatment options, biomarkers, and future perspectives. *Am. J. Clin. Dermatol.* 19, 303–317. doi: 10.1007/s40257-017-0325-6

Shams Ul Hassan, S., Ishaq, M., Zhang, W. D., and Jin, H. Z. (2021). An overview of the mechanisms of marine fungi-derived anti-inflammatory and anti-tumor agents and their novel role in drug targeting. *Curr. Pharm. Des.* 27, 2605–2614. doi: 10.2174/1381612826666200728142244

Shen, B., and Thorson, J. S. (2012). Expanding nature's chemical repertoire through metabolic engineering and biocatalysis. *Curr. Opin. Chem. Biol.* 16, 99–100. doi: 10.1016/j.cbpa.2012.03.006

Shimizu, T., Kawai, J., Ouchi, K., Kikuchi, H., Osima, Y., and Hidemi, R. (2016). Agarol, an ergosterol derivative from *Agaricus blazei*, induces caspase-independent apoptosis in human cancer cells. *Int. J. Oncol.* 48, 1670–1678. doi: 10.3892/ijo.2016.3391

Shriver, M., Stroka, K. M., Vitolo, M. I., Martin, S., Huso, D. L., Konstantopoulos, K., et al. (2015). Loss of giant obscurins from breast epithelium promotes epithelial-to-mesenchymal transition, tumorigenicity and metastasis. *Oncogene* 34, 4248–4259. doi: 10.1038/onc.2014.358

Sjoblom, T., Jones, S., Wood, L. D., Parsons, D. W., Lin, J., Barber, T. D., et al. (2006). The consensus coding sequences of human breast and colorectal cancers. *Science* 314, 268–274. doi: 10.1126/science.1133427

Song, J., and Shi, W. (2018). The concomitant apoptosis and EMT underlie the fundamental functions of TGF-beta. *Acta Biochim. Biophys. Sin.* 50, 91–97. doi: 10.1093/abbs/gmx117

Suhonen, V., Rummukainen, J., Siiskonen, H., Mannermaa, A., and Harvima, I. T. (2021). High regional mortality due to malignant melanoma in Eastern Finland may be explained by the increase in aggressive melanoma types. *BMC Cancer* 21:1155. doi: 10.1186/s12885-021-08879-1

Sung, H., Ferlay, J., Siegel, R. L., Laversanne, M., Soerjomataram, I., Jemal, A., et al. (2021). Global cancer statistics 2020: GLOBOCAN estimates of incidence and mortality worldwide for 36 cancers in 185 countries. *CA Cancer J. Clin.* 71, 209–249. doi: 10.3322/caac.21660

Tan, W., Pan, M., Liu, H., Tian, H., Ye, Q., and Liu, H. (2017). Ergosterol peroxide inhibits ovarian cancer cell growth through multiple pathways. *Onco Targets Ther.* 10, 3467–3474. doi: 10.2147/OTT.S139009

Tuntithavornwat, S., Shea, D. J., Wong, B. S., Guardia, T., Lee, S. J., Yankaskas, C. L., et al. (2022). Giant obscurin regulates migration and metastasis via RhoA-dependent cytoskeletal remodeling in pancreatic cancer. *Cancer Lett.* 526, 155–167. doi: 10.1016/j.canlet.2021.11.016

Whiteman, D. C., Green, A. C., and Olsen, C. M. (2016). The growing burden of invasive melanoma: Projections of incidence rates and numbers of new cases in six susceptible populations through 2031. *J. Invest. Dermatol.* 136, 1161–1171. doi: 10.1016/j.jid.2016.01.035

Wright, G. D. (2019). Unlocking the potential of natural products in drug discovery. *Microb. Biotechnol.* 12, 55–57. 10.1111/1751-7915.13351

Wu, H. Y., Yang, F. L., Li, L. H., Rao, Y. K., Ju, T. C., Wong, W. T., et al. (2018). Ergosterol peroxide from marine fungus *Phoma* sp. induces ROS-dependent apoptosis and autophagy in human lung adenocarcinoma cells. *Sci. Rep.* 8:17956. doi: 10.1038/s41598-018-36411-2

Xia, Y., Xu, F., Xiong, M., Yang, H., Lin, W., Xie, Y., et al. (2021). Repurposing of antipsychotic trifluoperazine for treating brain metastasis, lung metastasis and bone metastasis of melanoma by disrupting autophagy flux. *Pharmacol. Res.* 163:105295. doi: 10.1016/j.phrs.2020.105295

Xie, F., Ling, L., van Dam, H., Zhou, F., and Zhang, L. (2018). TGF-beta signaling in cancer metastasis. *Acta Biochim. Biophys. Sin.* 50, 121–132. doi: 10.1093/abbs/gmx123

Yan, S., Qi, C., Song, W., Xu, Q., Gu, L., Sun, W., et al. (2021). Discovery of GOT1 inhibitors from a marine-derived *Aspergillus terreus* that act against pancreatic ductal adenocarcinoma. *Mar. Drugs* 19:588. doi: 10.3390/md19110588

Yi, M., Lin, S., Zhang, B., Jin, H., and Ding, L. (2020). Antiviral potential of natural products from marine microbes. *Eur. J. Med. Chem.* 207:112790. doi: 10.1016/j.ejmech.2020.112790

Young, P., Ehler, E., and Gautel, M. (2001). Obscurin, a giant sarcomeric Rho guanine nucleotide exchange factor protein involved in sarcomere assembly. *J. Cell Biol.* 154, 123–136. doi: 10.1083/jcb.200102110

Zhou, B., Liang, X., Feng, Q., Li, J., Pan, X., Xie, P., et al. (2019). Ergosterol peroxide suppresses influenza A virus-induced pro-inflammatory response and apoptosis by blocking RIG-I signaling. *Eur. J. Pharmacol.* 860:172543. doi: 10.1016/j.ejphar.2019.172543

Zhu, Y., Zuo, W., Chen, L., Bian, S., Jing, J., Gan, C., et al. (2019). Repurposing of the anti-helminthic drug niclosamide to treat melanoma and pulmonary metastasis *via* the STAT3 signaling pathway. *Biochem. Pharmacol.* 169:113610. doi: 10.1016/j.bcp.2019.08.012

Ziogas, D. C., Konstantinou, F., Bouros, S., Theochari, M., and Gogas, H. (2021). Combining BRAF/MEK inhibitors with immunotherapy in the treatment of metastatic melanoma. *Am. J. Clin. Dermatol.* 22, 301–314. doi: 10.1007/s40257-021-00593-9

Frontiers in Microbiology

Explores the habitable world and the potential of microbial life

The largest and most cited microbiology journal which advances our understanding of the role microbes play in addressing global challenges such as healthcare, food security, and climate change.

Discover the latest Research Topics

See more →

Frontiers

Avenue du Tribunal-Fédéral 34
1005 Lausanne, Switzerland
frontiersin.org

Contact us

+41 (0)21 510 17 00
frontiersin.org/about/contact